FCC-ee Machine Detector Interface Alignment System Concepts

Léonard Watrelot

▶ **To cite this version:**

Léonard Watrelot. FCC-ee Machine Detector Interface Alignment System Concepts. Other [cond-mat.other]. HESAM Université, 2023. English. NNT : 2023HESAC016 . tel-04234967

HAL Id: tel-04234967

https://theses.hal.science/tel-04234967v1

Submitted on 10 Oct 2023

HAL is a multi-disciplinary open access archive for the deposit and dissemination of scientific research documents, whether they are published or not. The documents may come from teaching and research institutions in France or abroad, or from public or private research centers.

L'archive ouverte pluridisciplinaire **HAL**, est destinée au dépôt et à la diffusion de documents scientifiques de niveau recherche, publiés ou non, émanant des établissements d'enseignement et de recherche français ou étrangers, des laboratoires publics ou privés.

HESAM UNIVERSITÉ

le cnam

ÉCOLE DOCTORALE SCIENCE DES MÉTIERS DE L'INGÉNIEUR

ORGANISATION EUROPÉENNE SUR LA RECHERCHE NUCLÉAIRE

THÈSE

présentée par : **Léonard WATRELOT**
soutenue le : **19 septembre 2023**

pour obtenir le grade de : **Docteur d'HESAM Université**

préparée au : **Conservatoire national des arts et métiers**

Discipline : **Mécanique, génie mécanique, génie civil**

Spécialité : **Métrologie**

Concepts de systèmes pour l'alignement de la MDI du FCC

THÈSE dirigée par :
M. DURAND Stéphane Maître de conférences, Laboratoire Géomatique et Foncier, CNAM

et co-encadrée par :
M. SOSIN Mateusz Ingénieur, Organisation Européenne pour la Recherche Nucléaire

Jury

M. Andreas WIESER	Prof. Dr., Institute of Geodesy and Photogrammetry, ETH Zurich	Président
M. Andreas ARCHENTI	Prof. Dr., Center for Design and Management of Manufacturing Systems (DMMS), KTH Royal Institute of Technology	Rapporteur
Mme. Cornelia ESCHELBACH	Prof. Dr., Laboratory for Industrial Metrology, Frankfurt University of Applied Sciences	Rapporteuse
Mme. Mika MASUZAWA	Prof. Dr., High Energy Accelerator Research Organization (KEK)	Examinatrice

THÈSE

HESAM UNIVERSITÉ

le cnam

SCIENCE DES MÉTIERS DE L'INGÉNIEUR DOCTORAL SCHOOL
EUROPEAN ORGANISATION FOR NUCLEAR RESEARCH

THESIS

Presented by : **Léonard WATRELOT**
Submitted : **19.09.2023**

in partial fulfillment of the requirements for the degree of : **Doctor of HESAM University**

prepared in : **Conservatoire national des arts et métiers**

Discipline : **Mechanics, mechanical engineering, civil engineering**

Speciality : **Metrology**

FCC-ee Machine Detector Interface Alignment System Concepts

THESIS directed by :
M. DURAND Stéphane Associate professor, Laboratoire Géomatique et Foncier, CNAM

and co-directed by :
M. SOSIN Mateusz Engineer, European Organisation for Nuclear Research

Jury

M. Andreas WIESER	Professor Doctor, Institute of Geodesy and Photogrammetry, ETH Zurich	President
M. Andreas ARCHENTI	Professor Doctor, Center for Design and Management of Manufacturing Systems (DMMS), KTH Royal Institute of Technology	Reviewer
Mme. Cornelia ESCHELBACH	Professor Doctor, Laboratory for Industrial Metrology, Frankfurt University of Applied Sciences	Reviewer
Mme. Mika MASUZAWA	Professor Doctor, High Energy Accelerator Research Organization (KEK)	Examiner

THÈSE

Acknowledgments

I would like to thank the various people who contributed in one way or another to this PhD study:

First and foremost, I would like to thank Dr. Stéphane Durand from the Laboratoire Géomatique et Foncier, CNAM for supervising and examining my PhD thesis. His patience and professionalism allowed me to pursue my research interests while also improving my work from the computation to the redaction. I am truly grateful for all the time spent on mathematical clarifications, administrative procedures, and especially for the careful reviewing of the papers and the thesis. Thank you.

Then I would like to deeply thank Dr. Mark Jones, for proposing the subject of this thesis and for introducing me to the challenges of this subject. His deep knowledge on particle colliders alignment, from the geoid modeling to the smoothing of the alignment in the MDI, was invaluable and helped me a lot along my studies. Thank you.

I would like to thank Mr. Mateusz Sosin, from CERN, for his deep technical knowledge, especially on Frequency Scanning Interferometry. I'm also very thankful for the test bench design for the In-line Multiplexed and Distributed FSI, and his comments and advices for the redaction of papers and the thesis. Thank you.

I would like to sincerely thank Dr. Helene Mainaud Durand, from CERN, for the support along the study. Her expertise was priceless, and she was always wiling to share both contacts and experience on the particle colliders alignment. I am also extremely grateful for her advices and time spent on the different presentations given during the study and on the thesis document. Thank you.

I would like to thank Dr. Manuela Boscolo, for welcoming me in the Machine Detector Interface working group. This accelerated the design thanks to fruitful discussions with the experts of the working group. I'm also very thankful for the invitations to present at multiple events, which punctuated my thesis and motivated me towards the design of a new system. Thank you.

I would like to thank Dr. Michael Koratzinos from CERN, for the availability of the elegant FCC-ee MDI design, that allowed me to design a system and get the sizes at stake. I'm also very grateful

for the comments and advices given on the system, and the stimulation induced by his interest in my study. Thank you.

I would like to thank Dr. Mika Masuzawa from KEK, for her expertise and for sharing the data and challenges that have been faced at SuperKEKB/Belle II MDI. Thank you.

I would like to thank the colleagues from the Istituto Nazionale di Fisica Nucleare, Dr. Fabrizio Palla, Mr. Luigi Pellegrino and Mr. Francesco Fransesini for sharing their experience on the DAFNE/KLOE MDI and the ongoing mechanical study of the FCC-ee MDI. I'm also very grateful for their feedback on my system and their multiple comments on the mechanical design, underlining the challenges that will need to be faced. Thank you.

I would like to thank Mr. Camille Vendeuvre and Mr. Vivien Rude from CERN for the computing and the mathematical advices given all along the study. Thank you.

I would like to thank Mr. Guillaume Kautzmann and Dr. Juergen Gutekunst from CERN, for their support and reactivity on the LGC++ software. I am very grateful for the multiple sub-versions created for my study. Thank you.

I would like to thank Mr. Andreas Herty, Mr. Dirk Mergelkuhl and Mr. Patrick Bestmann for their share of experience of the LHC, the detectors and the sensors used at CERN. Thank you.

I would like to thank Mr. Michel Rousseau and Mr. Okan Dag for their mechanical advices and the making of the prototypes and test benches all along the thesis. Thank you.

I would like to thank my familly for their encouragement along these years of study. Thank you.

Résumé

Cette thèse a été effectuée dans le cadre de l'étude du collisionneur de leptons faisant partie du projet de futur collisionneur circulaire (FCC) au CERN, devant être construit en 2040, après l'amélioration du grand collisionneur d'hadrons. Cette étude se concentre en particulier sur l'alignement et le suivi de composants de l'accélérateur installés à l'intérieur du détecteur. Cette zone correspond à l'interface entre l'accélérateur et le détecteur (appelée machine detecteur interface – MDI), proche du point d'interaction où se déroulent les collisions. Les éléments à aligner (quadrupôles, solénoïdes) vont être très difficiles d'accès et dans des conditions particulières : radiations, champs magnétiques et températures cryogéniques. Des tolérances d'alignement très exigeantes sont aussi attendues, de l'ordre de quelques dizaines de micromètres. L'étude des MDI existantes, ainsi que des projets de MDIs pour les collisionneurs du futur, ont montré que les systèmes existants ne sont pas capables d'atteindre les attentes de ce projet en termes d'alignement. Une nouvelle stratégie est donc proposée, basée sur deux systèmes distincts : un premier système d'alignement mesurant les positions des éléments situés dans le détecteur, et un second système permettant le transfert de cet alignement entre les deux côtés du détecteur. Ce deuxième système sera composé d'un réseau dense de mesures de distance basé sur la technologie d'interférométrie par balayage de fréquence (Frequency Scanning Interferometry – FSI), permettant d'utiliser la mesure multicible, densifiant le réseau sans en augmenter la complexité. Le système interne est quant à lui composé d'un système de mesure de déformation (du support des éléments étudiés) effectué grâce à une nouvelle technologie. Ce capteur est capable de mesurer les longueurs 3D de plusieurs portions d'une même fibre optique, séparées par des miroirs semi-réfléchissants. Un réseau de plusieurs de ces fibres placées en formes d'hélices permet une mesure précise des déformations du support étudié. Des simulations sur ce système faites par un code python, écrit dans le cadre de cette thèse, montrent une précision micrométrique de la mesure de déformation. Des simulations prenant en compte les deux systèmes d'alignement montrent également une précision

micrométrique pour l'alignement des composants de la MDI. Il est important de noter que le design de la MDI du FCC-ee est encore balbutiant et que de nombreux changements sont attendus, changements qui impacteront les précisions calculées jusqu'ici. La deuxième partie de la thèse se concentre sur le capteur au sein du système mesurant les déformations, basé sur la mesure de distance le long d'une fibre optique. Deux technologies sont capables d'effectuer ces mesures : le SOFO (Surveillance d'Ouvrages par Fibres Optiques) qui est actuellement resté au niveau de prototype, et le FSI (interférométrie par balayage de fréquence) actuellement développé au CERN. Un banc de test a été créé afin étudier ce capteur FSI et de vérifier sa capacité à mesurer simultanément et indépendamment plusieurs portions d'une même fibre, en permettant une mesure simultanée avec une mesure de distance interférométrique classique. L'utilisation de connecteurs de fibres optiques classiques en tant que miroirs semi-réfléchissant est responsable d'un bruit de mesures trop élevé du système pour son utilisation voulue. Mais, cela est corrigé par l'utilisation de miroirs semi-réfléchissants directement imprimés dans la fibre grâce à un laser UV, diminuant le bruit de mesure à 2 μm. La dernière partie de la thèse est consacrée aux explorations, notamment des autres utilisations possibles du système de mesure de déformation, ou encore d'un système de déplacement des composants de la MDI à distance, sans avoir à les démonter. Enfin, une réflexion est proposée sur la possible communication entre le système d'alignement de la MDI et les systèmes d'alignement des sous détecteurs.

Mots-clés : FCC, Métrologie, MDI, Alignement, FSI, Déformation

Abstract

This thesis is in the framework of the lepton collider part of the Future Circular Collider project, aiming to be the next flagship project at CERN after the High Luminosity upgrade of the Large Hadron Collider, in 2040. The study focuses on the alignment, and monitoring of the alignment, of some accelerator components located inside the physics detector, close to the collision point. This area corresponds to the interface between the accelerator and the detector, called the machine detector interface (MDI). The studied components (quadrupoles, solenoids) will be very difficult to access and in harsh conditions, as high radiations doses, magnetic fields and cryogenic temperatures are expected. Tight alignment requirements are also needed, being only tens of micrometers for these components. These conditions prevent the use of existing systems installed in other MDIs, but also for project systems planned for next generation colliders. A new strategy for the alignment of this area has therefore been proposed, based on two sub-systems. One of these systems is operating on the components, inside the detector, while the second will be used to transfer the alignment from one side of the detector to the other. This last system is composed of a dense network of interferometric distance measurements, based on the frequency scanning interferometry (FSI), and could therefore use its multitarget capabilities to keep satisfactory uncertainties. The system placed inside the detector, measuring on the studied components, is based on a new technology used for the monitoring of the deformation of the components support, indirectly determining their alignment. This new technology is a sensor able to measure simultaneously and independently the 3D lengths of multiple portions of a single optical fiber, separated by semi-reflective mirrors. A network of such sensors, placed in helical shapes along the support, allows a precise deformation monitoring of this support. Simulations, performed with a python code written in the framework of this thesis, showed micrometric uncertainties for the alignment monitoring of two components located on opposite sides of the detector, which is satisfactory. Though, it must be kept in mind that the design of both the detector and the accelerator

are still under study and will most likely change, which will impact the design of the alignment system and its performances. The second part of the thesis is dedicated to the study of the new technology used for the deformation sensor. Two systems are currently able to perform such measurements: the SOFO (Surveillance d'Ouvrage par Fibre Optique) currently locked and stopped at a prototype state, and an FSI system currently developed at CERN. A test bench has been created to study and confirm this FSI sensor characteristics and behavior. This bench had a multiple portions fiber, studied by comparison with regular interferometric distance measurements. Results were very satisfactory, with independent and simultaneous measurement, as expected. Even though the measurement noise was too big when using fiber connectors as semi-reflective mirrors, it has been corrected by using semi-reflective mirrors printed directly inside the fiber thanks to a UV laser, going down to a 2 μm. The last part of the thesis is dedicated to exploration, starting by the other possible applications of the deformation system. The study of additional systems, such as an adjustment system for the components difficult to access was discussed, underlining their advantages in such complex design. Finally, a reflexion about a link between the design alignment system and the physic detector alignment systems was proposed, as such communication and interaction between two different entities, rarely done so far, could represent advantages for both.

Keywords : FCC, Metrology, MDI, alignment, FSI, deformation

Contents

List of Tables

List of Figures

Introduction

The Organisation Européenne pour la Recherche Nucléaire (European Organisation for Nuclear Research, CERN) is the largest particle physics laboratory in the world, currently composed of 23 member states and located at the border between France and Switzerland, near Geneva. CERN was formed in 1954 and since then has designed, constructed and exploited multiple particle accelerators, colliders, and experiments. A collider is composed of an accelerator, which bring particles to the desired energy, before colliding them at the center of detectors, which study the consequences of the collisions. Colliders and detectors depend on multiple parameters including the type of particle used for the collisions, the particles studied by the detector, the collision energy and so on. It impacts the shape of the collider and the components used to accelerate and steer the beam. The two main categories of collider shapes are linear and circular, each of which have advantages and disadvantages.

Linear colliders accelerate particles in a straight line from each side of the detector located at the Interaction Point (IP). The main advantage of the linear layout is the absence of energy loss due to steering of the beam. This loss is synchrotron radiation, emitted by charged particles when the beam is steered for its trajectory, to form a circle, for example. Therefore, this loss is not the limitation for linear collider. Other limitations include the unique use of the accelerated beam, which is not recovered after collisions. There is also the space required by the accelerator, which needs to be as compact as possible in order to accelerate the particle to collision energy while not taking too much space. Finally, it implements only one IP, which can limit the confirmation or redundancy of measured discoveries done by the detector. To answer that challenge, some future linear colliders propose two detectors in push-pull configuration, having one being used while the other is in maintenance position. Circular colliders, on the other hand, are implementing a circular trajectory, which allows to accelerate the beams to higher energies and recover the beams after the collisions to reuse them. It also allows to place multiple detectors on the beam path in order to multiply the amount of physics data. But the beam is degraded after each collision, and therefore not too many detectors can be installed along the collider. Depending on the size of the machine, the particle accelerated, and many other variables, a collider can usually host from one to four detectors. Finally, the main limitation of the circular collider is the synchrotron radiation emission when steering the beam, representing an energy loss for the colliders, and therefore limiting the maximum energy of the beam.

Some colliders are famous, such as the Tevatron in the Fermi National Accelerator Laboratory in the United States [15], the SuperKEKB in the High Energy Accelerator Research Organisation in

Japan [16], The Beijing Electron-Positron Collider II (BEPCII) in China [17] and the Large Hadron Collider (LHC) at CERN [18]. The LHC is the biggest circular particle accelerator in the world, with a 27 km circumference tunnel, buried 100 m underground. It feeds collisions to four big detectors: ATLAS (A Toroidal LHC Apparatus) , CMS (Compact Muon Solenoid), LHCb (LHC beauty) and ALICE (A large Ion Collider Experiment). The LHC started taking data in 2009 and performed the discovery of the Higgs boson in 2012. It is currently running and will do so until the end of 2025 where it will be upgraded to become the High-Luminosity LHC (HL-LHC), boosting its performances [19]. While this period of exploitation of the HL-LHC is known and prepared, the CERN future after this machine is still unknown. Three projects are competing: the Muon Collider, the Compact Linear Collider and the Future Circular Collider.

The Muon Collider aims to do powerful collisions with muons rather than leptons or hadrons, to explore the high energy frontier [20, 21]. The advantages of accelerating muons being that they are fundamental particles requiring less energy to run the collider, with reduced energy losses when curving the beam. But even though muons emit about two billion times less synchrotron radiations than electrons, their lifetime of 2.2 microseconds make them difficult to deal with. The technology required to handle these particles is not entirely ready yet, and therefore this project is the least advanced of the three, with no conceptual design report available yet.

The Compact Linear Collider (CLIC) is a multiple stages project of a linear collider, to collide electrons and positrons at energies ranging from 380 GeV to 3 TeV [5]. Following this energy spectrum, the site hosting the machine would range from 11 to 50 km long. Goals for the machine are the study of the Higgs Boson and precise measurements of the top quark, among many others. This machine plans to use a two beams acceleration concept, decelerating a high intensity electron beam (the “drive beam”) through a special power extraction structure to feed Radiofrequency (RF) power needed to accelerate the main beam. A conceptual design report [5] has been written, underlining the maturity of the project.

The last project aiming to be the next flagship project after the High-Luminosity upgrade of the LHC is the Future Circular Collider (FCC) [22]. It is a multiple stages project of 91 km long circular colliders. The first stage would implement a lepton version of the FCC (FCC-ee), studying the electron-positron collisions, while the second stage would be a hadron version of the FCC (FCC-hh). The main goal is to push the energy and intensity frontiers by reaching collision energies of 100

TeV. A conceptual design report has been edited, and the FCC community is currently working on a technical and financial feasibility study. This thesis is part of that framework and more precisely on the lepton stage, the FCC-ee.

Each collider requires an interface between the accelerator (also called "machine") and the detectors. While the accelerator brings the particles to the desired energy and prepare the beams for the collisions, the detector reads the consequences of the collisions in order to study the physics behind it. The area and components composing this interface between the machine and the detector, also called Machine Detector Interface (MDI), are changing diametrically depending on the collider. But, for all of them, the alignment of that specific area is extremely important in order to reach the designed luminosity, which is the number of particles that can be squeezed through a given space in a given time [23], directly linked to the number of collisions and therefore to the probability of new physics discoveries. The alignment of the MDI is a common challenge for all the projects, as these projects are implementing more and more advanced concepts and tight requirements in order to push the technical limits. These concepts translate in a more dense MDI with more components to align, at precision never asked before. These requirements translate to nanometer scale beams and impressive luminosity values. But in return, the alignment system asks reaches never seen levels of complexity and needs to adapt to difficult conditions while being stable and accurate. Conditions are so difficult to face that no solution have been found for the alignment of the MDI of the last generation colliders and for the current projects. For all of them, the alignment and even the monitoring of the components have been asked, underlining the need for such system.

The overall aim of this work is to propose a system able to monitor the alignment components inside the FCC-ee MDI at the requested specifications. The goal is to have a robust and accurate system, being versatile enough to adapt to the multiple changes which will occur in the still evolving FCC-ee MDI. In order to do so, three objectives have been identified. First, a careful study of the situations in the FCC-ee MDI is performed, in order to be aware of the challenges to face. The study of the design, the components, and their location, the requirements and so on, is important in order to have a complete view of the subject. Then, a careful study of the existing infrastructures and systems around the world is performed. This allows concluding if any system can be used in the FCC-ee with or without modifications and/or improvements. This will finally lead to the design of a system that can be used in the FCC-ee MDI, for the alignment components.

In order to cover these objectives, the thesis is composed of five chapters. The first chapter will cover the general description of the machine detector area, underlining the alignment procedure for that zone. The elegant but complex design of the FCC-ee MDI will be described in details, and the challenges highlighted. The second chapter will list existing MDIs across the world, sharing similar characteristics with the FCC-ee MDI. Ongoing projects and their systems are also studied. Chapter three will describe the proposed alignment strategy for the FCC-ee MDI, underlining the equations and technologies. The fourth chapter will cover the technical aspects, with the study of the in-line multiplexed and distributed FSI, a new sensor technology planned to be used in the FCC-ee MDI alignment monitoring system. Finally, the fifth chapter will discuss further developments to explore in the future, to extend the possibilities for the alignment and monitoring system.

Chapter 1

The Machine Detector Interface

1.1 Introduction to the Machine Detector Interface notion

The MDI is usually defined as the area which covers the aspect of common concern of both the accelerator and the detector. It is a really important area for the exploitation of the machine and the reach of the designed luminosity, as it is where the beams are prepared for the collisions. to do so, specific components only found in the MDI are installed and operated, like the final focusing quadrupoles for example. The MDI, sometimes called "Machine Experiment Interface" or "Collider Experiment interface", can be of multiple layouts depending on the type of collider, the physics studied, and the technology used. Some are extremely long and wide, with accelerator components and detector components well separated, while some are dense and have accelerator components inside the detector. Conditions in this area are usually harsh, especially with a lack of space, radiations and intense magnetic fields. Sometimes, the final components are also cooled down to cryogenic temperatures. A generic definition for the MDI notion is near impossible, as each collider has a different MDI. Some aspects are similar between different machines, like focusing and cleaning of the beam, and sometimes the same components can be found in two different MDI. But shape, size, positions, and design change with each MDI, making them all different and unique. A precise definition of the geographical and responsibility boundaries, and the components included, also depends on the expert describing it. Therefore, the MDI according to the physicists will be different from the one by the cryo-experts, the vacuum experts, or the surveyors. This difference can be up to more than 100 m of components between two definitions. The MDI definition used for this thesis, close to the one currently adopted by surveyors, will be expressed precisely in the section.1.3.

Finally, the last layer covering the MDI is the responsibility layer. At CERN, for example, the responsibility of the accelerator and the detector are not to the same entity. While the accelerator is managed by CERN, the detectors are operated by collaborations of multiple institutes from all over the world. These collaborations share the detector to the institutes, which build a concept, assemble and operate a subdetector depending on their expertise.

1.2 Alignment of the MDI

The alignment of an MDI is similar to the alignment of the rest of a collider, and refers to 3 actions: pre-alignment, monitoring and re-adjustment (if needed). The main difference is that, in an

MDI, complex design, specific components and tight requirements make the alignment raise new and exotic challenges.

1.2.1 Pre-alignment of the MDI

The pre-alignment corresponds to the process of positioning the elements (dipoles, quadrupoles, sextupoles, ...) from their assembly to the installation in the tunnel. This process starts with the measurement of the main axis of the components: magnetic, electrical or mechanical axis depending on the type of component studied. The axis is measured with respect to a set of alignment reference points scattered on the outside of the object, in a process called fiducialisation. Then, these points are used for the positioning and the alignment of the object in an assembly it is part of, or directly in the tunnel. Pre-alignment of some particular couples of components is very important, such as for the Beam Position Monitor (BPM) and its associated quadrupole, for example. The knowledge of their respective misalignment is very important in order to perform a Beam Based Alignment (BBA) at the beginning of the run of the machine. This BBA notion is described in more details in the section 1.2.4. Fiducialisation and pre-alignment is usually done thanks to laser trackers, for both the assembly and installation in the tunnel. A Coordinate Measuring Machine (CMM) and micro-triangulation can also be used for the assembly of more stringent alignment and positioning requirements [24], when the size of the components allows it.

1.2.2 Monitoring the alignment of the MDI

Once the pre-alignment done, a smoothing is performed to correct big offsets between consecutive components. The collider can be started, and the pilot beam can be sent. But the alignment deteriorates with time as the tunnel and the caverns move due to seasonal changes, earth tides and settlement of the tunnel after construction. Moreover, vibrations, mechanical constraints from vacuum or cooling down and aging of the structures, can displace the components. Therefore, the alignment needs to be monitored regularly, and measurement campaign must be performed during shutdowns and technical stops. When possible, the alignment is asked to be monitored continuously, even during the run of the machine, allowing a follow-up of the position of the components. By doing that, the beam position can be known in real time, allowing the beam diagnostic teams to tune the magnets on the beam path accordingly. Periodic and punctual monitoring of the alignment is done thanks to laser trackers,

digital levels and wire offsets measurement devices, while continuous monitoring is usually carried out by specific sensors. In the LHC, for example, a combination of 3 sensor systems is used to monitor in real time the position of the low-β quadrupoles, the last components before the IP [25]. These systems are the Wire Positioning System (WPS), the Hydrostatic Leveling System (HLS) and the Distance Offset Measurement Sensor (DOMS) [26]. They are permanently installed on the components and are measuring non-stop the radial, vertical and longitudinal position of the quadrupoles respectively. These systems are described in more details in the next chapter. It is interesting to note that the importance given to that continuous monitoring of the last accelerator components is underlined by the requirements of most of the next generation colliders to have such system installed in their MDI.

1.2.3 Re-adjustment of the MDI

When the MDI is aligned and the alignment regularly monitored, sometimes, large displacements of components occur, requiring an intervention to re-align them. This operation is called readjustment. This is usually done just after the monitoring campaign (when the monitoring is punctual) or during shutdowns when the machine can be accessed. It is mainly done manually, acting directly on the supports of the components. In some rare situations, components are placed on remote controllable actuators. It is the case in the LHC, where the low-β quadrupoles can be remotely displaced from the control room [27]. This implementation works in tandem with the sensors installed and continuously monitoring the position of these elements. This re-adjustment is regularly asked for the next generation of colliders, but depends heavily on the complexity of the MDI design. Moving very important objects remotely is still a risky operation, especially when there is cryogenic cooling or vacuum connections involved. This is why implementations of such systems are still rare occurrences.

1.2.4 Beam Based Alignment

Additional documents describe the BBA and provide some examples of use in accelerators [28, 29, 30, 31, 32, 33, 34, 35].

The BBA uses the particle beam itself for the alignment, aiming at micron-level. This technique is standard in many particle accelerators and colliders. It is based on a variation of the strength of a quadrupole, which impacts the trajectory of the beam. The created deflection is then measured as a function of the quadrupole strength, and the offset between the beam and the quadrupole is deduced.

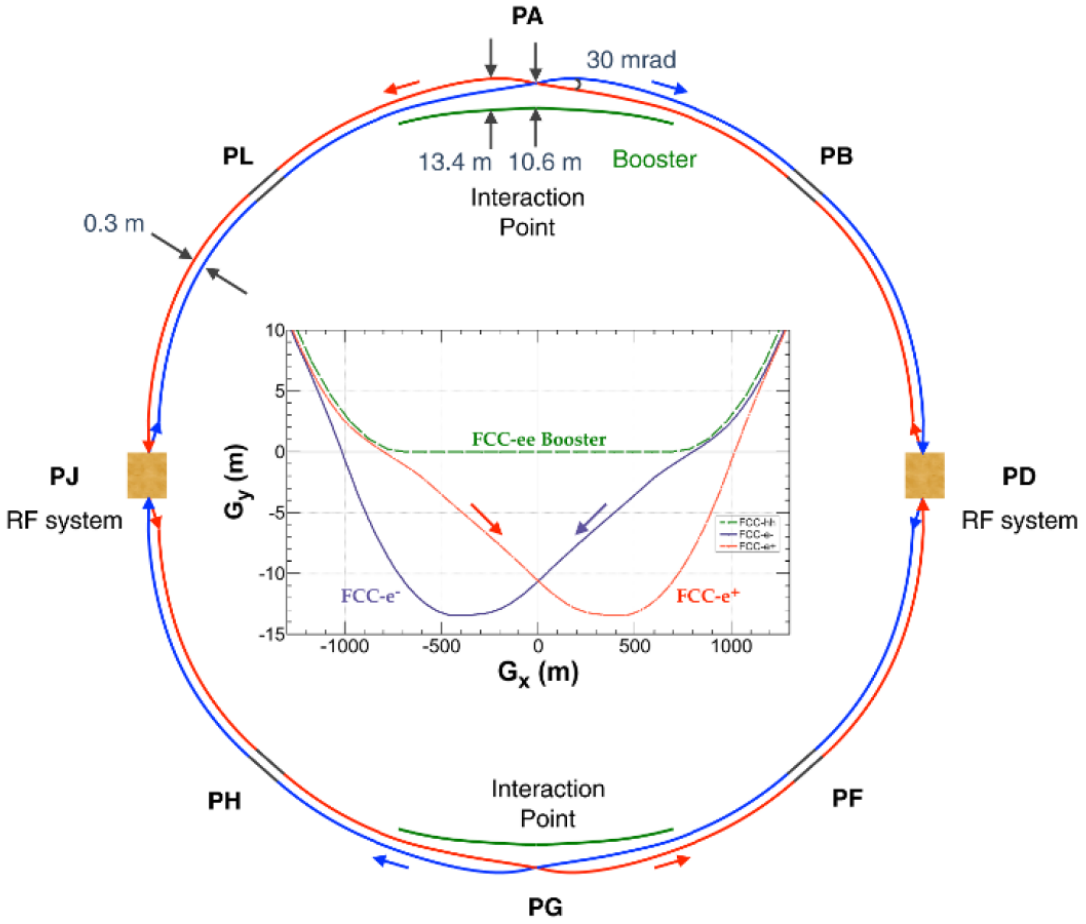

Figure 1.1: Current layout of the FCC-ee, with a zoom on the IP [2].

The beam position is measured thanks to the BPM placed after the quadrupole. Some accelerators are changing the beam energy, which also implies a deflection of the beam that can be measured by a BPM.

This procedure is extremely precise, but it can have some limitations. The first one being that it requires the beam to circulate in the machine, in order to be able to modify its direction. It implies to use regular survey techniques to reach a good alignment, to be able to perform the BBA. A second limitation may be when quadrupoles are not tuneable individually as, sometimes, several are powered by the same power line. Then, the offset between the quadrupole and the BPM should also be known very precisely, as the range and precision of the BPM can limit the precision of the BBA. Finally, if the misalignment of a quadrupole is too big, an intervention in the tunnel is required, in order to re-align the quadrupole.

1.3 The FCC-ee MDI

Being a next generation collider, the FCC-ee will implement the latest upgrades and optimizations in order to make it as profitable for the physics research as possible.

1.3.1 FCC-ee MDI design

Fig.1.1 shows the overall layout of the FCC-ee with a zoom on the interaction regions. The eight access points (from PA to PL) are also represented. For now, detectors will be located in PA and PG, where the beams are crossing at a 30 mrad angle. RF systems, used for the acceleration, are planned to be placed in PD and PJ. The booster, used to bring the beams to the wanted energy, will be located in the same tunnel. Interaction regions are represented in more details in the zoom in the center of the figure, highlighting the crossing angle and the booster location.

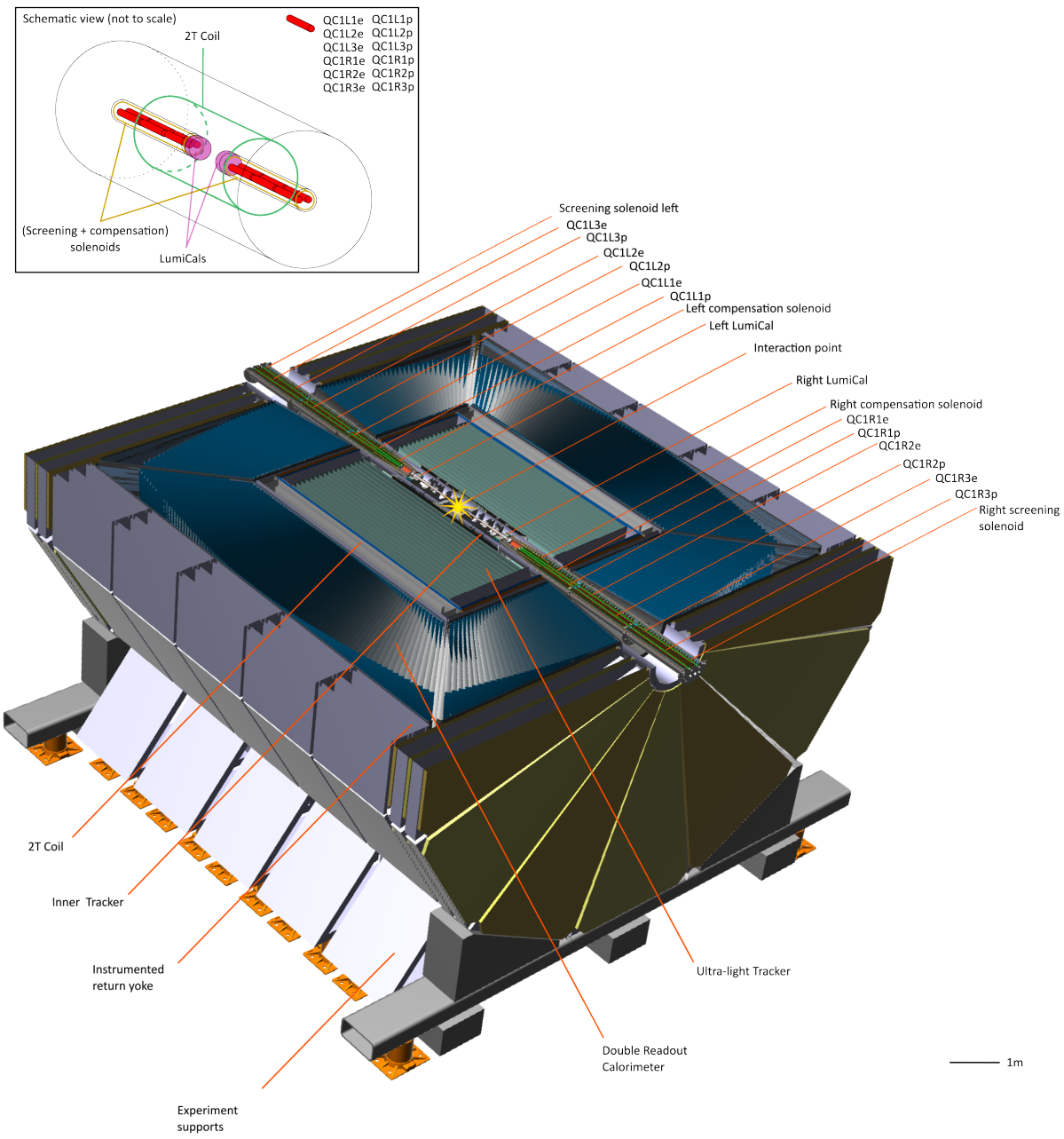

Figure 1.2: Initial design of the FCC-ee MDI (Courtesy of the MDI working group, 2023)

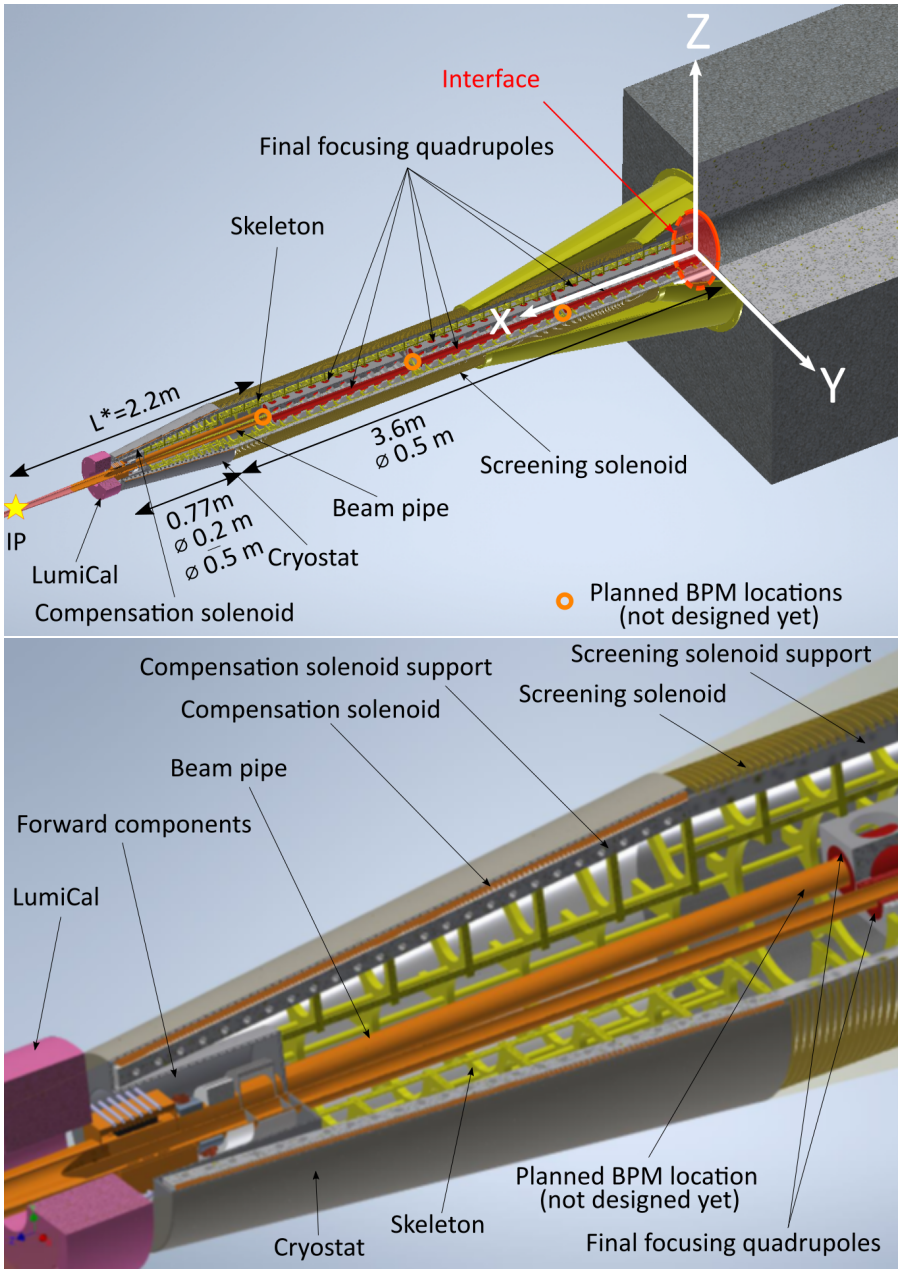

Figure 1.3: Inner components, original assembly. On the top picture, a general view of the assembly and the coordinate system associated to the plate. The second picture is zoomed in order to see the different elements, from the inside out: the beam pipe (orange), the final focusing quadrupoles (red), the skeleton (yellow), the support and cooling structure for the solenoids (gray), the screening and compensation solenoids (orange) and the thin cryostat (gray). The Free Lenght (L*) corresponds to the distance between the IP and the face of the closest quadrupole. The interface used as reference for the deformation monitoring system is placed at the outer end of the assembly. (Courtesy of Michael Koratzinos, 2023).

The 30 mrad crossing angle comes from the crab-waist configuration of the FCC-ee, implemented in order to reach the designed luminosity. This configuration implies to have a big Piwinski angle, which is obtained by decreasing the horizontal beam size and increasing the crossing angle [36]. The 30 mrad crossing angle can be seen on Fig. 1.1, as long straight sections are required for the incoming beam before the detector, and a more bent section is required after the detector in order to catch up to the layout. The goal of this straight section before the collision is to avoid synchrotron radiation, generated by any bend of the beam, to be directed toward the detector. This radiation is emitted after the collision in the bent section, and will irradiate the tunnel wall rather than the detector. The straight sections will be implemented over almost one kilometer on each side of the IP, to decrease the synchrotron radiation to a satisfactory lever at the detectors level. At some points, the incoming straight beam and the outgoing bent beam will be separated by more than 12 m. This separation, in addition to the layout of the booster and the FCC-hh (aiming to take the FCC-ee place at the end of its run) implies to have a widening tunnel when coming close to the detector, going from a 5 m wide tunnel to an almost 25 m wide tunnel. Looking more closely near the IP as illustrated in Fig.1.3, this increased crossing angle allows having distinct final focusing quadrupoles for the two beams. The distance between the IP and the final focusing quadrupoles (called the free-length and noted L*) can also be smaller, allowing a better focusing of the beam, which leads to a smaller beam size and a higher resulting luminosity. The 2.2 m L* implies to have the final focusing quadrupoles inside the detector as shown on Fig.1.2. This figure shows the complexity of the MDI, as not only the final focusing quadrupoles, but an entire assembly shown on Fig. 1.4 will need to fit and sit inside the detector. This assembly, entirely supported in a cantilever configuration, from the outside of the detector thanks to a skeleton, will hold six final focusing quadrupoles (in the shape of a 15 cm diameter cylinder and 1 m long, design not definitive), multiple BPM (no design available yet), and a Luminometer (LumiCal, 280 mm diameter cylinder, 116 mm long) located at the extremity. The final focusing quadrupoles will need to be protected from the detector's magnetic field by two solenoids: the screening solenoid in the shape of a 3.6 m long cylinder with a 0.25 cm radius, and the compensation solenoids, a 0.77 m long truncated cone going from 0.25 m radius to 0.1 m radius. The final focusing quadrupoles and the two solenoids will operate at cryogenic temperature, requiring a cryostat around the assembly. This cryostat is currently designed to be a skin-like cryostat, composed of a 2 mm vacuum layer trapped in between two 1 mm layers of steel. The beam pipe, on the other hand, will be at room temperature,

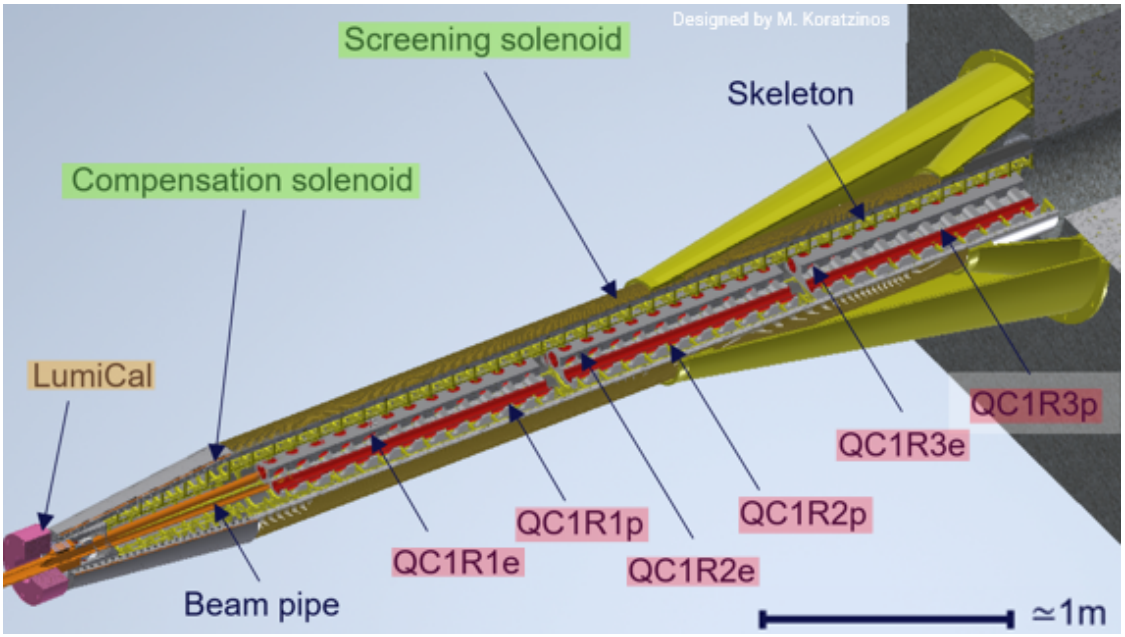

Figure 1.4: Current design of one side of the MDI: final focusing quadrupoles, highlighted in red, and solenoids (highlighted in green) are inside a thin cryostat. These elements, and the LumiCal at the end, are supported by a skeleton.(Courtesy of Michael Koratzinos, 2023)

implying to have another very big temperature gradient in the MDI. Such assembly will be installed on each side of the detector, making this region extremely dense in terms of number of components and challenges. The maximum deformation allowed by the distance between the cryostat and the inner wall of the detector is 2 mm. In case of bigger deformation of the assembly, the cryostat would enter in contact with the detector causing damage to both, and therefore must be avoided. Longitudinally, the problem is similar, and the deformation must not be too big to limit the strain on the vacuum bellows connecting the assembly and the center of the detector.

1.3.2 Challenges of the FCC-ee MDI

The MDI area, being a strategic point in the collider, houses a lot of technical challenges and really tight requirements. First, the available space inside the detector is extremely limited, as the detector experts want as much space as possible for their sensors. The dense assembly will need to be carefully designed in order to fit all the components. Then, intense magnetic fields will be generated, from both the detector and the assembly. The cryogenic temperature and temperature gradients will also be a challenge when designing supports and sensors to go near the final focusing quadrupoles, and high

radiation doses are expected inside the detector [37]. Finally, additional difficulties, due to vacuum, vibrations or any other reason, may also appear later in the design process.

Parallel to these challenges, tight alignment requirements and a continuous monitoring have been asked for the final focusing quadrupoles, solenoids, BPMs and LumiCals [2]. The FCC-ee conceptual design report specified these to be 0.1 mm (1 σ) alignment requirement for final focusing quadrupoles on the same side of the detector and 0.2 mm (1 σ) from one side to the other, which were the values asked for the LHC MDI alignment. But since then, tighter requirements have been requested for these components, going towards a 30 μm requirement for the alignment of the final focusing quadrupoles [38, 39] and 50 μm requirement for the alignment of the LumiCals [40]. Even though values are given, the definition of what needs to be aligned is still not clear, and it is usually assumed to be the magnetic or electrical axis of the component. Having magnets and solenoids inside a magnetic field will generate torque between these components, due to the Lorentz force. This justifies the monitoring of the solenoid position in order to minimize this force, which can reach multiple tons if these solenoids are not well aligned [41]. The alignment monitoring system will need to be able to deal with all these harsh conditions while being small enough to fit and precise enough to reach the requested requirements. This configuration, long and narrow space constraints with no stable reference point at the end, is one of the most difficult situation for surveyors in general. The measurement uncertainties at the end will therefore depend only on the measurements along the path, which are not in an ideal configuration, favorable to error propagation. In such situations, long networks are strengthened by stable physical reference, not depending on measurement. A wire, taking the shape of a straight line (from a top view) and having a sag (from a lateral view) is used at CERN for example, with sensors measuring that reference, which do not lose precision with the distance. A water level is also a stable reference used around the world. It follows the geoid, which can be approximated as simpler shapes depending on the distance: a plane in short distances, for example. Sadly, none of these stable references can be implemented in the FCC-ee MDI, therefore requiring to deal with that difficult configuration.

Another challenge will be caused by the responsibility sharing, that will multiply the contacts for the design, and therefore it will increase the complexity of the integration process.

Finally, the last big challenge is the still evolving design. Having shapes and positions changing with each iteration makes the design of an alignment and monitoring system a difficult operation.

1.4 Discussion

Even though the MDI notion can refer to the ± 1 km around the interaction point, this thesis will focus only on the components inside the detector: the twelve final focusing quadrupoles, the BPMs, the two LumiCals, the two compensation and the two screening solenoids and eventual additional components added later. The monitoring of this specific area (inside a long and cylindrical assembly) is a very difficult situation to deal with as a surveyor. Usually, physical references are used in such situations, like a stretched wire or a water surface. It allows to have a low error propagation over long distances, as underlined by the use of such techniques in the LHC, as showed later in section2.1.3. But, in our case, these physical references cannot be installed. Therefore, so far, there is no solution to align and monitor the alignment of this MDI. Regarding the target measurement uncertainty, numbers available are from various working group presentations. But these numbers are stated for specific reasons, like limiting one type of radiation of to reach a certain beam stability. But these numbers are just iterations converging toward final definitions. Some numbers have been chosen for our studies (the most constraining value at the time, in order to satisfy everyone): 30 μm (1 σ) for the final focusing quadrupoles and the BPMs, 50 μm (1 σ) for the LumiCals and 100 μm (1 σ) for the solenoids. These requirements have not been clearly defined yet and are understood to be requirements between elements from both side of the detector. These numbers are defined for the translation offsets between the components, and angle requirements will need to be on the same order of magnitude in the μrad range. It is important to note that these requirements have been stated as general requirements which need to be broken down in specification for the alignment system but also requirements for the manufacturing, the assembly, the magnetic, or electric field measurement and so on [42]. Experience from previous accelerator projects indicates that a reasonable assumption for the relative radial alignment precision can be derived by applying a factor 1/3, resulting in a target measurement uncertainty of around 10 μm for the alignment sensors.

Even though the straight and bent section before and after the detector do not have any alignment requirement stated yet, the design of an alignment system for that area is less difficult thanks to all the space available around the accelerator, as the tunnel is widening to meet the accelerator cavern size in these areas. In addition, some solutions exist, like for the HL-LHC project [19] or for linear colliders like CLIC [43], which usually have tighter alignment requirement. Therefore, the accent will

be put on the design of a monitoring system for the inside of the detector, which have been asked multiple times in the past for other accelerator project but have never been answered yet. This will be developed in the next chapter.

It is also important to keep in mind the timescale of the project, that will be built in a few tens of years, at the end of the HL-LHC operation planned to be around 2040 [19]. The design may change a lot and the technology available too.

Chapter 2

Study of existing solutions for the MDI alignment

Content

2.1 Existing MDI

In order to find an alignment monitoring system for the FCC-ee MDI, existing systems had to be studied, to see if any of these could be used for the FCC-ee MDI. Only a few MDI could be compared to the FCC-ee one due to the specific configuration shown previously. Four existing machines and three projects have been chosen to highlight the challenges, even though more have been studied (Beijing Electron-Positron Collider II (BEPCII) [44, 45], Relativistic Heavy Ion Collider (RHIC) [46, 47], Hadron-Electron Ring Accelerator (HERA) [48, 49], ...). One of these, the LHC/ATLAS MDI, rather different from the FCC design, was reviewed for the alignment system implemented.

2.1.1 DAFNE/KLOE MDI

2.1.1.1 Introduction

The first machine studied was the Double Annular Φ Factory for Nice Experiments (DAΦNE or DAFNE), which is an electron-positron collider located at Frascati in Italy, in the INFN Frascati National Laboratory. It is a 100 m long machine, with two accelerator rings, colliding electrons and positrons since 1999. Leptons were accelerated to collide in the K LOng Experiment (KLOE) detector from 2000 to 2006 and then has been followed by the KLOE II detector in 2014 [50].

2.1.1.2 Design

This machine has been studied for its specific MDI configuration: like for the FCC-ee, the final focusing quadrupoles of the DAFNE accelerator are located inside the KLOE experiment. But contrarily to the FCC-ee, the support system is not in a cantilever configuration, but is done thanks to an assembly of 4.5 m going through the entire detector. This assembly includes accelerator components (like the final focusing quadrupoles) but also detector components, like the copper colored inner tracker, which can be seen on Fig.2.1. Two bellows have been placed near the center to allow movements for a fine-tuning of the alignment.

2.1.1.3 Alignment procedure

Alignment requirements for this MDI are less stringent than those for the FCC-ee, being 150 μm (1 σ) for the final focusing quadrupoles (between the measured and theoretical position of the magnetic

Figure 2.1: Photo taken before the insertion of the central assembly inside the detector. The orange cover on top is used for the support during installation. Accelerator components are hidden under the wires on each side of the inner tracker (copper colored in the middle).(Courtesy of Luigi Pellegrino, 2023)

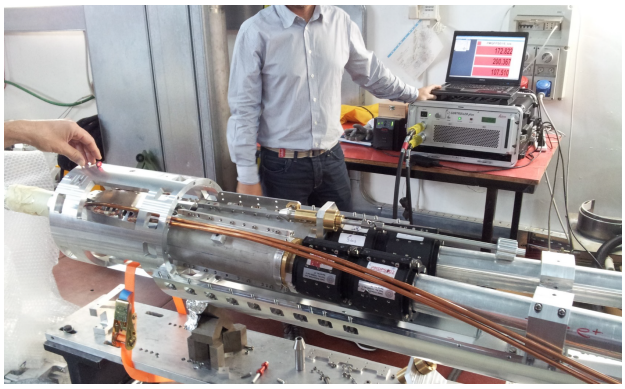

Figure 2.2: Photo taken during the assembly of the final components on the girder. Each component was carefully aligned thanks to a laser tracker (a corner cube reflector can be seen on the left and the measurement on the computer screen). (Courtesy of Luigi Pellegrino, 2023)

centers of the quadrupole). To reach that objective, all the components in the MDI were aligned carefully during the assembly using a laser tracker, as illustrated on Fig.2.2. Once all the components were aligned on the girder, everything has been inserted inside the detector, and once in the detector, the laser tracker target support paired with the support screws, shown in Fig.2.3 can be used for the fine alignment. After the alignment procedure and the closing of the detector, some laser tracker target supports were not visible anymore, due to cables and pipes blocking the line of sight, preventing any alignment checking campaign.

2.1.1.4 Conclusion

Even though this innovative and well-designed MDI integrates an alignment system (and even the possibility to monitor the alignment), the design is too different from the FCC-ee one and the alignment requirements of 150 μm (1 σ) are too far away from the 30 μm of the FCC-ee. Technologies used at that time (laser tracker) were enough for the alignment of the DAFNE/KLOE MDI, but cannot fulfill the requirements for the FCC-ee MDI and cannot be used for a continuous monitoring. Also, the FCC-ee MDI will be more than two times larger than the DAFNE/KLOE MDI. The DAFNE alignment solution can not be adapted to the FCC-ee MDI.

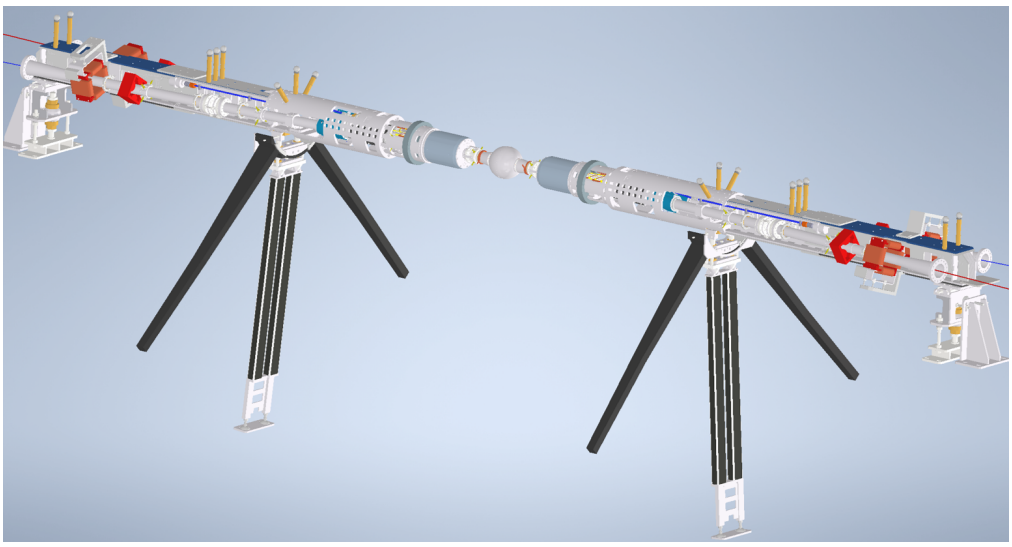

Figure 2.3: Drawing of the assembly located inside the detector. The eight yellow rods on each side are the laser tracker targets supports used for the alignment. The supports of the assembly, on each side, comprise screws to move and direct the two halves (which can move thanks to the two bellows).(Courtesy of Luigi Pellegrino, 2023)

2.1.2 SuperKEKB/Belle II

2.1.2.1 Introduction

The SuperKEKB accelerator is a 3016 m long circular collider located at KEK (High Energy Accelerator Research Organization) in Tsukuba, Japan [16]. This machine feeds electron-positrons collisions to the Belle II experiment. It is the upgrade of the KEKB accelerator, operating since 2018 and which is currently the highest instantaneous luminosity record holder.

2.1.2.2 Design

This luminosity record was allowed by the upgraded final focusing quadrupoles in the MDI. As in the KEKB accelerator (and the FCC-ee), the final focusing quadrupoles are located inside the detector, in a cantilever configuration. In the SuperKEKB, these final focusing quadrupoles are superconducting ones [51] and, so, cooled down to cryogenic temperatures. Therefore, four final focusing quadrupoles (and multiple corrector coils) are hosted in a cryostat for each side, which also serves as supports. This machine has the closest design to the FCC-ee one, with the final focusing quadrupoles inside a cryostat and inside the detector. The main difference being that the SuperKEKB/Belle II MDI is asymmetric:

there is one low energy ring and one high energy ring, resulting in different magnet configurations on each side of the detector and, so, different cryostat lengths [3].

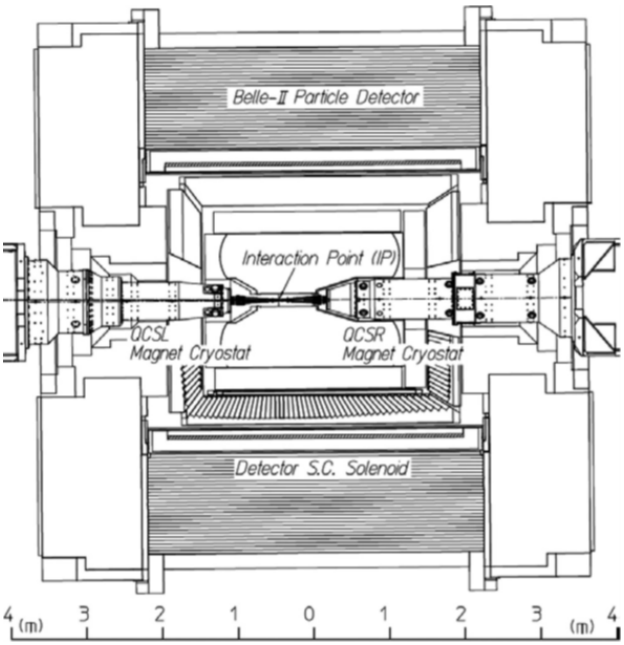

Figure 2.4: Drawing of the Belle II detector with the two cryostats holding the final focusing quadrupoles inside. The 8 m long experiment holds a less than 3 m long cryostat on one side and a 4 m long cryostat on the other side (cf. [3]).

Figure 2.5: Picture of the MDI of SuperKEKB, the detector being in the maintenance position. The asymmetric cryostats (shining metallic part) can be seen in their cantilever configuration at the center of the picture (cf. [3]).

2.1.2.3 Alignment procedure

The alignment of elements inside the cryostats was performed by laser tracker reaching 50 μm for the error of the magnet position [3]. Once everything was installed, the cryostat was fiducialised: points were placed outside the cryostat and the position of the inner components was measured with respect to these points. This allows to know the components position with respect to these points, even when the cryostat is closed and without direct measurement towards the inner components possible. The closed cryostat is then installed in the tunnel, the magnets inside being put in their design position, referring to the points outside the cryostat and the reference network on the tunnel wall. Once ready, the cryostats are rolled in the detector via their support. Then the alignment of the final focusing quadrupoles is checked using the Single Stretched Wire (SSW) method [1]. This system, shown on Fig.2.6, integrates two precision moving stages (SSW units A and B on the figure) for the X and Y

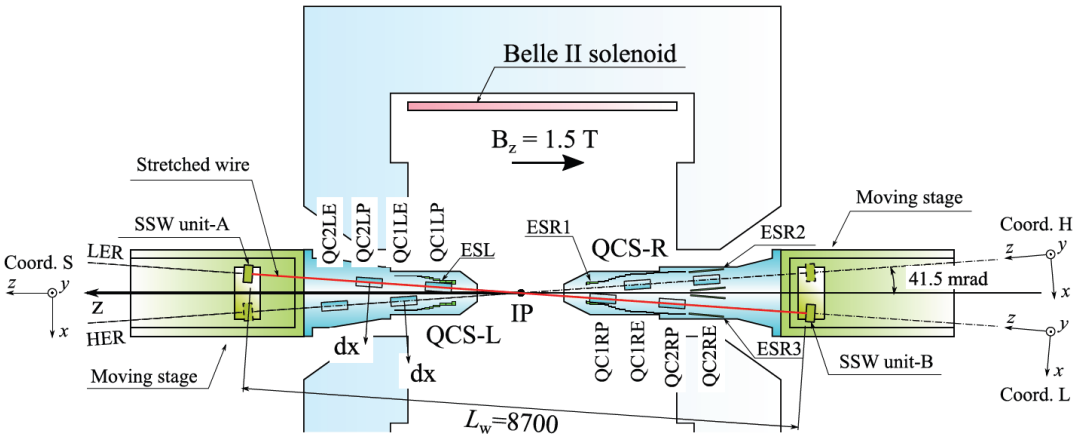

Figure 2.6: Drawing of the layout for the SSW measurements done to check the position of the final focusing quadrupoles inside the cryostats (cf.[1]).

directions. These plates control the movement of wires going through the entire detector and the final focusing quadrupoles on the path, inside the cryostats on both sides of the detector. The repeatability is of 0.1 μm for the X and Y axis. They are used to monitor the two ends of a conducting wire, which are aligned to the beam line. This wire is then vibrated to allow the measurement of the magnet position at cryogenic conditions in two states: energized to nominal current and non energized, in order to see the impact of the Lorentz force from the Belle II solenoid. The results obtained are shown in 2.1. This table shows the results of the measurement campaign using the SSW method. Offsets are measured from a wire in the X and Y directions and the roll angle for each of the quadrupoles. Statistical errors were less than 10 μm for the high energy ring magnets and 20 μm for the low energy ring. The final tuning is done by BBA (explained in section 1.2.4). The table shows vertical offsets of all the quadrupoles and additional big X offsets on some components, of sometimes more than 0.2 mm. There is no alignment monitoring system installed in this MDI.

2.1.2.4 Conclusion

This MDI is the closest design to the FCC-ee MDI design: final focusing quadrupoles inside the detector, at cryogenic temperature and supported in a cantilever configuration. The installation procedure could be used for the FCC, but an additional alignment monitoring system would have been extremely convenient to avoid the offsets measured by the SSW method, done at the end of the MDI installation. And currently, such alignment monitoring system is missing. One of the goals of the

Quads.	X-offset		Y-offset		$\Delta\theta$
	Solenoid		Solenoid		Solenoid
	on	off	on	off	on
QC1LE	−0.21	−0.16	−0.29	−0.56	−1.6
QC2LE	0.13	0.11	−0.54	−0.68	−1.5
QC1RE	0.25	0.14	−0.37	−0.54	0.0
QC2RE	0.08	0.07	−0.58	−0.63	−0.7
QC1LP	−0.03	−0.14	−0.21	−0.38	−1.7
QC2LP	−0.31	−0.41	−0.68	−0.83	−4.0
QC1RP	0.64	0.69	−0.30	−0.43	2.0
QC2RP	0.43	0.45	0.04	−0.19	−1.7

Table 2.1: Measured offsets in x and y and roll angle with respect to the design position. Length in mm and angles in mrad (cf.[1]).

system would be to avoid this situation, in which offsets are notified too late in the assembly process. Such a monitoring system would also allow to perform extremely early tests, even on the assembly site, in order to check if the components are at their designed place while still being able to disassemble and reassemble in case of unacceptable offsets. So, a monitoring system is required, being even more helpful for the FCC as the FCC-ee MDI is planned to be larger than the SuperKEKB one: an 8 m long detector and around 3.5 m long cryostat for the SuperKEKB MDI against the 10 m long detector and more than 4 m long cryostat for the FCC-ee, which would increase the unexpected offsets.

2.1.3 LHC/ATLAS

2.1.3.1 Introduction

The LHC is a 27 km long collider, located at the border between France and Switzerland near Geneva. The accelerator feeds 4 major experiments: ATLAS, CMS, ALICE and LHCb. In all these four MDIs, the situation is very different from the situation in the FCC-ee MDI, mostly because the LHC is a hadron collider whereas the FCC-ee will be a lepton collider. ATLAS and CMS are two general physic experiments, meaning that they are composed of detectors studying multiple physics particles or phenomenon, as opposed to ALICE and LHCb which are more specific physics experiments. ATLAS and CMS are confirming the results of each other by using different kind of detectors, necessary to validate any discovery. These two experiments are the two largest and most important in the LHC, and therefore they are slightly better equipped regarding the alignment monitoring. Both of these MDI have a survey dedicated gallery to pass the alignment around the physics experiment. These galleries are not present in the other LHC experiments. In this section, the LHC/ATLAS will be

developed, as it is one of the fully equipped MDI, and it is representative of the strategy used for all the others MDIs.

2.1.3.2 Design

The LHC MDIs have a free length L* greater than the detector size and a very small crossing angle, so final focusing quadrupoles are located outside the detector, 25 m away from the IP. These final focusing quadrupoles are in 8 and 12 m long separated cryostats weighting around 15 T and placed in the tunnel. The MDI is large from a surveyor point of view, being around 100 m long from the first component to measure to the last. It makes the alignment a difficult operation, even though the components are placed in the tunnel and space is available around them.

2.1.3.3 Alignment procedure

The elements are first fiducialised during assembly: targets are placed on the outside of the cryostats while the cold masses inside (containing the magnets) are still visible. Then the cryostats are closed and placed in the tunnel, using the targets, so the inner components are at their designed positions. Once done, a smoothing is performed: components are aligned with respect to their two adjacent counterparts, so the beam goes in a smooth trajectory and does not encounter any big offset. Fiducialisation is done by a laser tracker, and smoothing is performed by precision levels and measurements of offsets from a wire [52]. Once aligned, the final focusing quadrupoles, and more precisely their cryostat, have their alignment monitored [53] using HLS, WPS and DOMS, shown in Fig.2.9 and illustrated in situation in Fig.2.8. The layout of these monitoring systems is shown on Fig.2.7. These systems are all based on the capacitive measurement technique. The WPS is composed of 4 electrodes which are measuring the air capacitance to a conducting wire. The wire pass near the middle between two horizontal electrodes and two vertical electrodes, allowing a measurement (plus control by redundancy) in horizontal and vertical. The sensor itself is passive and only modify a signal sent by an electronic board via specific cables. These electronic are placed as far away from the tunnel as allowed by the maximum length of the cables (30 m) [54], to protect the electronic board from the radiations. The HLS is similar to the WPS, but has only one electrode measuring the air capacitance to a water surface. It performs height difference measurements between the sensors measuring on the same gravity equipotential (modeled by the water). The DOMS also has only one

electrode, measuring the air capacitance to a metallic target. DOMS and HLS are also passive and have their electronics located away from the beam line, like for the WPS. The resulting measurement of all these sensors is a distance measurement towards the target (wire, water or metallic target) with micrometric uncertainty [55].

The vertical position of the final focusing quadrupoles and the roll angle are monitored by the HLS, the radial position is monitored by the WPS and the longitudinal position by the DOMS. This monitoring is carried out on the entire MDI (both sides of the experiment, so around 100 m total), bypassing the detector by going into survey dedicated galleries. The cryostats of the final focusing quadrupoles are also equipped with a readjustment system able to remotely adjust one or multiple components. This is performed by actuators placed under the cryostats. This system works paired with the monitoring system, which measures the offsets that the readjustment system needs to correct. The aim was to align the components to 0.1 mm in vertical and 0.2 mm in radial from left to right side [56].

It is important to underline the space required by the sensors in that MDI. HLS and WPS require both an important infrastructure that can be seen on Fig.2.8. The WPS require a stable wire going along the components. That wire is stretched between two pillars, one of which is equipped with a wire stretcher. The wire is protected over its entire length to isolate it from physical stimuli (wind, contacts during maintenance) shown in blue on Fig.2.8. The HLSs require a water network (8 cm diameter pipe) going along the components to align, linked to the sensors by soft tubing. This network is installed on stable pillars and needs to be linked to a filling and purging station, used for both security and for on site calibration. The HLS system is highlighted in green on Fig.2.8. The sensors themselves also have a non-negligible size, as can be seen on Fig.2.9.

2.1.3.4 The High Luminosity upgrade

After the LS3 (Long Shutdown 3, foreseen to take place from December 2025 to January 2029) the LHC will receive an upgrade of nearly 1.2 km of components to increase even more its luminosity. The MDI and the alignment system will also be updated. First, more components will be monitored as a wider area will be studied (400 m rather than the 100 m currently monitored). Moreover, alignment requirements will be more stringent as the requirements of the LHC (currently used for a 100 m area) will be applied to the HL-LHC monitored area of 400 m: alignment requirements of

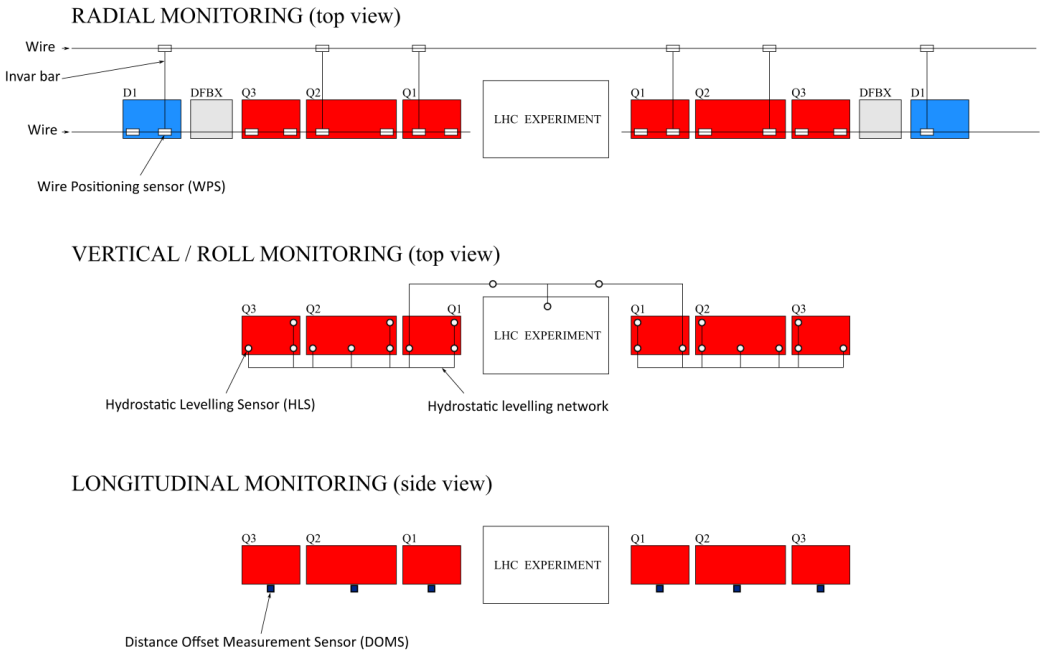

Figure 2.7: Drawing of the monitoring systems installed in an LHC MDI. The parallel wire bypassing the experiment goes through a survey dedicated gallery (cf.[4]).

Figure 2.8: Picture of the installation in the tunnel near the experiment. The HLS infrastructure has been highlighted in light green: stable support pillars, water network, sensors and soft connection pipes. The WPS infrastructure has been highlighted in light blue: sensor, wire and wire protection.

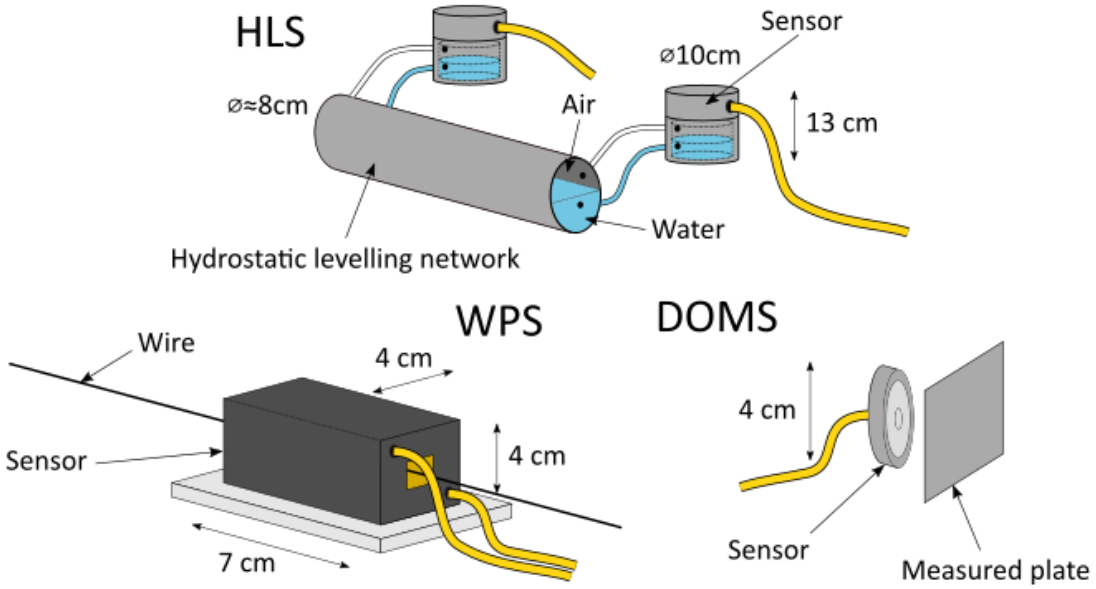

Figure 2.9: Drawing and sizes of each of the three main sensors used for the alignment monitoring of the LHC MDI.

the components to 0.1 mm in vertical and 0.2 mm in radial from left to right side. The monitoring system will also be completed: additional sensors will be installed, by enhancing the existing network but also by installing new types of sensors. This will provide redundancy with different types of measurements and backup solutions in case of sensor failure. Some new sensors, like inclinometers, will be added to the array of systems already used and available. DOMS and HLS, both currently using the capacitive technology, will be replaced by interferometric ones. The design is the same, and the measurement will be extremely similar, done on water and a retroreflector. These interferometric sensors, using the FSI (which will be explained in details in section 4.1.2) measurement, are as precise as the capacitive ones [57] but more resistant against radiations [58, 14]. The interferometer can be located far away from the passive sensors, thanks to the optical fibers as they have less noise than regular copper cable [59]. Monitoring will also go one step deeper in the components, by continuously determining the position of the cold mass with respect to its vacuum vessel across a huge temperature gradient, providing more information on the position of the cold mass during operation. This will be performed by interferometric distance measurements from outside the cryostat, measuring on targets placed on the cold mass at an accuracy of better than 10 μm [14]. This FSI monitoring system has the advantage of being able to monitor the cold mass position immediately after installation, allowing

the monitoring during the transport, for example, to control any displacement after the journey. But the main advantage is that it allows an alignment of the MDI with respect to the cold masses directly, which is closer to the magnetic axis, rather than with respect to the cryostat. Finally, the entire alignment solution, based on sensors and actuators, is also required for safety reasons. A remote alignment allows the survey teams to spend less time in the tunnel, as the radiations in the HL-LHC MDI area will be around ten times higher than in the LHC MDI [60].

2.1.3.5 Conclusion and discussion

The MDIs in the LHC are very different from the ones in FCC-ee, but this is the only working example of an alignment system, monitoring the MDI in real time and even able to realign the components remotely if needed. One could ask why not applying the LHC MDI monitoring system to the FCC-ee. The first reason is the space available. In the LHC case, having the final focusing quadrupoles in the tunnel leaves some space to implement a monitoring system around them, space which is not available for the FCC-ee MDI. A scaling of the number of sensors would also be required, and as the FCC-ee will have six independent final focusing quadrupoles on each, each quadrupole would require at least the same number of sensors as an HL-LHC low-β quadrupole. This represents a total of 18 WPS, 18 HLS, 6 inclinometers and 6 interferometric distance measurement sensors to be fitted inside a 4 m long 50 cm diameter cryostat, already full of components and cooled down to cryogenic temperature. Lines of sight, space for the water network and stable support pillars cannot be found in the FCC-ee, without mentioning the incompatibility of water and cryogenic temperatures.

One could note that, even though this alignment monitoring system cannot be adapted to the components inside the FCC-ee detector, this system could be installed on the straight section before the IP. It is a place where the tunnel is widening for a transition between the arc tunnel (5 m in diameter) to the experiment cavern (more than 30 m large) [2] where space can be found to install the infrastructure required for these sensors. But clear alignment requirement values are needed in order to validate the use of these sensors in this area.

2.2 MDI of project colliders

2.2.1 Compact Linear Collider

2.2.1.1 Introduction

The CLIC is a project of a linear collider at CERN [5], which also aims to be the next flagship project after the High Luminosity upgrade of the LHC, in competition with the FCC. The "compact" adjective comes from the technology used to accelerate the beams: two beams are circulating in parallel, one being decelerated to feed energy for the acceleration of the other. The decelerated beam will be in a drive linac while the accelerated beam will be in the main linac, heading to a collision in the center of the detector. Linear colliders have several advantages compared to circular collider. The main one is not being subject to synchrotron radiation caused by any turn of the beam, which allows them to reach higher energies for the collisions and therefore study specific interactions. The CLIC is a multiple stage project, going from 380 GeV to 1.5 TeV and 3 TeV, having its length increasing at each iteration, going from 11 km to 50 km. The construction was planned to start by 2026 to have the first beams by 2035 [61].

2.2.1.2 Design

The CLIC MDI was extremely complex at the beginning: the MDI was planned to have two detectors in a push-pull configuration, as shown in Fig.2.10. As a linear collider, there is only one IP, but a two detectors configuration has been studied to confirm physics measurement with two different sets of sensors. While one was positioned at the IP, the other one would be in "maintenance" position, ready to be swapped. The swapping was planned to take less than three days [5], taking into account the displacement of the two detectors, the reinstallation of the final focusing quadrupoles inside them and the realignment. The low L* implied to have the final focusing quadrupole (named QD0) inside the experiment, but contrarily to the FCC-ee MDI, there is only one final focusing quadrupole per side, and they are operated at ambient temperature. These quadrupoles were supposed to be supported in a cantilever configuration from outside the detector, and the pre-alignment requirements for QD0 were very stringent: 10 μm (3 σ) to the beam. The two different detectors were implying two different L*: 3.5 m for the CLIC Silicon Detector (SiD) and 4.335 m for the CLIC International Large Detector (ILD) [5].

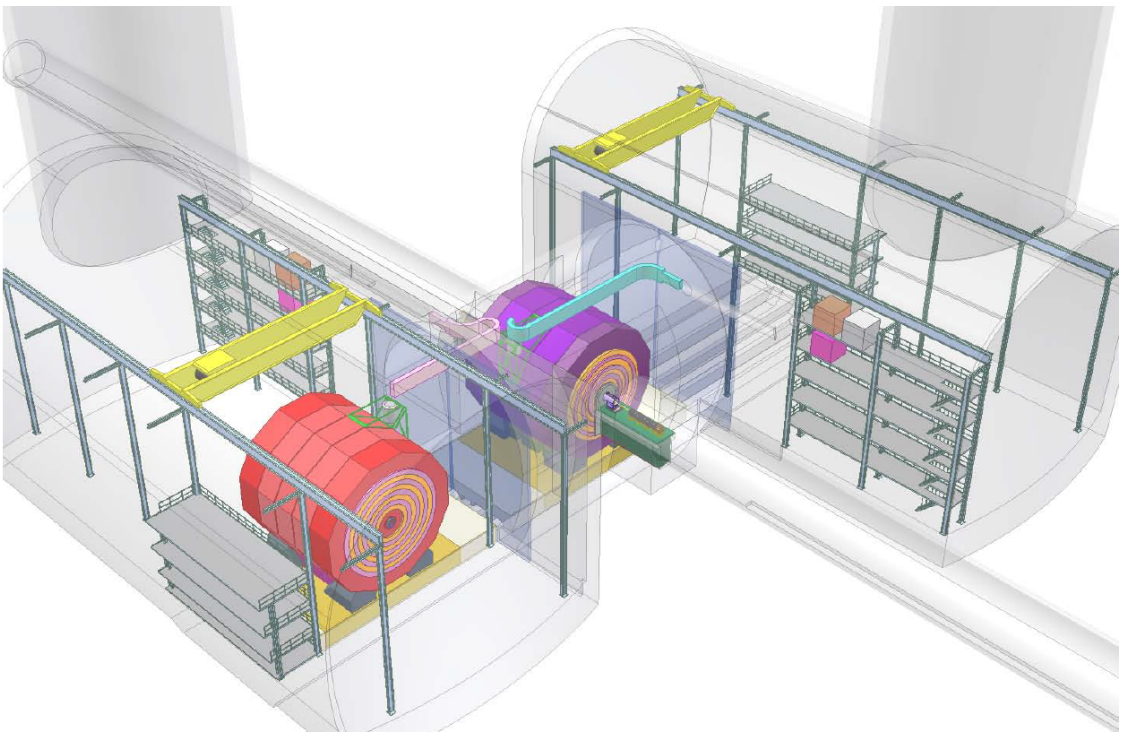

Figure 2.10: Drawing of the initial CLIC MDI, with the two detectors in push-pull configuration. The purple one being in operation position, while the red one is in maintenance position (cf.[5]).

As constraints for the assembly in the detector were too tight, it was proposed in 2010, and later in 2018, to increase the L*. Resulting from that decision, the final focusing quadrupoles are now placed in the tunnel rather than in the detector [62, 63, 64] which was confirmed and validated in 2019 [61].

2.2.1.3 Proposition for the alignment monitoring for the initial MDI

The alignment of the QD0 being extremely stringent, an alignment monitoring system was required for this MDI. The plan was to monitor the alignment of QD0 and transfer it away from the beamline in order to have enough space for the alignment system to be installed, as explained in [65]. As shown on Fig.2.12, precision alignment rings were placed around QD0 and linked to it. Then, ZERODUR® (glass like material with a very low coefficient of thermal expansion) spokes were transferring any movement of QD0, by contact, away from the beam line. These spokes, sliding in tubes, had their other end in the line of sight of a Red Alignment System NIKhef (RASNIK) [66], alignment system, monitoring their movement and thus, the movement of the alignment ring. Even though the system was well detailed, no tests or simulations have been done yet. Work remains to be done to prove

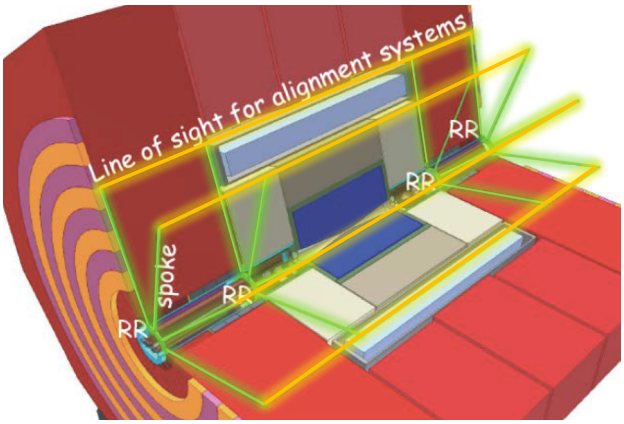

Figure 2.11: Drawing of the alignment monitoring system proposed for the CLIC MDI. The ZERODUR® spokes are shown in green, perpendicular to the beam direction. The line of sight for the optical alignment system is also shown in yellow, parallel to the beam direction (cf.[6]).

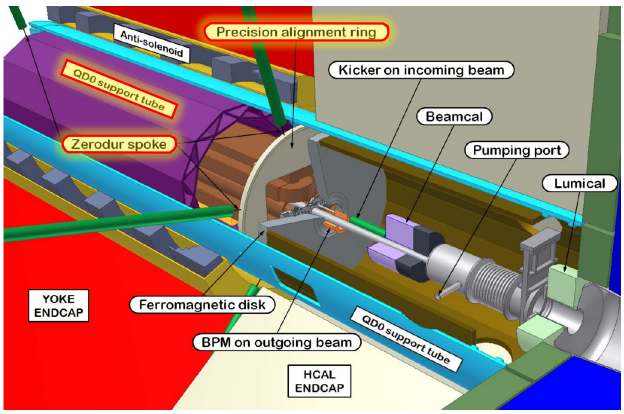

Figure 2.12: Closer look at the internal alignment system proposition. Precision alignment rings were attached to QD0, and their position was monitored thanks to ZERODUR® spokes by contact. The movement of the ring was then transferred by the spokes further away from the beamline where a line of sight for the optical alignment system could be installed (cf.[5]).

the feasibility of this system. First, the confirmation about the possible use of detector space for an alignment monitoring system should be asked. Once it is known that this system could be physically inserted, tests and simulations should be done as the network seems not optimal to monitor the roll and the longitudinal translation. Moreover, the rods are multiple meters long and may deform due to their length, weight and possible friction in their tubes. This friction can also lead to adverse constraint on the QD0 support and should be studied carefully. The deformation of the rods may lead to an accuracy loss for the system. Finally, simulations with the real size setup should be done to estimate the accuracy of the RASNIK in this situation.

2.2.1.4 Implementation of a readjustment system for the current design

At the beginning, having the final focusing quadrupoles inside the detector was preventing the use of a re-adjustment system. But, as the project evolved, the final focusing quadrupoles ended up in the tunnel, in the current design. Having QD0 out of the detector allowed to place them on readjustment systems, originally designed for the Beam Delivery System, in the shape of cam-movers.[43, 67]. These cam movers can position components at an accuracy of 1 μm [68].

2.2.1.5 Conclusion

This MDI was relatively close to the FCC-ee one in its original version, having final focusing quadrupoles inside the experiment in a cantilever configuration. Even though an alignment monitoring system had been proposed, it was never qualified. Now the MDI has changed, increasing L* from 3 to 6 m, resulting in a configuration with the final focusing quadrupoles being installed in the tunnel. The non-mature solution proposed for the original design of the MDI underlines the difficulty of the situation, which has been simplified by increasing the L* and by placing the QD0 in the tunnel.

2.2.2 International Linear Collider

2.2.2.1 Introduction

The International Linear Collider (ILC) aims to be a linear accelerator, colliding electrons and positrons at 500GeV collision energy at the beginning, upgradable up to 1 TeV. It will be 30 km long and the most likely location is in Japan. This project is in competition with the CLIC project of a next generation linear collider. These two projects are differing mainly by their beam acceleration technology, the CLIC using the exotic energy recovering technology, while the ILC uses the well known RF cavities. Now, these two projects are united under the Linear Collider Collaboration, which combines the efforts for the research on these two machines.

The construction date of the ILC is still not known, but the project seems still active at this day [69].

2.2.2.2 Design

The design is extremely similar to the CLIC design: a linear accelerator, with two detectors in a push-pull configuration [70] (as shown in Fig.2.13), and a final focusing quadrupole (also named QD0) supported in a cantilever configuration inside the detector. As for the CLIC, the detector exchange process was estimated to take no more than a few days [8], including the disassembly of the MDI, the detector swap, the reassembly of the MDI and the re-alignment. In addition, as shown in Fig.2.14, QD0 is cooled down to cryogenic temperatures, and thus is placed inside a cryostat. This cryostat will also be used as support for QD0 through two sets of supports: one set going from the cold mass to the heat shield and the other going from the heat shield to the outer cryostat. Alignment requirements

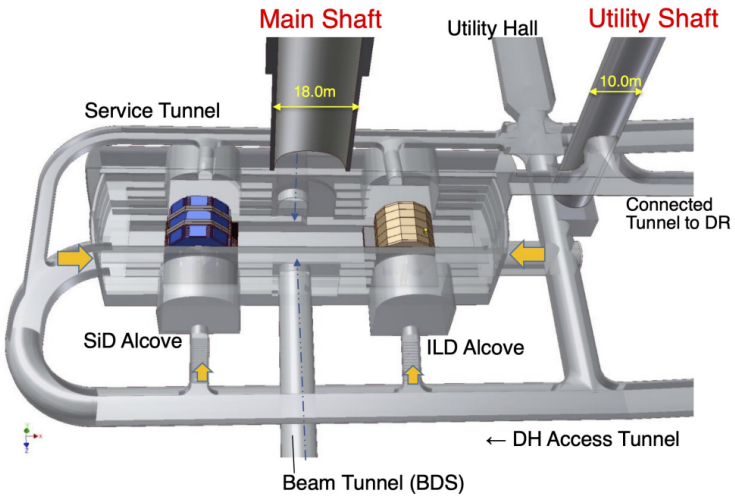

Figure 2.13: Drawing of the ILC MDI, with both detectors in their dedicated alcove around the beam tunnel (cf.[7]).

for QD0 is set to 50 μm along the x and y axis, and 20 μrad in roll, pitch, and yaw [71], so a precise beam based alignment can be done after.

2.2.2.3 Proposition for the alignment monitoring

In the ILC MDI, the final focusing quadrupoles are cooled down to cryogenic temperatures. As illustrated in Fig.2.14, in order to support these quadrupoles inside the cryostat, a first set of support posts have been placed between the cold mass (containing the final focusing quadrupoles) and a heat shield and a second set between the heat shield and the cryostat. The figure shows how crowded is the inside of the cryostat. In order to monitor these QD0 and monitor the alignment between the two sides of the detector, a network of interferometric distance measurements have been designed [72]. Another system have been proposed, the Monitoring Alignment and Stabilization with High Accuracy (MONALISA) shown in Fig.2.15, aiming at monitoring the QD0 independently from the particle beams using a combination of a frequency scanning interferometry (FSI) and a fixed frequency interferometry in order to reach a sub-micrometer precision [73].

Even though these studies were very promising, no final system was proposed for the monitoring of the QD0s and studies on that specific subject seem to be in stand by.

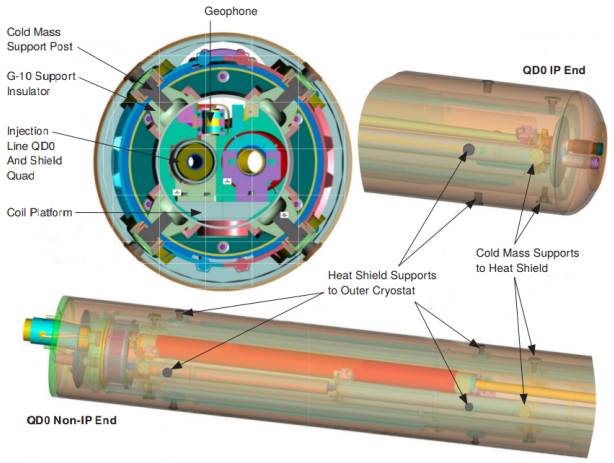

Figure 2.14: Drawing of the QD0 in his cryostat. Support is done by the cryostat, thanks to posts from the cold mass to the heat shield and from the heat shield to the outer cryostat ([8]).

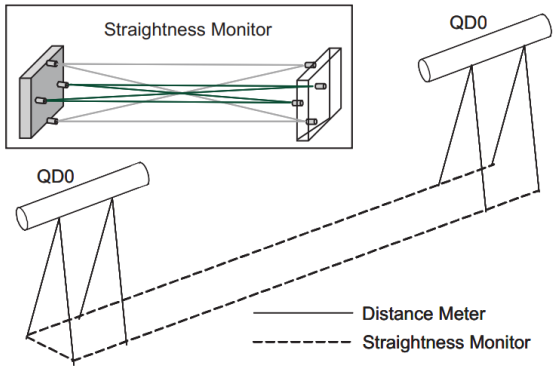

Figure 2.15: Setup of the MONALISA system for the monitoring of QDO in the ILC MDI (cf.[9]).

2.2.2.4 Conclusion

The ILC MDI is also very similar to the FCC-ee one, sharing numerous challenges with it, but the alignment monitoring system for QD0 is still far from being ready. Even if the distance measurement network was an interesting idea, the simulations, and tests were never concluded.

2.2.3 Circular Electron Positron collider

2.2.3.1 Introduction

The Circular Electron Positron Collider (CEPC) is a 100 km long circular collider project planned to be built in China. This project is also articulated around two machines: first a lepton collider (CEPC), which will later be replaced by a hadron collider, the Super Proton-Proton Collider (SPPC). The CEPC and the FCC-ee have very similar parameters, underlining the interest of the scientific community for these next generation giant circular colliders. The construction, originally planned to start in 2022 [10] was delayed to 2026 [74].

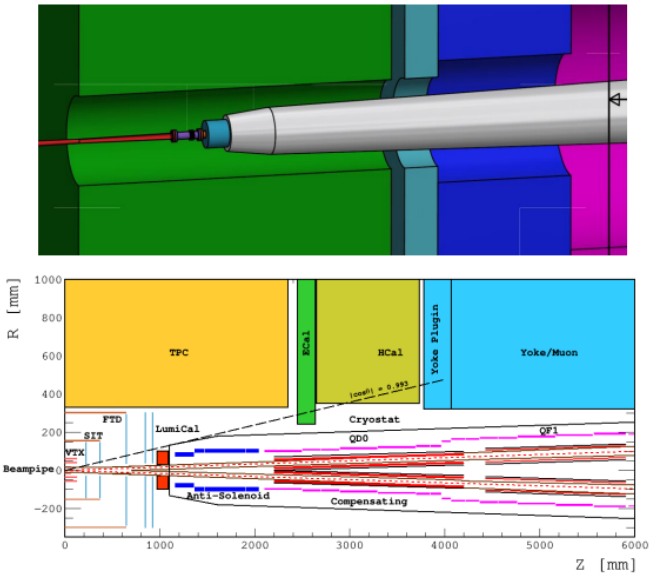

Figure 2.16: In the top picture, the cryostat (gray) supporting the final focusing quadrupole can be seen in the detector parts (green, blue, and pink). In the bottom drawing, representing a section through the middle of the cryostat, we can see the overall layout with the Lumical, solenoids and final focusing quadrupoles, being inside the different subdetectors (cf.[10]).

2.2.3.2 Design

The CEPC will implement a crab waist configuration with a crossing angle of 33 mrad and an L* of 2.2 m [10]. These parameters imply having the final focusing quadrupoles inside the detector. Fig.2.16 illustrates the situation: the final focusing quadrupoles are surrounded by an anti solenoid and a compensating solenoid, themselves being inside a cryostat. This assembly sits inside the detector in a cantilever configuration, supported by the cryostats. The resulting MDI is extremely similar to the FCC-ee design. Conditions inside are very harsh, with cryogenic cold, radiation, and magnetic fields. Alignment requirements are non entirely defined yet, and current values are about 30 μm for the final focusing quadrupoles [75].

2.2.3.3 Proposition for the alignment of the MDI

Alignment in the MDI is not entirely detailed yet and for the moment, the plan is to align as precisely as possible the components during the assembly. Laser tracker will be used for the initial alignment, using laser tracker stations on each side of the detector and the tunnel control network. The following alignment step, illustrated on Fig.2.17, will use two laser collimators and targets, creating

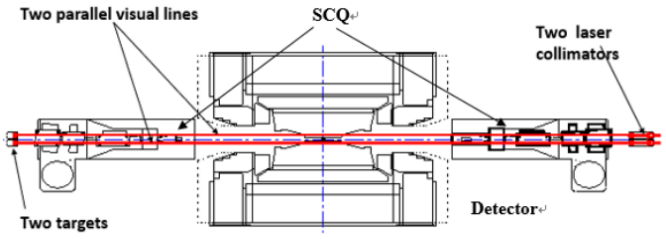

Figure 2.17: Drawing of the alignment system for the MDI. It plans to utilize the visual lines between both sides of the MDI, once the elements are at their nominal position, to pass two laser collimators that will be used for a refined alignment of the superconducting quadrupoles (SCQ) (cf.[10]).

a positional reference system for the alignment of the components to the beam orbit. The accuracy goal is 0.1 mm for the relative alignment accuracy of the final focusing quadrupoles [10]. Even though development and research is going very fast, the alignment system and even the alignment requirements for the MDI are not entirely defined yet.

2.2.3.4 Conclusion

The CEPC will implement an MDI extremely similar to the FCC-ee one, regarding both the design and the requirements. But, for now, the alignment process is only partial, and no alignment monitoring system has been proposed. This underlines the difficulty of the situation.

2.3 Limits of other existing sensors

2.3.1 Introduction

As shown previously, no existing system can deal with the challenges faced in the FCC-ee MDI. The radiations, intense magnetic fields, cryogenic cooling and most importantly the lack of space prevent the use of any existing system. It is also important to underline that the shape and disposition of the components inside the MDI is not ideal, and limits the technologies that could be used. In fact, similar challenges have already been faced in the past for the CLIC and the ILC MDI. They ended proposing only partial solutions for the monitoring of their MDI. This struggle for both studies underlines the difficulty of the situation. But since these studies, the technology evolved. What was not possible ten years ago could have become possible now.

In this section, we will review the most common sensors currently used in survey and metrology, highlighting their strengths and weaknesses with regard to a use in a situation similar to the FCC-ee MDI.

2.3.2 Optical sensors

The first sensors studied are the optical sensors. These sensors are based on an optical measurement technique, using a Charge-Coupled Device (CCD), a Complementary Metal Oxide Semiconductor (CMOS) or any other array of optical detectors. They are used to monitor a wide range of references, like a wire, a water surface, targets on an object or even the object directly. These sensors are widely used, precise and usually cheap. Some examples of such sensors: Boston CCD Angle Monitor(BCAM) [76], Optical Wire Positioning Sensor (OWPS) [77], Optical Hydrostatic Levelling Sensor (OHLS) [78], Red Alignment System NIKhef (RASNIK) [79], Red Alignment System for CLIC (RASCLIC) [80]. BCAMs are a system using CCD image sensors to measure the bearing of a light source. This light source can be another BCAM (as they have laser diodes implemented) or the sensor measuring on itself thanks to a reflector (corner cube or other). RASNIK system is composed of three main components: an optical system (composed of a light source, a diffuser and a coded mask), a lens and a sensor (a CMOS). The alignment between the three parts is monitored by measuring the position of the image of the mask over the CMOS. RASCLIC, based on the RASNIK system, is also a 3-point alignment system: a laser is emitted through a diffraction plate, producing a diffraction pattern on a camera.

The alignment is then measured with the displacement of the image [81].

The main weakness of optical based sensors in particle accelerator environment is their sensibility to radiations [82, 83]. In the FCC-ee MDI, 37 kW and 7 kW radiations are expected from solenoids and quadrupoles respectively [37], in addition to the debris from the collisions a few meters away. This prevents the use of optical based alignment sensors in the FCC-ee MDI.

2.3.3 Capacitive sensors

Capacitive sensors are also widely used in accelerator alignment. They are precise, accurate, and can be declined in a vast range of uses with the adapted infrastructure. Typically, they perform offset measurements with respect to wires, water surface or a metallic surface. Some examples of these sensors are the WPS, HLS, DOMS (as shown previously). Different versions of sensors exist depending on the lab that designed them, their main weakness being the infrastructure required for their measurements, as described earlier.

The infrastructure required to implement those sensors is even strengthened in highly radioactive areas. In the HL-LHC for example, the radiation will prevent people from working in the tunnel for extended periods of time, and so, additional safety and redundancy solutions are required. It requires additional infrastructure such as a wire replacement system for the WPS, composed of a wire stretcher, a clamping system and a vacuum system. For the HLS, it implies to have more redundancy, on the water lines and valves. In addition, even though the sensor is radiation hard, the cable and the electronic, required to operate the sensor, are not. They either need to be built in radiation hard materials or to be localized in a radiation safe place. Radiation hard constructions are more expensive and complex, so for the HL-LHC, a relocation of the cable and electronics was chosen. But this increase of cable length has an impact on the noise of the sensor and decreases the precision [54].
The extremely stringent space requirements, in addition to the highly radioactive area of the FCC-ee MDI, prevent the use of such sensors.

It is interesting to note that, even though they are not based on a capacitive measurement, some sensors are also subject to the same space limitation by requiring the same infrastructure. It is the case for the ultrasonic version of the HLS, developed at Deutsches Elektronen-Synchrotron (German Electron Synchrotron, DESY) [84] or for the Wire Position Monitor (WPM) developed at SLAC (Stanford Linear Accelerator Center) which is based on an inductive measurement [85, 86]. Even

though the sensing technique changes, the infrastructure required is very similar, and therefore the limits are the same. Finally, some sensors are limited by both the infrastructure and the radiations, as it is the case for the optical version of the HLS which requires the same infrastructure as the capacitive version while being also an optical based sensor [87].

2.3.4 Interferometric sensors

Interferometric sensors are already widely used in accelerator alignment due to their precision, simplicity, resistance, and versatility. Currently, they are mainly used to perform distance measurements through air, from an emitting head towards a reflective target (corner cube or glass bead for example) in a network configuration [88, 14]. Some studies are analyzing the implementation of these sensors in HLS and WPS (which will not resolve the infrastructure problem). Current head designs, for the monitoring of cold masses from the cryostat, are around 10 to 20 cm diameter for 10 cm height [57].

Sadly, their current form prevents them to be used in the FCC-ee MDI. An only distance measurements network would be too space consuming for the monitoring of the final focusing quadrupoles. The number of measurements required to reach the requested precision in addition to the head and target designs, and the clear lines of sight required toward the targets are too space consuming to be implemented. Regarding the current measurements of the fiber length, they are punctual and an implementation of such sensor is not trivial for the monitoring of position of components. But these are still "young sensors" and a lot of development is possible.

2.4 Conclusion

A nonstandard and careful alignment of the collider MDIs is always required. The initial alignment can be performed during assembly, using laser trackers like in SuperKEKB. This alignment can also be performed with even more precise assembly methods, carried out in a room with controlled temperature using a CMM for example. But the limitation lies in the knowledge of the position when the assembly is closed. Until the LHC, requirements were not tight enough to necessitate an alignment monitoring system. In the LHC, space was available to implement a full alignment monitoring system. The challenge starts with the next generation colliders, such as the CLIC, the ILC, the CEPC and of course the FCC, where a monitoring system is mandatory to reach the requirements. But proposed

systems for these projects are not mature yet, and the set of sensors currently used in collider alignment cannot face the limitation present in the FCC-ee MDI. The focus will therefore be centered on the monitoring system for the FCC-ee MDI as it is the most difficult part, and it is where a breakthrough would be the most valuable for the collider operation, as initial alignment during assembly can already be performed, as shown by the DAFNE/KLOE and SuperKEKB/Belle II MDIs.

Chapter 3

Proposition for a new alignment monitoring system

Content

3.1 Introduction

Chapter 1 described the complex design of the MDI and the challenges regarding the alignment requirements. Chapter 2 underlined the lack of available systems able to deal with both the harsh conditions and the very tight requirements. The emphasis of this third chapter has been put on the monitoring rather than on the pre-alignment, as some procedures and systems are already available to perform such tasks. This chapter will only develop on the monitoring of components inside the detector and not in the straight section before reaching the detector. The reason is that this study tried to tackle the most complex part of the MDI, where no system can be used. For the straight section, located outside the detector in a large tunnel, some existing systems could be adapted without too many modifications. The monitoring of the components inside the detector being required and extremely complex, this chapter explores in details a new system aiming at overcoming these difficulties and proposing a solution for the monitoring of the accelerator components inside the detector. All the simulations and results shown are computed using a python code developed by my own.

3.2 Mathematical tools

3.2.1 Vocabulary and definitions of metrology

The terminology and definitions used in this document are from the Bureau International des Poids et Mesures (BIPM) [89, 90].

- Quantity: it is the property of a phenomenon, body or substance, where the property has a magnitude that can be expressed as a number and a reference.
- Quantity value: it is the number and reference together expressing magnitude of a quantity.
- Measured quantity value: it is the quantity value representing a measurement result.
- Measurand: it is the quantity intended to be measured.
- True quantity value: also called true value of a quantity or simply true value, it is the quantity value consistent with the definition of quantity.
- Measurement: it is the process of experimentally obtaining one or more quantity values that can reasonably be attributed to a quantity.
- Accuracy: also called measurement accuracy, accuracy of measurement or simply accuracy, it is the closeness of agreement between a measured quantity value and a true quantity value of a measurand.
- Uncertainty: also called measurement uncertainty or uncertainty of measurement, it is the non-negative parameter characterizing the dispersion of the quantity values being attributed to a measurand, based on the information used.
- Standard uncertainty: also called standard measurement uncertainty or standard uncertainty of measurement, it is the measurement uncertainty expressed as a standard deviation.
- Precision: also called measurement precision, it is the closeness of agreement between indications or measured quantity values obtained by replicate measurements on the same or similar objects under specified conditions.

3.2.2 Least-squares adjustment

In order to process the data generated by simulations described in the next sections, the least-squares adjustment method has been chosen. This adjustment method has been preferred as it is the one used currently at CERN in the Logiciel Général de Compensation (LGC++) application developed by the section in charge of software programs and which would also be the method used in case of realization of the FCC. This method is described in many documents [91] and only a quick summary, with the relevant information necessary to understand our work, will be given here.
The least-squares adjustment method allows estimating a set of parameters linked through equations to measured quantity values gathered in a functional model. In a perfect (and impossible) situation, the measured quantity value would be equal to the true quantity value (which corresponds to the value that we ultimately want). In reality, the true quantity values differ from the measured quantity values by measurement errors: the systematic measurement errors and the random measurement errors. The least-squares method only deals with random error measurements. Systematic errors must have been included in the functional model or corrected after a calibration, for example, leaving only the random error measurements. The resulting system is written in eq.3.14:

$$f(X)+V=L \quad \text{with} \quad X=\begin{pmatrix} x_1 \\ \vdots \\ x_m \end{pmatrix}, \quad L=\begin{pmatrix} l_1 \\ \vdots \\ l_n \end{pmatrix} \quad \text{and} \quad V=\begin{pmatrix} v_1 \\ \vdots \\ v_n \end{pmatrix} \tag{3.1}$$

Where L is a vector containing n measured quantity values, V is a vector containing n random measurement errors, X a vector containing m parameters to be estimated and f the vector describing the functional model. The least-squares adjustment method is a way to estimate the best fitting set of parameters for a given (and over-abundant) set of measured quantity values. This set of parameters is defined by the set $\hat{X}$ minimizing the square of the norm of the vector $L-f(X)$:

$$\hat{X} \quad \text{is solution when} \quad \hat{X}=\min_{X\in\mathbb{R}^m}((L-f(X))^T P(L-f(X))) \tag{3.2}$$

Where m is the number of parameters and P the matrix defining the norm to use, allowing, if necessary, to attribute weights to the measurements.

In practice, in a least-squares adjustment, it is common to define the P matrix from the covariance matrix associated with the random measurement errors. Let Σ_L designates the a priori covariance matrix associated with the random measurement errors vector V, and ${s_0}^2$ define the variance factor of unit weight. A usual approach is to make the assumption that the V vector follows a standard normal distribution, with ${s_0}^2\Sigma_L$ covariance matrix. And to use P as the inverse of Σ_L.

In this work, we also make the assumption that all the uncertainty information is included in the Σ_L matrix, and thus that $s_0^2 = 1$.

The procedure for the determination of $\hat{X}$ will be described for f non-linear with respect to the parameters.

The first step towards the resolution of the system in 3.1 is to linearize f around an approximated value of the parameters, noted X_0. It is carried out by developing the first-order Taylor series expansion of f around that point:

$$f(X) \underset{X_0}{\approx} f(X_0) + \frac{\partial f(X_0)}{\partial X}(X - X_0) \tag{3.3}$$

Where $f(X_0) \in \mathbb{R}^n$ is the f value in X_0 and $\frac{\partial f(X_0)}{\partial X}$ is the value of Jacobian of f with respect to the parameters in X_0. It is a $\mathbb{R}^{n*m}$ matrix which, from now on, will be noted:

$$A = \frac{\partial f(X_0)}{\partial X} = \begin{pmatrix} \frac{\partial f(X_0)}{\partial x_1} & \dots & \frac{\partial f(X_0)}{\partial x_n} \end{pmatrix} \tag{3.4}$$

Considering X_0 being close enough to $\hat{X}$ so we can use the linearization of f, 3.4 could be written as:

$$L = f(X_0) + A(X - X_0) + V \tag{3.5}$$

Noting the vector B gathering the constant terms:

$$B = L - f(X_0) \tag{3.6}$$

The system becomes:

$$B = A(X - X_0) + V \tag{3.7}$$

Now that the problem is linearized, we can solve it. Let N define the normal matrix and C the second member of the normal equation:

$$N = A^T PA, \quad C = A^T PB \tag{3.8}$$

Noting σ_i the a priori uncertainty of observation L_i, and σ_{ij} the covariance between random errors associated with observations i and j, the P matrix corresponds to:

$$P = \begin{pmatrix} {\sigma_1}^2 & \sigma_{1,2} & \dots & \sigma_{1,n} \\ \sigma_{2,1} & \ddots & \ddots & \vdots \\ \vdots & \ddots & \ddots & \sigma_{n-1,n} \\ \sigma_{n,1} & \sigma_{n,2} & \dots & {\sigma_n}^2 \end{pmatrix}^{-1} \tag{3.9}$$

If the system is well established, the N matrix is invertible, and the system can be solved:

$$\begin{aligned} \hat{X} - X_0 &= N^{-1}C = (A^T PA)^{-1} A^T PB \\ \hat{X} &= N^{-1}C + X_0 \end{aligned} \tag{3.10}$$

In order to deal with the approximation caused by the linearization of the functional model, iterations on the approximate values X_0 are performed, until the difference $|\hat{X} - X_0|$ is smaller than a defined convergence criteria. Once done, one obtains the least-squares solution (after convergence), noted $\hat{X}$, and can compute the vector of residuals, useful criteria of the quality of the adjustment process:

$$\hat{V} = L - f(\hat{X}), \quad \text{with} \quad \hat{V} = \begin{pmatrix} \hat{v}_1 \\ \vdots \\ \hat{v}_n \end{pmatrix} \tag{3.11}$$

Another useful criteria is the estimated variance factor (of unit weight) $\hat{s}_0^2$:

$$\hat{s}_0^2 = \frac{\hat{V}^T P \hat{V}}{n-m} \tag{3.12}$$

For random measurement errors following a standard normal distribution, $\hat{s}_0{}^2$ is a non-biased estimator of s_0^2. With the assumption that, in our case, all the uncertainty information is included in the Σ_L matrix (i.e., $s_0^2 = 1$), the estimated variance factor ($\hat{s}_0^2$) shall be a value close to 1.

In the least-squares adjustment method, it is also possible, in addition to the estimated values, to compute the estimated covariance of the solution $\Sigma_{\hat{X}}$:

$$\Sigma_{\hat{X}} = \hat{s}_0^2 N^{-1} = \hat{s}_0^2 (A^T P A)^{-1} = \hat{s}_0^2 \begin{pmatrix} \hat{\omega}_1{}^2 & \hat{\omega}_{12} & \dots & \hat{\omega}_{1n} \\ \hat{\omega}_{21} & \ddots & \ddots & \vdots \\ \vdots & \ddots & \ddots & \hat{\omega}_{n-1,n} \\ \hat{\omega}_{n1} & \hat{\omega}_{n2} & \dots & \hat{\omega}_n{}^2 \end{pmatrix} \tag{3.13}$$

Where $\hat{s}_0 \hat{\omega}_{i,j}$ is the covariance between the parameters x_i and x_j and $\hat{s}_0 \hat{\omega}_i$ is the standard uncertainty of the parameter x_i.

3.2.3 The covariance propagation law

Also called Law of covariance or Law of propagation of covariance, described in [91], the covariance propagation law is very useful in our study, as it links the covariance matrices of two random vectors with linear dependency.

For a set of two vectors X and Y linearly linked:

$$Y = CX + C_0 \tag{3.14}$$

The covariance matrix of Y, noted Σ_Y, can be expressed as a function of the covariance matrix of X, noted Σ_X, thanks to the formula:

$$\Sigma_Y = C \Sigma_X C^T \tag{3.15}$$

In case of non-linear link between the two vectors:

$$Y = f(X) \tag{3.16}$$

The function f needs to be approximated by its first order Taylor series expansion around a value $\hat{U}$ (equation 3.3). In that case, the covariance law is:

$$\Sigma_Y = C\Sigma_X C^T \quad \text{with} \quad C = \frac{\partial f(\hat{U})}{\partial X} = \begin{pmatrix} \frac{\partial f(\hat{U})}{\partial x_1} & \cdots & \frac{\partial f(\hat{U})}{\partial x_n} \\ \vdots & \ddots & \vdots \\ \frac{\partial f(\hat{U})}{\partial x_1} & \cdots & \frac{\partial f(\hat{U})}{\partial x_n} \end{pmatrix} \tag{3.17}$$

This propagation law is widely used after a least-squares adjustment, to compute the covariance matrix of the solution after a coordinate transformation. In this case, the $\hat{U}$ value corresponds to the estimated value. In this work, this propagation law is also used to retrieve the uncertainties on the mesurands from the estimated ones.

3.3 Proposed alignment monitoring strategy

In order to achieve the physics goals of the FCC project, the alignment requirements given in section 1.3.2 have been established. But we saw in chapter 2 that no existing system could deal with both the tight requirements and the harsh conditions of the FCC-ee MDI. In order to face these challenges, new paths have been explored, trying to integrate new types of sensors in new exotic configuration in order to fulfill all the requirements. The resulting proposition plans to divide the problem and deal with it via two subsystems. One of these subsystems will measure the components deep inside the detector with respect to an interface, located towards the outside of the detector, while the other subsystem will monitor this interface and link the alignment with the rest of the machine. These systems are named "internal monitoring system" and "external monitoring system". While the external monitoring system will be a network of distance measurements, the internal monitoring system will implement a novel method, monitoring the 3D deformation of a cylinder.

3.4 Alignment monitoring system based on relative measurements

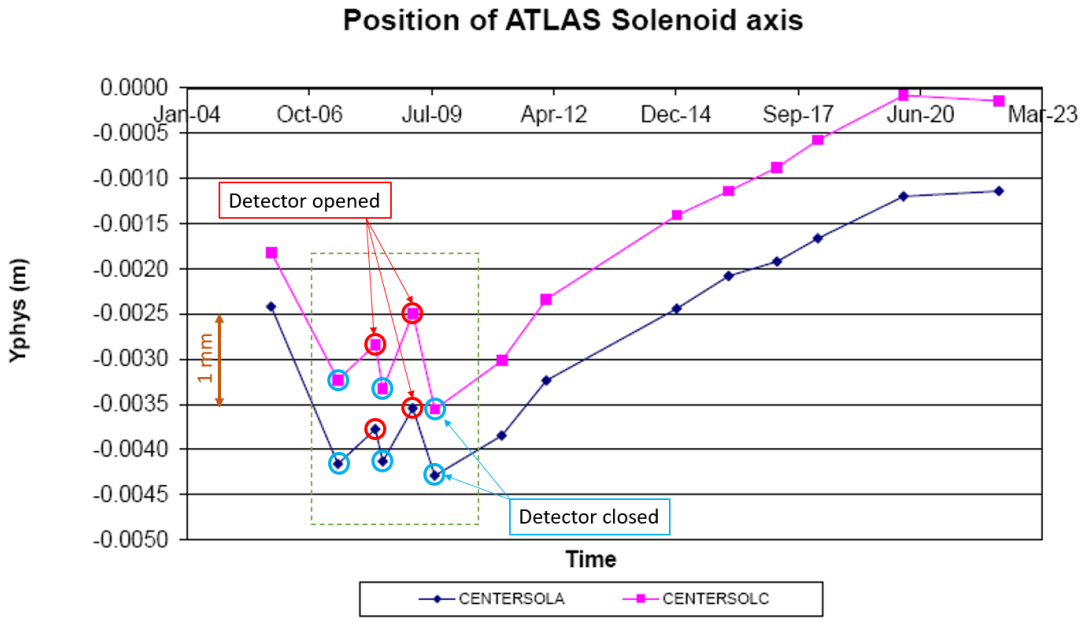

Figure 3.1: Measurements of the ATLAS solenoid axis done while the detector is open during maintenance. In 2008, some measurements were done while the detector was closed. The comparison highlighted a movement of more than a millimeter of the solenoid axis between the open and closed state ([11]).

The monitoring of the MDI aims to be autonomous, continuous, and absolute. Currently, the measurements of the detectors in the LHC, such as ATLAS, are performed during shutdowns, where the detectors are opened for maintenance. During that time, some targets, uniquely visible during these maintenance stops, are measured in order to determine their position. Then, the detectors are closed and the knowledge of the position of the inner components rely on these rare measurements for the following years, until the next maintenance. But it is known that parts are moving and that positions of components are not stable when closing a multiple hundred tons of more than 100 cubic meters. Fig. 3.1 shows the displacement of the solenoid axis between the opened and closed state of the detector [11]. On this illustration, two points on the solenoid were measured (pink and blue) in different detector configurations. The interesting point being the comparison between measurements with the detector opened, and the detector closed, between which there is an offset of 1 mm. These measurement campaigns are rare as, once closed, it is difficult to measure elements inside

the detector. In addition, some parts are cooled down, adding thermal contraction to the problem, and everything is in an intense magnetic field, adding magnetic forces between the quadrupoles. All these effects have impacts on the position of the components at the millimeter level, which is too big to be negligible. This is underlined by the offsets measured in the SuperKEKB/BelleII MDI during the SSW measurement, and the one expected for the FCC-ee MDI should be even greater as the MDI is bigger and more complex. The accuracy of the positioning of the component is therefore degraded. A continuous measurement system, by providing uninterrupted information on the component position, allows knowing its movements during closing and cooling down of the detector while keeping a better measurement uncertainty. This is the strategy chosen for the monitoring of the low-β quadrupoles and the crab-cavities in the HL-LHC, where the cold masses are monitored with respect to their cryostat using FSI distance measurements. This strategy is also chosen for the monitoring of the FCC-ee MDI.

3.5 Internal alignment system

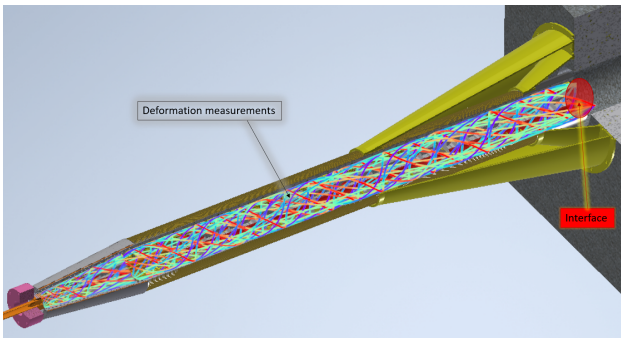

Figure 3.2: The first step is to monitor the deformation of the cylinder supporting the screening and compensation solenoids via the fiber network.

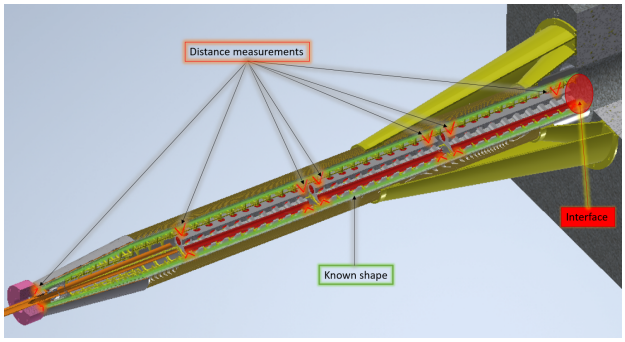

Figure 3.3: The second step is to measure the internal components using distance measurements with respect to the cylinder.

3.5.1 Goal and challenges

The first system, described in Fig.3.2 and Fig.3.3 aims to monitor the position of the inner component, namely the final focusing quadrupoles, the BPMs, the LumiCals, the solenoids and any other components not yet added by the design team. The advantages of such a system are that it allows to continuously measure the position of the inner components while the MDI is closed, it also grants good accuracy of the position knowledge. It is important to note that it can also be used during

construction and initial testing of the assembly. Allowing such testing capabilities could be extremely convenient in case of finding of an unexpected offset or displacement during the assembly, permitting to perform the repositioning while still being in the assembly facility. This system would also allow to follow the position of the inner components during the transport between the assembly facility, the different testing locations (cryogenic, vacuum) and the tunnel where it will finally sit.

This system should be able to deal with the conditions inside while being accurate enough to fulfill the requirements. The idea is to perform the monitoring in two steps: first, measure the deformation of the supports of the elements and then measure from that precisely known shape towards the inner components via distance measurements. The proposed solution is using optical fibers as distance measurement sensors. Nowadays, multiple technologies allow us to measure the length of different portions of an optical fiber independently and simultaneously. These technologies are developed in the Chap 4. Similar sensors are already used in civil-engineering to monitor buildings such as bridges, dams, skyscrapers and so on [12]. But for these applications, the sensors are used to monitor 1D deformation or 1D+1D [92], which is not enough for us.
The first step was to define clearly the deformations used for the simulations.

3.5.2 Reference frame and deformation definition

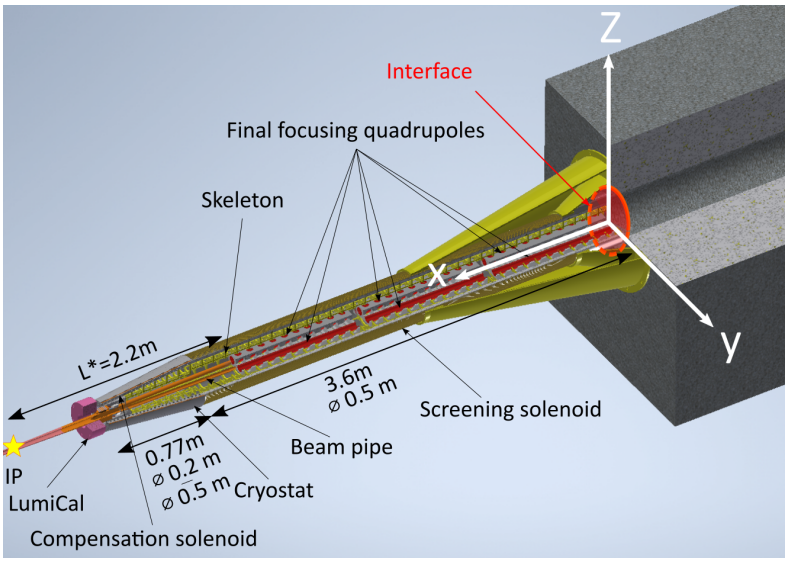

Figure 3.4: A general view of the assembly and the coordinate system associated to the interface. The different elements can be seen, from the inside out: the beam pipe (orange), the final focusing quadrupoles (red), the skeleton (yellow), the support and cooling structure for the solenoids (gray), the screening and compensation solenoids (orange) and the thin cryostat (gray). The interface used as reference for the deformation monitoring system is placed at the outer end of the assembly.

Deformations are defined in the (O, O_x, O_y, O_z) Euclidean system linked to the interface plate, shown in Fig.3.4. The origin of this system is the center of the plate, the O_x is perpendicular to the plate, O_y is the intersection of the plane of the plate and the plane formed by the incoming and outgoing beams and O_z is the last vector in order to form an oriented orthogonal system. O will be located between the intersections of the beams and the plate plane. As opposed to a physicist definition, where O_z is along the beam direction, here O_z is towards the zenith, which corresponds to the surveyor definition of the coordinate system (for an easier link with other monitoring systems). This definition aims to be versatile and to adapt to any MDI design update.

In that system, as shown in (3.18), we can express the usual (x, y, z) point coordinates on a cylinder thanks to a set of functions, to later include deformations and to compute point positioning formal

precision:

$$\begin{cases} C_X(x,y,z) = x \\ C_Y(x,y,z) = r\sin(\phi), \quad \text{with} \quad \phi = \arctan 2\,(y,z) \\ C_Z(x,y,z) = r\cos(\phi) \end{cases} \tag{3.18}$$

Where C_X, C_Y and C_Z are the three coordinates of the point, r is the radius of the cylinder and ϕ is the angular position of the point on the cylinder It is interesting to note that, without any deformations: $C_X(x,y,z) = x$, $C_Y(x,y,z) = y$, $C_Z(x,y,z) = z$.

As the design is still at an early stage, and we don't know precisely the forces at stake, deformations will be modeled by polynomials in order to be able to simulate a wide range of deformations. In our current analysis process, six deformation polynomials are used, as indicated in eq.(3.19). Polynomials allow to play with their degree to model simpler or more complex deformations. The constant is not studied as it corresponds to the initial position of the cylinder in the MDI. The measure of these constants will be done by the external monitoring system and will allow to link the coordinate system to other points of interest, like the beam axis, the vertical and so on.

$$\begin{gathered} \forall u \in \mathbb{R} \\ P_x(u) = \sum_{i=2}^{n} a_i u^i,\ P_y(u) = \sum_{i=1}^{n} b_i u^i,\ P_z(u) = \sum_{i=1}^{n} c_i u^i, \\ P_\theta(u) = \sum_{i=2}^{n} d_i u^i,\ P_{ry}(u) = \sum_{i=1}^{n} e_i u^i,\ P_{rz}(u) = \sum_{i=1}^{n} f_i u^i \end{gathered} \tag{3.19}$$

With P the polynomials, u the abscissa, $n \in \mathbb{N}$ and $\forall i \in [\![0;n]\!]$, $\quad a_i, b_i, c_i, d_i, e_i, f_i \in \mathbb{R}$.

The impacts of these polynomials are represented in 3.5, where they are applied to a cylinder with the same characteristics as the screening solenoid support, and in the Cartesian coordinate system of the interface: the first deformation is the longitudinal deformation P_x. The two following deformations modeled by P_y and P_z are radial deformations. Then there is a torsion P_θ and finally two radius deformations P_{ry} and P_{rz} which model the flattening of the cylinder in both directions. Thanks to these polynomials, we are able to model the deformed cylinder, subject to all the forces endured by the assembly once in the detector (gravity, Lorentz force, cooling effects, and so on).

In case of deformations, the coordinates of the points stated in (eq.3.18) are expressed as:

$$\begin{cases} C_{Xd}(x,y,z) = x + P_x(x) \\ C_{Yd}(x,y,z) = (r + P_{ry}(x))\sin(\phi + P_\theta(x)) + P_y(x) \\ C_{Zd}(x,y,z) = (r + P_{rz}(x))\cos(\phi + P_\theta(x)) + P_z(x) \end{cases} \tag{3.20}$$

It allows to express the points coordinates altered by the deformations. Examples of such deformed points are represented later in this chapter, in Fig.3.19.

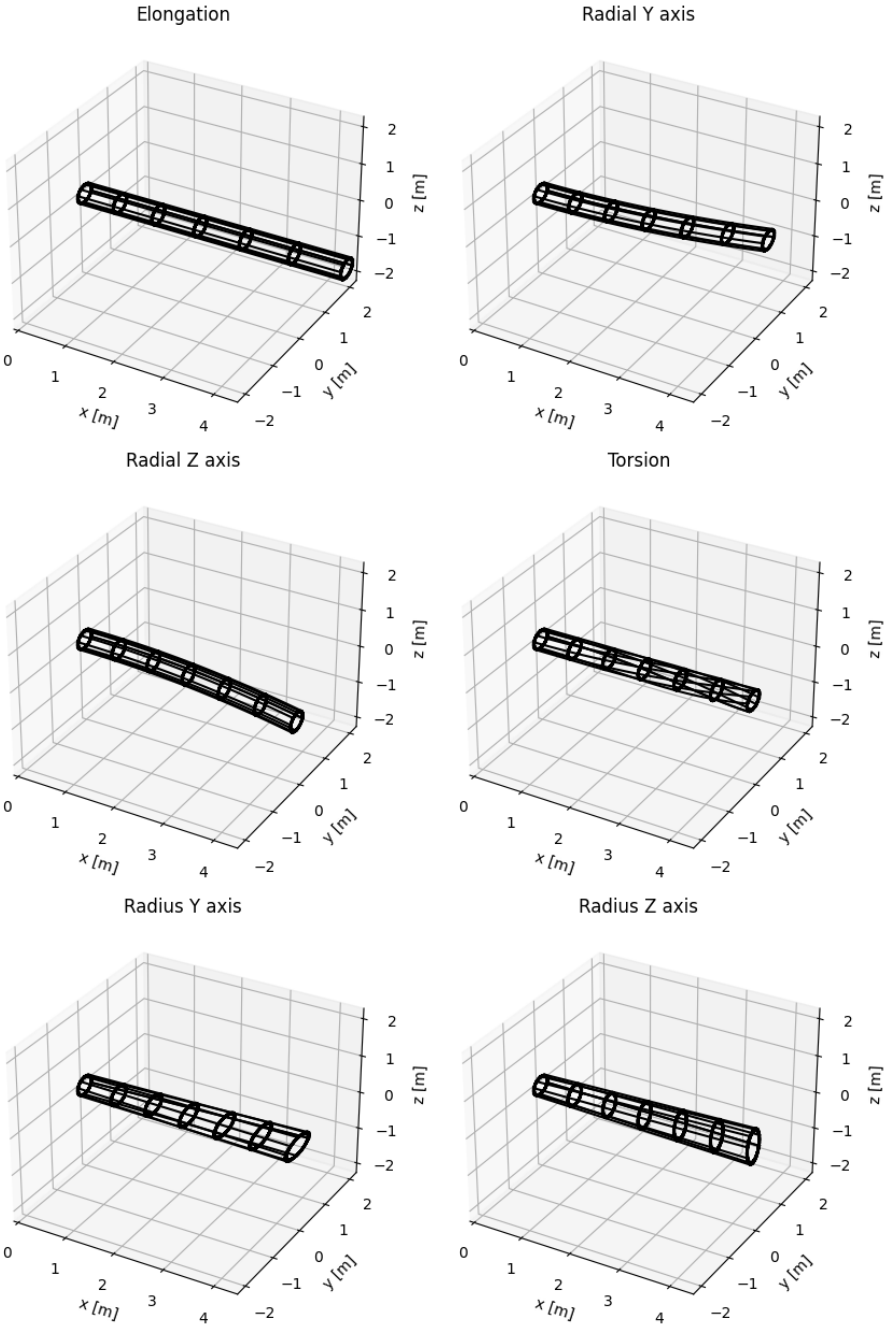

Figure 3.5: Deformation visualization (magnified approximately 1000 times) from top to bottom and left to right: longitudinal deformation, radial deformation in the horizontal plane, in the vertical plane, torsion and finally radius deformation in the horizontal plane and in the vertical plane.

This model may not be optimal, but it will serve as a first approximation, while waiting for a more mature design. Mechanical simulations on the 3D models have been asked, but none could be

performed for now.

3.5.3 Creation of the network

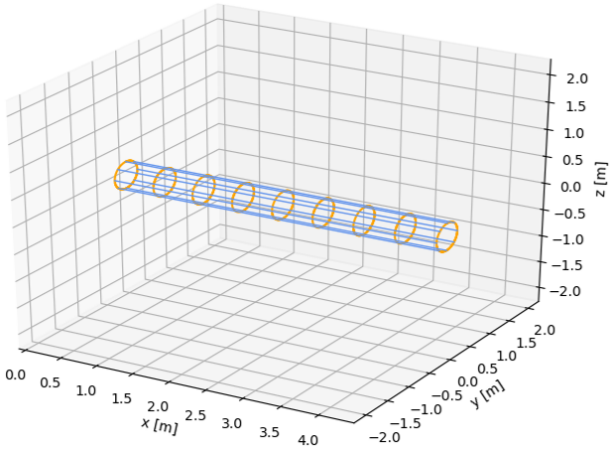

Figure 3.6: Original idea for the disposition of the fibers on the cylinder, with fibers installed in circles (orange) and other longitudinally (blue). But deformations are not well monitored.

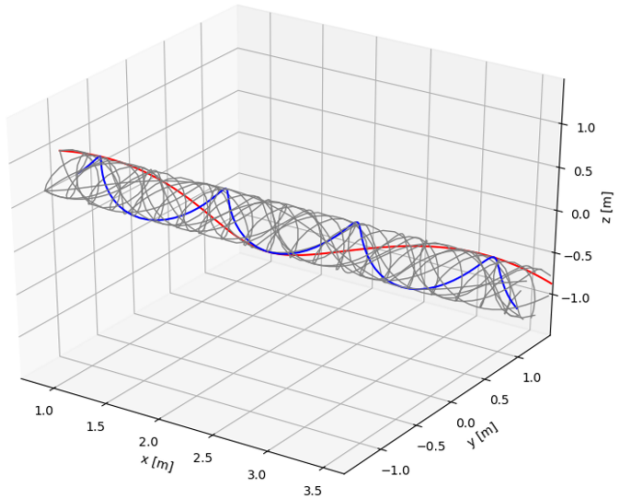

Figure 3.7: Example of network with enough different direction and steps to differentiate the deformations. Two helices have been highlighted: a small step right-handed helix (blue) and a big step left-handed helix (red).

Once the deformations modeled, we can work on the network of fibers. The proposition is an exotic solution: the idea is to monitor the shape of a cylinder thanks to a network of optic fiber placed along the cylinder. These fibers have multiple measuring portions along their length. Each of these portions are measured independently and simultaneously.

Knowing the existence of that technology, the first test was to place them longitudinally and in circles, as in Fig.3.6. But, this network installation showed to be not consistent enough, as it was not able to distinguish an elongation deformation from a torsion deformation. The idea was then to place some fibers in “diagonal” which on a cylinder corresponds to a helix. A helix could monitor all the deformations, but by doing so, it is difficult to isolate the parameters for their resolution. As an example, a helix alone could not differentiate a torsion from an elongation. But, by installing two helices in different directions, these 2 deformations would be measurable. By completing the network with helices with different characteristics (such as the step, direction, and even radius) it is possible to measure everything and compute every parameter. For example, two helices with different directions

allow a good differentiation between elongation and torsion. It can also be done by two helices of the same direction but different steps, but less precisely.

On the other hand, two different steps allow a precise differentiation of the coefficients of the elongation deformation polynomial. Such conditions on the various characteristics of the helices guided the development of the network from the Fig.3.6 to the Fig.3.7. It is important to keep in mind that, even though it looks dense, this network is composed of optical fibers which are around 0.1 mm in diameter, resulting in a cylinder of 0.5 mm maximum thickness in case of 5 fibers crossing at the same location.

3.6 Internal alignment system

The goal is to measure elements installed inside a cylinder of 3.6 m long and 25 cm radius, ended by a 0.77 m truncated cone with a start at a 25 cm radius towards a 10 cm radius. This system will perform two types of measurements: deformation measurements and regular distance measurements. The distance measurements are only to locate the component with respect to the cylinder. The position of the component is deduced by the positioning of multiple targets placed on it and measured by multiple heads located on the cylinder. The distance measurements are not detailed here and will be taken into account for the general computation in section 3.8. This part focuses on the deformation measurements, which represents the key system to monitor the alignment in this MDI.
The fibers are placed in a network of helices inside the cylinder, so a wide range of deformations can be monitored. The deformations studied are modeled by a 4th order polynomial as a first approximation, as a sweet spot between a simple model but not detailed enough and a model over-detailed, complex and long to compute. This simulation leaves some room for further optimization. For the simulations, fibers have been defined to be able to measure 100 portions of the same size along their length.

3.6.1 Equations

The first step is to express the helix equation on a cylinder in the coordinate system defined in fig.3.4. The equation of a helix in that situation is:

$$\begin{cases} h_x(x) = x \\ h_y(x) = \varepsilon r \sin\left(\dfrac{x}{p} + \alpha\right) \\ h_z(x) = r\cos\left(\dfrac{x}{p} + \alpha\right) \end{cases} \tag{3.21}$$

Where ε corresponds to ± 1 to define if the helix is right-handed or left-handed, r corresponds to the radius of the helix, p corresponds to the step and α corresponds to the angle in the (O, O_y, O_z) plane from which the helix starts. The impact of deformations on these helices can be modeled by

adding the polynomials to eq.(3.21) resulting in eq.(3.22):

$$\begin{cases} h_{x_d}(x) = x + P_x(x) \\ h_{y_d}(x) = \varepsilon(r + P_{ry}(x)) \sin\left(\dfrac{x}{p} + \alpha + \varepsilon P_\theta(x)\right) + P_y(x) \\ h_{z_d}(x) = (r + P_{rz}(x)) \cos\left(\dfrac{x}{p} + \alpha + \varepsilon P_\theta(x)\right) + P_z(x) \end{cases} \tag{3.22}$$

The implementation of the deformations in the helix equation is not perfect. In reality, radial deformations impact the longitudinal one. In our case, we simplified the equations, as the expected deformations would not exceed 2 mm at the extremity of the 4 m long and 25 cm radius cylinder. These deformations are limited by the mechanical design: 2 mm is the space available for the cryostat to move inside the detector, before touching it. If the deformations are bigger than 2 mm, the cryostat will be in contact with the detector as underlined in section 1.3.1 and won't deform more. In general, in case of larger deformations, second range impact (such as longitudinal deformation implied by the radial deformation) can appear and equations have been written (cf. annexeA). But for the studied deformation range, these second range deformations are negligible (deformations smaller than 1 μm).

In addition, the helix equations eq.(3.21) have been modified to take into account a variable radius, to measure the deformation up to the truncated cone supporting the compensation solenoid:

$$\begin{cases} h_{x_d}(x) = x + P_x(x) \\ h_{y_d}(x) = \varepsilon(r(x) + P_{ry}(x)) \sin\left(\dfrac{x}{p} + \alpha + \varepsilon P_\theta(x)\right) + P_y(x) \\ h_{z_d}(x) = (r(x) + P_{rz}(x)) \cos\left(\dfrac{x}{p} + \alpha + \varepsilon P_\theta(x)\right) + P_z(x) \end{cases} \tag{3.23}$$

The point equation can also incorporate the variable radius, as expressed in eq.(3.24):

$$\begin{cases} x_d(x) = x + P_x(x) \\ y_d(x) = (r(x) + P_{ry}(x)) \sin(\alpha + P_\theta(x)) + P_y(x) \\ z_d(x) = (r(x) + P_{rz}(x)) \cos(\alpha + P_\theta(x)) + P_z(x) \end{cases} \tag{3.24}$$

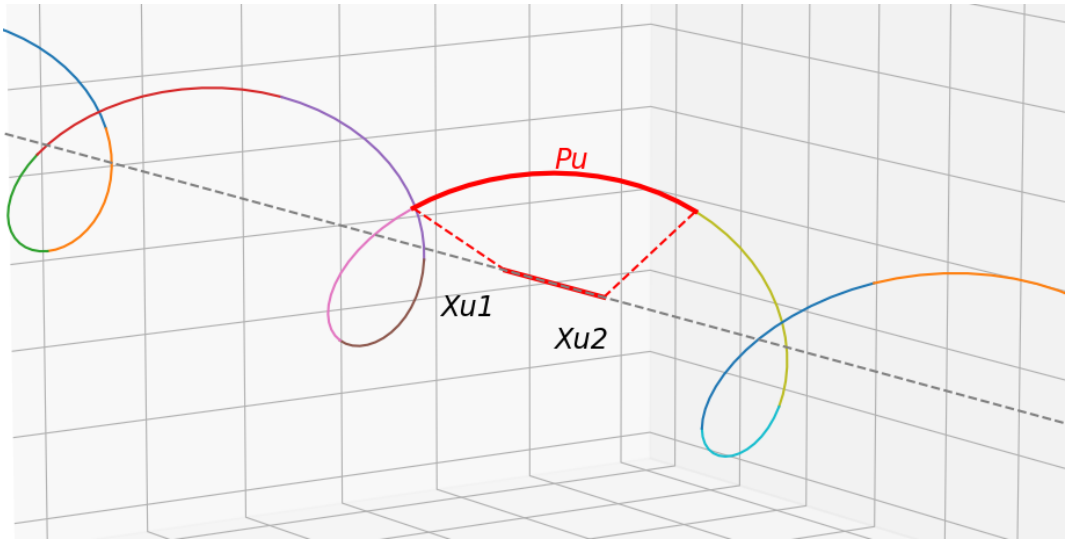

Figure 3.8: Visualization of a fiber portion p_u between two consecutive semi-reflective interfaces in the fiber located at abscissas x_{u1} and x_{u2}.

Fig.3.8 illustrates the portion p_u between two consecutive semi-reflective interfaces located at the abscissas x_{u1} and x_{u2}, and the corresponding length is expressed in eq.(3.25):

$$d(p_u) = \int_{x_{u1}}^{x_{u2}} \sqrt{\dot{h_{xd}}(x)^2 + \dot{h_{yd}}(x)^2 + \dot{h_{zd}}(x)^2}\,\mathrm{d}x \tag{3.25}$$

In this equation, the notation $\dot{f}(x)$ corresponds to the derivative of the function $f(x)$ with respect to the variable x.

This equation links the portion length of a helix portion with deformation coefficients. By constructing the Jacobian matrix, deriving the equation with respect to each parameter for all the measurements, it is possible to compute the parameters using the least-squares adjustment computation.

The A matrix in the least-squares adjustment is:

$$A = \begin{pmatrix} \frac{\partial d(p_1)}{\partial a_1} & \frac{\partial d(p_1)}{\partial a_2} & \cdots & \frac{\partial d(p_1)}{\partial a_4} & \frac{\partial d(p_1)}{\partial b_1} & \cdots & \frac{\partial d(p_1)}{\partial f_4} \\ \frac{\partial d(p_2)}{\partial a_1} & \frac{\partial d(p_2)}{\partial a_2} & \cdots & \frac{\partial d(p_2)}{\partial a_4} & \frac{\partial d(p_2)}{\partial b_1} & \cdots & \frac{\partial d(p_2)}{\partial f_4} \\ \vdots & \vdots & & \vdots & \vdots & & \vdots \\ \frac{\partial d(p_m)}{\partial a_1} & \frac{\partial d(p_m)}{\partial a_2} & \cdots & \frac{\partial d(p_m)}{\partial a_4} & \frac{\partial d(p_m)}{\partial b_1} & \cdots & \frac{\partial d(p_m)}{\partial f_4} \end{pmatrix} \tag{3.26}$$

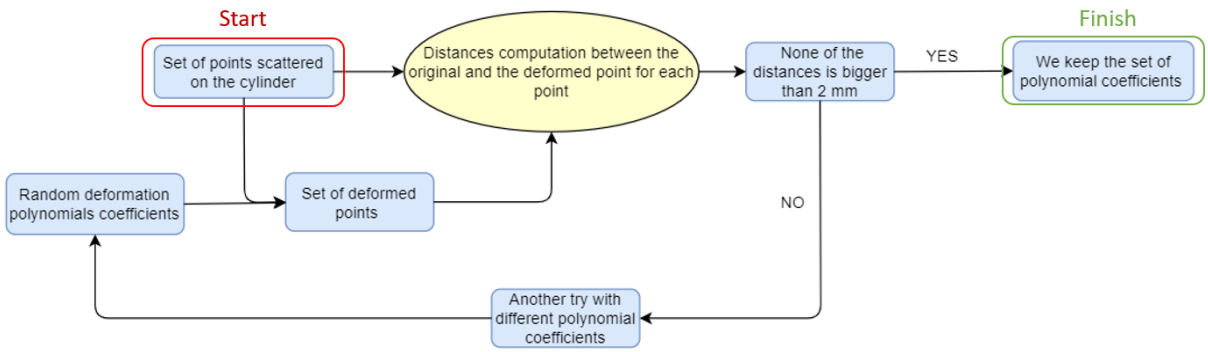

Figure 3.9: Process for the generation of polynomial coefficients

3.6.2 Simulations

In order to test the system, simulations have been carried out. The goal of the system is to be able to compute the deformation (in the form of the polynomial coefficients) from a set of measurements done by the helices. To compute the deformations, we needed to generate coefficients and create artificial measurements to feed our computation.

3.6.2.1 Generation of artificial measurements

At the beginning, as shown on Fig.3.9, coefficients were randomly generated, and then applied to a set of randomly and uniformly scattered points on a cylinder (that has the shape of the studied support of the screening solenoid) using the equation 3.20 to quantify the deformation effect on the entire cylinder. These deformed points are compared with the original and non-deformed set of points. The comparison is carried out by computing the 3D distances between each point and its deformed version, resulting in a list of offsets represented on Fig. 3.10. As the maximum deformation allowed in the MDI is 2 mm, if all the offsets are below 2 mm, the set of coefficients is stored, and if not, the computation is performed again with another set of coefficients. But more than 99.99% of the generated coefficients were not fulfilling this test, as the resulting deformation were bigger than 2 mm at the extremity of the cylinder. Therefore, boundaries were added for the generation of coefficients: rather than being entirely randomly generated, the polynomial coefficients were generated between a minimal and maximal value (defined for each coefficient), therefore avoiding deformations that were, for sure, bigger than 2 mm. These boundary values for the coefficients were chosen by hand testing. Fig.3.11 and Fig.3.12 show the 3000+ sets of coefficients generated that validated the test,

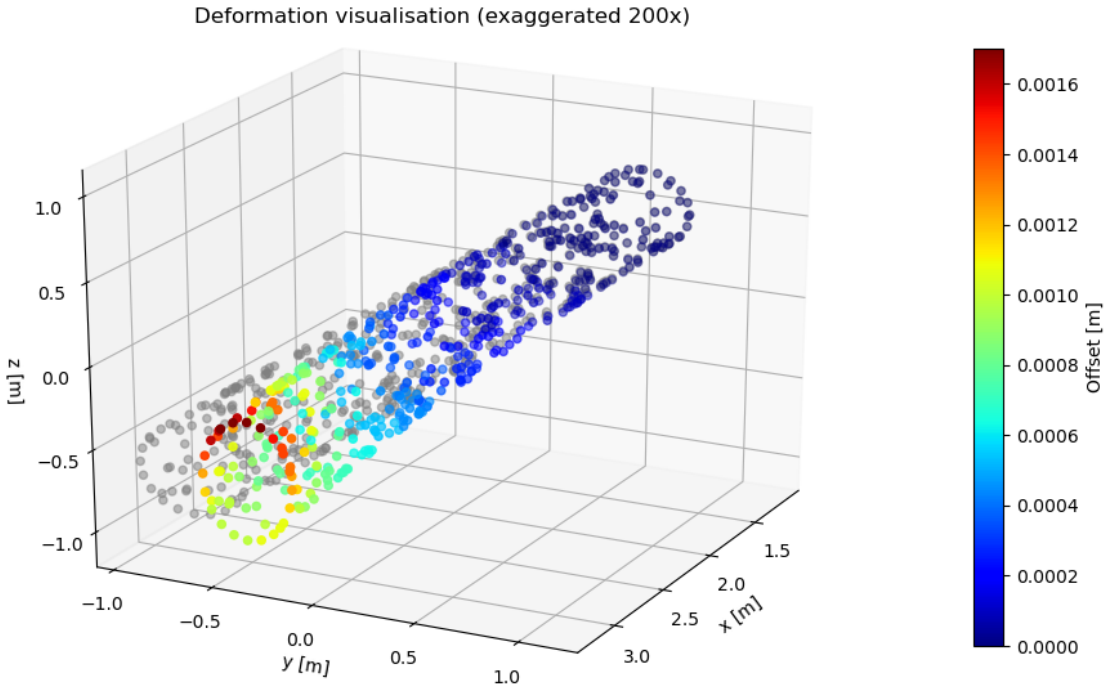

Figure 3.10: Result of the comparison between points on the cylinder and points deformed in the generation of coefficient process

creating deformations smaller than 2 mm at the extremity of the cylinder. These graphs represent the distribution of coefficients that validated the test out of a uniform law with boundaries. The lower order coefficients are still close to a uniform law between the two boundaries after the selection, while the higher order are closer to a Gaussian law. The hypothesis is that all the coefficients kept should follow a Gaussian shaped distribution, but it would imply to be at the limit of passing the 2 mm maximum deformation test for all the coefficients, resulting in a lot of rejects at the test. One could ask if it would create any kind of bias to have limited the coefficient generation, but it should not, as it is centered. Moreover, even though they haven't been tested, the coefficients not taken into account can be computed by the system. It is important to note that these deformations will be as small as possible in the finished assembly after optimization from the mechanical team. The effort of the mechanical design team, especially about the stiffness optimization of the support design will also limit the high order coefficients of the polynomials.

Once again, this generation could be optimized, but provided a good sample with a wide range of deformations to study our system.

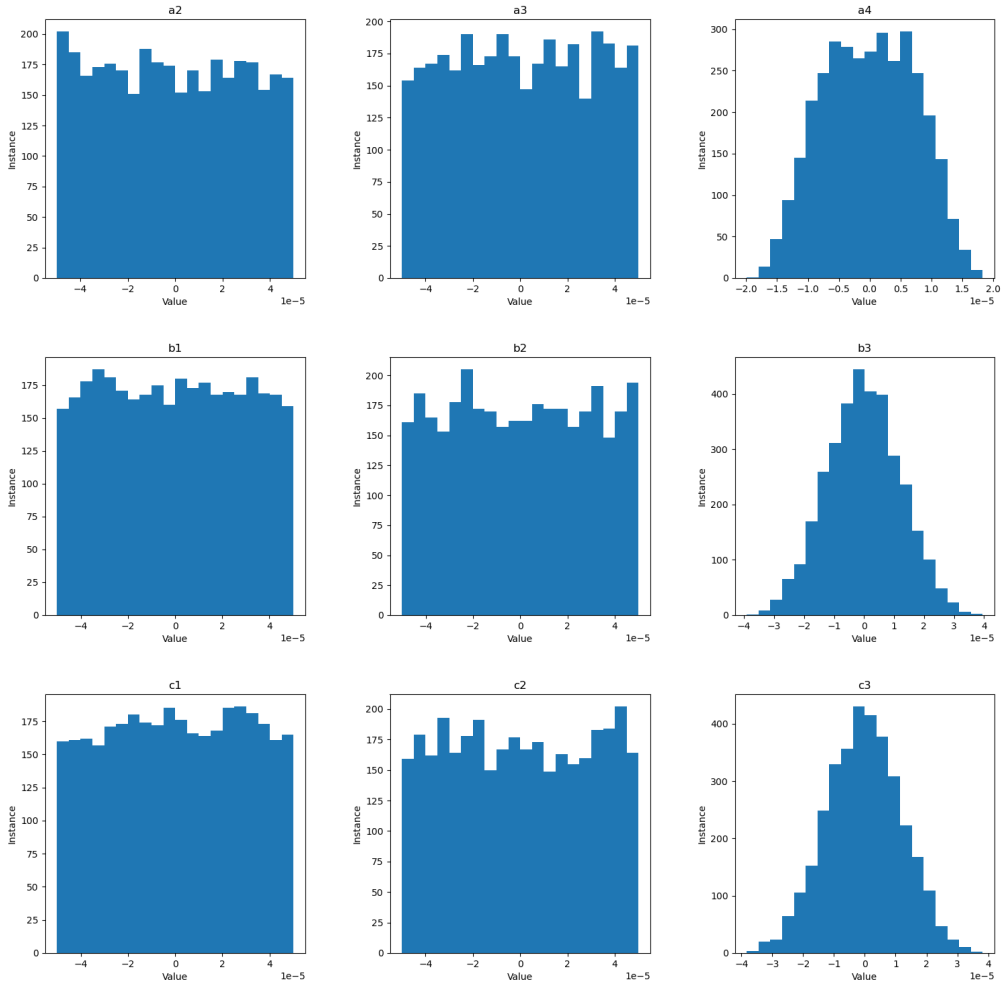

Figure 3.11: Histograms showing the coefficients generated for the longitudinal deformation (first line) the horizontal radial deformation (second line) and vertical radial deformation (third line). All the lower orders are close to a uniform distribution, while the highest order is close to a Gaussian distribution.

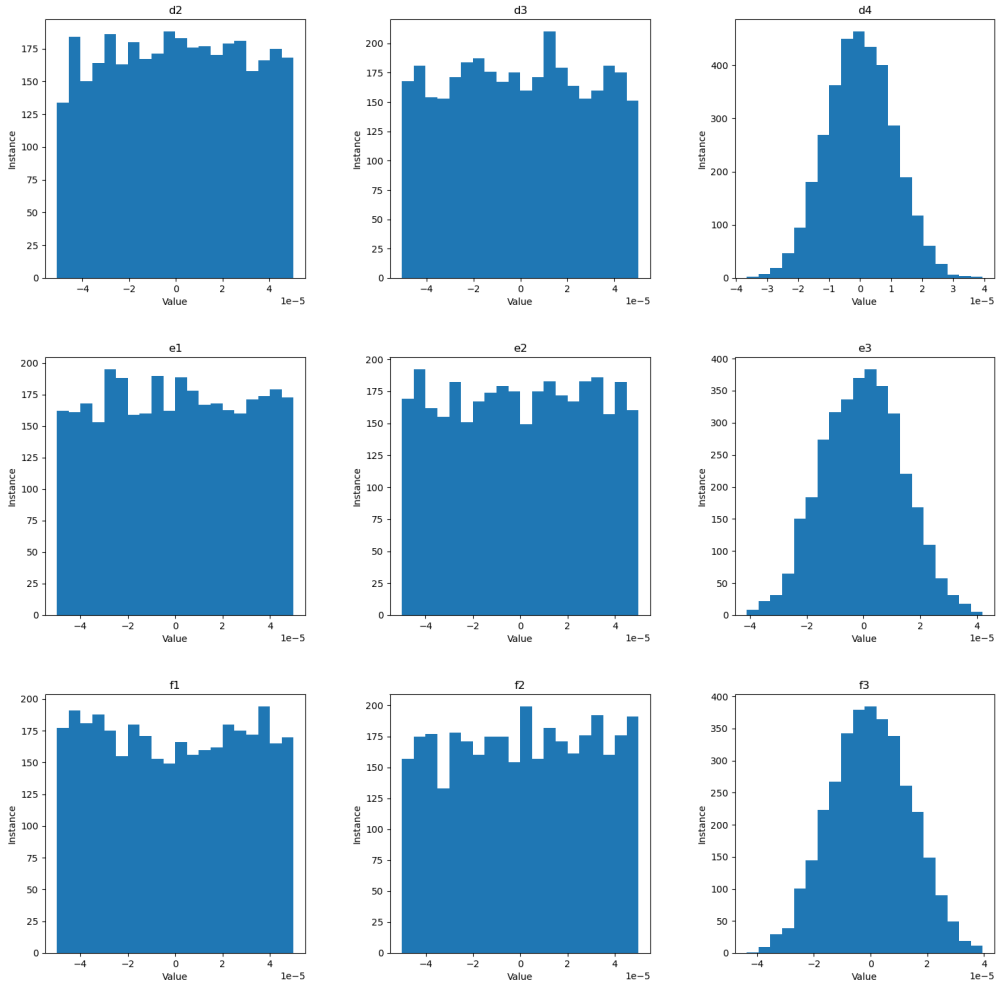

Figure 3.12: Histogram showing the coefficients generated for the torsion (first line), the horizontal radius deformation (second Line) and the vertical radius deformation (third line). All the lower order are close to a uniform distribution, while the highest order is close to a Gaussian distribution.

Once a set of coefficients is found, we can artificially construct helix portion measurements using the process shown on Fig. 3.13. Knowing the helices characteristics and the deformation coefficients, eq.3.25 can be used to generate a set of observations. These observations are then altered, by adding an artificial random measurement error, in the form of a random value following a centered normal distribution, with a standard deviation of 1 μm (assumed to be the precision of the system, developed further in chap.4).

Once the artificial measurements are created, we can use the least-squares adjustment method to compute adjusted polynomial coefficients.

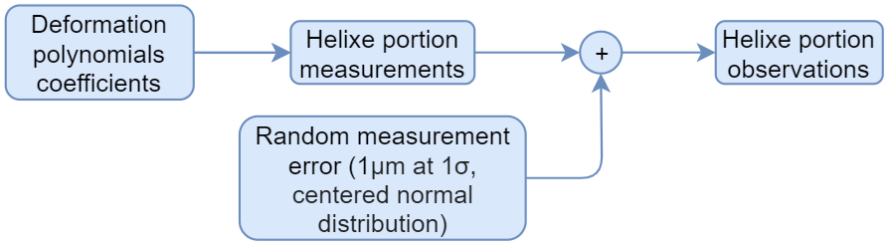

Figure 3.13: Process for the generation of artificial observations

3.6.2.2 Shaping of the results

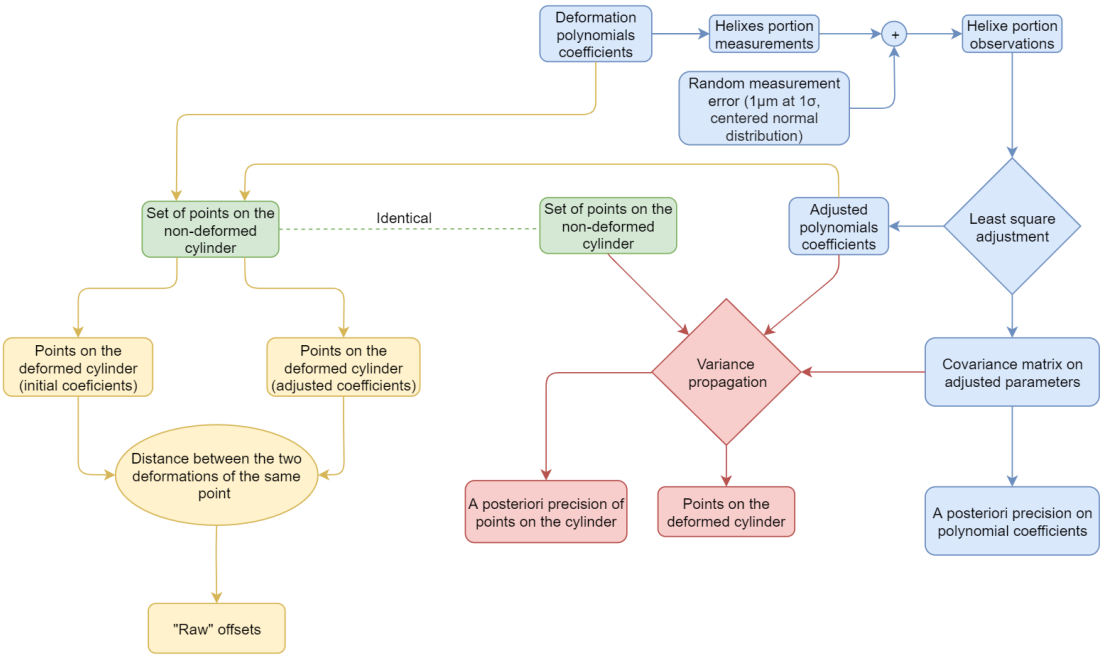

Figure 3.14: Process in order to do a simulation of the system. The results of the adjustment have been used in two different ways to express the uncertainties of the point positions.

The standard uncertainty out of the adjustment computation is found in the covariance matrix of the parameters. This defines the uncertainty of the polynomial coefficients, which is not the easiest to interpret. Moreover, it is a data rather difficult to share as, usually, point positions and target uncertainties over these positions are preferred. In order to compute this information, two different ways have been explored and are shown in Fig.3.14. The first way, the yellow path on Fig.3.14, was an attempt for a fast and easy indication of the point position uncertainties by comparing the position of

a set of points deformed by both the initial set of deformation chosen for the simulations and the set of deformation outputted by the adjustment computation. The indication of the position uncertainty over each point is given by the distance computed between the two deformations of the same point. The second way, corresponding to the red path on Fig.3.14, is using the covariance law, via the covariance matrix of the coefficients coming from the adjustment computation, and the Jacobian matrix of the eq.3.20 with respect to the coefficients. This equation was used to form the Jacobian matrix in x_s, the studied point from which we want to have the position uncertainty:

$$\begin{aligned} J &= \begin{pmatrix} \frac{\partial x_d(x_s)}{\partial a_1} & \frac{\partial x_d(x_s)}{\partial a_2} & \dots & \frac{\partial x_d(x_s)}{\partial a_n} & \frac{\partial x_d(x_s)}{\partial b_1} & \dots & \frac{\partial x_d(x_s)}{\partial f_n} \\ \frac{\partial y_d(x_s)}{\partial a_1} & \frac{\partial y_d(x_s)}{\partial a_2} & \dots & \frac{\partial y_d(x_s}{\partial a_n} & \frac{\partial y_d(x_s)}{\partial b_1} & \dots & \frac{\partial y_d(x_s)}{\partial f_n} \\ \frac{\partial z_d(x_s)}{\partial a_1} & \frac{\partial z_d(x_s)}{\partial a_2} & \dots & \frac{\partial z_d(x_s)}{\partial a_n} & \frac{\partial z_d(x_s)}{\partial b_1} & \dots & \frac{\partial z_d(x_s)}{\partial f_n} \end{pmatrix} \\ &= \begin{pmatrix} \frac{\partial P_x(x_s)}{\partial a_1} & \frac{\partial P_x(x_s)}{\partial a_2} & \dots & \frac{\partial P_x(x_s)}{\partial a_n} & 0 & \dots & 0 \\ 0 & 0 & \dots & 0 & \frac{\partial P_y(x_s)}{\partial b_1} & \dots & 0 \\ 0 & 0 & \dots & 0 & 0 & \dots & \frac{\partial P_{rz}(x_s)}{\partial f_n} * \cos(\alpha + P_\theta(x_s)) \end{pmatrix} \end{aligned} \tag{3.27}$$

Now, by applying the covariance propagation law to the covariance matrix resulting from the least-squares adjustment, we can compute the standard measurement uncertainty on the point position, as the result of the system computation.

$$\Sigma_{points} = J\Sigma_{coefs}J^T \tag{3.28}$$

3.6.3 Results

Simulations were performed using 36 helices of 100 portions of the same length for a total of 3600 measurements. The impact of the deformation on the portion length are shown in Fig.3.15. On this figure, we can see the fiber network placed on the cylinder, colored with the change of length of the fiber portion as a function of the deformation. The blue color represents the lowering of the length, while the red color is towards the increasing of the length of the fiber. It is interesting to see that each deformation has a different impact on the network of helices. The elongation has the same impact on the helices of both direction and same step, while a difference appears between helices with different steps. Radial deformations impact similar portions, but separated by an angle $\frac{\pi}{4}$. Torsion deformations impact differently the right-handed helices and the left-handed helices. The impact is

also depending on the step of the helices. Finally, both radius deformations impact the same portions, also separated by an angle $\frac{\pi}{4}$. The radius deformation and radial deformation do not affect the same helices. This underlines the computability by the least-squares adjustment method, as this network is able to distinguish the different deformations using the different helices.

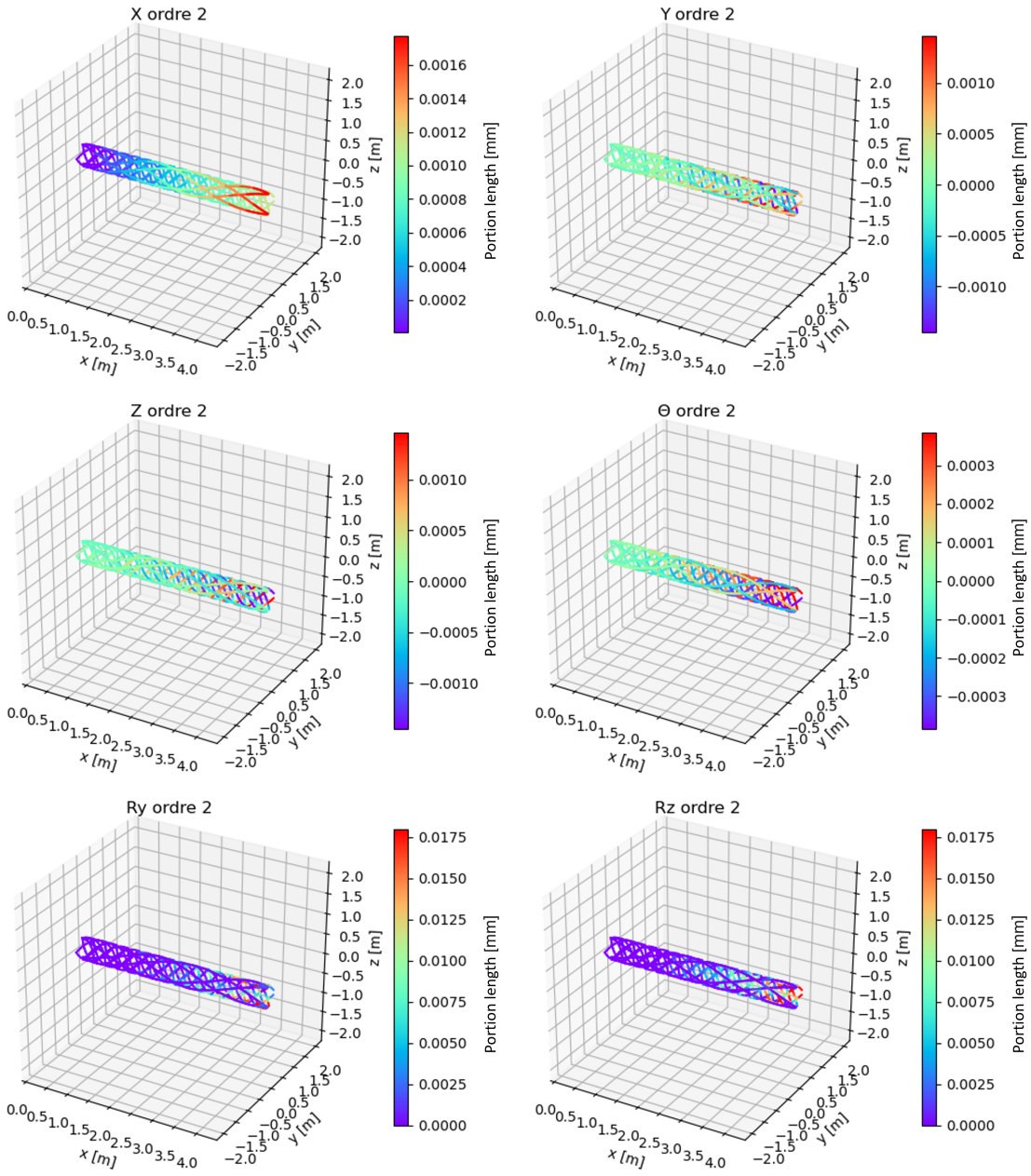

Figure 3.15: Deformation impact on the portions lengths. The impact of the deformations are on different locations of the fibers.

3.6.3.1 First results: raw offsets

The first study of the results was performed by taking the original deformation polynomials and the polynomials out of the least-squares adjustment. Then their difference was evaluated by applying them both on the same cloud of points. Each of the points generates two deformed points from the two sets of deformations, and the offsets between these resulting points are studied. This computation corresponds to the yellow path in Fig.3.14. For these results, more than 3000 sets of coefficients generated have been used (in the 2 mm range of deformation). For a point located at the extremity of the cylinder near the IP, three distances (one along each axis) have been computed between the original point and the points deformed by the generated coefficient.

These three distances have been represented on Fig.3.16. It represents the superposition of 20 histograms, one for each of 20 points uniformly scattered at the extremity of the cylinder towards the center of the experiment, where the deformations are the biggest. Each histogram is composed of more than 3000 distances between the original point and the points deformed. The data of 20 points have been superposed, as there is a bias depending on the y and z position on the cylinder, the x position being a centered Gaussian even without superposition. When superposed, the overall shape is a centered Gaussian for the y and z axes.

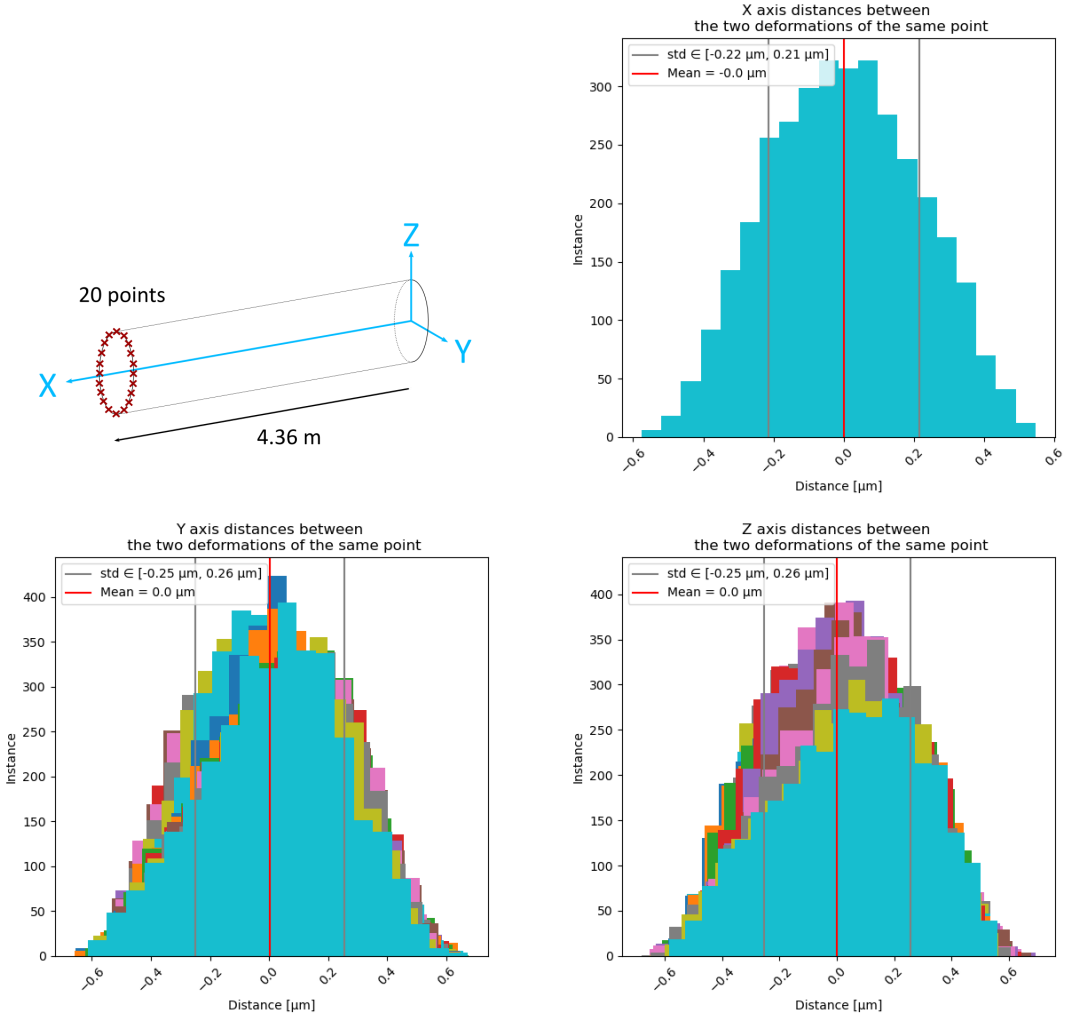

Figure 3.16: 20 points distribution at the end of the cylinder towards the inside of the detector. For each axis, superposition of 20 histograms of offsets due to 3400 different sets of coefficients.

The means are equal to 0.2 μm, 0.5 μm and 0.4 μm for X axis, Y axis and Z axis respectively. These results give a good first impression and are very promising. They encouraged to search for a cleaner way to express the precision of the system.

3.6.3.2 Covariance law

The second technique used to study the results was the covariance law shown in section 3.2.3.l This computation corresponds to the red path in Fig.3.14. The measurement uncertainty has been set to 1 μm. The uncertainty on the position has been computed for 500 points, and was highlighted on

a set of twelve points placed at specific locations. These points, shown in Fig.3.17, are placed at the beginning, middle and end of the cylinder and at the cardinal points in the cylinder section.

The final result is shown in fig.3.18, where the uncertainty on the position of the 500 points is plotted. On this figure, the longitudinal location of the twelve points of interest has been highlighted. The uncertainties of these points have been gathered in table.3.1. The results are showing uncertainties being worst the further we advance in the cylinder away from the interface, going from smaller than 0.01 μm to 0.27 μm for the x axis and 0.55 μm for the y and z axis. The shape of the helices and the multiple steps chosen allow a better determination of the X position, resulting in an overall lower uncertainty on that coordinate compared to the Y and Z coordinates. The widening that can be seen on the uncertainty values of these two coordinates is caused by the location of the points on the cylinder. Even though these values have been sorted by their longitudinal position, their Y and Z positions are still random, and the uncertainty depends on that value. It is important to note that the Y and Z uncertainty values are both in the same envelope, one being maximum when the point is on to or on the bottom of the cylinder while the other is minimal and the opposite when the point is located on the side of the cylinder. This behavior is underlined by the table 3.1: the Y uncertainty of point 9 (on top of the cylinder) is worse than its Z uncertainty, and it is the opposite case with the same values for the point 10 (on the side of the cylinder). This symmetry in the Y and Z axis is explained by the symmetry of the fiber network.

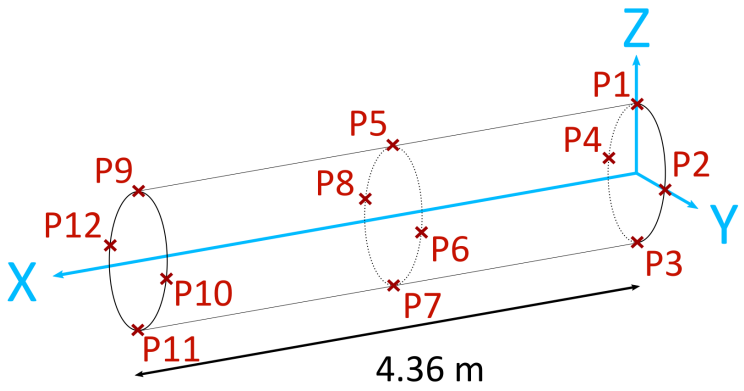

Figure 3.17: Location of the twelve points used for the result output

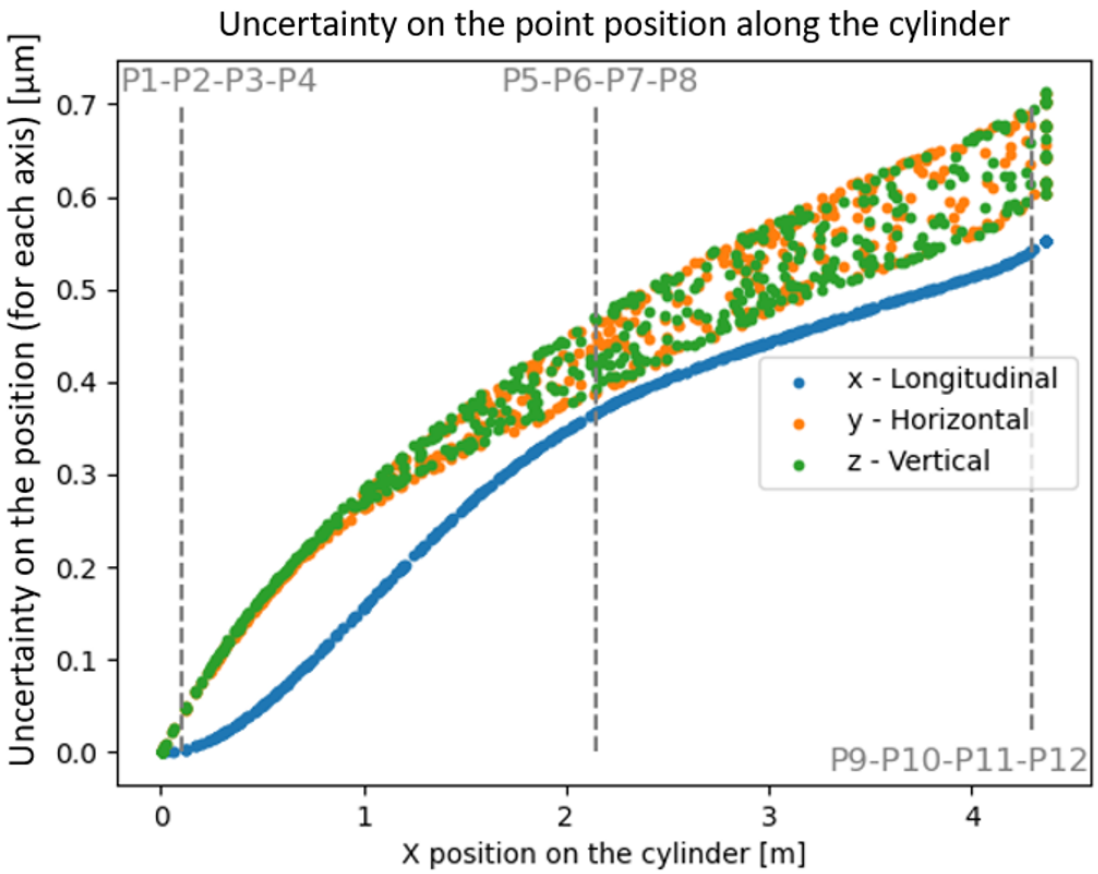

Figure 3.18: Uncertainty on the point position for 500 points randomly scattered on the cylinder (sorted by their longitudinal position). The X position of the points P1 to P12 (at the beginning, middle and end of the cylinder) have been highlighted.

The adjustment and variance propagation have been applied to more than 3000 generated coefficient sets, from which is resulting a wide range of deformations as shown on Fig.3.19.

	Uncertainty [μm]		
Points	X	Y	Z
Pt1	<0.01	0.03	0.03
Pt2	<0.01	0.03	0.03
Pt3	<0.01	0.03	0.03
Pt4	<0.01	0.03	0.03
Pt5	0.23	0.36	0.29
Pt6	0.23	0.29	0.36
Pt7	0.23	0.36	0.29
Pt8	0.23	0.29	0.36
Pt9	0.34	0.53	0.45
Pt10	0.34	0.45	0.53
Pt11	0.34	0.53	0.45
Pt12	0.34	0.45	0.54

Table 3.1: Position uncertainty (1σ) for the coordinates of the 12 selected points

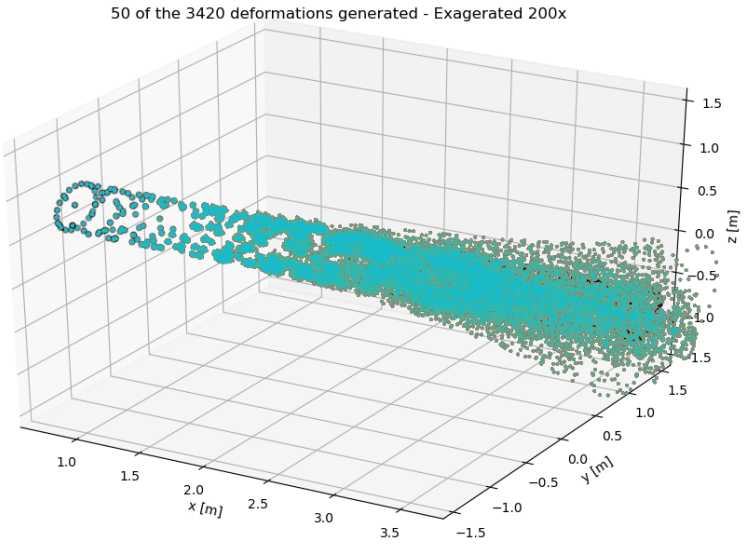

Figure 3.19: 50 sets of deformations applied to 500 points, exaggerated 200 times.

The results are the position uncertainty over each of the coordinates. From these, 50 random points have been extracted and illustrated in Fig.3.20, where the position uncertainties on each axis are shown. The representation shows the mean, first and third quartiles and the density distribution of the values

coming from more than 3000 simulations. For an easier visualization, the first and third quartile, and the density distribution have been stretched 5 times around the mean. Similarly to Fig.3.18, the uncertainty worsens when moving forward on the cylinder, for all three axes. While the values have been sorted with their X coordinate, explaining the smooth evolution for the X uncertainties, their Y and Z value depend on the Y and Z coordinates (as the network is not entirely symmetrical), resulting in a "non-smooth" transition. For all the axes, the difference between the third and first quartiles and the density distribution are stretching with the X coordinate growing. It goes from a difference between the third and first quartiles of almost 0 top 0.01 μm for the X axis and from 0 to 0.02 μm for the Y and Z axis. The density distribution is also symmetrical around the mean, where it is the maximum. The slight difference between the Z and Y values is due to the position of the point on the cylinder as, once again, the network is not symmetrical. These numerous simulations confirm the results shown on Fig.3.18.

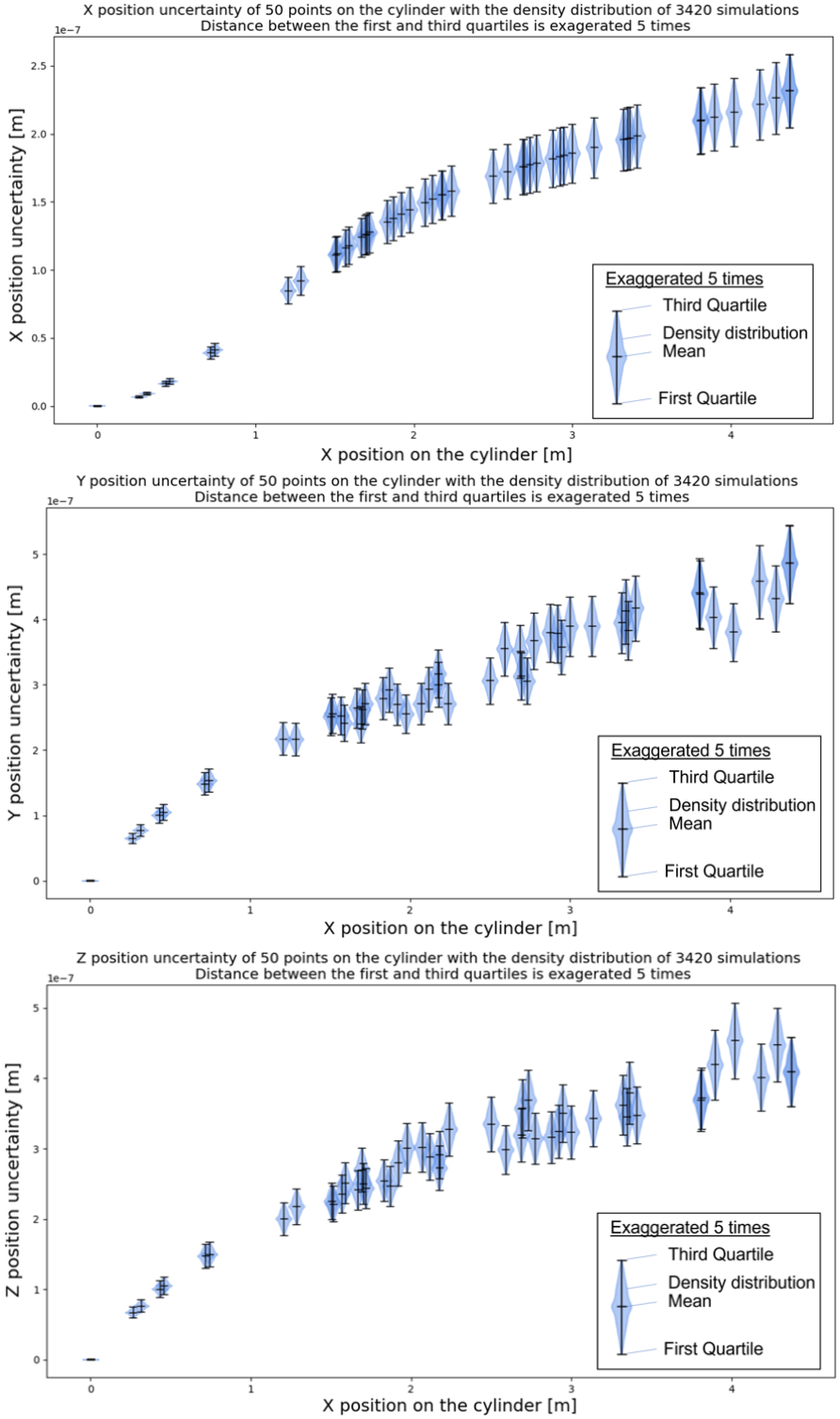

Figure 3.20: Position uncertainties of 50 points scattered along the cylinder, with the density distribution of the 3420 simulations done. Their representation has been stretched 5 times around the mean value for an easier visualization of the density distribution.

Even though these are preliminary results, with simple models, they are very promising. These values would be good enough to reach the requested measurement accuracy. But this system needs to be refined, and some implementation has been added to the model in order to make it more realistic.

3.6.4 Additional implementations and testing

The number of measurement, in addition to the complexity of the calculation, made the least square adjustment computation a very time-consuming process (up to an hour). Therefore, a simple model has been adopted for initial testing and first results. Now that these results have been judged promising, some studies to make the model more realistic have been performed.

3.6.4.1 Number of portions

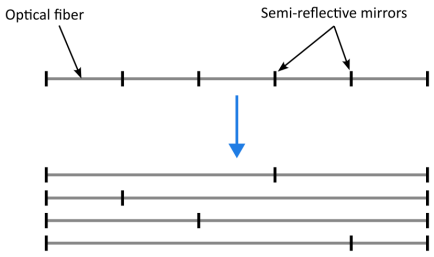

Figure 3.21: Drawing of a fiber with its semi-reflective mirrors and the implemented equivalent, with fibers having less portions. These fibers never have twice the same portion length.

As stated previously, the simulations were performed using fibers composed of 100 portions along their length. Even though this configuration may be possible at one point, current technology cannot have so many portions, and they are typically limited to 5–10 portions maximum [13], the main limitation being the return power after multiple reflections. This limitation could be bypassed using frequency scanning interferometry rather than low coherence interferometry (further developed in Chap.4), with different mirrors. In order to keep the high longitudinal definition while having a realistic number of portions per fiber (for current limitations), it has been chosen to replace one fiber with a high number of portions by multiple fibers with a lower number of portions, as shown on Fig.3.21. In our specific case, each 100 portions fiber has been replaced by 10 fibers with 10 measuring portions. It is more realistic regarding the number of portions, but it also allows defining these lengths, all different on each fiber. This point will be developed in more details in Chap.4, but interferometer

cannot distinguish two portions if they are the same length, they need to be different of more than 1 mm. As multiple fibers can be powered by one interferometer, all the lengths on one fiber must be different. A python program was created to automatically generate a given number of fibers with a given number of portions, so none of the portions has the same length while covering homogeneously the length of the cylinder. An output of this small code is plotted in Fig.3.22 and the mirror locations are listed in Table 3.2. By doing so, an unrealistic hundred portions fiber is replaced by a strip composed of ten fibers with ten measuring portions acting artificially as a hundred portion fiber. In this strip, the fibers are placed side by side, glued together and to the support, so each of the fiber are deformed almost the same way. In fact, there is no need for the fibers to undergo the exact same deformations and the fiber could be separated in a more complex network, but the strip of fiber allows an easier installation and less space occupation. The total width of the strip being the number of fibers times their diameter, for a 10 fibers strip, the width would be around a millimeter.

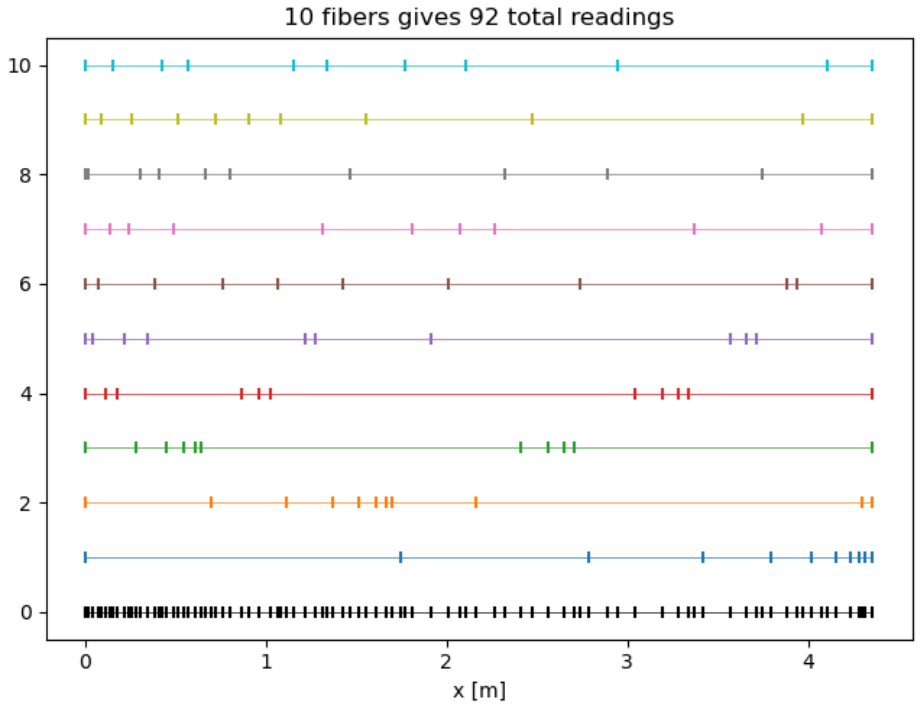

Figure 3.22: Plot showing the semi-reflective mirrors along all the fibers, delimiting ten portions, which are all of different lengths. The resulting resolution of the stripe over its length is shown by the black dots at the bottom.

Fiber	1	2	3	4	5	6	7	8	9	10
Mirror locations [m]	0.000	0.000	0.000	0.000	0.000	0.000	0.000	0.000	0.000	0.000
	1.744	0.698	0.279	0.112	0.045	0.071	0.138	0.018	0.088	0.154
	2.790	1.116	0.446	0.179	0.219	0.386	0.243	0.306	0.257	0.425
	3.418	1.367	0.547	0.865	0.346	0.765	0.487	0.410	0.511	0.571
	3.795	1.518	0.607	0.965	1.217	1.062	1.313	0.665	0.724	1.156
	4.021	1.608	0.643	1.026	1.277	1.428	1.811	0.805	0.905	1.335
	4.157	1.663	2.414	3.042	1.911	2.012	2.072	1.464	1.084	1.771
	4.238	1.695	2.564	3.192	3.569	2.742	2.263	2.323	1.554	2.108
	4.287	2.163	2.655	3.283	3.659	3.885	3.369	2.891	2.474	2.951
	4.316	4.298	2.709	3.337	3.714	3.940	4.075	3.746	3.972	4.108
	4.360	4.360	4.360	4.360	4.360	4.360	4.360	4.360	4.360	4.360

Table 3.2: List of the mirror generated for the ten fibers of Fig.3.22. Distances measured by the sensor are between two consecutive mirrors.

3.6.4.2 Overlapping of fiber

The second implementation was to make the fiber crossing at two different radii. In the original simulation, the fibers were all intersecting at the same radius, which is impossible in reality. This has been corrected by making one of the two fibers go over the other at the intersection. This feature has been added after the implementation of the strip of fibers described earlier. In order to make the two strips overlap, the first step is to compute the intersections of the helices. Two helices of the same radius do intersect if they have opposite directions and/or if they have different steps. If one of these condition is fulfilled, the intersections can be found by resolving the following system:

$$\begin{cases} {h^1}_x(t) = t \\ {h^1}_y(t) = a\sin(A(t)t+\alpha) \\ {h^1}_z(t) = a\cos(A(t)t+\alpha) \end{cases} = \begin{cases} {h^2}_x(t) = t \\ {h^2}_y(t) = \varepsilon a\sin(B(t)t+\beta) \\ {h^2}_z(t) = a\cos(B(t)t+\beta) \end{cases}$$

Where h^1 and h^2 are the two helices from which we want to know the intersections, a the radius of the helices, $A(t)$ and $B(t)$ are the steps of the helices (which could be variable in that case, developed in more details in section3.6.4.3), ε corresponds to ± 1 which defines if the helix is right-handed or left-handed, and α and β correspond to the angle in the (O, O_y, O_z) plane from which the helices start.

Solving this system corresponds to solve:

$$\begin{cases} \sin(A(t)t+\alpha) = \varepsilon \sin(B(t)t+\beta) \\ \cos(A(t)t+\alpha) = \cos(B(t)t+\beta) \end{cases} \tag{3.29}$$

If the two helices are of the same direction, ε is equal to 1 and if not, it is equal to -1.

When $\varepsilon = 1$:

$$\begin{cases} 2\sin\left(\frac{A(t)t - B(t)t + \alpha - \beta}{2}\right) cos\left(\frac{A(t)t + B(t)t + \alpha + \beta}{2}\right) = 0 \\ -2\sin\left(\frac{A(t)t - B(t)t + \alpha - \beta}{2}\right) sin\left(\frac{A(t)t + B(t)t + \alpha + \beta}{2}\right) = 0 \end{cases} \tag{3.30}$$

Which is verified if:

$$\begin{aligned} &\sin\left(\frac{A(t)t - B(t)t + \alpha - \beta}{2}\right) = 0 \\ &\Leftrightarrow A(t)t - B(t)t + \alpha - \beta = 2n\pi \quad ,n \in \mathbb{Z} \\ &\Leftrightarrow (A(t) - B(t))t = 2n\pi + \beta - \alpha \quad ,n \in \mathbb{Z} \end{aligned} \tag{3.31}$$

When $\varepsilon = -1$:

$$\begin{cases} 2\cos\left(\frac{A(t)t - B(t)t + \alpha - \beta}{2}\right) sin\left(\frac{A(t)t + B(t)t + \alpha + \beta}{2}\right) = 0 \\ -2\sin\left(\frac{A(t)t - B(t)t + \alpha - \beta}{2}\right) sin\left(\frac{A(t)t + B(t)t + \alpha + \beta}{2}\right) = 0 \end{cases} \tag{3.32}$$

Which is verified if:

$$\begin{aligned} &\sin\left(\frac{A(t)t + B(t)t + \alpha + \beta}{2}\right) = 0 \\ &\Leftrightarrow A(t)t + B(t)t + \alpha + \beta = 2n\pi \quad ,n \in \mathbb{Z} \\ &\Leftrightarrow (A(t) + B(t))t = 2n\pi - \beta + \alpha \quad ,n \in \mathbb{Z} \end{aligned} \tag{3.33}$$

This computation is performed for all the possible couples of helices in the network, in order to find all the intersections. Once the intersections are found, we can locate the transitions, the distance prior to the intersection required by the fiber to go from one radius to the other. When working with strips, as multiple fibers are side by side, some intersections will be very close and the fiber will go over the entire strip rather than fiber per fiber.

In that case, the first intersection of the fiber with the strip will be seen as the point at which ends the radius transition in order to pass over the strip, and the last intersection will be the start of the radius transition back to normal. This change of radius needs to be smooth in order to be realistic,

as fibers have a minimal curvature radius to respect if we want to avoid any loss or breaking of the fiber. In the simulations, an approximation has been made as shown in Fig.3.23: curved transitions between the radii have been replaced by straight lines. This approximation has been made to reduce the complexity of the calculation and therefore the computing time.

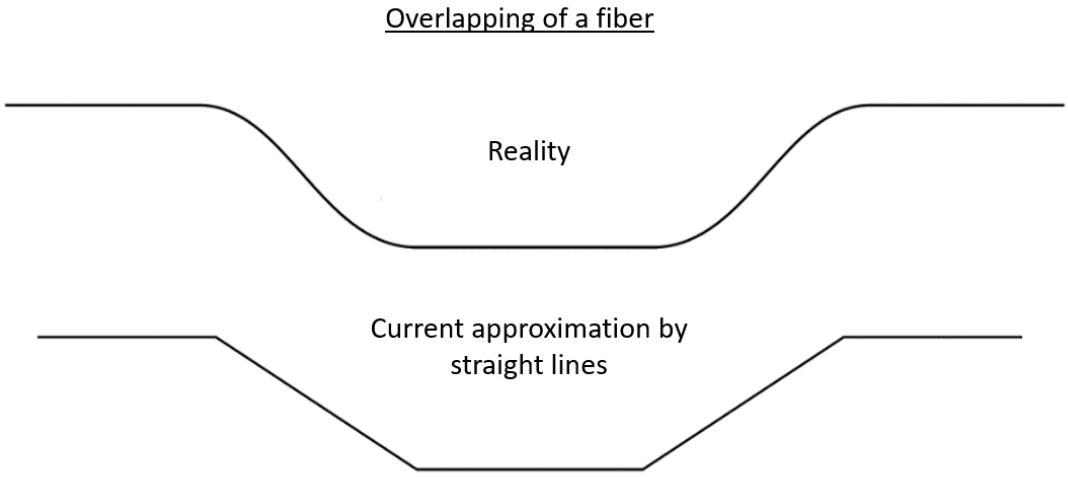

Figure 3.23: Approximation made for the overlapping of the fibers: curves have been replaced by straight lines.

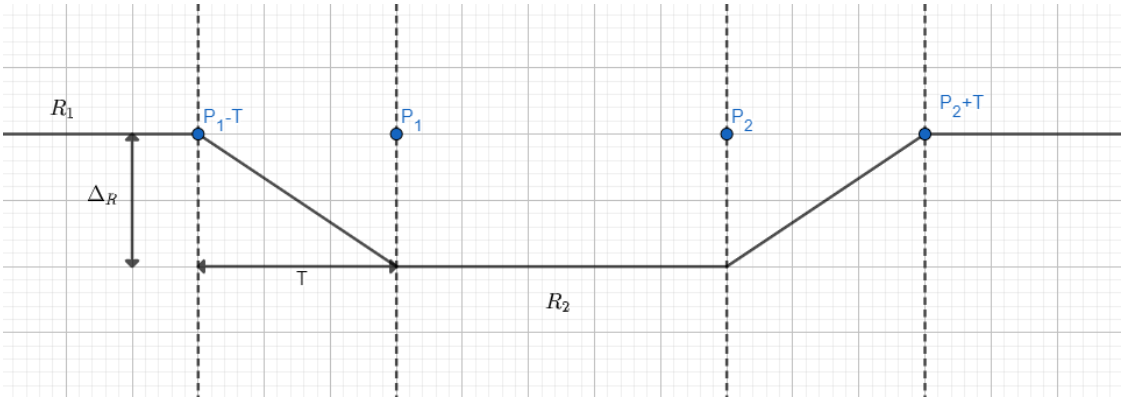

Figure 3.24: Drawing showing the parameters used to model the change of radius when one fiber pass over the other.

During the overlapping, only the radius definition changes in the helix equation. Below are expressed the different radius depending on their position with respect to the intersections. The notations are highlighted in fig.3.24, where P_1 is the location of the first intersection, and P_2 is the last, T is the

transition required to pass from one radius to the other, Δ_R is the difference between the two radii.

$$
\begin{aligned}
&* \forall x \notin [P_1 - T; P_2 + T], r = 0.25 \\
&* \forall x \in [P_1 - T; P_1], r = -\Delta_R \left(\frac{x - P_1 + T}{T} \right) + 0.25 \\
&* \forall x \in [P_1; P_2], r = 0.25 - \Delta_R \\
&* \forall x \in [P_2; P_2 + T], r = \Delta_R \left(\frac{x - P_2}{T} \right) + (0.25 - \Delta_R)
\end{aligned}
\tag{3.34}
$$

Fig.3.25 and Fig.3.26 are showing the end result of this radius change.

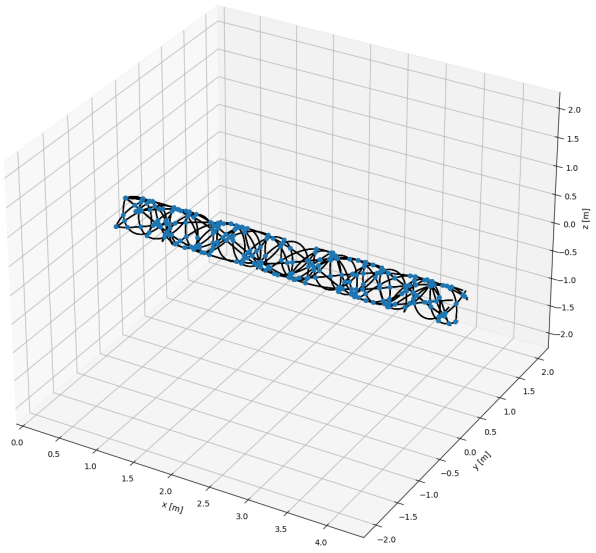

Figure 3.25: Example of computation of the intersections in a network

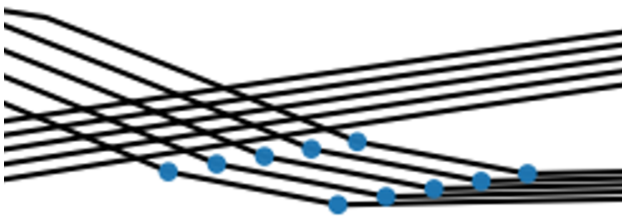

Figure 3.26: Zoom at the intersection between two strips of five fibers. One of the strip change radius to pass over the other.

Simulations have been performed after the implementation of the overlapping and the setting of a realistic number of divisions.

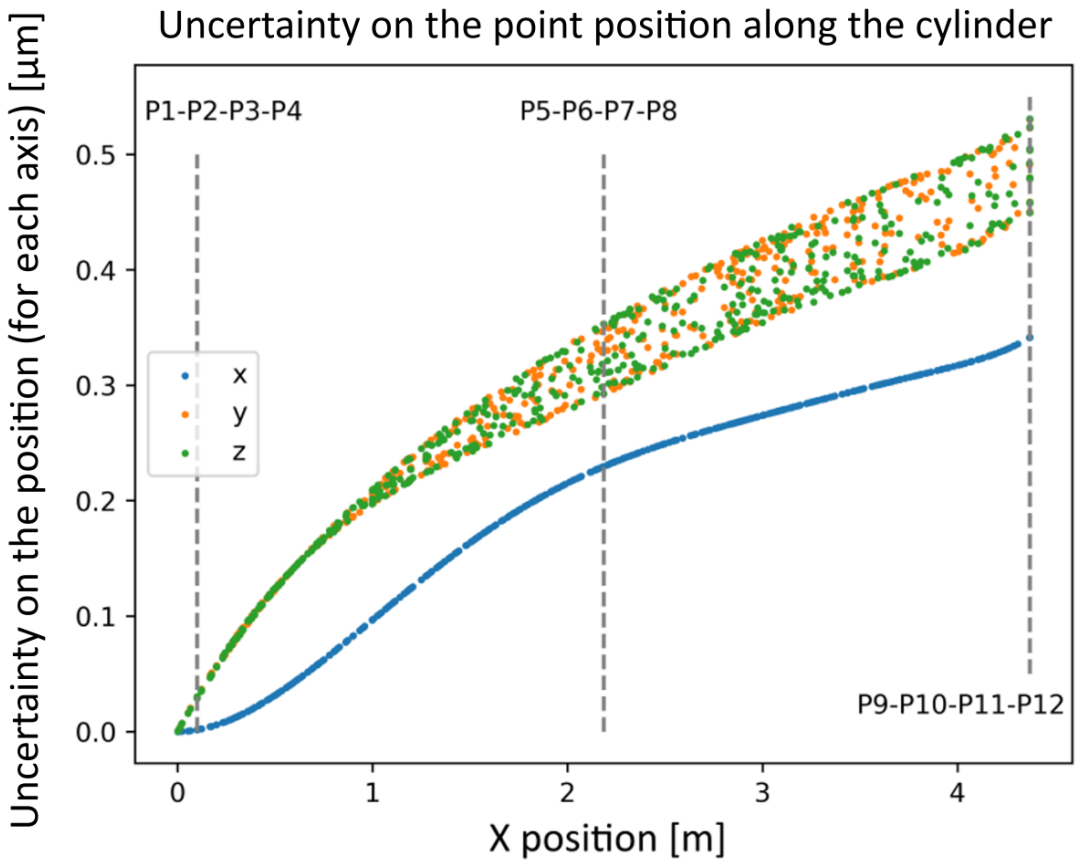

Figure 3.27: Simulations with additional implementations. Uncertainty on the point position for 500 points randomly scattered on the cylinder (sorted by their longitudinal position). The X position of the points P1 to P12 have been highlighted.

Some interesting features can be underlined on Fig.3.27. First, uncertainties are lower than the previous simulations, which can be explained by the even higher redundancy between the measurements, due to the increase of the number of fibers. This configuration can also be the reason for a better longitudinal uncertainty. It is important to note that the computation time is greatly increased, almost four times longer, by the additional complexity brought by the higher number of fibers, the slicing into portions of different lengths, the intersection computation and the modification of the radii for the overlapping. This implementation is still not perfect, but for such small changes of radius (around 1 mm), the difference is very small. This has not been quantified yet, and the integral computing may require to be upgraded before this simplification. The development of a more realistic model is planned for the future.

3.6.4.3 Variable step helices

Another idea was to implement variable step helices. These helices could help to improve the measurement resolution at some places without increasing the number of fibers. Their equations are mentioned below:

$$\begin{cases} h_{x_d}(x) = x + P_x(x) \\ h_{y_d}(x) = \varepsilon(r + P_{ry}(x)) \sin\left(\dfrac{x}{p(x)} + \alpha + \varepsilon P_\theta(x)\right) + P_y(x) \\ h_{z_d}(x) = (r + P_{rz}(x)) \cos\left(\dfrac{x}{p(x)} + \alpha + \varepsilon P_\theta(x)\right) + P_z(x) \end{cases} \tag{3.35}$$

Where $p(x)$is the variable step. An example of a variable step helix and a network composed of variable step helices is shown in Fig.3.28 and Fig.3.29

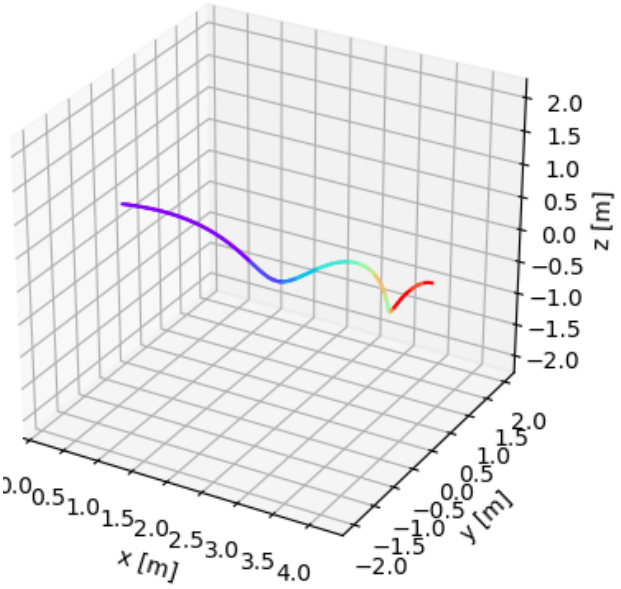

Figure 3.28: Visualization of variable step helix, having a greater step towards the end of the cylinder

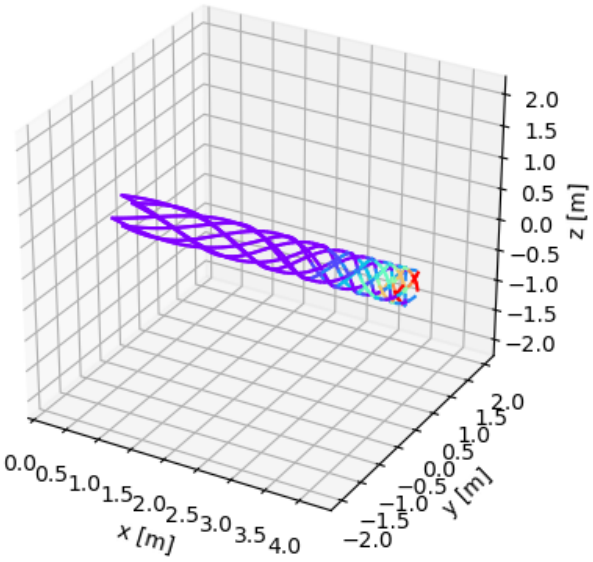

Figure 3.29: Visualization of variable step helices network.

In future network optimization, it could also help to focus more on some polynomial coefficients not determined precisely enough, using such variable step helices. For the moment, only feasibility and computation tests were performed. No extensive comparison with regular helices and no optimization have been done so far.

3.6.4.4 Error simulations

Initial error modeling have been coded. Simulations have been carried out for winding errors: one is a punctual change of step which impacts the rest of the helix and the second one is a punctual change of step, corrected right after by an opposite change of step, so the rest of the helix is not impacted. These two errors are represented in Fig.3.30 and Fig.3.31.

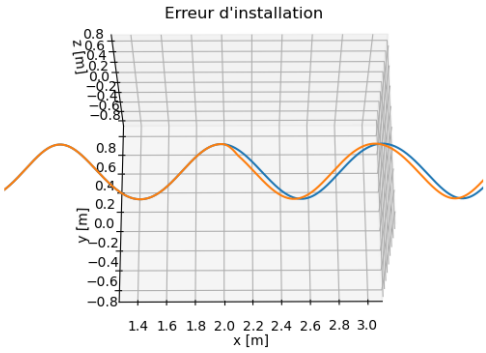

Figure 3.30: Visualization of a punctual step change during the winding, which impacts a big part of the helix.

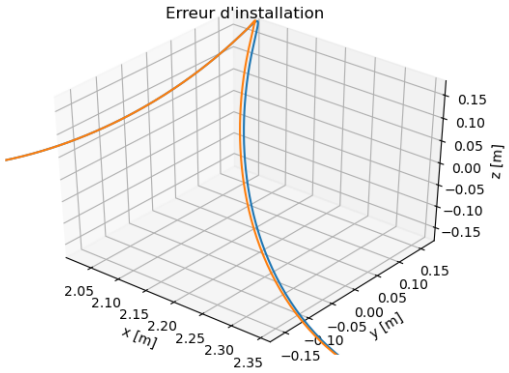

Figure 3.31: Visualization of a punctual step change during the winding immediately followed by an opposite step change, so the majority of the fiber is like designed.

Some simulations have been done with such errors. First, a set of measurements has been generated with a helices network including errors. Then, the adjustment has been performed supposing that the helices network was normal. In this situation, the measurements impacted by the errors were extremely simple to spot in the residues, using the huge redundancy of the system. This redundancy also allowed discarding the measurements impacted by the winding error, to still compute the system. It is important to note that, in our case, a winding machine for the solenoids could be used for our application. They are usually of the order of 50 μm uncertainty, and we can hope it will get even better by the time the FCC construction starts. A second note is that these errors can be taken into account in the equations by performing measurements of the helices network once installed. After the measurements, the equations can be adapted to the installed system and therefore the measurements can be used without deteriorating their uncertainties. Regarding the way to measure the network once installed, CMM, photogrammetry or Lidar are possible solutions. Another recommendation would be

to launch a study on a calibration procedure. The huge redundancy may enable the possibility to calibrate the system.

3.6.5 Discussion

This 3D deformation monitoring system is at a very early stage of its development. Simulations have been performed and are computing well, providing very promising results. The next steps on that particular system are:

1. Do some prototyping and test on real deformations. The goal is to compare the 3D deformation monitoring to another system (laser tracker, CMM or something else) and see if our deformation modeling using polynomials is robust enough. If not, another model will need to be defined and the equations updated with that new model.

2. Refine the fiber overlapping model, and make it closer to reality

3. Refine the adjustment computation in order to make it faster. The most complete model takes around an hour to be computed on an eight logical processor computer. Improvement could be done by an optimization of the python program or by using C++, better for such computations. Making the computation faster would leave some room for more complex and more realistic models.

4. Study the network optimization, trying to find a configuration with the fewer fibers while being able to determine and distinguish easily all the different deformation coefficients. This can only be done once the design is more mature and once the shapes, sizes, and locations of the components are known. It should include in the study the variable step helices.

5. Do some study on the FSI emitting head design. For now, the design is adapted to be installed in the FCC-ee MDI. Size, shape, support, and materials need to be studied.

This system shows that it is possible to monitor the 3D shape or even a structure using optical fiber. It is relatively simple and passive. Once the equation written and the fibers installed, no maintenance is required, and the computation is automatic, providing the deformations or the position of points on the monitored object with their uncertainty. Regarding the maintenance, the system is extremely simple and cannot really be repaired. If a fiber is broken, it means that the support withstood a

huge deformation, most likely big enough that the MDI is not safe anymore, or that it was hit. For redundancy, we can imagine putting a huge amount of fibers on the cylinder, and connect different sets to different interferometers in order to be able to measure even if one of the interferometer is down. It is important to note that connections between the interferometer and the fiber network will be simple and fast, and that any replacement of interferometer can be performed easily without touching at the system (as it wouldn't be possible anyway). Studies on the maximum fiber length should be started to estimate the maximum distance to the interferometer.

The system is also more environmental friendly than most of the other sensors, not requiring rare metals for electrodes, for example. This sensor is also relatively cheap, as one interferometer (the most expensive part of the system, around 20k €) can feed numerous fibers (theoretically up to hundreds) decreasing the cost per measurement drastically.

The system is currently used to monitor a cylindrical shape inside the detector, but it can easily be adapted to a similar shape elsewhere in the collider or even outside. A possible use would be the monitoring of other critical components in the collider such as the dumps, or the monitoring of less critical components but larger shape such as the tunnel walls. And it could also be used outside the collider on other structures such as pipelines, bridges, and other civil engineering infrastructures. With such a system installed, the behavior of the structures can be studied in order to optimize them in the future, for example. It can also be taken into account for the monitoring of smart structures [93], in tandem with actuators. This system can also be adapted to non-cylindrical structures, by modifying the equations to fit the studied object. One could also imagine very high refresh rate, allowing vibration measurements of the monitored objects.

3.7 External alignment system

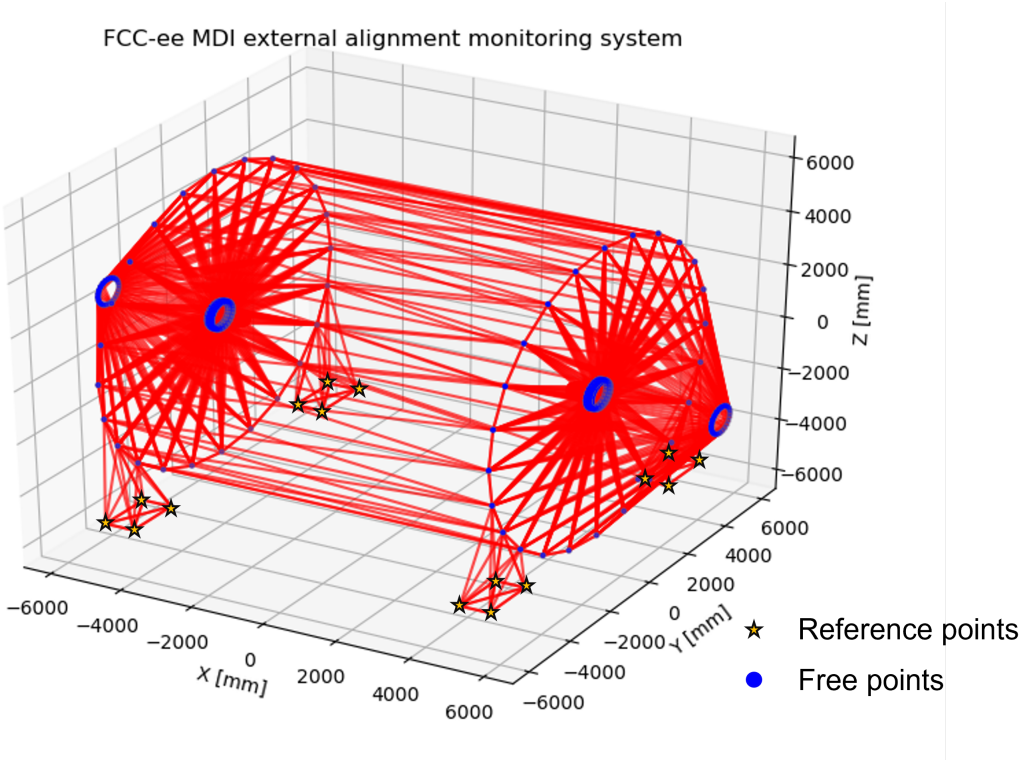

Figure 3.32: Layout of the measurements for the external alignment system. The 16 reference points can be seen on the supports of the detector.

3.7.1 Goal and challenges

Once the deformations on the cylinder known, the external alignment system comes into play, monitoring the interface at the end of the internal alignment system. By doing so, it allows the monitoring of the alignment between the inner components of each side of the detector, but also the alignment with respect to the rest of the accelerator, outside the MDI. This system can also be used to monitor the position of the detector solenoid, as, as seen in the section1.3.2, the alignment between the detector solenoid and the screening and compensation solenoids is very important. This system aims to stay simple, consisting of a dense network of distance measurements as shown on Fig.3.32, based on the FSI technology already available. A high number of measurements allows a monitoring of the relative alignment between the components, not requiring an absolute positioning of all the FSI heads and targets, as underlined in section 3.4. Only 16 reference points have been placed on the

support of the detector. This is a place where they should stay relatively stable and on which it is simple to measure. The density of the network provides a big redundancy in case of any problems, and would help to reach the alignment requirements. These numerous measurements are permitted by the multitarget FSI. This network has to adapt to the two different MDIs foreseen, as they are quite different depending on the physics detector used in the MDI. They may even be more designs in the future, as the FCC-ee project is going towards a four interaction points configuration.

3.7.2 Equations

This network consists of distance measurements over numerous points. Each of these points require enough measurements on them to allow the determination of their 3D coordinates, from at least 3 other points (more would be better for redundancy). The distance between two points $A\begin{pmatrix} X_A \\ Y_A \\ Z_A \end{pmatrix}$ and $B\begin{pmatrix} X_B \\ Y_B \\ Z_B \end{pmatrix}$ can be expressed as:

$$D_{AB} = \sqrt{(X_B - X_A)^2 + (Y_B - Y_A)^2 + (Z_B - Z_A)^2} \tag{3.36}$$

This is the equation used for the least-squares computation. D_{AB} are the observations, X_A, Y_A, Z_A are the observations and X_B, Y_B, Z_B the coordinates of a known point. This system requires to be linearized for the computation. This is done by computing the Jacobian matrix with respect to the three coordinates we want to compute:

This equation links the length of a helix portion with deformation coefficients. By constructing the Jacobian matrix J, deriving the equation with respect to each parameter for all the measurements in the point A_0, approximation of the point A, it is possible to compute the parameters using a least-squares adjustment.

$$J = \begin{pmatrix} \frac{\partial D_{AB}}{\partial X_A} & \frac{\partial D_{AB}}{\partial Y_A} & \frac{\partial D_{AB}}{\partial Z_A} \\ \frac{\partial D_{AC}}{\partial X_A} & \frac{\partial D_{AC}}{\partial Y_A} & \frac{\partial D_{AC}}{\partial Z_A} \\ \frac{\partial D_{AD}}{\partial X_A} & \frac{\partial D_{AD}}{\partial Y_A} & \frac{\partial D_{AD}}{\partial Z_A} \end{pmatrix} \tag{3.37}$$

With:

$$\begin{cases} \dfrac{\partial D_{AB}}{\partial X_A} = \dfrac{-(X_B - X_{A_0})}{\sqrt{((X_B - X_{A_0})^2 + (Y_B - Y_{A_0})^2 + (Z_B - Z_{A_0})^2)}} \\ \dfrac{\partial D_{AB}}{\partial Y_A} = \dfrac{-(Y_B - Y_{A_0})}{\sqrt{((X_B - X_{A_0})^2 + (Y_B - Y_{A_0})^2 + (Z_B - Z_{A_0})^2)}} \\ \dfrac{\partial D_{AB}}{\partial Y_A} = \dfrac{-(Z_B - Z_{A_0})}{\sqrt{((X_B - X_{A_0})^2 + (Y_B - Y_{A_0})^2 + (Z_B - Z_{A_0})^2)}} \end{cases} \tag{3.38}$$

In addition to these distance measurements, another observation is added, where the point position is given with an associated uncertainty for each of the coordinates. This observation is given for all the points except the 16 references. So the initial (and supposed) position of a point is defined (P_0), and then the observation of the point position (P_{obs}) with an associated uncertainty is expressed for that point:

$$\begin{cases} X_{obs} - X_0 = 0 \\ Y_{obs} - Y_0 = 0 \\ Z_{obs} - Z_0 = 0 \end{cases} \tag{3.39}$$

The uncertainty is used in the a priori covariance matrix of the observations, on the diagonal relative to the observation $\sigma_{X_{obs}}$

The adjustment of this system is performed by LGC++, which gives back the information needed for the uncertainty computation. This system has not been used alone, and has been completed using the internal monitoring system to form the full alignment monitoring system.

3.7.3 Discussion

For now, this is a simplistic view of the network, not taking into account the limitations of long interferometric measurement through air. But technics exist to deal with such long measurements while being extremely accurate, using the double wavelength FSI or the double side band FSI, for example [94, 95].

It is important to note that here, additional sensors could be added in order to have another measuring system. But for now, the design, and the conditions around the detector are not known yet, and therefore a basic network has been created, focusing more on the internal alignment system. Optimization of the external network shape could be performed too.

3.8 Full system

3.8.1 Overview and assumptions

In order to be able to monitor the FCC-ee MDI, both systems (the external alignment system and the internal alignment system) will need to be synchronized to have continuous relative alignment monitoring between the different components. As until now, only the external alignment system and the deformation monitoring of the supports of the solenoids are defined. The system requires to be completed by additional distance measurements from the cylinder (which deformation is monitored) to the inner components (final focusing quadrupoles). This results in a network of FSI distance measurements, defined by a set of measurement heads placed on the cylinder and a set of targets placed on the final focusing quadrupoles. Some assumptions have been made for these simulations. First, a big assumption on the design of the MDI has been made, taking the current shapes and locations for the computation, even though these can still drastically change. Then, assumptions on the uncertainties of the measurement systems have been made, from the measurement uncertainty itself to the machining and the positioning of the fibers, heads, and targets. These uncertainties will be updated at each step of the design process of the systems.

In order to study the feasibility of the operation of all the alignment systems at the same time, a simulation and automatic computation have been coded. This simulation uses both Python code developed in the thesis and LGC++ resolution in order to include all the sub-systems in the computation.

3.8.2 Process

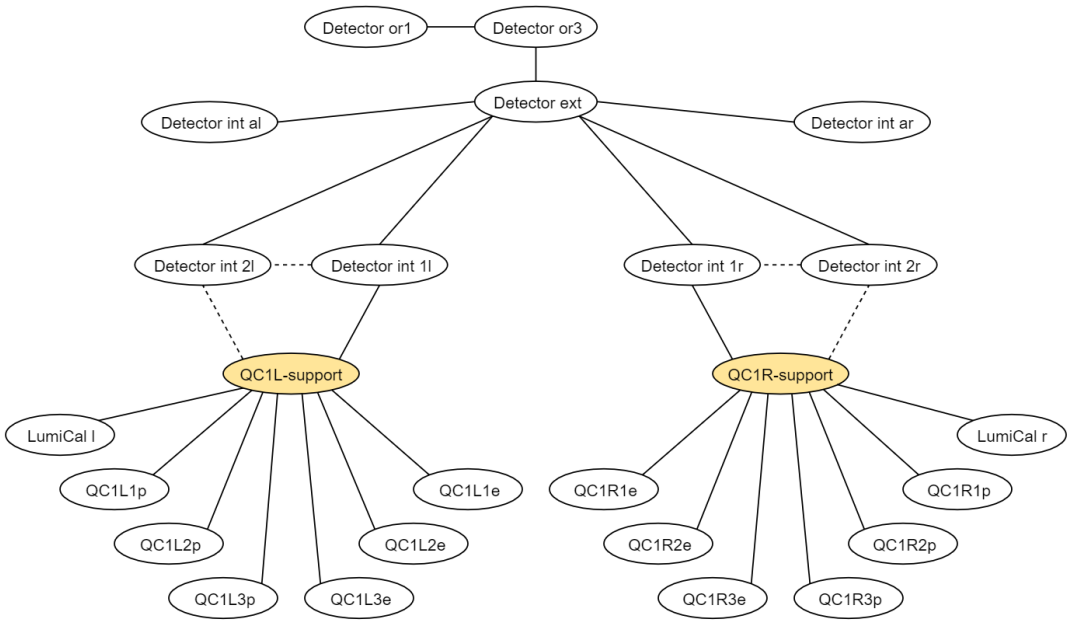

Figure 3.33: Tree representation of the frames composing the MDI. Lines are measurement between the frames, continuous ones are taken into account in LGC++ and dotted ones are not. The yellow frames have their deformations monitored.

In order to compute the alignment between the different components inside the MDI, "frames" have been created. These frames are objects used by LGC++, in which are gathered all the points (measuring head or target) of that object. By doing so, it allows avoiding writing all the constraints between these points, between which the distances are fixed. The only components in which this assumption is not made are the supports for the solenoids, in which the deformations are monitored using the internal alignment system. These frames are linked to each other by distance measurements carried out with FSI. A tree, showing all the frames used in the simulations and the measurements between them, is shown in Fig.3.33. Final focusing quadrupoles are at the bottom of this tree, at the end of the measurement chain. The yellow frames corresponds to the solenoid supports, which deformations are monitored thanks to the internal alignment system. Each of these frames has an associated coordinate system. These systems differ from one to another by a 3D transformation composed of three translations, three rotations and a scale factor. The goal is to find the deformation linking two objects and the uncertainties of its parameters. The parameters are the monitoring information, while

the uncertainties are the information needed to study how well the system can monitor the relative uncertainty between two objects.

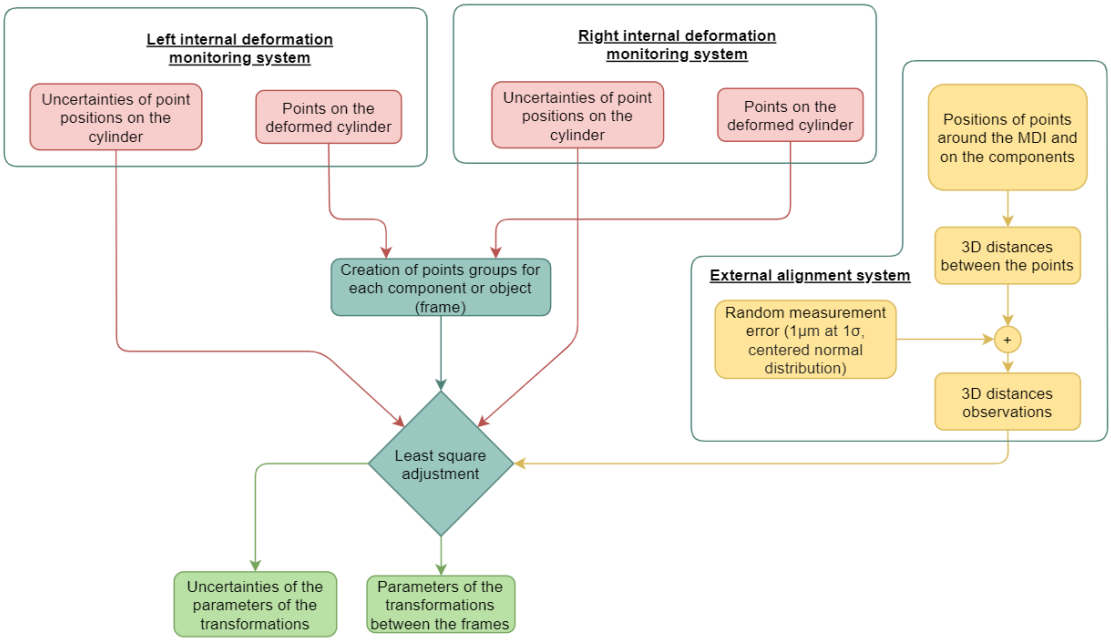

Figure 3.34: Drawing of the process for the computation of all the MDI alignment monitoring systems.

Figure 3.34 summarizes the process for the full computation of the MDI alignment monitoring. The deformations of the supports, measured by the internal monitoring system, need to be computed separately, as LGC++ is not able to do such computation for now. This part is resolved using the Python code, which gives back points position after deformation and their respective uncertainty. Once this data obtained, the LGC++ input file is written, shaped in function of the frames. All the 3D distances of the external alignment system are added, as well as some additional measurements between the support of the solenoids and the final focusing quadrupoles and the LumiCal. The uncertainties on the points on the solenoid supports, resulting from the deformation simulations, are written as such in the LGC++ input file, in order to take them into account for the computation. Then this file is processed in a simulation mode by LGC++, which generates a set of distance measurements altered by a random measurement error, modeled by a value following a centered normal distribution, with 1 μm at 1σ. Each time, the points on the supports are also randomly moved around their original position (which is the position given at the end of the Python computation) by a value following a centered normal distribution, with a standard deviation equal to the uncertainty resulting from the

adjustment performed for the deformations.

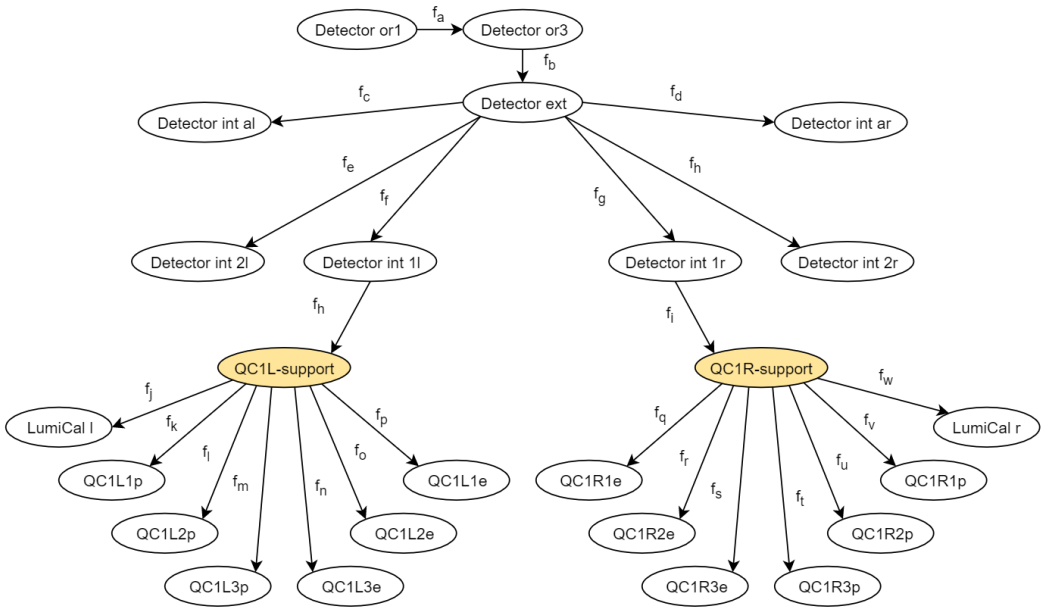

Figure 3.35: Tree representation of the frames and the different transformations computed by LGC++ between those frames.

The results given by the LGC++ computations are the parameters of the 3D transformations composed of three translations, three rotations and a scale factor, shown in Fig.3.35, f_1 to f_{24}. LGC++ is able to compute the deformations and their uncertainties from a child node to his parent node, but not from the parent node to the child node and also not between two child nodes. This is underlined by the arrows on the Fig.3.35. This limitation required to develop a software able to complete the LGC++ computation. The goal was to have the transformation in both direction, parent node to child node and from child node to parent node. This allowed composing multiple transformations along a path in the tree, in order to express the alignment and the uncertainties of the transformation parameters between the two objects.

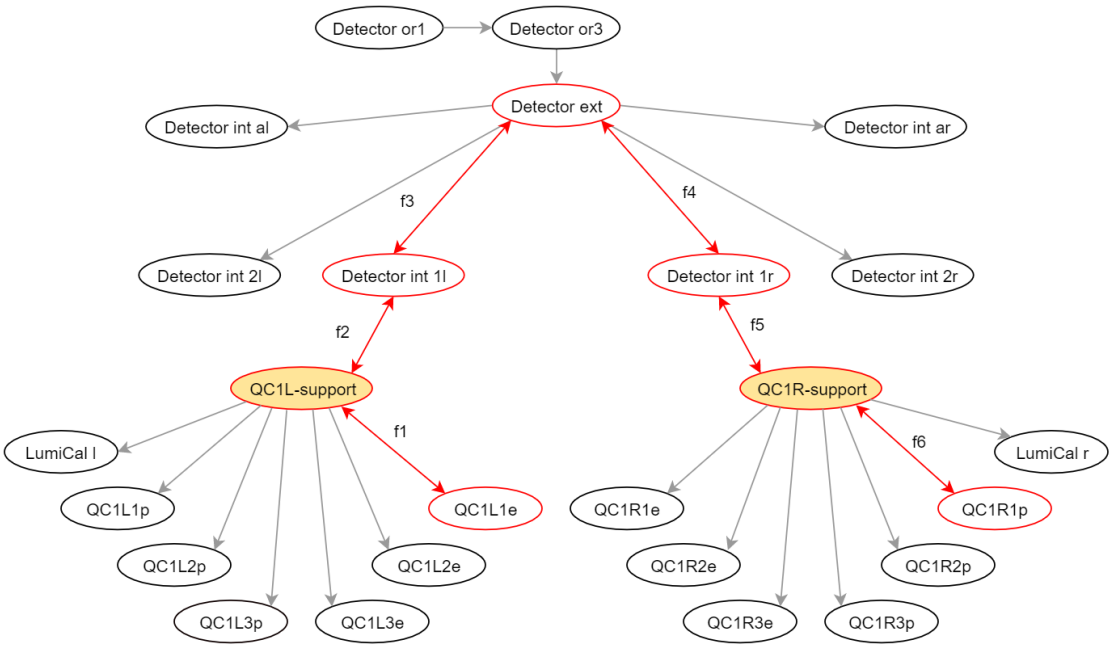

Figure 3.36: Example of a path to take to know the transformation between QC1L1e and QC1R1p, two final focusing quadrupoles on the opposite sides of the detector.

The LGC++ computation provides the transformations from the parent node to the child node of the entire tree, and the uncertainties associated to these transformations. If two points, $X_A \begin{pmatrix} x_A \\ y_A \\ z_A \end{pmatrix}$ and $X_B \begin{pmatrix} x_B \\ y_B \\ z_B \end{pmatrix}$ are respectively in the child node and in the parent node, the transformation between the two points can be written as:

$$X_B = sRX_A + T \tag{3.40}$$

With the parameters of the transformation from the parent frame to the child frame: s being the scale factor, T the translation and R the 3D rotation matrix, composed of R_x, R_y and R_z, rotations

matrix around the X, Y and Z axes respectively, as described below.

$$\begin{aligned} R &= R_x(\alpha)R_y(\beta)R_z(\gamma) \\ &= \begin{bmatrix} \cos\alpha & -\sin\alpha & 0 \\ \sin\alpha & \cos\alpha & 0 \\ 0 & 0 & 1 \end{bmatrix} \begin{bmatrix} \cos\beta & 0 & \sin\beta \\ 0 & 1 & 0 \\ -\sin\beta & 0 & \cos\beta \end{bmatrix} \begin{bmatrix} 1 & 0 & 0 \\ 0 & \cos\gamma & -\sin\gamma \\ 0 & \sin\gamma & \cos\gamma \end{bmatrix} \\ &= \begin{bmatrix} \cos\alpha\cos\beta & \cos\alpha\sin\beta\sin\gamma - \sin\alpha\cos\gamma & \cos\alpha\sin\beta\cos\gamma + \sin\alpha\sin\gamma \\ \sin\alpha\cos\beta & \sin\alpha\sin\beta\sin\gamma + \cos\alpha\cos\gamma & \sin\alpha\sin\beta\cos\gamma - \cos\alpha\sin\gamma \\ -\sin\beta & \cos\beta\sin\gamma & \cos\beta\cos\gamma \end{bmatrix} \end{aligned} \tag{3.41}$$

In order to go the other way, from the child frame to the parent frame, the following formula can be applied:

$$\begin{aligned} X_A &= s_{inv}R_{inv}X_B + T_{inv} \\ \text{with} \quad s_{inv} &= \frac{1}{s}, \quad R_inv = R^{-1}, \quad \text{and} \quad T_{inv} = -\frac{1}{s}R^{-1}T \end{aligned} \tag{3.42}$$

In the case of a composition of multiple transformations, the resulting transformation can be written as:

$$\begin{aligned} f(X_n) &= s_{tot}R_{tot}X + T_{tot} \\ &= s_1R_1\left(s_2R_2\left(\ldots\left(s_nR_nX_a + T_n\right)\ldots\right) + T_2\right) + T_1 \end{aligned} \tag{3.43}$$

Where s_i,R_i and T_i are defined by the equation 3.40 if the direction is from a parent frame to a child frame, and 3.42 if the direction is from the child to the parent. s_{tot}, R_{tot} and T_{tot} can be expressed as a function of the s_i, R_i and T_i transformations along the path:

$$\begin{cases} s_{tot} = \prod_{i=1}^{n} s_i \\ R_{tot} = \prod_{i=1}^{n} R_i \\ T_{tot} = s_1R_1\left(s_2R_2\left(\ldots\left(s_{n-2}R_{n-2}\left(s_{n-1}R_{n-1}T_n\right) + T_{n-1}\right)\ldots\right) + T_2\right) + T_1 \end{cases} \tag{3.44}$$

From these elements, we can extract the parameters of the complete transformation. While the scale factor and the translation are straight forward, the rotation angles can be expressed as a function of the $R_{tot} = \begin{bmatrix} R_{11} & R_{12} & R_{13} \\ R_{21} & R_{22} & R_{23} \\ R_{31} & R_{32} & R_{33} \end{bmatrix}$:

$$\begin{cases} \beta_a &= -\sin^{-1}(R_{31}) \\ \beta_b &= \pi + \sin^{-1}(R_{31}) \end{cases}, \begin{cases} \alpha_a &= \text{atan2}\left(\frac{R_{21}}{\cos(\beta_a)}, \frac{R_{11}}{\cos(\beta_a)}\right) \\ \alpha_b &= \text{atan2}\left(\frac{R_{21}}{\cos(\beta_b)}, \frac{R_{11}}{\cos(\beta_b)}\right) \end{cases}, \begin{cases} \gamma_a &= \text{atan2}\left(\frac{R_{32}}{\cos(\beta_a)}, \frac{R_{33}}{\cos(\beta_a)}\right) \\ \gamma_b &= \text{atan2}\left(\frac{R_{32}}{\cos(\beta_b)}, \frac{R_{33}}{\cos(\beta_b)}\right) \end{cases} \tag{3.45}$$

There is an ambiguity on the angle resolution, which is resolved by the definition of the systems associated to the objects. If the systems are defined as all the same except the position of their origin, differing from one another by translations. As rotations of more than π around one axis of the components are not expected (physically impossible), the ambiguity on the angle is solved by choosing the smallest. The resulting values are:

$$\begin{cases} \beta_{tot} = -\sin^{-1}(R_{31}) \\ \alpha_{tot} = \text{atan2}\left(\dfrac{R_{21}}{\cos(\beta)}, \dfrac{R_{11}}{\cos(\beta)}\right) \\ \gamma_{tot} = \text{atan2}\left(\dfrac{R_{32}}{\cos(\beta)}, \dfrac{R_{33}}{\cos(\beta)}\right) \end{cases} \tag{3.46}$$

These are the parameters extracted from the composition of deformations. Using these, we can follow the position of one element with respect to the other.

3.8.3 Uncertainty computation

Once the parameters are computed, their uncertainty can also be computed following the covariance law. First, the Jacobian matrix can be constructed, with the partial derivatives of the resulting parameters as a function of the parameters of the transformations along the path. Then, the covariance matrixes of the transformations along the path returned by LGC++ can be assembled.

The covariance matrix, gathering all the covariance of the parameters of the transformations along the path, can be expressed as:

$$\sigma_{tot} = \begin{bmatrix} \sigma^2_{\alpha_1} & cov(\sigma_{\alpha_1}, \sigma_{\beta_1}) & \dots & cov(\sigma_{\alpha_1}, \sigma_{s_n}) \\ cov(\sigma_{\beta_1, \sigma_{\alpha_1}}) & \sigma^2_{\beta_1} & \ddots & \vdots \\ \vdots & \ddots & \ddots & \vdots \\ cov(\sigma_{s_n}, \sigma_{\alpha_1}) & \dots & \dots & \sigma^2_{s_n} \end{bmatrix} \tag{3.47}$$

And the Jacobian matrix can be expressed as following:

$$J_{tot} = \begin{bmatrix} \frac{\partial \alpha_{tot}}{\partial \alpha_1} & \frac{\partial \alpha_{tot}}{\partial \beta_1} & \frac{\partial \alpha_{tot}}{\partial \gamma_1} & \frac{\partial \alpha_{tot}}{\partial T_{x1}} & \frac{\partial \alpha_{tot}}{\partial T_{y1}} & \frac{\partial \alpha_{tot}}{\partial T_{z1}} & \frac{\partial \alpha_{tot}}{\partial s_1} & \frac{\partial \alpha_{tot}}{\partial \alpha_2} & \cdots & \frac{\partial \alpha_{tot}}{\partial s_n} \\ \frac{\partial \beta_{tot}}{\partial \alpha_1} & \frac{\partial \beta_{tot}}{\partial \beta_1} & \frac{\partial \beta_{tot}}{\partial \gamma_1} & \frac{\partial \beta_{tot}}{\partial T_{x1}} & \frac{\partial \beta_{tot}}{\partial T_{y1}} & \frac{\partial \beta_{tot}}{\partial T_{z1}} & \frac{\partial \beta_{tot}}{\partial s_1} & \frac{\partial \beta_{tot}}{\partial \alpha_2} & \cdots & \frac{\partial \beta_{tot}}{\partial s_n} \\ \frac{\partial \gamma_{tot}}{\partial \alpha_1} & \frac{\partial \gamma_{tot}}{\partial \beta_1} & \frac{\partial \gamma_{tot}}{\partial \gamma_1} & \frac{\partial \gamma_{tot}}{\partial T_{x1}} & \frac{\partial \gamma_{tot}}{\partial T_{y1}} & \frac{\partial \gamma_{tot}}{\partial T_{z1}} & \frac{\partial \gamma_{tot}}{\partial s_1} & \frac{\partial \gamma_{tot}}{\partial \alpha_2} & \cdots & \frac{\partial \gamma_{tot}}{\partial s_n} \\ \frac{\partial T_{x,tot}}{\partial \alpha_1} & \frac{\partial T_{x,tot}}{\partial \beta_1} & \frac{\partial T_{x,tot}}{\partial \gamma_1} & \frac{\partial T_{x,tot}}{\partial T_{x1}} & \frac{\partial T_{x,tot}}{\partial T_{y1}} & \frac{\partial T_{x,tot}}{\partial T_{z1}} & \frac{\partial T_{x,tot}}{\partial s_1} & \frac{\partial T_{x,tot}}{\partial \alpha_2} & \cdots & \frac{\partial T_{x,tot}}{\partial s_n} \\ \frac{\partial T_{y,tot}}{\partial \alpha_1} & \frac{\partial T_{y,tot}}{\partial \beta_1} & \frac{\partial T_{y,tot}}{\partial \gamma_1} & \frac{\partial T_{y,tot}}{\partial T_{x1}} & \frac{\partial T_{y,tot}}{\partial T_{y1}} & \frac{\partial T_{y,tot}}{\partial T_{z1}} & \frac{\partial T_{y,tot}}{\partial s_1} & \frac{\partial T_{y,tot}}{\partial \alpha_2} & \cdots & \frac{\partial T_{y,tot}}{\partial s_n} \\ \frac{\partial T_{z,tot}}{\partial \alpha_1} & \frac{\partial T_{z,tot}}{\partial \beta_1} & \frac{\partial T_{z,tot}}{\partial \gamma_1} & \frac{\partial T_{z,tot}}{\partial T_{x1}} & \frac{\partial T_{z,tot}}{\partial T_{y1}} & \frac{\partial T_{z,tot}}{\partial T_{z1}} & \frac{\partial T_{z,tot}}{\partial s_1} & \frac{\partial T_{z,tot}}{\partial \alpha_2} & \cdots & \frac{\partial T_{z,tot}}{\partial s_n} \\ \frac{\partial s_{tot}}{\partial \alpha_1} & \frac{\partial s_{tot}}{\partial \beta_1} & \frac{\partial s_{tot}}{\partial \gamma_1} & \frac{\partial s_{tot}}{\partial T_{x1}} & \frac{\partial s_{tot}}{\partial T_{y1}} & \frac{\partial s_{tot}}{\partial T_{z1}} & \frac{\partial s_{tot}}{\partial s_1} & \frac{\partial s_{tot}}{\partial \alpha_2} & \cdots & \frac{\partial s_{tot}}{\partial s_n} \end{bmatrix} \tag{3.48}$$

The most complex derivatives have been underlined below:

$$\begin{cases} \frac{\partial \beta_{tot}}{\partial \alpha_i} &= -\frac{\partial R_{31}}{\partial \alpha_i}\left(\frac{1}{\sqrt{1-{R_{31}}^2}}\right) \\ \frac{\partial \beta_{tot}}{\partial \beta_i} &= -\frac{\partial R_{31}}{\partial \beta_i}\left(\frac{1}{\sqrt{1-{R_{31}}^2}}\right) \\ \frac{\partial \beta_{tot}}{\partial \gamma_i} &= -\frac{\partial R_{31}}{\partial \gamma_i}\left(\frac{1}{\sqrt{1-{R_{31}}^2}}\right) \end{cases}, \tag{3.49}$$

$$\begin{cases} \frac{\partial \alpha_{tot}}{\partial \alpha_i} = \frac{\frac{\partial R_{21}}{\partial \alpha_i}\cos(\beta) - R_{21}\frac{\partial \cos(\beta_{tot})}{\partial \alpha_i}}{\cos^2(\beta_{tot})}\left(-\frac{R_{21}}{\frac{{R_{21}}^2}{\cos^2(\beta_{tot})}+\frac{{R_{11}}^2}{\cos^2(\beta_{tot})}}\right) \\ \qquad + \frac{\frac{\partial R_{11}}{\partial \alpha_i}\cos(\beta_{tot}) - R_{11}\frac{\partial \cos(\beta_{tot})}{\partial \alpha_i}}{\cos^2(\beta_{tot})}\left(\frac{R_{11}}{\frac{{R_{21}}^2}{\cos^2(\beta_{tot})}+\frac{{R_{11}}^2}{\cos^2(\beta_{tot})}}\right) \\ \frac{\partial \alpha_{tot}}{\partial \beta_i} = \frac{\frac{\partial R_{21}}{\partial \beta_i}\cos(\beta_{tot}) - R_{21}\frac{\partial \cos(\beta_{tot})}{\partial \beta_i}}{\cos^2(\beta_{tot})}\left(-\frac{R_{21}}{\frac{{R_{21}}^2}{\cos^2(\beta_{tot})}+\frac{{R_{11}}^2}{\cos^2(\beta_{tot})}}\right) \\ \qquad + \frac{\frac{\partial R_{11}}{\partial \beta_i}\cos(\beta_{tot}) - R_{11}\frac{\partial \cos(\beta_{tot})}{\partial \beta_i}}{\cos^2(\beta_{tot})}\left(\frac{R_{11}}{\frac{{R_{21}}^2}{\cos^2(\beta_{tot})}+\frac{{R_{11}}^2}{\cos^2(\beta_{tot})}}\right) \\ \frac{\partial \alpha_{tot}}{\partial \gamma_i} = \frac{\frac{\partial R_{21}}{\partial \gamma_i}\cos(\beta_{tot}) - R_{21}\frac{\partial \cos(\beta_{tot})}{\partial \gamma_i}}{\cos^2(\beta_{tot})}\left(-\frac{R_{21}}{\frac{{R_{21}}^2}{\cos^2(\beta_{tot})}+\frac{{R_{11}}^2}{\cos^2(\beta_{tot})}}\right) \\ \qquad + \frac{\frac{\partial R_{11}}{\partial \gamma_i}\cos(\beta_{tot}) - R_{11}\frac{\partial \cos(\beta_{tot})}{\partial \gamma_i}}{\cos^2(\beta_{tot})}\left(\frac{R_{11}}{\frac{{R_{21}}^2}{\cos^2(\beta_{tot})}+\frac{{R_{11}}^2}{\cos^2(\beta_{tot})}}\right) \end{cases} \tag{3.50}$$

$$
\begin{cases}
\dfrac{\partial \gamma_{tot}}{\partial \alpha_i} = \dfrac{\frac{\partial R_{32}}{\partial \alpha_i}\cos(\beta_{tot}) - R_{32}\frac{\partial \cos(\beta_{tot})}{\partial \alpha_i}}{\cos^2(\beta_{tot})} \left(- \dfrac{R_{32}}{\frac{{R_{32}}^2}{\cos^2(\beta_{tot})} + \frac{{R_{33}}^2}{\cos^2(\beta_{tot})}} \right) \\
\qquad + \dfrac{\frac{\partial R_{33}}{\partial \alpha_i}\cos(\beta_{tot}) - R_{33}\frac{\partial \cos(\beta_{tot})}{\partial \alpha_i}}{\cos^2(\beta_{tot})} \left(\dfrac{R_{33}}{\frac{{R_{32}}^2}{\cos^2(\beta_{tot})} + \frac{{R_{33}}^2}{\cos^2(\beta_{tot})}} \right) \\
\dfrac{\partial \gamma_{tot}}{\partial \beta_i} = \dfrac{\frac{\partial R_{32}}{\partial \beta_i}\cos(\beta_{tot}) - R_{32}\frac{\partial \cos(\beta_{tot})}{\partial \beta_i}}{\cos^2(\beta_{tot})} \left(- \dfrac{R_{32}}{\frac{{R_{32}}^2}{\cos^2(\beta_{tot})} + \frac{{R_{33}}^2}{\cos^2(\beta_{tot})}} \right) \\
\qquad + \dfrac{\frac{\partial R_{33}}{\partial \beta_i}\cos(\beta_{tot}) - R_{33}\frac{\partial \cos(\beta_{tot})}{\partial \beta_i}}{\cos^2(\beta_{tot})} \left(\dfrac{R_{33}}{\frac{{R_{32}}^2}{\cos^2(\beta_{tot})} + \frac{{R_{33}}^2}{\cos^2(\beta_{tot})}} \right) \\
\dfrac{\partial \gamma_{tot}}{\partial \gamma_i} = \dfrac{\frac{\partial R_{32}}{\partial \gamma_i}\cos(\beta_{tot}) - R_{32}\frac{\partial \cos(\beta_{tot})}{\partial \gamma_i}}{\cos^2(\beta_{tot})} \left(- \dfrac{R_{32}}{\frac{{R_{32}}^2}{\cos^2(\beta_{tot})} + \frac{{R_{33}}^2}{\cos^2(\beta_{tot})}} \right) \\
\qquad + \dfrac{\frac{\partial R_{33}}{\partial \gamma_i}\cos(\beta_{tot}) - R_{33}\frac{\partial \cos(\beta_{tot})}{\partial \gamma_i}}{\cos^2(\beta_{tot})} \left(\dfrac{R_{33}}{\frac{{R_{32}}^2}{\cos^2(\beta_{tot})} + \frac{{R_{33}}^2}{\cos^2(\beta_{tot})}} \right)
\end{cases}
\tag{3.51}
$$

A software computing the covariance law have been written, allowing a simulation of the entire MDI computation.

3.8.4 Result

The layout of the distance measurements network used for the simulations is shown on Fig.3.37 and Fig.3.38. The external monitoring system is dense to keep the uncertainties of the alignment system as low as reasonably possible. The layout inside the assembly, shown in Fig.3.38 allows the measurement of the final focusing quadrupoles with respect to the support of the solenoids, which is also monitored by the deformation monitoring system. The measurements inside the assembly (cross-section A of the figure) have been placed on the sides in order to leave some space above and below, for access and operation (cooling, powering, shielding) of the elements further in the assembly. Additional longitudinal measurement have been added between the quadrupoles to compensate the weakness of the network regarding that direction. This layout is utilizing the multitarget measurement capability of the FSI.

BPM will also be present in that assembly and their alignment will need to be monitored, especially with respect to their associated quadrupole. But for the moment, the number, shape, and placement of these BPMs are still not clear. Once better defined, additional distance measurements will be

implemented to measure these BPMs.

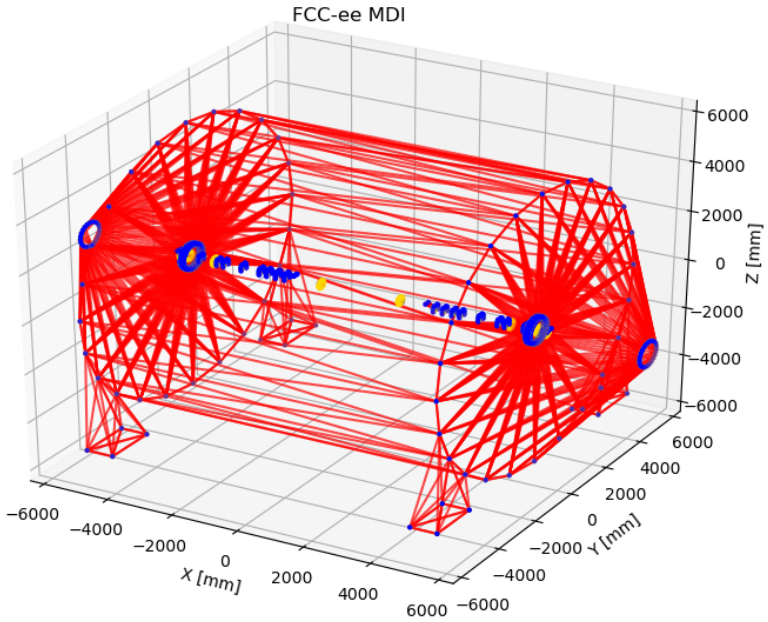

Figure 3.37: Layout of the FSI distance measurements (red) linking reference points (blue) and measured objects (yellow) around the detector.

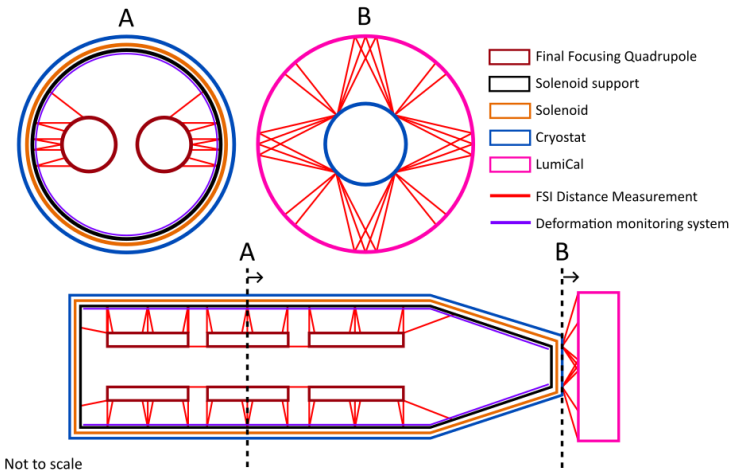

Figure 3.38: Layout of the distance measurements inside the assembly.

The results will be expressed using the transformation linking the coordinate system of the two studied objects. Fig.3.39 shows the two coordinate systems of QC1L1e and QC1R1e, two final focusing quadrupoles located on both sides of the detector. These two quadrupoles are measured with the alignment monitoring system and the transformation is determined following the process explained in section3.8.2. This computation also provides the uncertainty of the computed parameters of the transformation, which represents the key data for the alignment and monitoring system.

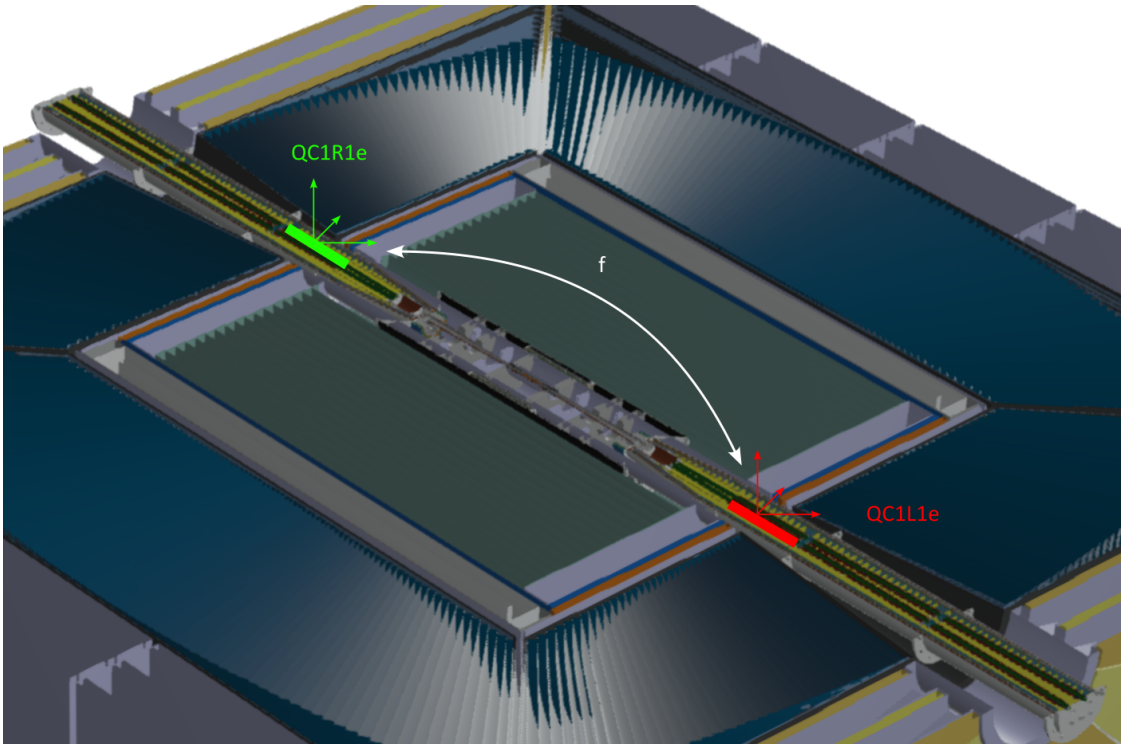

Figure 3.39: Coordinate systems of two final focusing quadrupoles, separated by the f function. This function will be used to quantify the uncertainties of the measured alignment between the two objects.

10 microns						
LumiCal_l	θx [μrad]	θy [μrad]	θz [μrad]	Tx [μm]	Ty [μm]	Tz [μm]
LumiCal_r	11.4	37.2	41.3	19.8	52.9	50.2

100 microns						
LumiCal_l	θx [μrad]	θy [μrad]	θz [μrad]	Tx [μm]	Ty [μm]	Tz [μm]
LumiCal_r	11.8	42.6	46.3	22.0	112.6	111.6

10 microns						
QC1_l1e	θx [μrad]	θy [μrad]	θz [μrad]	Tx [μm]	Ty [μm]	Tz [μm]
QC1_r1e	14.2	5.2	5.1	12.9	18.0	18.7
QC1_r1p	14.4	5.2	5.2	13.1	17.9	18.5
QC1_r2e	17.2	4.5	4.5	14.1	17.3	17.8
QC1_r2p	18.2	4.6	4.6	15.0	17.8	18.1
QC1_r3e	20.6	4.6	4.8	16.8	20.3	19.3
QC1_r3p	19.4	4.6	5.0	18.9	22.1	19.9
QC1_l2e	17.4	3.8	3.2	18.8	12.1	11.6
QC1_l3e	20.7	3.8	4.1	15.8	15.0	13.6
QC1_l1p	14.2	4.5	4.4	12.9	11.4	12.3
QC1_l2p	18.2	3.8	3.8	15.0	11.2	11.8
QC1_l3p	18.9	3.7	4.2	18.4	16.4	13.7

100 microns						
QC1_l1e	θx [μrad]	θy [μrad]	θz [μrad]	Tx [μm]	Ty [μm]	Tz [μm]
QC1_r1e	14.3	19.6	19.5	15.5	101.9	102.4
QC1_r1p	14.4	19.4	19.4	15.5	101.0	101.5
QC1_r2e	17.3	19.2	19.2	16.5	100.7	101.1
QC1_r2p	18.2	19.3	19.2	17.1	101.1	101.5
QC1_r3e	20.7	19.4	19.4	18.8	102.3	102.4
QC1_r3p	19.9	19.4	19.5	21.1	102.5	102.4
QC1_l2e	17.2	3.7	3.2	18.6	12.0	11.5
QC1_l3e	20.8	3.8	4.1	15.9	15.0	13.6
QC1_l1p	14.6	4.6	4.5	13.2	11.7	12.6
QC1_l2p	17.9	3.7	3.8	14.8	11.1	11.6
QC1_l3p	19.1	3.8	4.3	18.6	16.7	13.9

10 microns						
QC1_l1p	θx [μrad]	θy [μrad]	θz [μrad]	Tx [μm]	Ty [μm]	Tz [μm]
QC1_r1p	14.7	5.3	5.3	13.3	18.2	18.8
QC1_r2p	18.5	4.7	4.8	15.3	18.2	18.5
QC1_r3p	19.7	4.8	5.2	19.1	22.2	20.1
QC1_l2p	17.8	3.9	3.5	19.3	12.8	11.9
QC1_l3p	19.6	3.9	4.5	17.9	17.0	14.4

100 microns						
QC1_l1p	θx [μrad]	θy [μrad]	θz [μrad]	Tx [μm]	Ty [μm]	Tz [μm]
QC1_r1p	15.3	19.8	19.8	16.2	103.0	103.4
QC1_r2p	17.9	19.0	19.0	16.9	99.8	100.2
QC1_r3p	18.9	18.9	18.9	20.1	99.6	99.5
QC1_l2p	18.2	3.9	3.6	19.7	13.0	12.1
QC1_l3p	19.4	3.9	4.5	17.7	16.8	14.3

(a) (b)

Free						
LumiCal_l	θx [μrad]	θy [μrad]	θz [μrad]	Tx [μm]	Ty [μm]	Tz [μm]
LumiCal_r	11.8	51.8	54.9	32.8	191.6	191.9

Free						
QC1_l1e	θx [μrad]	θy [μrad]	θz [μrad]	Tx [μm]	Ty [μm]	Tz [μm]
QC1_r1e	14.2	35.0	34.9	28.7	184.7	185.9
QC1_r1p	14.5	35.0	34.9	28.8	184.5	185.7
QC1_r2e	17.6	34.8	34.7	29.4	184.3	185.4
QC1_r2p	17.9	34.9	34.8	29.6	184.5	185.6
QC1_r3e	20.7	34.9	34.8	30.6	184.8	185.8
QC1_r3p	19.4	34.9	34.8	31.8	185.0	185.8
QC1_l2e	17.2	3.8	3.2	18.6	12.0	11.5
QC1_l3e	20.9	3.8	4.1	15.9	15.1	13.7
QC1_l1p	14.8	4.7	4.6	13.4	11.9	12.8
QC1_l2p	18.4	3.8	3.9	15.1	11.4	11.9
QC1_l3p	19.2	3.8	4.3	18.7	16.8	14.0

Free						
QC1_l1p	θx [μrad]	θy [μrad]	θz [μrad]	Tx [μm]	Ty [μm]	Tz [μm]
QC1_r1p	15.1	35.0	34.9	29.0	184.5	185.7
QC1_r2p	17.8	34.9	34.8	29.6	184.3	185.4
QC1_r3p	19.1	35.0	34.9	31.7	185.2	186.1
QC1_l2p	18.4	4.0	3.6	19.9	13.2	12.3
QC1_l3p	18.9	3.8	4.4	17.3	16.4	13.9

(c)

Table 3.3: Tables showing the results of simulations of the full alignment system of the MDI, composed of translations and rotations between the coordinates systems of different components inside the MDI. Tests have been performed with different uncertainties associated to the initial point definition for eq.3.39, with 10 μm, 100 μm and free (point position determined only from other points around).

Results shown in Table 3.3 were computed with three different uncertainties on the point definition in eq.3.39 for the heads and targets of the external alignment system. The first simulation was performed with a 10 μm uncertainty associated with the point definition, as a result of a measurement of these points prior to turning on the alignment system. These uncertainties are not achievable currently, but may be by the time the FCC is constructed. The second simulation has been performed with a 100 μm uncertainty associated with the point definition, which is currently reachable, before turning on of the MDI alignment monitoring system. For the third simulation, the points were not defined before turning on the MDI alignment monitoring system. Their positions and the uncertainties were computed via triangulation from the reference points placed on the feet of the detector, during the general least squares adjustment computation. By doing so, a wide range of uncertainties are covered, which can help to decide how much effort has to be put in the measurement of these points.
For the 10 μm definition, results are below 20 μm for the translations and below 20 μrad for the rotations concerning the alignment between the quadrupoles. They are around 50 μm and below 45 μrad between the LumiCals. These uncertainties are homogeneous for the translations, while the θ_x rotation is slightly worse than the two other rotations, which could be explained by the geometry of the distance measurements inside the cryostat.
For the 100 μm definition, results are below 110 μm for the translations and below 25 μrad for the rotations concerning the alignment between the quadrupoles. They are around 110 μm and below 50 μrad between the LumiCals. Uncertainties on the T_x translation stay better than the two other translations, which can be explained by the geometry of the network being well constrained on the X axis. The weakness on the Y and Z axes comes from the transfer from one side of the detector to the other with long measurements. A gap in the uncertainty value can be seen between the components of the same detector side and the components on the two opposite sides, which require long distance measurements to compute their alignment.
Finally, for the last simulation with no definition on the points, results are below 200 μm for the translations and below 35 μrad for the rotations concerning the alignment between the quadrupoles. They are around 200 μm and below 55 μrad between the LumiCals. Once again, uncertainties on the X axis are better, due to a network better defined and constrained on that direction. The gap between the components on the same side and the component on the opposite side of the detector is still visible, and the values for the components on the same side are similar to the 10 and 100 μm

simulations. It is because this defined uncertainty is only for the points of the external alignment system, which are not involved in the computation between components on the same side.

In all these simulations, the only one with the 10 μm point definition of the external alignment system is close to the requested value, getting near to the 10 μm goal. Even though, an installation of the points at such uncertainty seems difficult, the network can be measured once installed, in addition to the network measurements. Later, the uncertainty associated to the point definition can be updated in the computation using the uncertainties computed by the network itself.

3.8.5 Discussion

These results are extremely preliminary, and their main objective was to prove the feasibility of the system and the correct computation of the full system. They are only indicative and could serve as a first iteration for network optimization, for example. The sensors used (helical optical fibers and interferometric distance measurements) are meant to be versatile, ready to be adapted to each evolution of the design that could be encountered. Even with a drastic change, like the use of the cryostat for the support of the assembly and not a skeleton, a combination of systems could be used. The same versatility exercise was performed for the computation software, which can easily implement polynomials with a higher degree for the deformations, different networks for both helices and distance measurements and update the system uncertainties with the laboratory tests carried out in parallel. Little optimization has been performed so far, waiting for a more mature system to adapt to the shapes and positions of the components.

A possible upgrade on the computation side is the optimization of the networks, both the helix network and the interferometric distance measurement network. More precise uncertainty definition could also be added, not having a 10 μm uncertainty on all the points of the external alignment system, but rather a computed value using the points around. Doing so, uncertainty would be closer to reality, having some points with a better uncertainty and others with a worse one. It could also allow updating that uncertainty value in time, at each computation of the network.

Regarding the hardware, additional testing and development are required in order to validate completely the system. The helix network, being simulated for the first time and looking forward to be implemented, requires a lot of development on that new sensor system. Long range FSI measurement, used in the external alignment system, are only hypothetical for the moment and the technique needs

to be confirmed as underlined in section 3.7.3.

Chapter 4

In-line multiplexed and distributed optical fiber sensors

Content

4.1 Technologies available

In order to make the simulated network of helices fiber work, an in-line multiplexed and distributed optical fiber distance sensor was required. Two possible technologies to implement in a such sensor are described below, the first one being "Surveillance d'Ouvrages par Fibres Optiques (SOFO)", and the second one being the Fourier-based FSI.

4.1.1 SOFO

The SOFO, described in details in [12, 96, 13], is based on the principle of low-coherence interferometry and path matching interferometers. This system, shown on Fig.4.1, uses the light emission of a Light-Emitting Diode (LED) sent into a coupler towards the two arms of the first interferometer. These arms are composed of a standard single mode fiber. This first interferometer, called the "sensor interferometer", has one of the two arms loose (the reference fiber), while the other one (the measurement fiber) is physically linked to the monitored structure following the deformations of the support. Each of these two arms is ended by a mirror, to send the light back to a second coupler, which then feeds the light to a second interferometer, the "analyzing interferometer". This interferometer is also composed of two fiber lines and has one arm fixed while the second one is ended by a movable mirror, controlled by a micrometric screw. While moving this mirror, a modulated signal, being a result of constructive and destructive interference, can be measured by the photodiode. Maximum of constructive interference is observed when the length difference between the analyzer interferometer arms compensates the length difference between the fibers in the structure to better than the coherence length of the source. The compensation position therefore indicates the deformation undergone by the structure relatively to the previous measurement point.

Even tough most of the SOFO systems currently used are of that configuration (measuring only one length at the time), a multiplexed sensor was investigated. This was performed by introducing semi-reflective mirrors in the fiber under the form of Fiber Bragg Grating (FBG). Such system, illustrated in Fig.4.2 has been tested with three portions [13], with a resulting precision always lower than 3 μm.

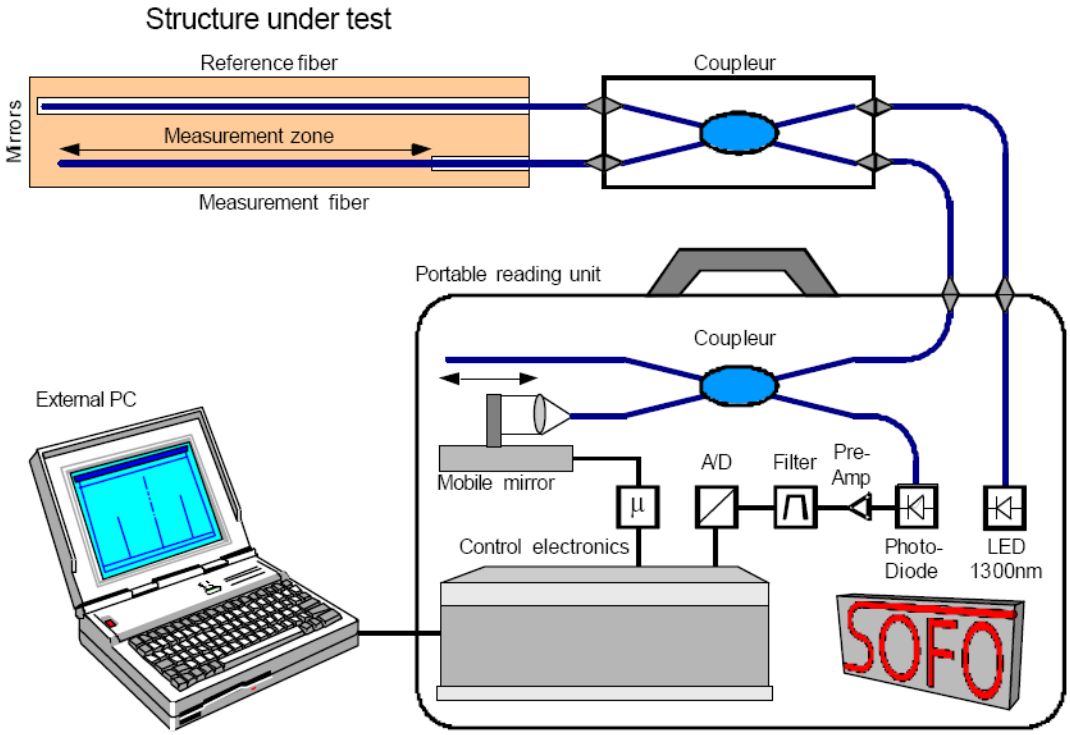

Figure 4.1: Scheme of the standard SOFO system (cf.[12]).

This configuration claims to work with up to 10 portions, by using increasingly reflective mirrors along the path [13].

Even though the SOFO system could work, it has some technical limitations: the principle behind the sensor allows independent measurements, but the measuring rate is too slow to consider these measurements simultaneous. Moreover, the more measurements there are on the same fiber, the longer it takes for their measure, as the mirror needs to move for all the portions. The sensor is also relatively complex and integrates mechanical movements, which increase the risk of failure. Finally, the development of the sensor has stopped, and it has never been released. The SOFO system being mostly used in civil engineering, the monitored structures are big enough to place multiple individual SOFO systems and therefore there is no need for the additional complexity of a multiplexed sensor, there is enough space to put two or more individuals systems in series and artificially build equivalent of an in-lined and multiplexed sensor.

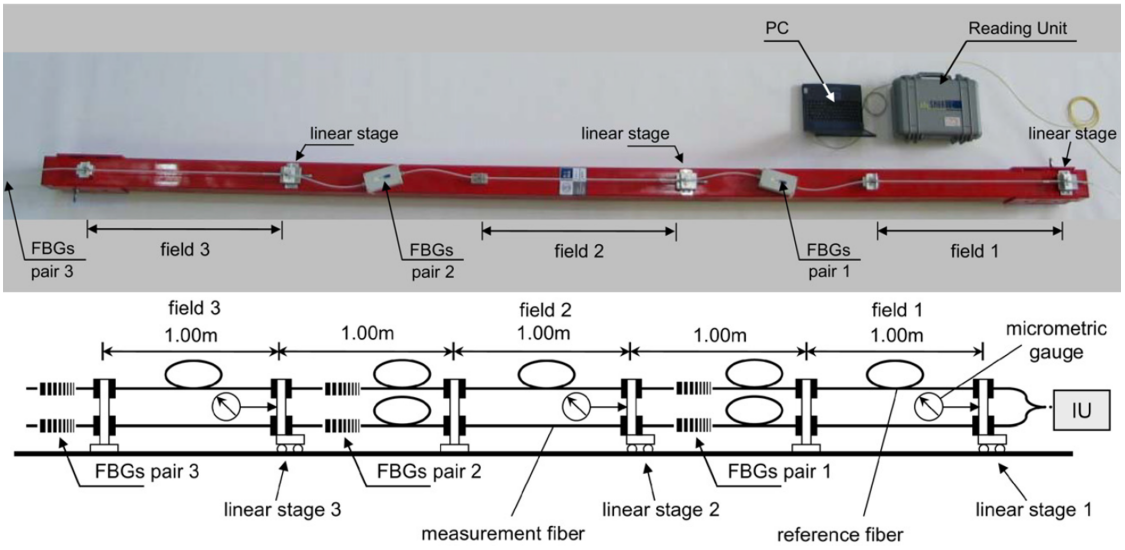

Figure 4.2: Laboratory test setup and scheme of the multiplexed SOFO prototype (cf.[13]).

4.1.2 FSI

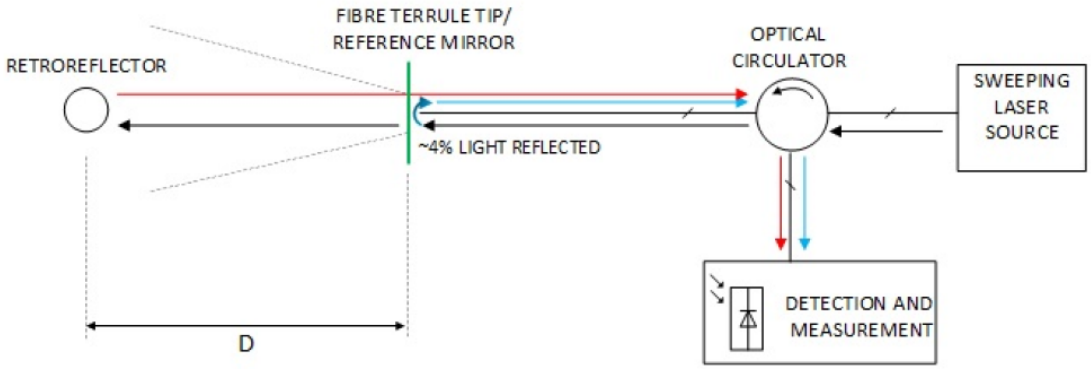

Figure 4.3: Scheme of the standard FSI system (cf.[14]).

The Frequency scanning interferometry is fully described in [14, 97, 98, 99, 100].

4.1.2.1 Regular FSI

This technology is based on a Michelson interferometer, as shown on Fig.4.3 (reference arm of interferometer is created by fiber and its ferrule tip), where the constant frequency laser is replaced by a sweeping laser source. By doing so, it is possible to compute the length difference between the two interferometer arms using the following formula:

$$D = c\frac{N}{2\Delta\nu n} \tag{4.1}$$

Where c is the velocity of light, $\Delta\nu$ is the change of laser frequency during the sweep, n is the refractive index of the light transmission medium and N is the number of phase cycles of the signal measured during the laser sweep in an unknown length interferometer. As the measurement of $\Delta\nu$ is difficult, a second interferometer, with a known length L is installed in parallel. By measuring the number of the measured interference signal cycles m in that interferometer, D can be precisely computed thanks to (eq.4.2)

$$L = c\frac{m}{2\Delta\nu n} \qquad D = L\frac{N}{m} \tag{4.2}$$

It is important to note that the measured length and the reference arm of the interferometer shall stay stable during the laser scan, otherwise the measurement will be burdened with error, coming from generation of supplementary synthetic phase cycles caused by optical path length change during scan.

4.1.2.2 Fourier based FSI

If more than only one retroreflector are placed in the laser beam, a set of beat frequencies relative to distance to the targets will be measured by the photodetector. When the laser sweeping α speed is constant, detected interferences become a constant beat frequency dependent on the distance D_n to the n-th target (eq.4.3).

$$f_{beat} = \alpha\tau = \alpha\frac{2D}{c} \qquad D_n = c\frac{f_{beat[n]}}{2\frac{d\nu}{dt}} \tag{4.3}$$

The Fourier transform technique is then used to retrieve the f_{beat} frequency component of each target, from the mixed multi-reflector interference signal. This system suffers similar limitations as the regular FSI as the target and the reference arm of the interferometer need to stay very stable to avoid any parasitic Doppler frequency shift of the beat frequency.

4.1.2.3 In-lined multiplexed and distributed FSI

FSI is commonly used with a fiber, directing the laser towards the target on which the sensor is measuring. In that case, and as shown on Fig.4.3, the end of the fiber is used as the mirror of the reference interferometer arm, while the retroreflector on which the measurement is carried out acts as the mirror of the measured arm. At CERN, a new way of using the FSI is studied: rather than using the configuration with an external reflector, an additional section of the fiber is added after the first fiber end (acting as a semi-reflecting mirror), creating a measurement cavity in the fiber instead of in the air. This technique allows the measurement of the length of the fiber itself and, in parallel, the distance in air towards a target. This configuration has advantages, like being immune to the atmospheric variation issues (for in-fiber distance measurement), measure the length of a 3D curve and not a straight line, being easily implementable in areas with harsh conditions, etc.

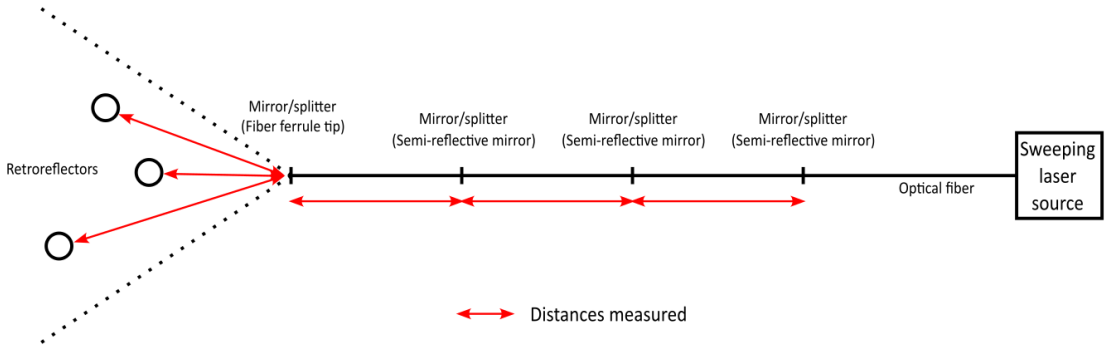

Figure 4.4: Drawing of the measurements allowed by the FSI system: multiple measurements along the fiber followed by multiple measurements on retroreflectors.

This system requires semi-reflective mirrors deployed on the light path, which is currently achieved by connecting two optical fiber connectors together, implying a change of refraction index hence Fresnel reflection in the fiber. The three main optical fiber connectors are the Fiber Connector - Physical Contact (FC-PC, back reflection smaller than -35 dB), the Fiber Connector - Ultra-Physical Contact (FC-UPC, back reflection smaller than -55 dB) and the Fiber Connector - Angled Physical Contact (FC-APC, back reflection smaller than -65 dB), [101] shown on Fig.4.5. While the FC-APC is the connector used when the losses need to be maximally avoided (reflections being directed away from the core), the two other connectors, when connected together or with each other, act as a semi-reflective mirror. This is due to a small gap trapped between the connectors' imperfect rugosity

surfaces, inducing a bigger change of refraction index and therefore a significant back reflection. Two of such connector ferrule mirrors on the same fiber can form an additional measurement cavity (arm) of the interferometer and so, the distance between these two mirrors can be measured. This way of measurement can be multiplexed along the fiber, only by having multiple semi-reflective mirrors in a row, while still being able to measure the distance to a target from the end of the fiber 4.4. Also, it measures the 3D length of the fiber portion separated by the two mirrors and not a punctual strain change as it is the case for the FBG, for example. By doing the analogy with the Fabry-Perot interferometers and their intrinsic and extrinsic configurations [102], the "in-air" measurement will be called extrinsic FSI (E-FSI), the "in-fiber" measurement of multiple portions will be called In-line Multiplexed and Distributed FSI (IMD-FSI).

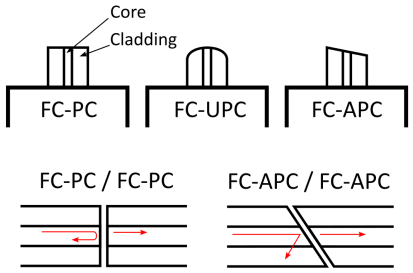

Figure 4.5: Drawing of the optical fiber connector shapes and reflections when connected.

This system has several advantages compared to the SOFO one. It can monitor different distances simultaneously, which is not the case for the SOFO system limited by the range of the motor. Moreover, it does not rely on movements or motor, simplifying the setup and the longevity. Semi-reflective mirrors are also very simple to create (two connectors for example) and does not need FBG. Finally, this system is still actively studied compared to the SOFO one, which does not reach the advantages of the FSI and is still remaining at a prototype state.

For these reasons, the focus has been put on the Fourier based FSI system, currently developed at CERN. The use of an FSI system able to perform such measurements was only initially tested in the past. A more complete test campaign was required in order to estimate the precision and the limits of the technology. The goals were to check if the system could be used for the inner alignment system and conclude on its basic behavior when exposed to different stimuli.

4.2 First tests

4.2.1 Setup and goal

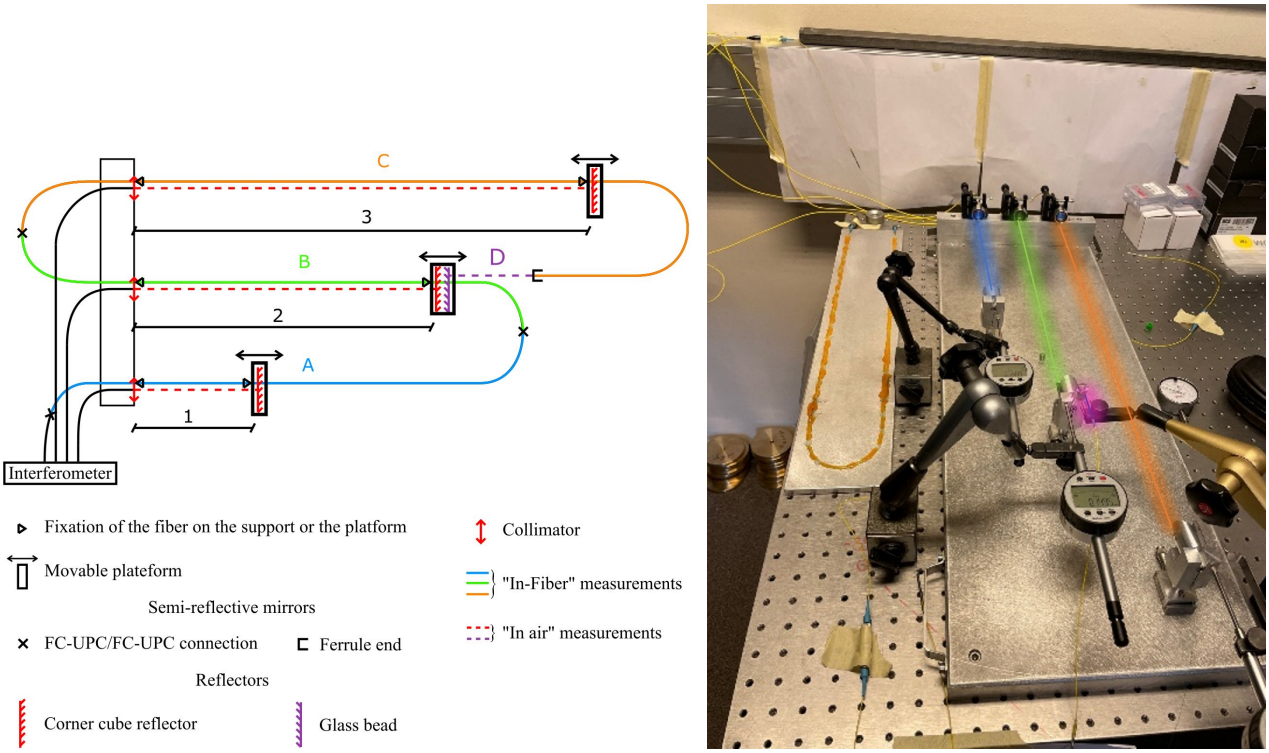

Figure 4.6: On the left: layout showing the different measurements performed on the test bench. A three portion (blue, green, and orange) fiber is tested using micrometric movable platforms. The displacement of the platforms is measured in real time by dial gauges. The portions are delimited by FC-PC connections. All the IMD-FSI measurements are also measured with a regular E-FSI measurement. An additional retroreflector has been added at the end of the portioned fiber to see if the fiber could perform some hybrid measurements. On the right: picture of the setup with the fibers highlighted and micrometric displacement sensors for the repeatability of the tests.

A dedicated bench has been designed in order to test the IMD-FSI and to compare it with a classic and well established E-FSI measurement system. Fig. 4.6 presents the layout and a picture of the bench. It is built to test a fiber divided in three portions. These portions are glued on both sides: on one side they are glued to a fixed bar and on the other side, they are glued to movable platforms in order to change the fiber length by stretching. In parallel, there are E-FSI measurements from the fixed bar towards a corner cube placed on the movable platform in order to compare the IMD-FSI to the E-FSI measurements. A glass bead has been placed in front of the end of the last portion of the fiber, to see if a E-FSI measurement can be performed after multiple IMD-FSI measurements. The

three portions are delimited by semi-reflective mirrors, made by the introduction of refractive index changes using two connectors of the FC-PC type.

The goal of this setup was to confirm the independence of the measurements and to estimate the uncertainty of the system.

4.2.2 Results

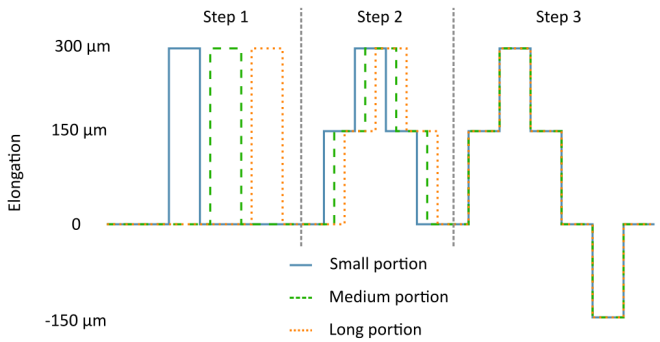

Figure 4.7: Planned length variation for the measurement campaign: first, all the portions are tested individually. Then, they have their distance increased step by step, overlapping with other portions. Finally, they are all moved at the same time.

The measurements plan, shown on Fig.4.7, consisted of, first, an elongation of each of the fibers individually, second, a gradual elongation of the portions with some overlapping. The final test was a simultaneous stretching followed by an un-stretching for all the portions. Results of these measurements are shown on Fig.4.8, on which are plotted the three measurement portions of the fiber and the E-FSI test at the end.

The results show that, first, the system detects the change of length of the portion and can measure it, as all the IMD-FSI measurements are following the E-FSI measurements. During the test, while decreasing the length of the smaller portion, a sag, which can be seen on Fig. 4.8, appeared. This is explained by the decrease of the E-FSI measurement, while the IMD-FSI was not decreasing anymore. It is important to underline that the elongation of a portion cannot be seen on the other measurements, highlighting the independence of the measurements. Regarding the accuracy of the system, it is a 10 μm repeatability for a 30 μm measurement uncertainty. This uncertainty is limited by a scale factor, which can be seen by the offsets on the big elongations, especially on the longer portions. This scale factor is due to the refraction index of the fiber core, not taken into account by

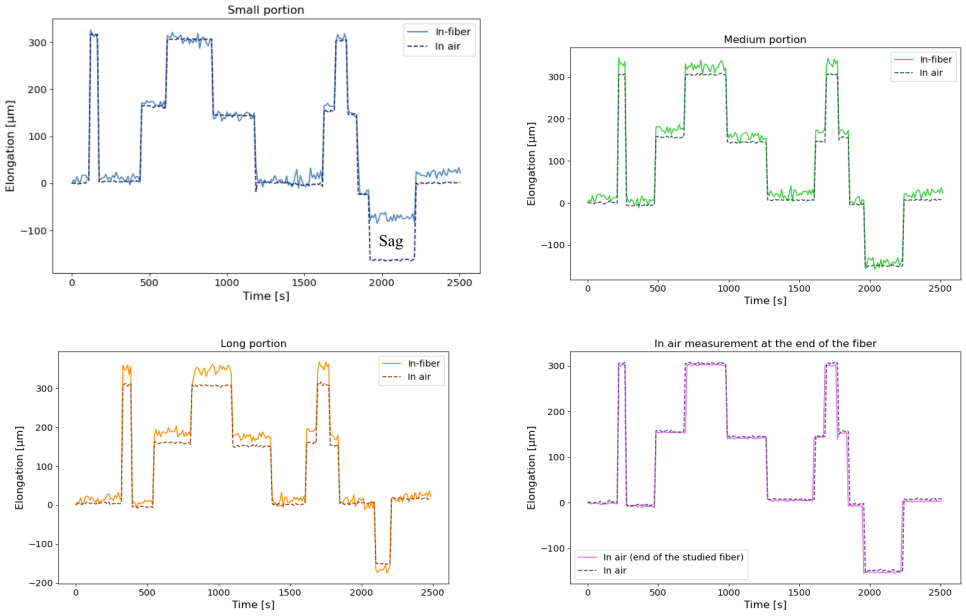

Figure 4.8: First results of the IMD-FSI measurements. Each portion has been tested, from top to bottom: small portion, medium portion, long portion and E-FSI measurement performed with the end of the studied fiber. The smallest portion studied was subject to sag when decreasing the distance between the platform and the reference, resulting in a decrease of the distance in air but not of the distance measured in fiber.

the interferometer software. This simple test validated the principle of the system, which can now be refined and optimized in order to reach the requested accuracy for the measurement of the deformation in the FCC-ee MDI.

4.3 Additional tests

4.3.1 An aluminum bar strain measurement

The first side test objective (which the corresponding setup is shown in Fig.4.9) was to monitor the deformation of an aluminum plate on which a fiber has been glued. The fiber installed had only one measuring portion and had been glued in a “U” shape using epoxy, on top of the plate. Then the length of the fiber was monitored while adding weight on the plate, illustrated in Fig.4.10. First, the weight was placed in the center of the bar, 3, 5 and 8 kg (they appear as negative values in the plot). Then, a steel bar was placed under the aluminum plate and the weight was placed at the extremities (the weight then appears in positive values in the plot).

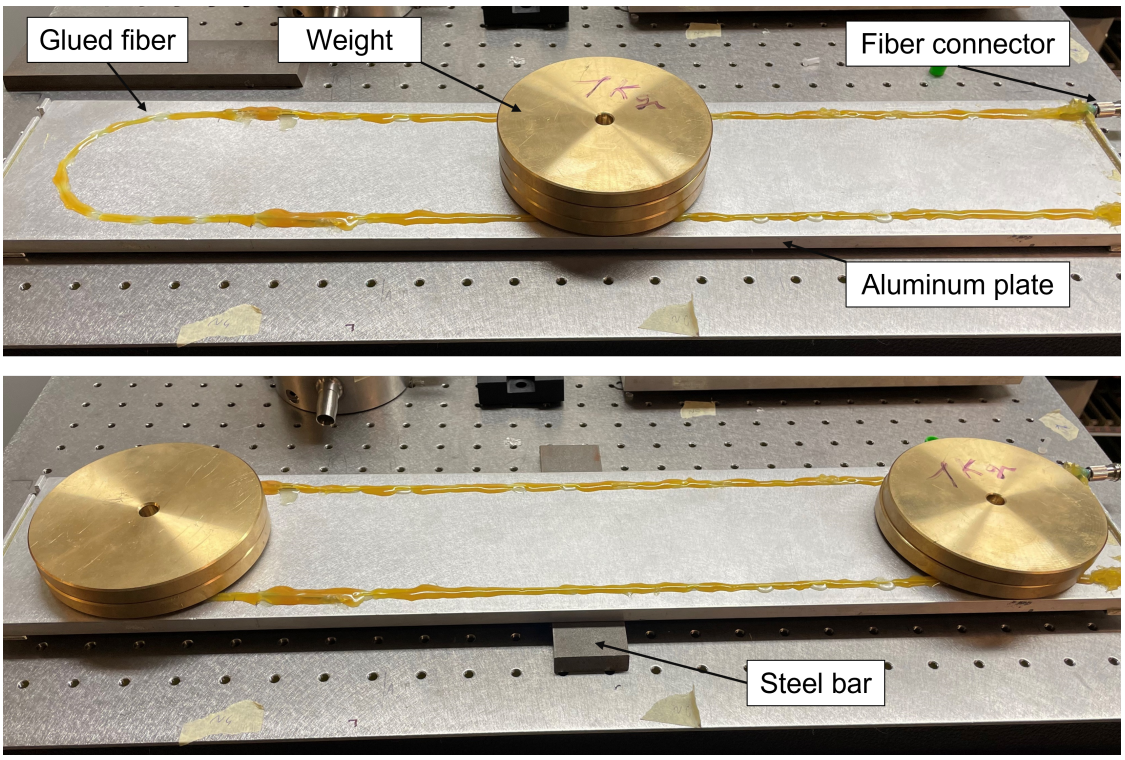

Figure 4.9: Picture of the setup for the monitoring of the deformation of an aluminum plate. An optical fiber has been glued at the surface of the plate and weight has been placed on it. First, the weight was positioned at the center of the plate. Then, a steel bar was placed in the middle and the weight was split and positioned at the extremities of the plate.

The results visible on Fig.4.10 show for the left graph part a temperature changes of the plate, followed by the right graph part weight tests. First, weights were added in the middle of the plate (3, 5 and 8 kg) and then displaced at the extremities. One can remark the drift along the measurements, which can be explained by the fact that the shielding of the fiber had not been removed, and it allowed the fiber to slowly creep inside it. The glue protected the fiber from the weight on top, acting as a hard shell.

This simple test showed that the fiber could measure a deformation, even though this simple setup did not allow a quantification of the plate deformation.

4.3.1.1 Semi-reflective mirrors printed in the fiber

The second test was the implementation of a change of the refractive index directly in the fiber, not relying on FC-PC connections. This change was performed by printing, exposing the short fiber

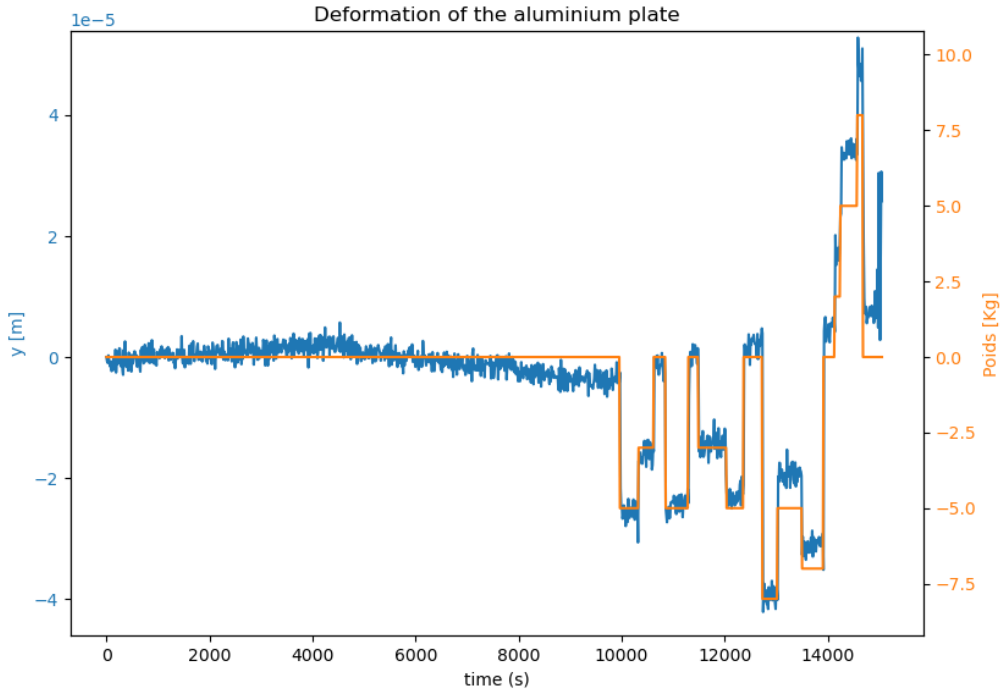

Figure 4.10: Plot of the measurement of the fiber placed on the aluminum plate.

section to a collimated Ultraviolet (UV) laser. As such implementation is not common, trial fibers have been ordered from a fiber manufacturer, with different imprinting characteristics to be tested. Twenty fibers were received, made with different laser power and exposition time. From the received batch, one of the fibers had satisfactory characteristics and provided enough reflection for our interferometer. Fig.4.11 shows the fiber, in which a fiber fault-finder laser is shining. At the location of the mirror, a reflection can be observed, and the right picture of Fig.4.11 shows a magnified view of the light dispersed on the fiber modified section.

As the interferometer was able to measure on that reflection, a stability test has been performed and the results were plotted on Fig.4.12. The repeatability is around 2 μm so almost 5 times better than the repeatability with the FC-PC connector.

Results from this fiber are extremely promising, and additional tests are foreseen to study in more details this printed mirror. These tests are listed in the discussion section below.

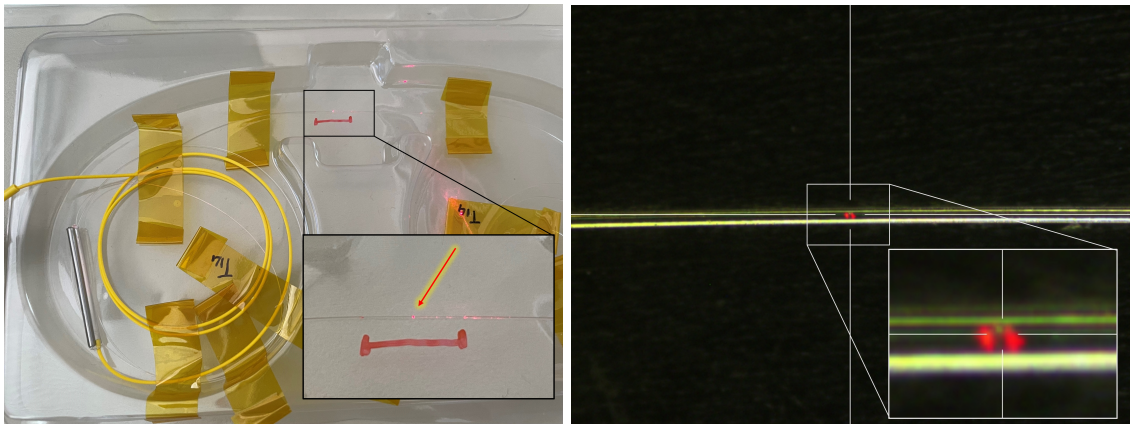

Figure 4.11: On the left: Picture of the fiber having a laser fiber fault-finder shining through it. The mirror can be visually located. On the right: a picture taken under the microscope, more zoomed in.

4.3.2 Next steps

Even though the tests performed are extremely promising for the use of this sensor in the FCC-ee MDI, improvements and a better understanding of the sensor behavior are required in order to ultimately confirm its use in the MDI. Therefore, additional tests of the sensor itself, its practical applications and possible upgrades are discussed.

The sensor could be tested and improved by studying in more details its different parts. The interferometer could be studied carefully and improved to get better optics, less signal noise and suppress vibration impact on the measurements. The system used for the tests is already 6 years old, and the technology is evolving at a very fast pace. The software collecting the raw data, processing and computing the interferogram and the distances could also be optimized, as it is still at a prototype stage.

Connectors, FC-PC currently used as semi-reflective mirrors, should be changed as they got some drawbacks. The connection is too bulky, and such connectors in the FCC-ee MDI would take too much space. Then, the connection intensities are not repeatable if not tightened with the same torque. Tests have been performed, and the returned signal was greatly impacted by the screwing force, up to a point where, when screwed too strongly, the connection didn't act as a semi-reflective mirror anymore and the signal from that connection was lost. Moreover, this setup reached 10 μm noise measurements, which is 10 times too high for the planned use of the sensor. This noise is likely due to scattering effects in the fiber impacting measurement uncertainty or the mirrors, as the usual

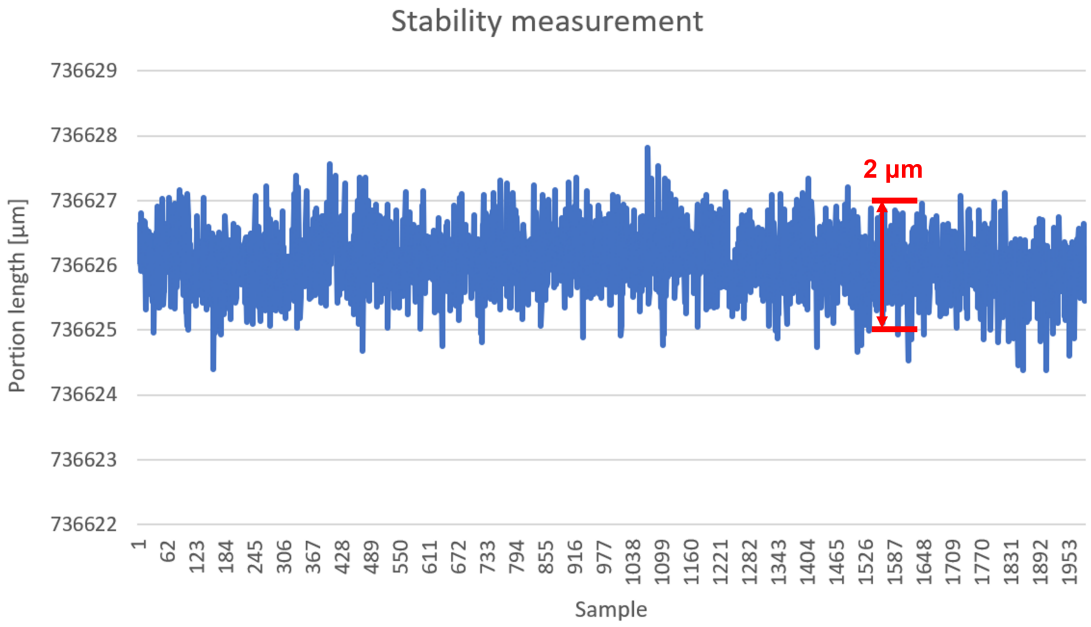

Figure 4.12: Graph of a stability test done on the distance measurement to the semi-reflective mirror.

E-FSI is around 1 μm noise only. Improvement could be done here, by another design for the creation of the semi-reflective mirror. An optimal solution would be to have a semi-reflective mirror within the fiber core size. This could be achieved by adding a defect like bubble in the fiber core, by doing a "bad quality" welding, or by laser imprinting the mirror directly in the fiber. The main difficulty, when thinking about adding a bubble or welding the fiber, is to make the process repeatable, for each of the semi-reflective mirrors that will be required in our case. This repeatability can be easily achieved with the laser printing, but this technique was not yet tested for this application, contrary to well known Bragg gratings implementation.

Some initial tests have been started on such laser printed semi-reflective mirror, shown in section 4.3.1.1. They underlined the impact of the connector on the noise of the sensor. Changing the connectors by a printed mirror divided the noise by 5. Additional tests need to be performed with these printed mirrors, like having multiple in the same fiber, doing some trials, and tuning the printing options.

The fiber could also be studied. The main limitation is the scatterings that can occur in the fiber: Raman, Brillouin and Rayleigh. These scattering are sometimes used for the measurements but as it is not our case, they may be seen as noise by the Fourier based FSI interferometer.

One answer to this scattering limitation is to use a so called Dynamic-FSI FSI with 2 opposite wavelengths sweeping. By doing a simultaneous and opposed frequency sweeping, we can correct the scattering and vibration impact on the fibers [103]. This adds to the cost of the interferometer (roughly the double), but makes the system almost ten times more precise than one of single wavelength FSI. The construction of such interferometer is foreseen at CERN in the next few years. Moreover, one needs to scale that price over the cost of the entire project.

Chapter 5

Discussion and future developments

Content

5.1 Versatility of the inner alignment system

As mentioned in Chap.1, the FCC-ee design is still at an early state. It is the case for both the accelerator and the detector. The designs may change drastically and at different paces as distinct working groups are studying the two objects. All the systems that will be implemented on those machines will need to adapt as much as possible to the multiple iterations and updates.

The inner alignment sensors and their design were chosen to be as adaptable as possible with regard to the possible changes of the MDI design. These sensors could be easily relocated with the design updates, and the network made denser for more redundancy and security. For example, a helix network could be added outside the cryostat or on the inner wall of the detector, enhancing the network. In fact, this system is not limited to the MDI and could be added on the walls to monitor the tunnel shape or other important quantities. As an example, some portions of the helices could also be linked to a material with a precise thermal expansion coefficient, and dedicate this portion as a thermometer. The change of strain of specific materials could allow using the fibers as a humidity sensor or pressure sensor.

This system could also be applicable to a lot of other situations, requiring only to adapt the equations and the deformation model to the studied case. Civil engineering structures are already monitored by simple shaped fiber networks, ending in monitoring of 1D deformation of some parts of the structure. 3D monitoring could be very valuable for specific structures requiring a careful follow-up of its shape changes. The deformation system has been thought in a way that it could adapt to the most extreme changes of the FCC-ee MDI design. The difficulty is in a clear definition of the problem. One would need to clearly define the unknowns (deformations, temperature, pressure changes ...) and then define the equations. Once everything is defined, the least-squares adjustment method can be applied.

The versatility of the external alignment system is similar, allowing to adapt to multiple shapes and could be used almost everywhere in the collider but also in civil engineering.

5.2 Link between the MDI alignment and sub-detector alignment

Currently, some subdetectors, which alignments are under the responsibility of collaborations and not directly from CERN, have their subcomponents monitored in order to know their position, one with respect to the others. It is the case in the ATLAS detector for example, where the SemiConductor Tracker (SCT), a sub-detector inside ATLAS, is monitored by FSI [88], and the Muon Spectrometer Endcaps is monitored using an optical alignment system (RASNIK and BCAMs) [104]. But this monitoring is not performed by the survey group at CERN. These subdetectors are monitored at a 100 μm accuracy, and can provide information about the beam position, and even the IP with respect to their position, for the use of the physicists operating the subdetector in question. These subsystems are therefore currently independent, under the responsibility of people part of the collaboration taking care of the detector. The subdetector local measurements are not linked to the CERN coordinate system on a regular basis, like in the top part of the Fig.5.1, being linked only during measurement campaigns performed when the detector is open for maintenance. For now, it is impossible to link the ATLAS network with the CERN coordinate system by continuous relative measurements. The main reason is that these systems have not been designed for such transfer, no lines of sight are reserved, and targets for distance measurements are only visible when the detector is opened. Physical obstacles, such as shielding, pipes and cables, prevent the creation of direct lines of sight between the two systems. This physical delimitation ended up splitting the responsibility of the survey campaign, asking to two different sections the management of the two systems. But a direct link between the two systems could have a lot of advantages.

5.2.1 Advantages

Having a direct and continuous link between the accelerator and the detector, like in the bottom part of the Fig.5.1, could indeed represent interesting advantages. First, it could increase the longevity of the detector, by having a better alignment with the accelerator and therefore lowering unwanted radiations or losses emitted towards the detector. It would also allow a faster calibration of the detector by the physicians, being closer to the aligned position of the detector (needed to start physics measurements) from the beginning, without requiring any beam for the alignment itself. This would be allowed by the knowledge of the real position of the detector once closed, and once different parts

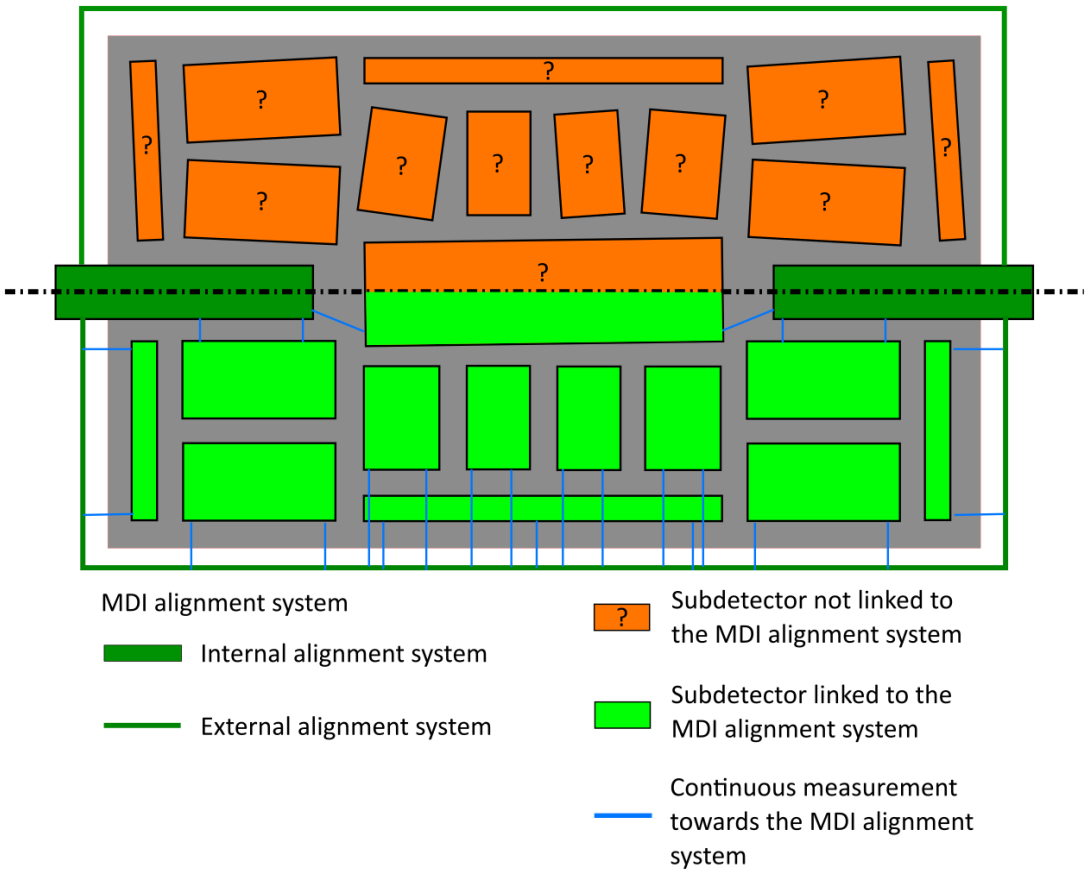

Figure 5.1: Drawing underlining the difference between monitored and not monitored subdetectors. In the top of the drawing, subdetector are not monitored, and their position is not known. In the bottom of the picture, continuous measurement link the subdetectors to the MDI alignment system, allowing to know the positions of the subdetectors.

are cooled down (by liquid gazes) or warmed up (by heating of the electronics) and the magnetic fields turned on. This configuration is not accessible currently by the survey campaigns, as geodetic reference targets are not visible once the detector is closed and the detector is not accessible once in operation. The system could also be used to speed up the closing process of the detector after maintenance, which is a critical but slow operation. Decreasing that time would increase the physics measurement time and increase the integrated luminosity. Such alignment between the accelerator and the detector would also represent a diminution of the radiation exposition of the personnel. It could also be useful to strengthen the overall network of distance measurements, adding redundancy and constraints at places in subdetectors where the access would be impossible for the MDI alignment system. It is important to note that this could improve the quality of the network for both sides as

the MDI alignment system could improve the network of the subdetector, adding constraints. This link has also advantages on the physics point of view as the subdetector could give information on the beam position and even the IP with respect to their position and, thanks to the link, to the accelerator. It would allow fine adjustment of the steering magnets and correctors to move the beams and make them collide as close as possible to the center of the detector.

5.2.2 Implementation

An idea would be to see the MDI alignment system studied earlier as a backbone system, autonomous with regard to the MDI components, on which could be added sub-systems for the alignment of subdetectors. These systems, only dedicated to the measurement of the subdetectors, could implement links to some points of the MDI alignment system (without disrupting it). In addition, these subsystems could implement links with each other. If started early enough, a small adjustment of the MDI alignment system could be added in order to simplify the connections with the subsystems, while not impacting the accuracy of the MDI alignment system.

5.2.3 Challenges

Such implementation could have a lot of advantages if well organized and if some security boundaries are set. The major one being that the MDI alignment system needs to be entirely autonomous and must not rely on any of the alignment sub-systems of the detector. These systems must not alter the measurement or precision of the MDI alignment system. In addition, these systems will require to be maintenance free, as access will be extremely difficult and sometimes even impossible. Conditions inside the detector are very likely to be harsh, as the electronics of the subdetector will heat up and ventilation will be used to disperse the heat. The careful consideration of the environmental conditions in the alignment algorithms would be required. Specific attention will need to be put on the difference of timescale and precision scale between the MDI alignment system and the subdetectors alignment systems.

5.3 Re-adjustment system implementation

One point that requires further development is the readjustment system.

These systems allow to move components after the initial alignment, when required. There is a very wide range of systems allowing movements, differing from the stroke, resolution, complexity, and speed of the motion, the possibility of remote use, the resistance against radiations and cryogenic temperatures, and many other aspects. The LHC ATLAS, ALICE, CMS and LHCb MDIs are equipped with a readjustment system, under the low-beta quadrupoles, which can re-align the components remotely from the control room according to the feedback of alignment sensors installed on the triplet components.

Such configuration could also be studied for an installation in the FCC-ee MDI, as it can represent a huge comfort and advantage for the use of the collider. It could allow to do some tuning once the cryostat and the components inside are assembled, in tandem with the alignment system which provides the information on the positions. Tests and adjustments could be performed during first powering and cooling tests. It could also allow small optimization movements once everything is installed in the detector, correcting the observed misalignment. Finally, an emergency procedure could be created, to do necessary misalignment if, for any reason, a component moved away from its aligned position right before or even during the run of the machine.

On the one hand, conditions inside the MDI (space, access, radiations, cold ...) make the design of a readjustment system an enormous challenge, but on the other hand, these conditions can also justify the use of such a system. It could allow small position tuning without disassembling the entire assembly (saving months of time) and with the very limited access for maintenance. Such misalignment could be caused by movements due to the cooling down, vacuum, Lorentz force or even the assembly process itself, that could have been mis-quantified.

To decrease the difficulty of the design of such a re-adjustment system, a solution could be to design it to work at room temperature only, and be fixed at cryogenic temperatures. Operation of the system would only happen during tests after assembly (first cooling down cycles) and at the end of shutdowns of the machine or technical stops, while the machine is still at room temperature. This system can also be designed only for particular components and not all of them. In fact, it could be designed to adjust only the support of the assembly, so the mean of the alignment of the different

components inside. This should be studied by mechanic experts as early as possible in the design, in order to estimate the advantages of the system compared to the complexity of its implementation and additional cost. On that point, one could look at systems used in deep space, as they are relatively close to our conditions (radiations, cold temperatures, vacuum ...).

Such system would have been very helpful for the SuperKEKB alignment for example as almost all the components were too low with respect to their designed positions once installed.

Looking even further in the future and with the progress in different domains, this system, in addition to the alignment system information, could be implemented in a "smart structure" or auto-adaptive structure [93]. These structures, being both sensible (thanks to sensors) and reactive (thanks to actuators), can react to their environment for different reasons (security, optimization ...) via a closed loop feedback control solutions. By implementing such a structure in the FCC-ee MDI, one could have an automatic readjustment of the components in case of a sudden movement or a slow drift away from the alignment requirements. Of course, such a system would need to take into account all the security boundaries of all the systems on which the alignment can have an impact.

5.4 Alignment of the rest of the FCC-ee MDI

The FCC-ee MDI definition can extend to further than the components inside the detector, and around 1 km of components on each side of the IP can also be seen as part of the MDI. As described in chap.1, the emphasis has been put on the components inside the detector as it is the area gathering the most challenges, and it is the area that still does not have any solutions, as underlined in chap.2. But the alignment of this area of 1 km on each side of the IP will be very important in order to limit as much as possible the synchrotron radiations to be emitted toward the detector. These areas will be placed in a wider tunnel than the regular tunnel, in the transition towards the experimental caverns, going from a 5.5 m large tunnel to a 17.8 m large tunnel just before the experimental cavern (which is more than 30 m large). This will leave some space for usual alignment systems, like the system installed on the Low-β quadrupoles in the LHC. A combination of HLS, WPS and FSI measurement could be implemented here. In case of requirements too tight for these systems, experience from studies done for linear colliders, such as the Particle Accelerator Components' Metrology and Alignment to the Nanometer scale (PACMAN) project [105], could be applied. In this project, high end fiducialisation procedures, and denser sensor networks are studied to fulfill the extremely constraining linear accelerator alignment requirements. The space also allows for new alignment systems to be developed without too constraining access limitations.

Conclusion

The FCC-ee MDI has been studied and the current challenges listed. The design, implementing a very dense assembly directly inside the physics detector, combined with a lack of space, difficult conditions as radiations, cryogenic temperatures, magnetic fields and very tight requirements make the alignment a complex operation. With 30 μm requirements for the alignment of the final focusing quadrupoles, 50 μm for the LumiCal and 100 μm for the screening and compensation solenoid, a robust alignment and monitoring system was required. These conditions and requirements are similar to other colliders and project colliders, such as in the DAFNE/KLOE MDI, the SuperKEKB/Belle II MDI or in the projects colliders such as the CLIC, the ILC, and the Circular Electron Positron Collider (CEPC). But none of these implement/propose a satisfactory alignment and monitoring solution. Existing machines with such an operational system, like the LHC, have a design too far from the FCC to have its system adapted. The study of existing sensors also underlines the limitations they are facing, mostly the lack of space and the radiation in the area. today, the limitations due to manufacturing tolerances are put aside as the project is still at an early stage, but these will need to be taken into account once the design is more mature. Alignment during the assembly of the machine detector interface is a known process, performed with laser trackers, for example. Even more precise ways to carry out this procedure could also be used, like the use of a CMM in a temperature controlled room to check each step of the assembly. As solutions were existing for this activity, the focus has been put on the design of a new monitoring system. Such a system is required for the next generation colliders, but no satisfactory solutions have been proposed. Therefore, a new system has to be implemented, able to tackle the challenges. A new strategy has been presented, using the combination of two subsystems: the external monitoring system and the internal monitoring system. The external monitoring system proposed is based on a network of interferometric distance measurements, a system versatile enough to adapt to the evolutions of the design. This system was designed to monitor the end of the assembly located inside the cryostat. The main difficulty, of measuring the inner components, is solved by using a new system based on the In-lined Multiplexed and Distributed FSI (IMD-FSI). This technology monitors the 3D lengths of fiber portions independently and simultaneously. The inner monitoring system is designed by installing helices inside the assembly, in order to follow the evolution of the shape of the assembly. Simulations show uncertainties of less than 1 μm in each of the three dimensions, for a point position on the studied cylinder, with a system implementing 36 helices of 100 portions each and a measurement uncertainty of 1 μm. From this known shape, another network

of interferometric distance measurements allows to obtain the position of the inner components with respect to that shape. Simulations combining all these systems present uncertainties of less than 15 μrad for the rotations and 20 μm for the translations between quadrupoles on opposites sides of the IP, for an initial point definition of the external alignment system of 10 μm. These numbers increase to 20 μrad and 110 μm for an initial point position uncertainty of 100 μm. It underlines a good step towards an alignment and monitoring system able to deal with the challenges of the FCC-ee MDI. The fibers used by the IMD-FSI do not take much space while being resistant to radiations and cryogenic cooling. The helices shaped network is also versatile for this system to be used in the FCC-ee MDI, adaptable to the upcoming changes of the MDI design, but also to other places around the MDI and even in the rest of the collider. The IMD-FSI, being a new system, has been investigated. A bench has been created to test the system and its behavior. The independence of its measurements has been proven, and the measurement uncertainty of a system using connectors as semi-reflective mirrors was of 10 μm. These tests were very promising. Another semi-reflective mirror has been tested, by printing directly the mirror in the fiber thanks to a UV laser. The first test sample had a measurement noise of only 2 μm, which is very promising for the future. This study being mainly composed of simulation due to the difficult access to the technology, a lot of R&D is required. The development of mirrors is foreseen to check how little the noise can be. But research on the software, on the hardware composing the interferometer could also be done. On the mathematical side, optimization of the helices network should be performed, once knowing in more details the MDI design. Computation optimization, calibration procedures, advanced error testing should also be studied.

Regarding the deformation monitoring system, additional implementation in the MDI should be studied, to monitor the inner wall of the detector, for example. It could also be used away from the IP, measuring different components, or even the tunnel shape itself. Its versatility and ability to measure strain, deformations, temperature and so on could allow its use in aeronautics or civil engineering, to monitor towers, bridges, and other large structures.

Bibliography

[1] Y. Arimoto, J. DiMarco, K. Egawa, T. Kawamoto, M. Masuzawa, J. Nogiec, Y. Ohsawa, N. Ohuchi, R. Ueki, G. Velev *et al.*, "Magnetic measurement with single stretched wire method on superkekb final focus quadrupoles," Fermi National Accelerator Lab.(FNAL), Batavia, IL (United States), Tech. Rep., 2019.

[2] M. Benedikt, V. Mertens, F. Zimmermann, F. Cerutti, T. Otto, J. Poole, O. Brunner, J. Gutleber, A. Milanese, A. Blondel *et al.*, "Fcc-ee: The lepton collider: Future circular collider conceptual design report volume 2," *Eur. Phys. J. Spec. Top.*, vol. 228, no. CERN-ACC-2018-0057, pp. 261–623, 2018.

[3] N. Ohuchi, Z. Zong, H. Yamaoka, Y. Arimoto, X. Wang, K. Tsuchiya, and T.-H. Kim, "Design and construction of the magnet cryostats for the superkekb interaction region," *IEEE Transactions on Applied Superconductivity*, vol. 28, no. 3, pp. 1–4, 2017.

[4] A. Herty and D. Mergelkuhl, "Alignment of the low-β magnets and the experiments in the LHC," CERN, Geneva, Tech. Rep., 2008. [Online]. Available: https://cds.cern.ch/record/1119534

[5] L. Linssen, A. Miyamoto, M. Stanitzki, and H. Weerts, "Physics and detectors at clic: Clic conceptual design report," *arXiv preprint arXiv:1202.5940*, 2012.

[6] L. Gatignon, "Clic mdi overview," *arXiv preprint arXiv:1202.6511*, 2012.

[7] R. Pöschl, "(selected) mdi issues of ild," Tech. Rep., 2020.

[8] M. Harrison, "International linear collider technical design report (volumes 1 through 4)," Brookhaven National Lab.(BNL), Upton, NY (United States), Tech. Rep., 2013.

[9] M. Warden, P. A. Coe, D. Urner, and A. Reichold, "MONALISA: A Precise System for Accelerator Component Position Monitoring," *eConf*, vol. C0802113, p. TU011, 2008.

[10] C. S. Group *et al.*, "Cepc conceptual design report: Volume 1-accelerator," *arXiv preprint arXiv:1809.00285*, 2018.

[11] W. NIEWIEM, "Atlas – larg barrel and extended barrels stability," 2022. [Online]. Available: https://edms.cern.ch/ui/file/2714642/1/20220309_LAr_stability.pdf

[12] D. Inaudi, "Fiber optic sensor network for the monitoring of civil engineering structures," Ph.D. dissertation, Verlag nicht ermittelbar, 1997.

[13] M. Pozzi, D. Zonta, H. Wu, and D. Inaudi, "Development and laboratory validation of in-line multiplexed low-coherence interferometric sensors," *Optical Fiber Technology*, vol. 14, no. 4, pp. 281–293, 2008.

[14] M. Sosin, H. Mainaud-Durand, V. Rude, and J. Rutkowski, "Frequency sweeping interferometry for robust and reliable distance measurements in harsh accelerator environment," in *Applied Optical Metrology III*, vol. 11102. SPIE, 2019, pp. 145–161.

[15] R. R. Wilson, "The tevatron," *Phys. Today*, vol. 30, no. 10, pp. 23–30, 1977.

[16] K. Akai, K. Furukawa, H. Koiso *et al.*, "Superkekb collider," *Nuclear Instruments and Methods in Physics Research Section A: Accelerators, Spectrometers, Detectors and Associated Equipment*, vol. 907, pp. 188–199, 2018.

[17] J. Wang, L. Ma, and Q. Qin, "Status and performance of bepcii," *pulse*, vol. 1, p. 1, 2010.

[18] L. Evans, "The large hadron collider," *New Journal of Physics*, vol. 9, no. 9, p. 335, 2007.

[19] O. Aberle, E. Carlier, E. Barzi, G. Ferlin, C. Parente, E. Skordis, K. Einsweiler, S. Atieh, A. Patapenka, R. Calaga *et al.*, *High-Luminosity Large Hadron Collider (HL-LHC): Technical design report*, ser. CERN Yellow Reports: Monographs. Geneva: CERN, 2020. [Online]. Available: https://cds.cern.ch/record/2749422

[20] D. Schulte, "The muon collider," *JACoW IPAC*, vol. 2022, pp. 821–826, 2022.

[21] C. Aimè, A. Apyan, M. A. Mahmoud, N. Bartosik, F. Batsch, A. Bertolin, M. Bonesini, D. Buttazzo, M. Casarsa, M. G. Catanesi *et al.*, "Muon collider physics summary," *arXiv preprint arXiv:2203.07256*, 2022.

[22] A. Abada, M. Abbrescia, S. S. AbdusSalam, I. Abdyukhanov, J. A. Fernandez, A. Abramov, M. Aburaia, A. Acar, P. Adzic, P. Agrawal *et al.*, "Fcc physics opportunities," *The European Physical Journal C*, vol. 79, no. 6, pp. 1–161, 2019.

[23] by James Gillies, "Luminosity? Why don't we just say collision rate?" 2011. [Online]. Available: https://cds.cern.ch/record/1997001

[24] H. Mainaud Durand, K. Artoos, M. Buzio, D. Caiazza, N. Catalan Lasheras, A. Cherif, I. P. Doytchinov, J.-F. Fuchs, A. Gaddi, N. Galindo Munoz, J.-C. Gayde, S. W. Kamugasa, M. Modena, P. Novotny, C. Sanz, G. Severino, S. Russenschuck, D. Tshilumba, V. Vlachakis, M. Wendt, and S. Zorzetti, "Fiducialisation and initial alignment of CLIC component with micrometric accuracy," 2016. [Online]. Available: https://cds.cern.ch/record/2237694

[25] W. Coosemans, H. M. Durand, A. Marin, and J. Quesnel, "The alignment of the lhc low beta triplets: review of instrumentation and methods," in *Proceedings of the Seventh International Workshop on Accelerator Alignment, SPring-8, Japan*, 2002, p. 218.

[26] A. Herty, *Micron precision calibration methods for alignment sensors in particle accelerators*. Nottingham Trent University (United Kingdom), 2009.

[27] J. Dwivedi, S. Goswami, V. Madhumurthy, M. Acar, H. M. Durand, A. Marin, and J. Quesnel, "The motorized alignment jacks for the lhc low beta quadrupoles," in *Proc. International Workshop on Accelerator Alignment (IWAA'06)*, 2006.

[28] F. Bulos, D. Burke, R. Helm, J. Irwin, A. Odian, G. Roy, R. Ruth, and N. Yamamoto, "Beam-based alignment and tuning procedures for e+ e-collider final focus systems," Stanford Linear Accelerator Center, Tech. Rep., 1991.

[29] I. Barnett, A. Beuret, B. Dehning, P. Galbraith, K. Henrichsen, M. Jonker, M. Placidi, R. Schmidt, L. Vos, J. Wenninger *et al.*, "Dynamic beam based alignment," in *AIP Conference Proceedings*, vol. 333, no. 1. American Institute of Physics, 1995, pp. 530–535.

[30] H. Jin, W. Decking, T. Limberg *et al.*, "Beam-based alignment in the european xfel sase1," in *Proc. 5th Int. Particle Accelerator Conf.(IPAC'14)*, 2013, pp. 2867–2869.

[31] Z. Man-Zhou, L. Hao-Hu, J. Bo-Cheng, L. Gui-Min, and L. De-Ming, "Beam based alignment of the ssrf storage ring," *Chinese Physics C*, vol. 33, no. 4, p. 301, 2009.

[32] C. Adolphsen, T. Lavine, W. Atwood, T. Himel, M. J. Lee, T. Mattison, R. Pitthan, J. Seeman, S. Williams, and G. Trilling, "Beam-based alignment technique for the slc linac," in *Proceedings of the 1989 IEEE Particle Accelerator Conference,.'Accelerator Science and Technology.* IEEE, 1989, pp. 977–979.

[33] G. Portmann, D. Robin, and L. Schachinger, "Automated beam based alignment of the als quadrupoles," in *Proceedings Particle Accelerator Conference*, vol. 4. IEEE, 1995, pp. 2693–2695.

[34] P. Tenenbaum and T. Raubenheimer, "Resolution and systematic limitations in beam-based alignment," *Physical Review Special Topics-Accelerators and Beams*, vol. 3, no. 5, p. 052801, 2000.

[35] K. Endo, H. Fukuma, F. Zhang *et al.*, "Algorithm for beam based alignment," in *KEK PROCEEDINGS.* NATIONAL LABORATORY FOR HIGH ENERGY PHYSICS, 1995, pp. V–427.

[36] M. Zobov, D. Alesini, M. Biagini, C. Biscari, A. Bocci, R. Boni, M. Boscolo, F. Bossi, B. Buonomo, A. Clozza *et al.*, "Test of "crab-waist" collisions at the da ϕ ne ϕ factory," *Physical review letters*, vol. 104, no. 17, p. 174801, 2010.

[37] M. Boscolo, N. Bacchetta, M. Benedikt, L. Brunetti, H. Burkhardt, A. Ciarma, M. Dam, F. Fransesini, M. Jones, R. Kersevan *et al.*, "Challenges for the interaction region design of the future circular collider fcc-ee," *arXiv preprint arXiv:2105.09698*, 2021.

[38] S. Sinyatkin, "Orbit errors at the fcc-ee due to the ff quadrupoles displacements," 2018. [Online]. Available: https://indico.cern.ch/event/694811/contributions/2863824/attachments/1594056/2523883/Sinyatkin_Misalign_FF.pdf

[39] M. Koratzinos, "Cct ff quad design status," 2018. [Online]. Available: https://indico.cern.ch/event/694811/contributions/2863797/attachments/1592462/2520805/FF_design_status_2.pdf

[40] M. Dam, "Requirements on luminometer geometrical precision," 2017. [Online]. Available: https://indico.cern.ch/event/665291/contributions/2724729/attachments/1528709/2391456/lumi170922.pdf

[41] M. Koratzinos and K. Oide, "The magnetic compensation scheme of the fcc-ee detectors," *arXiv preprint arXiv:2101.05704*, 2021.

[42] H. M. Durand, "Alignment requirements for the lhc low beta triplet," LHC-G-ES-0016, CERN, Tech. Rep., 2016.

[43] H. Mainaud Durand, M. Anastasopoulos, J. Kemppinen, V. Rude, S. Griffet, and M. Sosin, "Validation of the clic alignment strategy on short range," *eConf*, vol. 1209102, no. CERN-ATS-2012-272, p. 30, 2012.

[44] C. YU, "The design and realization of interaction region for bepcii," 2008. [Online]. Available: https://accelconf.web.cern.ch/fac08/TALKS/TUACH09_TALK.PDF

[45] C. Yu, Y. Wu, Z. Yin, J. Zhang, M. Wang, Q. Peng, J. Pang, Y. Yang, X. Dai, and Y. Liu, "Interaction region design and realization for the beijing electron positron collider," *Nuclear Instruments and Methods in Physics Research Section A: Accelerators, Spectrometers, Detectors and Associated Equipment*, vol. 608, no. 2, pp. 234–237, 2009.

[46] J. Murata, A. Al-Jamel, R. Armendariz, M. Brooks, T. Horaguchi, N. Kamihara, H. Kobayashi, D. Lee, T.-A. Shibata, and W. Sondheim, "Optical alignment system for the phenix muon tracking chambers," *Nuclear Instruments and Methods in Physics Research Section A: Accelerators, Spectrometers, Detectors and Associated Equipment*, vol. 500, no. 1-3, pp. 309–317, 2003.

[47] F. Karl, "Status of the relativistic heavy ion collider," 1999.

[48] D. Kaemtner and J. Prenting, "Straight line reference system (slrs) for the adjustment of the x-ray free-electron laser (xfel) at desy," in *Proceedings of the 9th International Workshop on Accelerator Alignment (IWAA), Stanford Linear Accelerator Center (SLAC), California, United States*, 2006.

[49] M. Schlösser and J. Prenting, "Status report on survey and alignment efforts at desy," in *Proceedings of the 9th International Workshop on Accelerator Alignment (IWAA), Stanford Linear Accelerator Center (SLAC), California, United States*, 2006.

[50] G. Amelino-Camelia, F. Archilli, D. Babusci, D. Badoni, G. Bencivenni, J. Bernabeu, R. Bertlmann, D. Boito, C. Bini, C. Bloise *et al.*, "Physics with the kloe-2 experiment at the upgraded daφne," *The European Physical Journal C*, vol. 68, pp. 619–681, 2010.

[51] M. Tawada, N. Ohuchi, M. Iwasaki, K. Tsuchiya, T. Oki, Z. Zong, and N. Higashi, "Design study of final focusing superconducting magnets for the superkekb," *Proceedings of IPAC11, WEPO027*, pp. 2457–2459, 2011.

[52] D. Missiaen and J.-F. Fuchs, "Smoothing the lhc during ls1," 2016.

[53] V. Rude, G. Kautzmann, H. Mainaud Durand, A. V. Naegely, M. Sosin, and M. Udzik, "3D calculation for the alignment of LHC low-beta quadrupoles," 2022. [Online]. Available: https://cds.cern.ch/record/2849052

[54] A. Marin and M. Udzik, "Mesures absolues avec de long cÂbles mulrad," CERN, Geneva, Tech. Rep., 2013. [Online]. Available: https://edms.cern.ch/ui/file/1259668/1/Tests_long_cables_MULRAD_WPS.pdf

[55] A. Herty, A. Marin, and H. Mainaud-Durand, "Test and calibration facility for hls and wps sensors," 2004.

[56] H. Mainaud Durand, "Alignment requirements for the LHC low-beta triplets," CERN, Geneva, Tech. Rep., 2006. [Online]. Available: https://edms.cern.ch/ui/#!master/navigator/document?D:1221578928:1221578928:subDocs

[57] M. Sosin, H. M. Durand, F. Micolon, V. Rude, J. Rutkowski *et al.*, "Robust optical instrumentation for accelerator alignment using frequency scanning interferometry," *measurement*, vol. 2, p. 3, 2021.

[58] E. Dimovasili, A. Herty, H. M. Durand, A. Marin, F. Ossart, and T. Wijnands, "Radiation induced effects on the sensors of the hydrostatic leveling system for the lhc low beta quadrupoles,"

in *2005 8th European Conference on Radiation and Its Effects on Components and Systems*. IEEE, 2005, pp. PH2–1.

[59] P. Singh Bahadur, S. Jaiswal, and R. Srivastava, "Optical fiber: Trending technologies," in *2021 2nd International Conference on Intelligent Engineering and Management (ICIEM)*, 2021, pp. 166–170.

[60] R. G. Alía, M. Brugger, F. Cerutti, S. Danzeca, A. Ferrari, S. Gilardoni, Y. Kadi, M. Kastriotou, A. Lechner, C. Martinella *et al.*, "Lhc and hl-lhc: Present and future radiation environment in the high-luminosity collision points and rha implications," *IEEE Transactions on Nuclear Science*, vol. 65, no. 1, pp. 448–456, 2017.

[61] M. Aicheler, P. Burrows, N. Catalan, R. Corsini, M. Draper, J. Osborne, D. Schulte, S. Stapnes, and M. Stuart, "The compact linear collider (clic)-project implementation plan," *arXiv preprint arXiv:1903.08655*, 2019.

[62] E. M. Lacoma, "Design and higher order optimisation of final focus systems for linear colliders," Ph.D. dissertation, Universitat Politècnica de Catalunya (UPC), 2012.

[63] G. Zamudio and R. Tomas, "Optimization of the CLIC 500 GeV Final Focus system and design if a new 3 TeV Final Focus system with L*=6.0 M," CERN, Geneva, Tech. Rep., 2010. [Online]. Available: https://cds.cern.ch/record/1368480

[64] F. Plassard, A. Latina, E. Marin, R. Tomás, and P. Bambade, "Quadrupole-free detector optics design for the compact linear collider final focus system at 3 tev," *Physical Review Accelerators and Beams*, vol. 21, no. 1, p. 011002, 2018.

[65] N. van Bakel, B. Bouwens, H. Gerwig, L. Gatignon, H. van der Graaf, H. Groenstege, J. van Heijningen, J. Koopstra, H. M. Durand, R. Rosing *et al.*, "Mdi alignment progress," 2012.

[66] H. Van der Graaf, H. Groenstege, P. Rewiersma, and F. Linde, "Rasnik, an alignment system for the atlas mdt barrel muon chambers: Technical system description," 2000.

[67] J. Kemppinen, F. Lackner, and H. Mainaud Durand, "Validation of clic re-adjustment system based on eccentric cam movers: One degree of freedom mock-up," Tech. Rep., 2011.

[68] J. Kemppinen, H. M. Durand, and A. Herty, "Improving high precision cam mover's stiffness," in *Journal of Physics: Conference Series*, vol. 1350, no. 1. IOP Publishing, 2019, p. 012137.

[69] H. Yamamoto, "The international linear collider project—its physics and status," *Symmetry*, vol. 13, no. 4, p. 674, 2021.

[70] K. Buesser, "Ild machine-detector interface and experimental hall issues," *arXiv preprint arXiv:1201.5807*, 2012.

[71] B. Parker, T. Tauchi, J. Hauptman, K. Buesser, P. Burrows, T. Markiewicz, A. Seryi, A. Mikhailichenko, and M. Oriunno, "Functional requirements on the design of the detectors and the interaction region of an e+ e-linear collider with a push-pull arrangement of detectors," Tech. Rep., 2009.

[72] K. Riles, H.-J. Yang, and T. Chen, "Update on FSI R&D for SiD Final Focus Magnet Alignment," University of Michigan, Tech. Rep., September 2011. [Online]. Available: https://agenda.linearcollider.org/event/5134/contributions/21717/attachments/17797/28658/GranadaSept2011.pdf

[73] A. Lancaster, "Absolute distance interferometry capable of long-term high frequency measurements of fast targets," Ph.D. dissertation, University of Oxford, 2015.

[74] H. Yang, "Overview of the cepc project," 2021, [Online; accessed in december 2020]. [Online]. Available: https://indico.in2p3.fr/event/22887/contributions/101484/attachments/67655/94909/FCC-France-2021-CEPC-Overview-Haijun.pdf

[75] S. Bai, "Cepc mdi," 2019. [Online]. Available: https://indico.cern.ch/event/783429/contributions/3379892/attachments/1830686/2997972/CEPC_MDI_baisha_revised2.pdf

[76] K. Hashemi, "Osi bcams," https://www.opensourceinstruments.com/HBCAM/BCAM.html.

[77] H. Mainaud Durand, P. Bestmann, A. Herty, A. Marin, and V. Rude, "oWPS VERSUS cWPS," CERN, Geneva, Tech. Rep., 2012. [Online]. Available: https://cds.cern.ch/record/1483222

[78] X. He, Z. Liu, K. Huang, S. Chen, Y. Zhao, and H. Zhang, "Some experiments on a new hydrostatic levelling system developed for bepcii."

[79] H. van der Graaf, H. Groenstege, F. Linde, and P. Rewiersma, "RasNiK, an Alignment System for the ATLAS MDT Barrel Muon Chambers: Technical System Description; 2.0," NIKHEF, Amsterdam, Tech. Rep., 2000. [Online]. Available: http://cds.cern.ch/record/1073160

[80] R. van der Geer, H. van der Graaf, and M. de Jong, "A diffraction simulation for rasclic," Ph.D. dissertation, M. Sc. thesis, Nikhef and Leiden University, The Netherlands, 2008.

[81] A. Seryi, "Investigations of slow motions of the slac linac tunnel," *arXiv preprint physics/0008195*, 2000.

[82] G. Hopkinson, C. Dale, and P. Marshall, "Proton effects in charge-coupled devices," *IEEE transactions on nuclear science*, vol. 43, no. 2, pp. 614–627, 1996.

[83] G. Hopkinson, "Radiation effects on solid state imaging devices," *Radiation Physics and Chemistry*, vol. 43, no. 1-2, pp. 79–91, 1994.

[84] M. Schlösser and A. Herty, "High precision survey and alignment of large linear colliders–vertical alignment," in *Proc. of 7th Int. Workshop on Accelerator Alignment (IWAA)*. SPring-8, Japan, 2002, pp. 343–355.

[85] N. Eddy, B. Fellenz, P. Prieto, A. Semenov, D. Voy, and M. Wendt, "A wire position monitor system for the 1.3 ghz tesla-style cryomodule at the fermilab new-muon-lab accelerator," *arXiv preprint arXiv:1209.4917*, 2012.

[86] D. Giove, A. Bosotti, C. Pagani, and G. Varisco, "A wire position monitor (wpm) system to control the cold mass movements inside the ttf cryomodule," in *Proceedings of the 1997 Particle Accelerator Conference (Cat. No. 97CH36167)*, vol. 3. IEEE, 1997, pp. 3657–3659.

[87] S. Xu, P. Wang, and Q. Yao, "Analysis of tidal effects on measurement accuracy of hls," *Proceedings of IPAC2013*, pp. 2989–2991, 2013.

[88] S. Gibson, P. Coe, A. Mitra, D. Howell, and R. Nickerson, "Monitoring the heart of atlas using frequency scanning interferometry," in *Proceedings of the Eighth International Workshop on Accelerator Alignment, CERN, Geneva*. Citeseer, 2004.

[89] M. Milton, "Bureau international des poids et mesures," https://www.bipm.org/en/committees/jc/jcgm/publications, [Online; accessed in december 2020].

[90] "Gum (2008)," http://www.iso.org/sites/JCGM/GUM/JCGM100/C045315e-html/C045315e.html?csnumber=50461, [Online; accessed in december 2020].

[91] D. E. Wells and E. J. Krakiwsky, *The method of least squares*. Department of Surveying Engineering, University of New Brunswick Canada, 1971, vol. 18.

[92] Z. Chen, D. Zheng, J. Shen, J. Qiu, and Y. Liu, "Research on distributed optical-fiber monitoring of biaxial-bending structural deformations," *Measurement*, vol. 140, pp. 462–471, 2019.

[93] A. Labrousse-Ansiaux, S. Magne, S. Rougeault, L. Maurin, G. Laffont, V. Dewynter-Marty, J. Boussoir, and P. Ferdinand, "L'instrumentation à fibre optique pour les structures intelligentes," in *Annales de Chimie-Science des Matériaux*, vol. 29, no. 6, 2004, pp. 65–80.

[94] M. Warden, "Absolute distance metrology using frequency swept lasers," Ph.D. dissertation, Oxford University, UK, 2011.

[95] K. Zhang, T. Lv, D. Mo, N. Wang, R. Wang, and Y. Wu, "Double sideband frequency scanning interferometry for distance measurement in the outdoor environment," *Optics Communications*, vol. 425, pp. 176–179, 2018.

[96] D. Inaudi, "Sofo sensors for static and dynamic measurements," in *Proceedings of the 1st FIG International Symposium of Engineering Survey for Constructions and Structural Engineering*, vol. 28, 2004.

[97] H. Kikuta, K. Iwata, and R. Nagata, "Absolute distance measurement by wavelength shift interferometry with a laser diode: some systematic error sources," *Applied optics*, vol. 26, no. 9, pp. 1654–1660, 1987.

[98] M. Suematsu and M. Takeda, "Wavelength-shift interferometry for distance measurements using the fourier transform technique for fringe analysis," *Applied optics*, vol. 30, no. 28, pp. 4046–4055, 1991.

[99] M. Campbell, B. Hughes, and D. Veal, "A novel co-ordinate measurement system based on frequency scanning interferometry," 2016.

[100] J. J. Martinez, M. A. Campbell, M. S. Warden, E. Hughes, N. J. Copner, and A. Lewis, "Dual-sweep frequency scanning interferometry using four wave mixing," *IEEE Photonics Technology Letters*, vol. 27, no. 7, pp. 733–736, 2015.

[101] A. K. Ahluwaliakanwatjitsingh, "Understanding fiber connector – fc, pc, upc or apc," 2019. [Online]. Available: https://www.linkedin.com/pulse/understanding-fiber-connector-fc-pc-upc-apc-kanwarjitsingh-ahluwalia

[102] P. Lu, N. Lalam, M. Badar, B. Liu, B. T. Chorpening, M. P. Buric, and P. R. Ohodnicki, "Distributed optical fiber sensing: Review and perspective," *Applied Physics Reviews*, vol. 6, no. 4, p. 041302, 2019.

[103] H.-J. Yang, S. Nyberg, and K. Riles, "High-precision absolute distance measurement using dual-laser frequency scanned interferometry under realistic conditions," *Nuclear Instruments and Methods in Physics Research Section A: Accelerators, Spectrometers, Detectors and Associated Equipment*, vol. 575, no. 3, pp. 395–401, 2007.

[104] S. Aefsky, C. Amelung, J. Bensinger, C. Blocker, A. Dushkin, M. Gardner, K. Hashemi, E. Henry, B. Kaplan, P. Keselman *et al.*, "The optical alignment system of the atlas muon spectrometer endcaps," *Journal of Instrumentation*, vol. 3, no. 11, p. P11005, 2008.

[105] H. M. Durand, K. Artoos, M. Buzio, D. Caiazza, N. C. Lasheras, A. Cherif, I. Doytchinov, J. Fuchs, A. Gaddi, N. G. Munoz *et al.*, "Status of the pacman project." these proceedings, 2016.

Synthèse

Cette thèse s'est déroulée dans le cadre du projet de Futur Collisionneur Circulaire (Future Circular Collider) au sein de l'Organisation Européenne pour la Recherche Nucléaire (CERN). Il s'agit d'un projet de construction de collisionneur en plusieurs étapes, qui se succèderont dans un tunnel de 91 km de long situé à environs 200 m sous terre. Ce tunnel hébergera dans un premier temps un collisionneur de leptons, le FCC-ee, avant d'héberger un collisionneur d'hadrons, le FCC-hh. Ces collisionneurs sont composés d'accélérateurs, qui amènent les particules aux énergies voulues, avant de les collisionner dans les détecteurs, qui vont étudier les résultats des collisions. La zone géographique autour de ces détecteurs, englobant à la fois le détecteur et les derniers éléments de l'accélérateur, s'appelle l'interface entre la machine et le détecteur (Machine Detector Interface, MDI). La configuration des MDI des collisionneurs varie grandement selon plusieurs paramètres, notamment le type de collisionneur (linéaire ou circulaire), le type de particules accélérées (leptons, hadrons, ions lourds...), les énergies auxquelles les particules sont accélérées, la technologie disponible, la stratégie d'étude adoptée, pour n'en citer que quelques-uns.

5.5 La MDI du FCC-ee

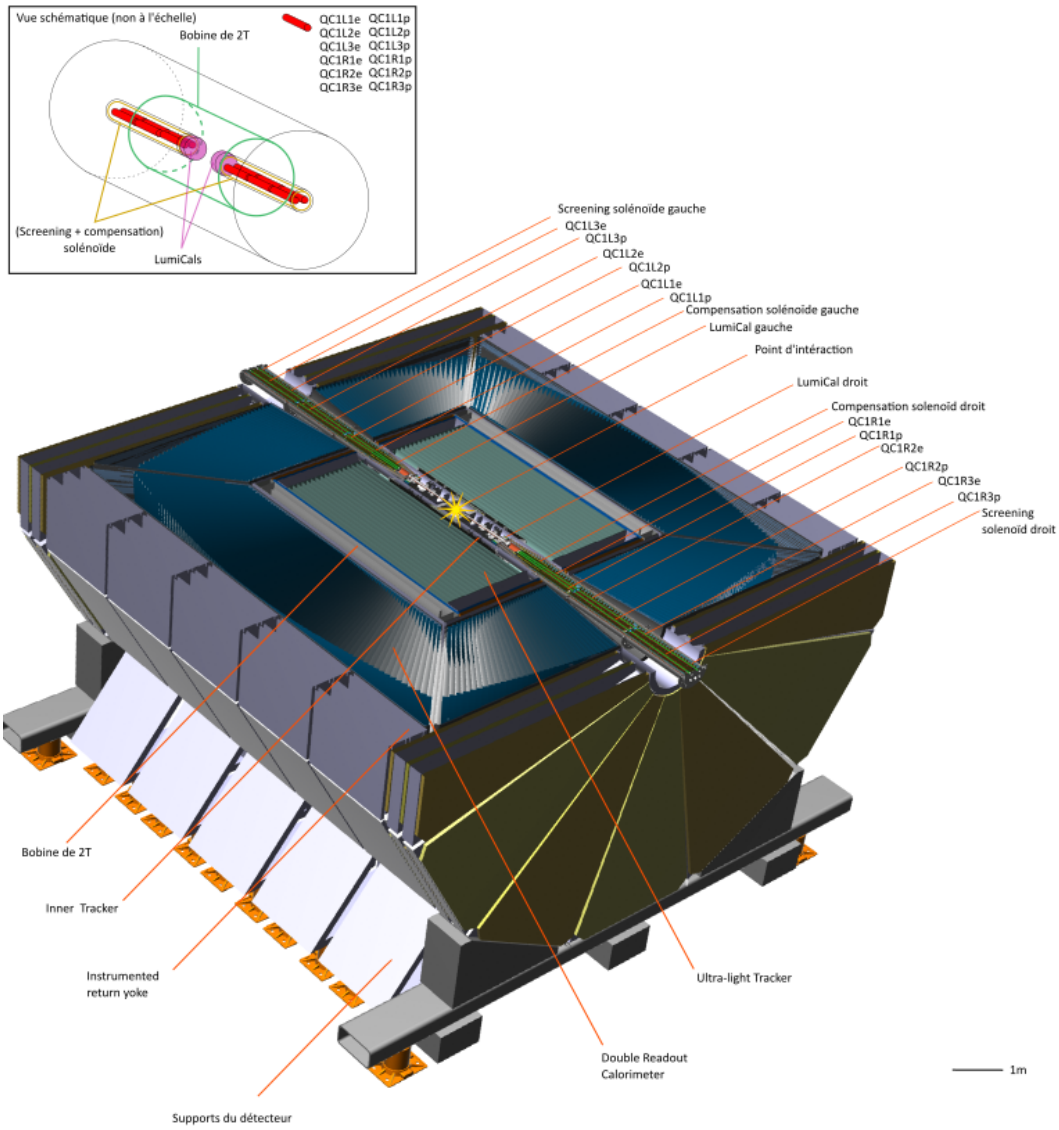

Figure 5.2: Vue 3D de la MDI du FCC-ee. Le detecteur et les derniers éléments de l'accélérateur sont représentés. Une vue schématique permet une localisation précise des différents éléments. Avec la permission accordée par le groupe de travail MDI.

La MDI du FCC-ee représentée dans la Fig.5.2, a un design particulier et complexe [2, 37, 36]. Le type de collisions ainsi que la précision recherchée pour l'alignement du détecteur impliquent d'avoir les derniers composants de l'accélérateur placés directement dans le detecteur. Ces derniers sont supportés en bras de levier depuis l'extérieur du détecteur, de manière que rien ne repose sur ce dernier.

Cette MDI, dont le modèle 3D est visible sur la Fig.5.3, comporte six quadrupôles de chaque côtés : trois d'entre eux servent à préparer l'un des deux faisceaux aux collisions tandis que les trois autres réceptionnent le faisceau après les collisions pour le réinsérer dans l'accélérateur. Ces quadrupôles cylindriques de 0.15 m de rayon et de 1 m de long, sont supportés par un squelette les enveloppant. Le tout est entouré de deux solénoïdes : le premier, cylindrique, de 3.6 m de long pour 0.25 m de rayon, le second, conique tronqué, allant d'un rayon de 0.25 m de à 0.1 m de rayon et de 0.77 m de longueur. Ces deux solénoïdes servent à protéger les faisceaux de particules accélérés du champ magnétique généré par le détecteur. L'ensemble de cet assemblage (quadrupôles, squelette, solénoïdes) est entouré d'un cryostat, pour l'isoler de l'extérieur et permettre son refroidissement à des températures cryogéniques, températures auxquelles les bobines des quadrupôles peuvent être rendues supraconductrices. Les LumiCals sont situés à l'extrémité de ces cryostats, au cœur du détecteur. Tout cet ensemble est maintenu depuis l'extérieur du détecteur en bras de levier. La présence de BPM (Beam Position Monitors, capteurs de suivi du faisceau) a été annoncée, mais leur localisation exacte n'a pas encore été clairement établie.

L'alignement de cette zone est très important pour le succès de l'opération de la machine. Il permet d'optimiser les collisions, tout en limitant les radiations dans le détecteur et ses alentours. Un alignement précis est demandé pour les solénoïdes, les quadrupôles et les LumiCals. Alors que les solénoïdes requièrent un alignement de l'ordre de 100 μm afin d'éviter des contraintes dues aux forces de Lorentz [41], les quadrupôles requièrent une précision d'alignement de 30 μm [38, 39] et les LumiCals de 50 μm [40]. Un suivi en temps réel de leur position est également demandé. Il est important de souligner la complexité de la situation et le caractère extrêmement contraignant des demandes en matière d'alignement. Aligner des composants si difficiles d'accès, installés dans des conditions extrêmes (froid cryogénique, radiations, champs magnétiques intenses) n'est pas chose facile.

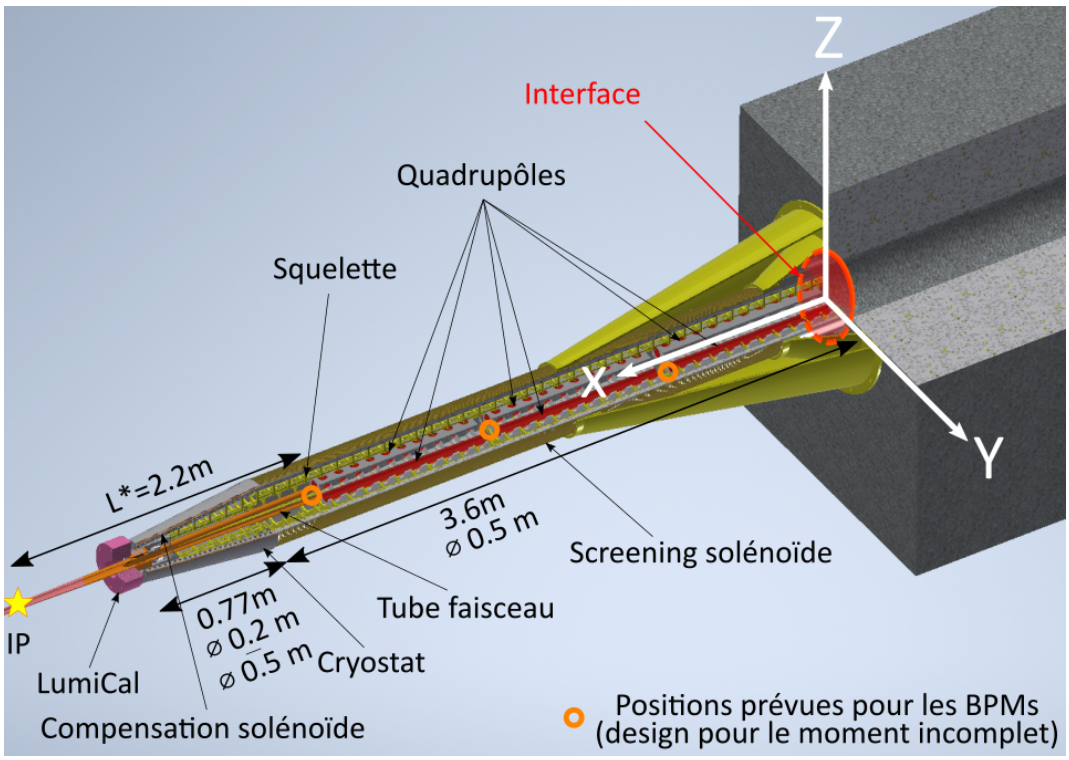

Figure 5.3: Vue 3D du cryostat, des solénoïdes, du squelette et des quadrupôles. Le repère servant pour les calculs ultérieurs a également été représenté. Les positions supposées des futurs BPM ont été indiquées.

5.6 Étude de l'existant

Plusieurs collisionneurs comportant une MDI plus ou moins similaire ont été étudiés, afin d'examiner les solutions d'alignement proposées et ainsi conclure quant à leur possible utilisation dans la MDI du FCC-ee.

Le premier collisionneur étudié fût DAFNE ou DAΦNE (Double Annular Φ Factory for Nice Experiments) [50] situé en Italie. Ce collisionneur comporte une MDI similaire à celle du FCC-ee, avec les derniers éléments de l'accélérateur positionnés dans le détecteur. Cependant, au lieu d'avoir deux assemblages supportés en bras de levier, un de chaque côté du détecteur, l'ensemble est installé sur une poutre traversant l'entièreté du détecteur. Cette poutre est utilisée non seulement pour porter des éléments de l'accélérateur, mais également pour porter des éléments du détecteur en son centre. L'alignement a été réalisé durant l'assemblage à l'aide d'un laser tracker, puis l'installation fût faite à

l'aide d'un laser tracker et de cibles positionnées sur la poutre. Cependant, ce procédé ne peut convenir pour l'alignement de la MDI du FCC, qui est trop différente et dont les précisions de positionnement attendues sont trop élevées.

Le second collisionneur étudié fût le collisionneur SuperKEKB situé au Japon [16]. Ce collisionneur comporte également une MDI similaire à celle du FCC-ee, avec les derniers éléments de l'accélérateur dans le détecteur, un assemblage comportant des quadrupôles installés au sein d'un cryostat [51] et supportés en bras de levier depuis l'extérieur du détecteur. L'assemblage de cette MDI s'est également fait au laser tracker, suivi par l'installation de points repères sur l'extérieur des cryostats. Ces points repères ont ensuite permis l'installation de l'ensemble dans le detecteur, une fois les cryostats fermés. Une fois la MDI complète, les positions des différents quadrupôles furent vérifiées à l'aide de la "Single Stretched Wire method" [1], qui consiste à tendre un fil conducteur à l'endroit où doit circuler le faisceau de particules et de le faire vibrer pour mesurer la position des aimants. Cette mesure a souligné des écarts importants entre l'alignement avant et après fermeture des cryostats, allant jusqu'à plus de 600 μm. Ce genre d'écarts seraient catastrophiques pour le FCC-ee, réduisant les performances de la machine si utilisée telle quelle, ou entrainant un retard important sur la période d'opération du collisionneur si la MDI doit être démantelée, réalignée et réassemblée.

La troisième MDI étudiée fût la MDI du detecteur ATLAS, une des MDI présentes dans le LHC (Large Hadron Collider, Grand Collisionneur de Hadrons) qui en comporte quatre dont le principe est identique. Cette MDI est très différente de celle du FCC-ee, étant donné que la limite entre accélérateur et détecteur est nette : les derniers éléments de l'accélérateur sont situés dans le tunnel, quelques mètres avant le détecteur. Ils ont donc beaucoup plus de place de disponible pour l'installation d'un système d'alignement permanent, qui est, encore actuellement, opérationnel. C'est pour ce système permanent que cette MDI a été étudiée. Les aimants, bien plus imposants que ceux de la MDI du FCC-ee (plusieurs mètres de long et plus de 10 tonnes), sont équipés d'un système de monitoring complet, permettant un suivi de leur alignement en temps réel [53]. Leur position est mesurée à l'aide de capteurs permettant une mesure d'écartométrie sur un fil tendu, tandis qu'un autre capteur permet de mesurer leur position verticale vis-à-vis d'une équipotentielle de pesanteur matérialisée par la surface d'un réseau d'eau, le Système de Nivellement Hydrostatique, (HLS). Enfin, un autre capteur vient mesurer la position

longitudinale. L'ensemble de ces capteurs est basée sur la technologie capacitive, et requiert une infrastructure conséquente pour fonctionner : les capteurs utilisés pour l'écartométrie nécessitent un fil tendu entre deux points extrêmement stables, ainsi qu'une protection autour de ce fil sur l'entièreté de la longueur, afin d'éviter les casses. Le système de mesure sur la surface d'eau nécessite un réseau d'eau situé tout autour des différents éléments à aligner. D'autres capteurs sont également ajoutés, comme notamment des inclinomètres pour la redondance des mesures. Ainsi, même si l'alignement de cette MDI est correctement connu, les systèmes utilisés sont trop imposants pour pouvoir être installés dans la MDI du FCC-ee. L'amélioration prévue pour le LHC après le prochain long arrêt de la machine, visant à le rendre encore plus performant, va implémenter de nouveaux capteurs. Ces capteurs vont permettre le suivi plus précis de la situation dans la MDI [57, 58, 14]. Cependant, ces capteurs effectuant des mesures de distances interférométriques ne permettent également pas de mesurer et de monitorer les éléments de la MDI du FCC.

Ensuite furent étudiés deux projets de collisionneurs : L'ILC (International Linear Collider, Le collisionneur Linéaire International) [5] et le CLIC (Compact Linear Collider, Collisionneur Linéaire Compact) [69]. Ces deux projets de collisionneurs sont des collisionneurs linéaires, ayant une configuration extrêmement similaire au niveau de la MDI. Les seules différences sont que dans l'ILC, il n'y a qu'un seul quadrupôle par côté du détecteur (contre 6 par côtés dans le LHC). Pour le CLIC, il n'y a également qu'un seul quadrupôle par côté et ils ne sont pas refroidis à des températures cryogéniques, ce qui ôte la nécessité du cryostat. Ces deux projets ont également des attentes en matière d'alignement bien plus contraignantes que les attentes du LHC, avec un alignement au niveau des quadrupôles demandé à 20 μm pour l'ILC et 10 μm pour le CLIC. Afin d'atteindre ces attentes, ces deux projets ont proposé des systèmes d'alignement et de suivi, mais inachevé et sans preuve de fonctionnement. Le CLIC se basait sur des barres en ZERODUR® venant en contact avec des disques fixés aux quadrupôles [65, 66]. Ces barres transféraient les déplacements du quadrupôle plus loin du centre du detecteur où seraient installés des capteurs optiques pour suivre leur extrémité. Mais, il n'y a pas de preuve que ce système fonctionne et les difficultés à surmonter pour l'implémenter sont encore nombreuses. Pour l'ILC, un réseau de mesures de distances interférométriques [72, 73] avait été proposé, mais il est encore en phase de développement et beaucoup de travail reste à accomplir pour le rendre opérationnel.

Le dernier collisionneur étudié fût le CEPC (China Electron Positron Collider, Collisionneur

d'électrons et de positrons chinois) [10]. La situation au sein de cette MDI est extrêmement similaire avec celle du FCC-ee, avec une configuration identique : même nombre de quadrupôles, même stratégie de support, même stratégie de refroidissement... Mais, le design est encore loin d'être définitif et aucune solution satisfaisante n'est proposée pour l'alignement et le suivi de cette MDI.

En parallèle, une veille technologique fût effectuée, afin d'étudier les capteurs à notre disposition pour créer un éventuel nouveau système. Cependant, les capteurs se heurtent tous à des limites lors de leur utilisation dans la MDI du FCC-ee. Comme vu précédemment, les capteurs capacitifs sont limités par la place disponible, qui n'est pas suffisante pour l'installation des infrastructures nécessaires à leur utilisation. Les capteurs optiques, basés sur les dalles CCD ou CMOS, sont très sensibles aux radiations [82, 83], qui seront très présentes au cœur de la MDI du FCC-ee[37]. Enfin, les capteurs basés sur les mesures de distances interférométriques prennent également trop de place dans leur version actuelle (notamment à cause de la ligne de visée requise) et ne conviennent pas pour une utilisation dans la MDI du FCC-ee. La liste des capteurs n'est pas exhaustive, mais l'immense majorité des technologies utilisées dans les capteurs non abordés ici ont des limites très similaires à celles des trois technologies développées (principalement place disponible et sensibilité aux radiations). Nous avons donc été conduits très rapidement dans notre travail à développer un nouveau système d'alignement, capable de fonctionner dans des conditions extrêmes tout en réalisant des mesures précises.

5.7 Proposition d'un nouveau système d'alignement

5.7.1 Stratégie

Nous avons vu que l'alignement et le suivi de l'alignement au sein de la MDI du FCC-ee sont de vrais challenges, et qu'aucun système existant ne permet de réaliser ces opérations. Il a donc fallu créer un système de toutes pièces capable de répondre à ces attentes. La demande en matière d'alignement est définie au niveau d'un côté (les quadrupôles d'un même côté doivent être correctement alignés) mais également entre les deux côtés du détecteur (les quadrupôles des deux côtés de l'expérience doivent également être alignés). La stratégie pour l'alignement de cette MDI se définit comme suit : l'alignement se fait au moment de l'assemblage à l'aide de laser tracker, photogrammétrie ou équivalent. Durant cet assemblage, un système de suivi est également installé. Ce système de suivi sera capable de mesurer les positions des éléments dans le cryostat par rapport à une interface située vers le côté

extérieur du détecteur, à l'extrémité du cryostat. Cette interface sera ensuite mesurée en continu via un deuxième système d'alignement, contournant le détecteur et permettant ainsi d'avoir une donnée sur l'alignement entre les deux côtés du détecteur. Le premier système, s'occupant de l'alignement au sein du cryostat, sera appelé "Système d'alignement interne", tandis que le deuxième système, utilisé pour faire le lien entre les deux côtés du détecteur, sera appelé "Système d'alignement externe".

5.7.2 Système d'alignement interne

La zone se situant à l'intérieur du cryostat concentre toutes les difficultés de l'alignement. Le très faible espace disponible, les radiations, le champ magnétique intense, ainsi que les demandes d'alignement très contraignantes font de cet endroit un des plus complexes à aligner. Pour faire cela, un nouveau système a été créé, basé sur une mesure interférométrique. Ce système utilise le FSI (Frequency Scanning Interferometry, Interférométrie par Balayage de Fréquence) qui est habituellement utilisé pour une mesure interférométrique de distance dans l'air. Dans notre système, le FSI est utilisé pour mesure la longueur 3D d'une fibre disposée dans la MDI. Ce système est détaillé plus en détails dans la partie 5.8. Il permet de mesurer simultanément et indépendamment plusieurs longueurs sur une même fibre, portions étant délimitées par un changement d'indice de réfraction ponctuel dans le cœur de la fibre. L'idée est ensuite de disposer des fibres composées de plusieurs portions en forme d'hélice au sein du cryostat. Leur installation se ferait sur le support du solénoïde cylindrique. Avec un nombre suffisant d'hélices et de portions par fibres, il est possible de mesurer la forme du cylindre sur lequel est installé ce réseau de fibres optiques.

Pour nos calculs, qui ont été codés en langage Python, la maquette 3D de la MDI du FCC-ee n'était pas assez mature pour faire les simulations de déformation. Nous avons donc simplifié la situation de manière à faire les simulations initiales avec ce nouveau système. Dans un premier temps, nous avons isolé le cylindre sur lequel sont disposées les fibres, puis nous avons simulé des déformations sur ce cylindre, qui est un objet relativement simple, comparé à la MDI entière. Le but étant, dans un premier temps, de fournir une preuve de faisabilité.
Les déformations sont définies dans le repère Euclidien (O, O_x, O_y, O_z), représenté dans la Fig.5.4. L'origine de ce repère étant situé au centre de l'interface placée à l'extrémité du cryostat, l'axe O_x est perpendiculaire à cette interface, O_y est l'intersection du plan de l'interface avec le plan formé par

le faisceau entrant et le faisceau sortant. Le vecteur O_z est le dernier vecteur de manière à former un repère orthonormal direct. Il est intéressant de noter que O_z n'est pas orienté dans la direction du faisceau comme dans une définition de physique, mais vers le zénith, suivant une définition plus répandue chez les géomètres.

Dans ce système, on peut exprimer les points (x,y,z) à l'aide des fonctions qui permettront la prise en compte des déformations ultérieures :

$$\begin{cases} C_X(x,y,z) = x \\ C_Y(x,y,z) = r\sin(\phi), \quad \text{with} \quad \phi = \arctan 2\,(y,z) \\ C_Z(x,y,z) = r\cos(\phi) \end{cases} \tag{5.1}$$

De ce fait, sans déformation : $C_X(x,y,z) = x$, $C_Y(x,y,z) = y$, $C_Z(x,y,z) = z$.

Comme indiqué précédemment, les déformations seront modélisées par des polynômes. Ces polynômes ont été choisis de degré 4, restant simples à manipuler tout en permettant de modéliser assez finement les déformations. Le choix d'utiliser des polynômes permet de rester versatile et de modifier les degrés des polynômes selon le niveau détail voulu et/ou le temps de calcul par exemple. Ces polynômes sont définis comme suit :

$$\begin{aligned} &\forall u \in \mathbb{R} \\ P_x(u) = \sum_{i=2}^{n} a_i u^i,\ P_y(u) = \sum_{i=1}^{n} b_i u^i,\ P_z(u) &= \sum_{i=1}^{n} c_i u^i, \\ P_\theta(u) = \sum_{i=2}^{n} d_i u^i,\ P_{ry}(u) = \sum_{i=1}^{n} e_i u^i,\ P_{rz}(u) &= \sum_{i=1}^{n} f_i u^i \end{aligned} \tag{5.2}$$

Avec $n \in \mathbb{N}$ et $\forall i \in [\![0;n]\!], \quad a_i, b_i, c_i, d_i, e_i, f_i \in \mathbb{R}$.

Chacun de ces polynômes a pour but de modéliser une déformation spécifique : P_x modélise une déformation longitudinale, P_y et P_z sont des déformations radiales, horizontale et verticale, P_θ est une déformation de torsion, et P_{ry} et P_{rz} sont des déformations de rayon, horizontale et verticale. En combinant ces différents polynômes, on peut générer une très vaste gamme de déformations, que l'on peut affiner à l'aide des degrés des polynômes. Le but étant de fournir une preuve de faisabilité en attendant que la maquette 3D soit plus mature.

En prenant en compte les polynômes, les équations des points (eq.5.1) deviennent :

$$\begin{cases} C_{Xd}(x,y,z) = x + P_x(x) \\ C_{Yd}(x,y,z) = (r + P_{ry}(x))\sin(\phi + P_\theta(x)) + P_y(x) \\ C_{Zd}(x,y,z) = (r + P_{rz}(x))\cos(\phi + P_\theta(x)) + P_z(x) \end{cases} \tag{5.3}$$

Une fois les déformations du cylindre modélisées, on peut s'attaquer à leur mesure à l'aide du réseau de fibres optiques. Ce réseau est composé de fibres optiques installées en hélices, comme représenté sur la Fig.5.4. Cette installation des fibres en hélices revêt plusieurs avantages, le plus important étant une exposition réduite aux déformations, notamment longitudinales, comparé à une installation rectiligne. En effet, lors du refroidissement, la longueur du cryostat (et donc des fibres placées sur le cylindre à l'intérieur) seront grandement impactées. Ainsi, la durée de vie de la fibre est optimisée, les déformations n'ayant qu'un impact partiel sur cette dernière. Malgré un impact seulement partiel, ces fibres peuvent mesurer les déformations, et cette disposition en hélice permet à une fibre de mesurer toutes les déformations à la fois. C'est à double tranchant : d'un côté, il faut assez de fibres pour mesurer, mais aussi dissocier ces déformations, néanmoins cela procure une redondance très importante sur les mesures dans le système.

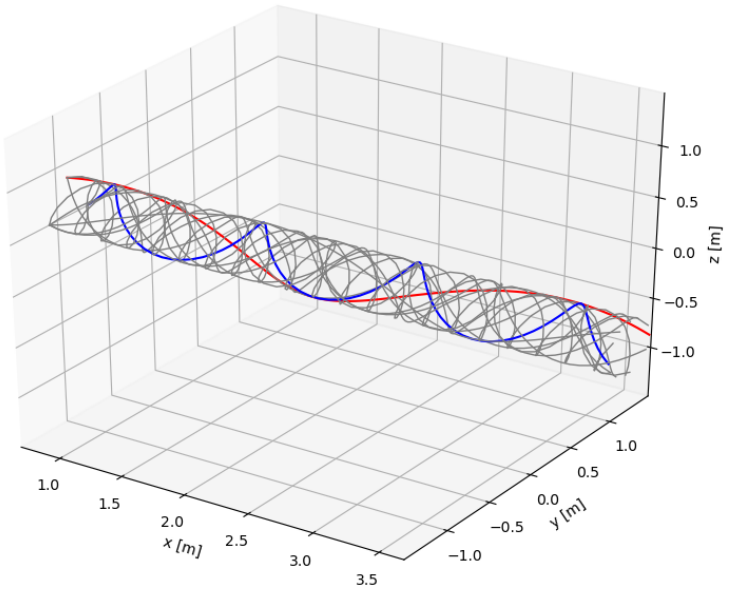

Figure 5.4: Visualisation d'un réseau de fibres installé sur le cylindre. Deux fibres ont été surlignées, la rouge ayant un pas important, tandis que la bleue possède un pas plus faible.

L'équation d'une hélice placée à la surface du cylindre est :

$$\begin{cases} h_x(x) = x \\ h_y(x) = \varepsilon r \sin\left(\dfrac{x}{p} + \alpha\right) \\ h_z(x) = r\cos\left(\dfrac{x}{p} + \alpha\right) \end{cases} \tag{5.4}$$

Avec ε correspondant à ± 1 qui défini si l'hélice est dextre ou senestre, r correspond au rayon de l'hélice, p correspond au pas et α correspond à l'angle dans le plan (O, O_y, O_z) duquel l'hélice démarre.

En intégrant les polynômes à l'équation précédente, on obtient :

$$\begin{cases} h_{x_d}(x) = x + P_x(x) \\ h_{y_d}(x) = \varepsilon(r + P_{ry}(x)) \sin\left(\dfrac{x}{p} + \alpha + \varepsilon P_\theta(x)\right) + P_y(x) \\ h_{z_d}(x) = (r + P_{rz}(x)) \cos\left(\dfrac{x}{p} + \alpha + \varepsilon P_\theta(x)\right) + P_z(x) \end{cases} \tag{5.5}$$

Cette implémentation des déformations dans l'équation de l'hélice n'est pas parfaite. La déformation longitudinale impliquée par la déformation radiale n'est pas prise en compte dans ces calculs. Cependant, il s'agit d'un impact très léger qu'il a été choisi de négliger dans cette étude de faisabilité. Ce choix est également justifié par les très faibles déformations attendues pour la MDI du FCC-ee. Une des raisons est que la déformation maximale de l'ensemble sera limitée à 2 mm à l'extrémité du cylindre, car au-delà le cryostat entrera en contact avec le détecteur, occasionnant de lourds dégâts et nécessitant d'importantes réparations.

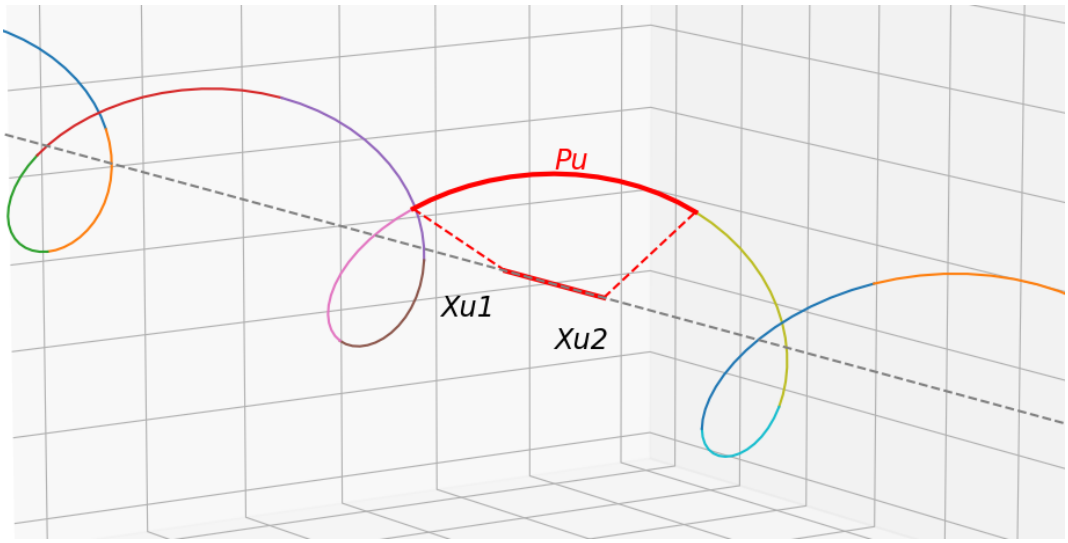

Figure 5.5: Représentation d'une portion de fibre p_u entre deux interfaces semi-réfléchissantes d'une fibre, entre les abscisses x_{u1} et x_{u2}.

La Fig.5.5 illustre une portion de fibre installée en hélice. L'idée est de mesurer les longueurs de ces portions afin de remonter aux déformations. La longueur de cette portion peut être exprimée comme

suit :

$$d(p_u) = \int_{x_{u1}}^{x_{u2}} \sqrt{\dot{h_{xd}}(x)^2 + \dot{h_{yd}}(x)^2 + \dot{h_{zd}}(x)^2}\,\mathrm{d}x \tag{5.6}$$

Dans cette équation, la notation $\dot{f}(x)$ correspond à la dérivée de f par rapport à la variable x. Cette équation lie la longueur d'une portion de fibre aux coefficients des polynômes de déformation. Ainsi, en ayant assez de mesures de longueurs de portions, il est possible de remonter aux polynômes de déformations grâce à un calcul d'ajustement par moindres carrés. Après avoir automatisé la génération de coefficients de polynômes n'impliquant pas une déformation du cylindre supérieure à 2 mm, puis généré les longueurs des portions de fibres grâces à ces coefficients, nous avons réalisé un calcul d'ajustement par moindres carrés. Ce calcul nous permet de remonter aux coefficients des polynômes à partir des mesures de distance des portions. Les incertitudes résultantes de ce calcul d'ajustement sont cependant exprimées sur les coefficients des polynômes. Un calcul de propagation de variance fut appliqué aux incertitudes a posteriori sur les coefficients afin de déterminer l'incertitude sur des points à la surface du cylindre.

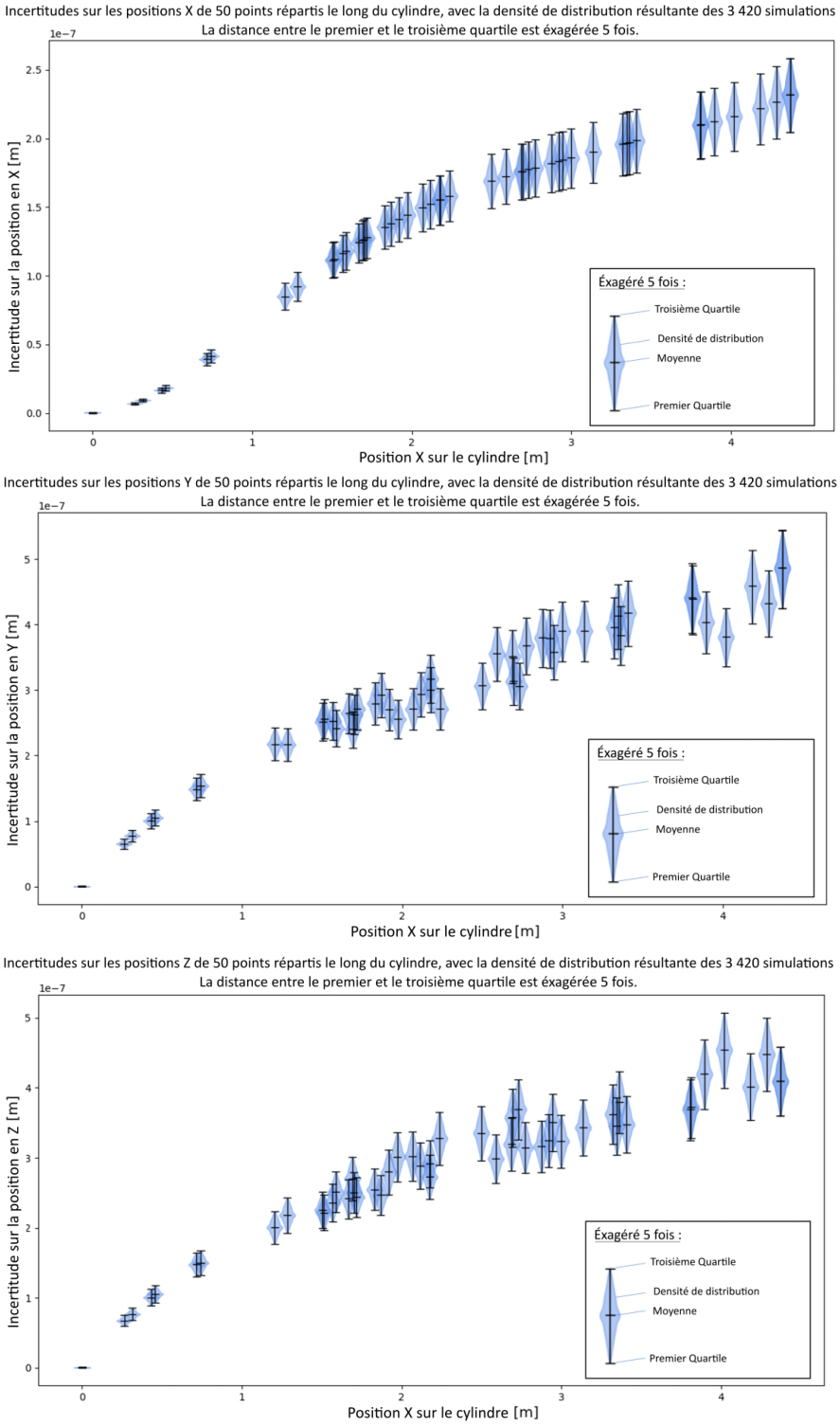

Figure 5.6: Incertitudes sur les coordonnées de 50 points répartis sur la longueur du cylindre, avec la représentation de la densité de distribution des 3 420 simulations réalisées. La représentation de ces distributions est exagérée 5 fois.

Les résultats sont représentés sur la Fig.5.6, sur laquelle sont représentées les incertitudes sur les coordonnées de 50 points répartis à la surface du cylindre. La densité de distribution résultante du calcul de 3 420 jeux de données différentes est aussi représentée. On peut observer la moyenne, le premier et le troisième quartile ainsi que la densité de distribution pour chacun de ces points. On peut observer que les incertitudes se dégradent en se déplaçant vers l'extrémité du cylindre. Ces valeurs ont été triées selon leur abscisse, ce qui explique le caractère continu du graphe des incertitudes sur le paramètre x. Les incertitudes sur les coordonnées y et z dépendent de leurs coordonnées y et z ce qui explique l'absence de continuité de leur graphique. Pour tous les axes, l'écart entre le premier et le troisième quartile augmente en avançant le long du cylindre. Les densités de distributions sont symétriques autour de la moyenne, où se situe le maximum.

Il s'agit de résultats extrêmement prometteurs, qu'il faudra confirmer au fur et à mesure du développement de la maquette 3D.

Le modèle fut ensuite complété de manière à le rendre plus réaliste. La première amélioration consiste en le remplacement d'une fibre comportant 100 portions par 10 fibres côte à côte comportant chacune 10 portions, mais délimitées à des abscisses différentes. Ce remplacement est justifié par le fait qu'actuellement, il est impossible de savoir si le capteur sera capable de mesurer 100 portions sur une seule fibre, tandis que 10 portions par fibres sont bien plus réalistes et réalisables [13].

La deuxième implémentation fût un croisement des fibres plus réaliste au niveau des intersections dans le réseau. Dans le modèle initial, les fibres se croisent dans le même plan, ce qui est impossible en réalité. Un changement de rayon progressif de la fibre autour de l'intersection permet un passage au-dessus de l'autre fibre. Ce croisement plus réaliste, ou plus précisément la modification des équations que cela impliquait, fût ajouté au modèle.

Le troisième développement fût la définition d'hélices à pas variable, permettant une mesure complémentaire et permettant de densifier les mesures à certains endroits voulus (zones où sont attendues de fortes déformations par exemple) tout en évitant d'augmenter le nombre de fibres.

Des simulations d'erreurs ont également été réalisées, principalement des erreurs d'installation des fibres. La première erreur modélisée est une erreur ponctuelle, où le pas d'une hélice est modifié ponctuellement et revient à son pas normal (après un contrôle de la machine servant à l'installation par exemple). La deuxième erreur modélisée est un changement de pas de l'hélice, mais qui se répercute sur le reste de l'hélice, résultant en un écart entre la position réelle et théorique. Dans ces deux

cas, la redondance du réseau d'hélice permet d'identifier instantanément les fibres ou portions de fibre où se situent les erreurs et de les retirer du calcul.
Les prochaines étapes sont la réalisation d'un prototype afin de réaliser des tests sur de vraies déformations, un affinement du modèle de croisement entre les fibres (qui peut être encore amélioré), une optimisation du programme python et une optimisation du réseau d'hélices.

5.7.3 Système d'alignement externe

Une fois les déformations du cylindre connues, le système d'alignement externe permet le suivi des interfaces aux extrémités des cryostats, à l'aide d'un dense réseau de mesures de distances interférométriques. Ce réseau permet de lier les données d'alignement d'un côté du detecteur à l'autre côté. Ces mesures seront faites à l'aide du système FSI. Le réseau sera assez dense pour permettre à chacun de ses points d'être déterminé grâce aux points voisins, évitant ainsi de devoir effectuer des campagnes de mesures pour déterminer régulièrement les différents points du réseau. Les 16 points de référence de ce réseau sont définis aux pieds du détecteur, faciles d'accès et stables. La densité du réseau permet une bonne redondance et permettra d'atteindre les demandes en matière de précision d'alignement. Cette densité de réseau est permise par la capacité du FSI à mesurer plusieurs cibles en même temps. La résolution de ce réseau se fait à l'aide d'un calcul d'ajustement par moindres carrés basé sur l'équation de distance 3D entre les points ainsi que l'incertitude a priori sur les points du réseau (déterminées lors de leur installation). Cette partie du calcul est traitée par le Logiciel Général de Compensation (LGC++) développé au CERN et actuellement utilisé pour l'alignement des différentes machines.

5.7.4 Système d'alignement complet

Le calcul d'alignement complet prend en compte les deux sous systèmes précédents, complétés par quelques mesures de distances depuis le cylindre déformé vers les éléments qu'il renferme (notamment les quadrupôles, mais ultérieurement s'ajouteront les BPMs). Il est important de souligner que ces simulations sont faites à partir d'un modèle extrêmement simplifié qu'est la situation actuelle de la maquette 3D.

Le calcul se fait donc en partie sur LGC++ (calculs du système d'alignement externe) dont les matrices de covariances sont extraites afin de les injecter dans un programme python, qui s'occupe du

reste du calcul. Le système d'alignement complet est donc composé du système d'alignement externe, comme représenté sur la Fig.5.7, du réseau de fibres optiques placé dans le cryostat et de mesures de distances depuis le système de mesures de déformation, représenté sur la Fig.5.8. Ces systèmes servent à mesurer les translations et rotations entre les repères des différents éléments au sein de la MDI, comme représenté sur la Fig.5.9.

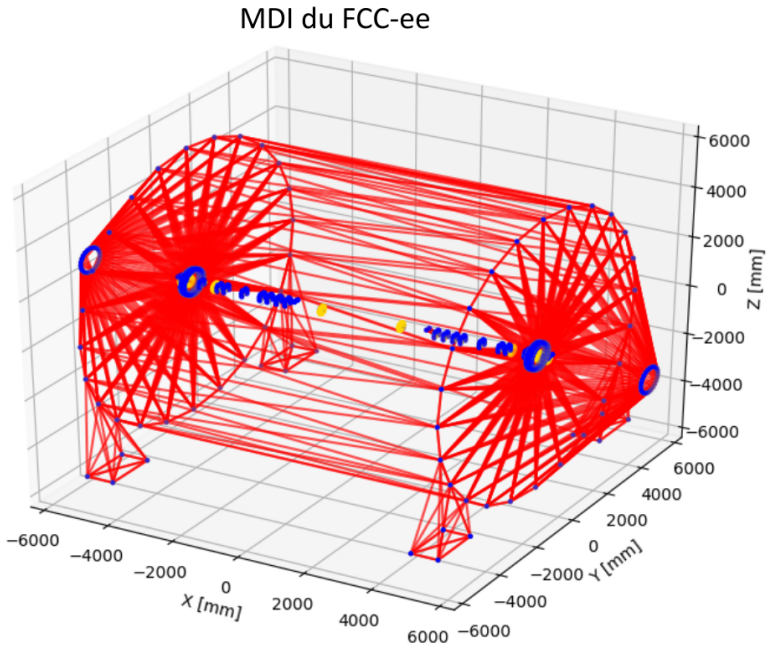

Figure 5.7: Représentation du système d'alignement externe, composé d'un réseau de mesures de distances interférométriques. Ces mesures de distances (en rouge) relient les points de référence (en bleu) et les objets mesurés (en jaune).

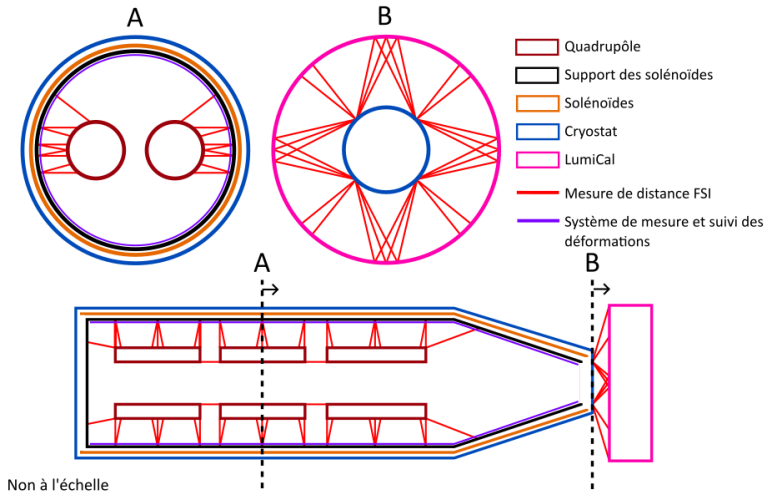

Figure 5.8: Représentation des mesures de distances faites dans le cryostat.

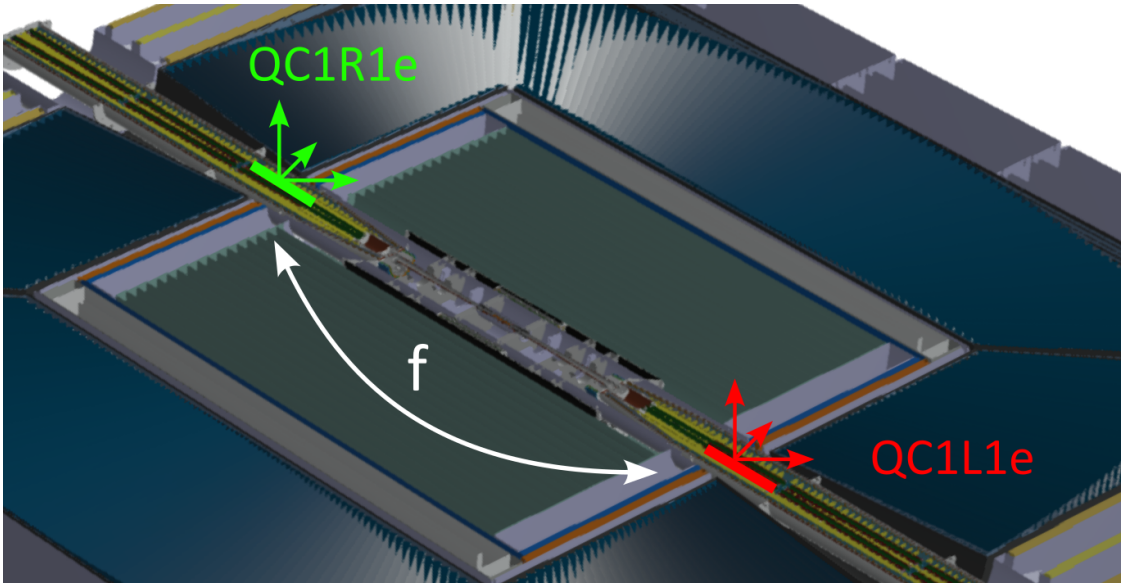

Figure 5.9: Systèmes de coordonnées de deux quadrupôles, séparés par une similitude spatiale f. Les paramètres de cette fonction (trois translations et trois rotations), ainsi que leurs incertitudes, sont mesurés par notre système d'alignement.

Les résultats du calcul complet sont représentés dans les tableaux 5.1. Ces tableaux ont été obtenus à partir de plusieurs hypothèses sur l'incertitude de définition des points du réseau externe (soit l'incertitude à laquelle ils ont été mesurés après installation). Le premier tableau (en haut à gauche) suppose une détermination de ces points à 10 μm, un autre (en haut à droite) à 100 μm et le

dernier (en bas) se base sur le calcul des points grâce aux autres points du réseau. Ces trois scénarios ont pour but de couvrir une large plage de possibilités : tandis que les 100 μm correspondent à ce qui est possible actuellement, les 10 μ tendent à correspondre à ce qui sera sans doute possible lors de la réalisation du FCC. La situation de résolution totale du système dans le calcul peut arriver en cas de perte de données, la pire situation possible.
Pour la configuration à 10 μm, les incertitudes sont inférieures à 20 μm pour les translations et 20 μrad pour les rotations entre deux quadrupôles. Ces incertitudes montent à 50 μm et 45 μrad pour les rotations et les translations entre les LumiCals.

Pour la configuration à 100 μm, les incertitudes sont inférieures à 110 μm pour les translations et 25 μrad pour les rotations entre deux quadrupôles. Ces incertitudes montent à 110 μm et 45 μrad pour les rotations et les translations entre les LumiCals.

Pour la configuration sans précisions attribuées, les incertitudes sont inférieures à 200 μm pour les translations et 35 μrad pour les rotations entre deux quadrupôles. Ces incertitudes montent à 200 μm et 55 μrad pour les rotations et les translations entre les LumiCals.
Les différents écarts d'incertitudes entre les translations ou les rotations d'une même configuration sont dues à la géométrie du réseau, qui n'est pas symétrique selon les axes Y et Z. Pour ce qui est des incertitudes, seules celles issues du calcul à 10 μm sont satisfaisantes vis-à-vis des attentes. Même si une installation des points à ces précisions semble difficile, le réseau peut être mesuré une fois installé. Il est aussi intéressant de remarquer que les incertitudes du réseau peuvent être actualisées à chaque calcul d'ajustement du réseau grâce aux incertitudes a postériori sur ces points ajustés.

10 microns						
LumiCal_l	θx [µrad]	θy [µrad]	θz [µrad]	Tx [µm]	Ty [µm]	Tz [µm]
LumiCal_r	11.4	37.2	41.3	19.8	52.9	50.2

10 microns						
QC1_l1e	θx [µrad]	θy [µrad]	θz [µrad]	Tx [µm]	Ty [µm]	Tz [µm]
QC1_r1e	14.2	5.2	5.1	12.9	18.0	18.7
QC1_r1p	14.4	5.2	5.2	13.1	17.9	18.5
QC1_r2e	17.2	4.5	4.5	14.1	17.3	17.8
QC1_r2p	18.2	4.6	4.6	15.0	17.8	18.1
QC1_r3e	20.6	4.6	4.8	16.8	20.3	19.3
QC1_r3p	19.4	4.6	5.0	18.9	22.1	19.9
QC1_l2e	17.4	3.8	3.2	18.8	12.1	11.6
QC1_l3e	20.7	3.8	4.1	15.8	15.0	13.6
QC1_l1p	14.2	4.5	4.4	12.9	11.4	12.3
QC1_l2p	18.2	3.8	3.8	15.0	11.2	11.8
QC1_l3p	18.9	3.7	4.2	18.4	16.4	13.7

10 microns						
QC1_l1p	θx [µrad]	θy [µrad]	θz [µrad]	Tx [µm]	Ty [µm]	Tz [µm]
QC1_r1p	14.7	5.3	5.3	13.3	18.2	18.8
QC1_r2p	18.5	4.7	4.8	15.3	18.2	18.5
QC1_r3p	19.7	4.8	5.2	19.1	22.2	20.1
QC1_l2p	17.8	3.9	3.5	19.3	12.8	11.9
QC1_l3p	19.6	3.9	4.5	17.9	17.0	14.4

(a)

100 microns						
LumiCal_l	θx [µrad]	θy [µrad]	θz [µrad]	Tx [µm]	Ty [µm]	Tz [µm]
LumiCal_r	11.8	42.6	46.3	22.0	112.6	111.6

100 microns						
QC1_l1e	θx [µrad]	θy [µrad]	θz [µrad]	Tx [µm]	Ty [µm]	Tz [µm]
QC1_r1e	14.3	19.6	19.5	15.5	101.9	102.4
QC1_r1p	14.4	19.4	19.4	15.5	101.0	101.5
QC1_r2e	17.3	19.2	19.2	16.5	100.7	101.1
QC1_r2p	18.2	19.3	19.2	17.1	101.1	101.5
QC1_r3e	20.7	19.4	19.4	18.8	102.3	102.4
QC1_r3p	19.9	19.4	19.5	21.1	102.5	102.4
QC1_l2e	17.2	3.7	3.2	18.6	12.0	11.5
QC1_l3e	20.8	3.8	4.1	15.9	15.0	13.6
QC1_l1p	14.6	4.6	4.5	13.2	11.7	12.6
QC1_l2p	17.9	3.7	3.8	14.8	11.1	11.6
QC1_l3p	19.1	3.8	4.3	18.6	16.7	13.9

100 microns						
QC1_l1p	θx [µrad]	θy [µrad]	θz [µrad]	Tx [µm]	Ty [µm]	Tz [µm]
QC1_r1p	15.3	19.8	19.8	16.2	103.0	103.4
QC1_r2p	17.9	19.0	19.0	16.9	99.8	100.2
QC1_r3p	18.9	18.9	18.9	20.1	99.6	99.5
QC1_l2p	18.2	3.9	3.6	19.7	13.0	12.1
QC1_l3p	19.4	3.9	4.5	17.7	16.8	14.3

(b)

Free						
LumiCal_l	θx [µrad]	θy [µrad]	θz [µrad]	Tx [µm]	Ty [µm]	Tz [µm]
LumiCal_r	11.8	51.8	54.9	32.8	191.6	191.9

Free						
QC1_l1e	θx [µrad]	θy [µrad]	θz [µrad]	Tx [µm]	Ty [µm]	Tz [µm]
QC1_r1e	14.2	35.0	34.9	28.7	184.7	185.9
QC1_r1p	14.5	35.0	34.9	28.8	184.5	185.7
QC1_r2e	17.6	34.8	34.7	29.4	184.3	185.4
QC1_r2p	17.9	34.9	34.8	29.6	184.5	185.6
QC1_r3e	20.7	34.9	34.8	30.6	184.8	185.8
QC1_r3p	19.4	34.9	34.8	31.8	185.0	185.8
QC1_l2e	17.2	3.8	3.2	18.6	12.0	11.5
QC1_l3e	20.9	3.8	4.1	15.9	15.1	13.7
QC1_l1p	14.8	4.7	4.6	13.4	11.9	12.8
QC1_l2p	18.4	3.8	3.9	15.1	11.4	11.9
QC1_l3p	19.2	3.8	4.3	18.7	16.8	14.0

Free						
QC1_l1p	θx [µrad]	θy [µrad]	θz [µrad]	Tx [µm]	Ty [µm]	Tz [µm]
QC1_r1p	15.1	35.0	34.9	29.0	184.5	185.7
QC1_r2p	17.8	34.9	34.8	29.6	184.3	185.4
QC1_r3p	19.1	35.0	34.9	31.7	185.2	186.1
QC1_l2p	18.4	4.0	3.6	19.9	13.2	12.3
QC1_l3p	18.9	3.8	4.4	17.3	16.4	13.9

(c)

Table 5.1: Tableau contenant les résultats des simulations du système d'alignement complet, comprenant incertitudes sur les translations et rotations entre les repères des différents objets au sein de la MDI. Chacun de ces tableaux correspond à un calcul avec une incertitude associée à la définition des points du réseau externe. Il y a donc un tableau où les points du réseau externe sont supposés connus à 10 μm, un autre à 100 μm et le dernier où les points ne sont pas connus et le réseau les détermine lors du calcul.

Ces résultats sont extrêmement préliminaires et leur objectif est principalement de prouver la faisabilité du calcul. Beaucoup de choses seront à actualiser au fur et à mesure des avancées du design ainsi que les incertitudes sur les points mesurés (en fonction des avancées de la technologie).

5.8 Présentation du nouveau système de mesure

Le capteur utilisé pour mesurer dans les fibres optiques (dans le système d'alignement interne), peut reposer sur deux technologies : SOFO (Surveillance d'Ouvrages par Fibres Optiques) [12, 96, 13] ou FSI[14, 97, 98, 99, 100]. La mesure du système SOFO de plusieurs portions d'une même fibre fût proposée [13], mais ne quitta jamais le stade de prototype. Le FSI fait quant à lui toujours l'objet de recherches actives au CERN. Nous nous sommes donc penchés sur cette deuxième technologie. C'est une technologie basée sur un interféromètre de Michelson, les deux bras étant des changements d'indice de réfraction de la fibre (mesure dans la fibre) où, un bras étant l'extrémité de la férule, l'autre est le retour du rétro réflecteur (mesure dans l'air). Le laser à fréquence constante est quant à lui remplacé par un laser à balayage de fréquences, permettant une mesure de distance absolue.

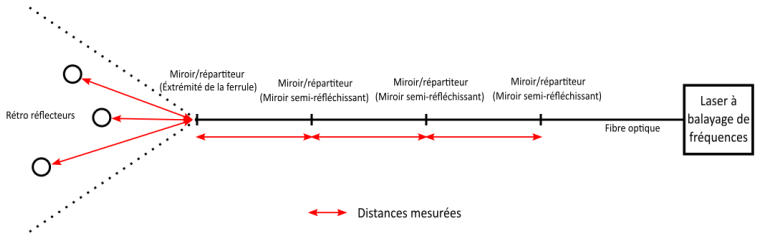

Figure 5.10: Représentation des mesures possibles par le système FSI : plusieurs mesures le long de la fibre suivies de multiples mesures sur rétro réflecteurs dans l'air.

Bien que la théorie fût connue, cette nouvelle utilisation du FSI (pour mesurer dans les fibres) nécessitait des tests approfondis afin de mieux quantifier ses capacités. Un banc, visible sur la Fig.5.11, fût créé pour l'étudier. Une fibre de trois portions a été testée sur ce banc avec, pour chaque portion, un point solidement fixé sur une barre et l'autre fixé sur une vis micrométrique. Grâce à ces vis, il était possible de changer les longueurs des portions qui étaient en parallèle contrôlées par des mesures interférométriques.

La campagne de mesure est représentée dans la Fig.5.11, le but était de prouver l'indépendance

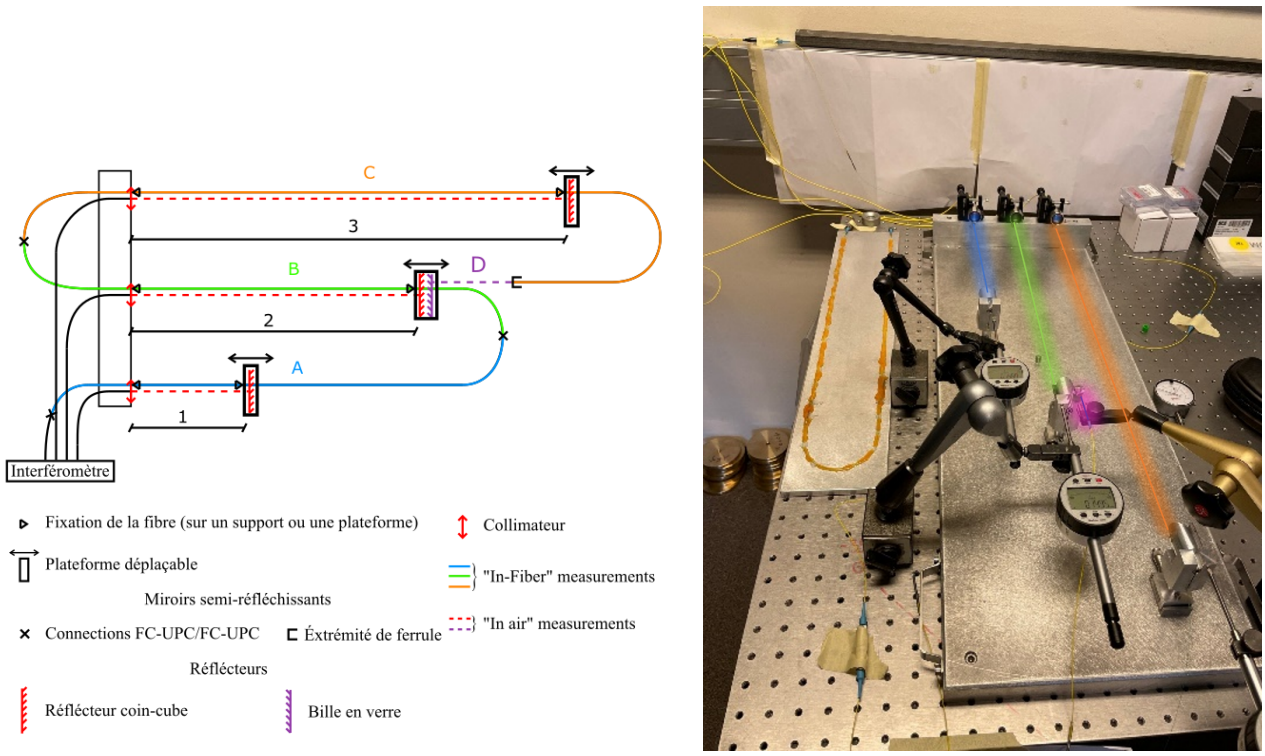

Figure 5.11: Image de gauche : schéma des différentes mesures réalisées par le banc. Une fibre optique découpée en trois portions (bleue, verte et orange) est testée à l'aide de plateformes à translation micrométrique. Les portions sont délimitées par la jonction de deux connecteurs de fibres optiques. Trois portions sont étudiées ainsi qu'une mesure dans l'air à l'extrémité de la fibre. Image de droite : photo du banc réalisé avec les portions de fibre surlignées.

des mesures et faire une première estimation de la précision du système. Les changements d'indice de réfraction sont matérialisés par des connecteurs entre lesquels une fine couche d'air joue le rôle de changement d'indice.

Les résultats sont représentés dans la Fig.5.13 dans lesquels on peut voir qu'en effet les mesures sont bien indépendantes. L'incertitude de mesure est autour de 30 μm tandis que la répétabilité est de l'ordre de 10 μm. Cette incertitude est principalement due à un facteur d'échelle qui s'explique par un réglage du FSI, paramétré pour faire une mesure dans l'air et non une mesure dans le verre. Bien qu'encore loin des attentes en matière de précision, ce test a permis de valider le système de mesure. Des études sont en cours pour améliorer ces mesures, la principale étant le développement d'un nouveau type de changement d'indice de réfraction du cœur de la fibre. Actuellement des connecteurs de fibre optique sont utilisés, mais ils sont trop imposants et impliquent une perte de répétabilité (sur le

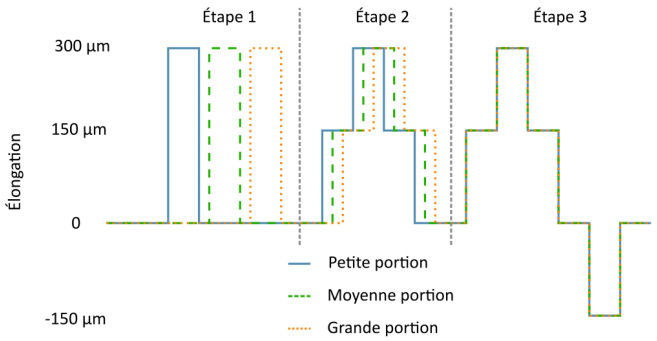

Figure 5.12: Planification des différents tests à réaliser : dans un premier temps modification d'une longueur de fibre à la fois, puis progressivement plusieurs en même temps pour finir sur une modification simultanée de toutes les portions.

couple de serrage entre les connecteurs notamment). Une nouvelle technique est étudiée, qui consiste à imprimer grâce à un laser UV un miroir semi-réfléchissant directement dans la fibre. Les premiers tests ont été réalisés et sont extrêmement prometteurs. L'échantillon reçu, visible sur la Fig.5.14, implique un bruit de seulement 2 μm ce qui serait bien plus proche des attentes en termes de précision.

5.9 Discussion

Il est intéressant de souligner la versatilité du système de suivi des déformations, qui utilise les fibres en hélices. Ce système peut être utilisé à plusieurs endroits de la MDI du FCC-ee : dans le cryostat (comme étudié actuellement), mais aussi à la surface extérieure du cryostat ou sur l'intérieur du détecteur. Il pourrait être également utilisé plus loin dans la machine. On peut aussi imaginer une utilisation directement sur les murs du tunnel, pour suivre sa forme générale au cours du temps. Enfin, il pourrait être utilisé hors du CERN, pour mesurer des structures et autres bâtiments comme des ponts ou des tours.

Une réflexion est également proposée pour la création d'un lien entre le système d'alignement de la MDI (décrit tout au long de cette thèse) et les systèmes d'alignements, pour le moment indépendants [88, 104], des sous détecteurs. Il serait intéressant de connaitre et de suivre la position de ces ensembles, données qui sont souvent perdues après la fermeture du detecteur et les mouvements impliqués par cette opération. La solution serait de prévoir une série de mesures entre les systèmes utilisés par les sous-détecteurs et les systèmes d'alignement de la MDI. Le système d'alignement de la MDI resterait une base, capable de fonctionner indépendamment, et les sous-systèmes auraient le choix de lier leurs

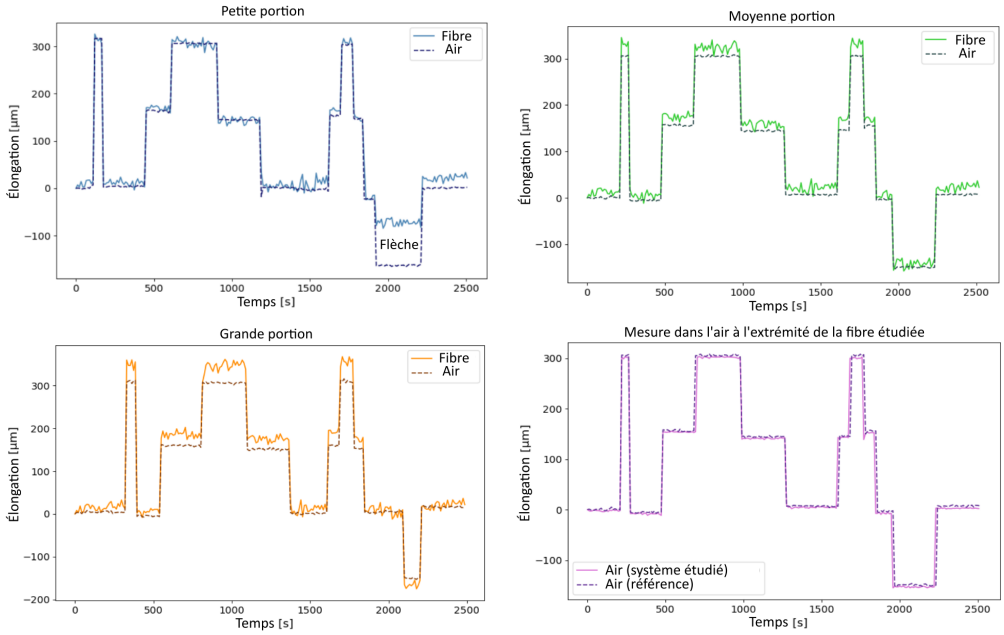

Figure 5.13: Premiers résultats des mesures dans la fibre. Toutes les portions furent testées, de haut en bas : petite portion, moyenne portion, grande portion et mesure dans l'air. La petite portion fût sujette à une chaine lorsque la distance fût trop diminuée, ce qui eu pour effet d'avoir une distance dans l'air qui a diminué, tandis que la distance dans la fibre est restée la même.

mesures ou non. Cela serait bénéfique pour les deux côtés, étant donné que du côté détecteur, ils gagnent le suivi en direct de la position de leur sous-detecteur vis-à-vis de l'accélérateur, du point d'interaction (où se déroulent les collisions) et des autres sous-détecteurs, permettant une initialisation réduite et une prise de données plus rapide, tandis que de l'autre côté, cela permettrait de consolider le système d'alignement de la MDI, proposant un complément de mesures, ainsi qu'une meilleure géométrie.

Une reflexion est également proposée sur l'implémentation d'un éventuel système de réajustement, qui permettrait de déplacer à distance certains éléments sans avoir à démonter la MDI pour accéder à ces composants. Le design d'un tel système est extrêmement difficile compte tenu des conditions qui règnent au sein de la MDI. Cependant, un tel système se révèlerait extrêmement pratique en cas de mauvaise installation ou de déplacement non prévu, évitant un coûteux et long démantèlement de la MDI pour corriger l'erreur.

Enfin, la dernière reflexion fut faite sur le système d'alignement s'occupant du reste de la MDI, pour la section avant et après le détecteur. Pour cette section, l'espace présent [2] permet l'utilisation de

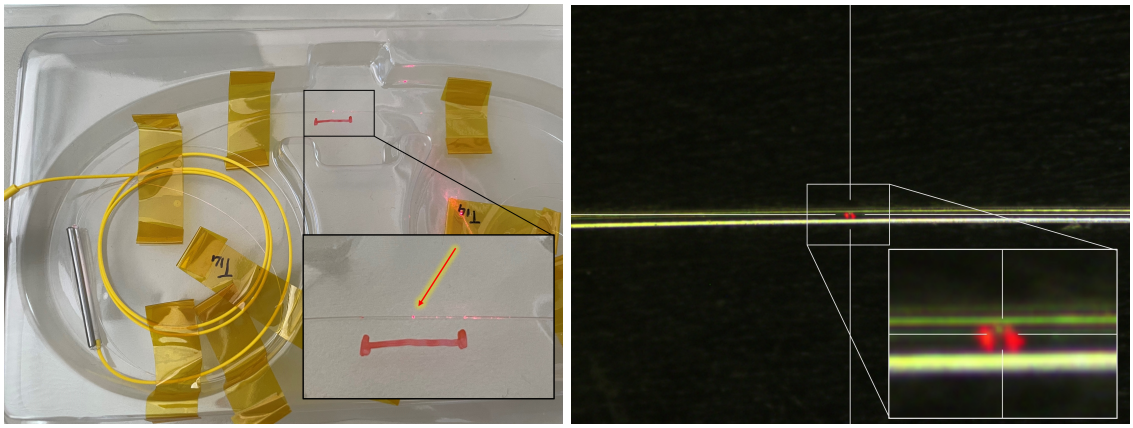

Figure 5.14: Image de gauche : photo avec le miroir semi-réfléchissant mis en valeur par un laser passant dans la fibre. Photo de droite : image faite au microscope du miroir semi-réfléchissant.

systèmes plus classiques, comme ceux utilisés dans le LHC. Des études devront être réalisées afin d'estimer si ces systèmes suffiront à répondre à la demande en matière d'alignement. En cas de besoin, l'expérience acquise lors des études réalisées pour le CLIC (cf. PACMAN project) pourrait être appliquée.

Appendices

Appendix A

Approximation of the deformations: impact of radial deformations on longitudinal deformation

In the simulations, radial deformations do not have an impact on the longitudinal deformation, even though they could. Deformations are very small, and those secondary effects have been simplified. But in reality, the y deformation implies a deformation on the x-axis. Our computation is simplified to gain computing time and simplicity. Though, here is a path to be even closer to reality. Fig.A.1 shows the geometry for a better model of the deformation.

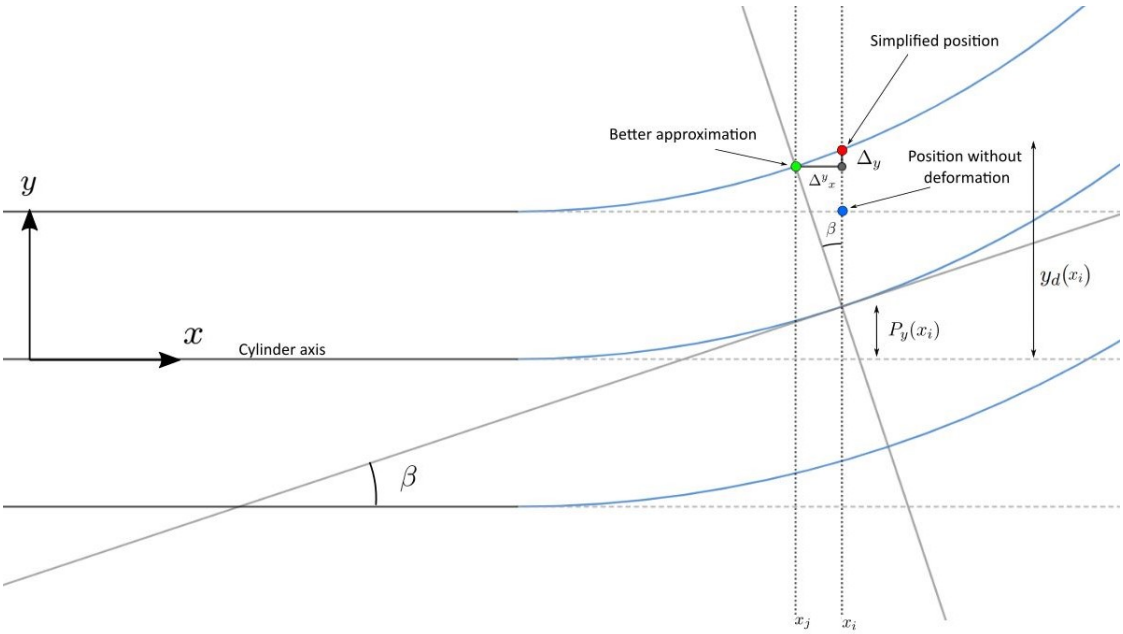

Figure A.1: Impact of the radial deformation on the longitudinal deformation. Simplification done is also represented.

For a set of deformations applied to helices :

$$\begin{cases} h_{x_d}(x) = x + P_x(x) \\ h_{y_d}(x) = \varepsilon(r + P_{ry}(x)) \sin\left(\dfrac{x}{p} + \alpha + \varepsilon P_\theta(x)\right) + P_y(x) \\ h_{z_d}(x) = (r + P_{rz}(x)) \cos\left(\dfrac{x}{p} + \alpha + \varepsilon P_\theta(x)\right) + P_z(x) \end{cases} \tag{A.1}$$

Additional $\Delta^y{}_x, \Delta^z{}_x, \Delta_y$ and Δ_z need to be added to these equations. When a point at x_i is deformed by a radial deformation, the abscissa is not x_i anymore and became x_j. First we need to find x_j defined as:

$$x_j \quad \text{such that} \quad \int_0^{x_j} \sqrt{1 + \frac{\mathrm{d}P_y(t)}{\mathrm{d}t}^2}\, \mathrm{d}t = x_i \tag{A.2}$$

Which gives us the $\Delta^y{}_x$. The process to get $\Delta^z{}_x$ is the same. Now to get the Δ_y we need to compute β, thanks to the slope of the projection of the tangent of h_{y_d} in the plane, as shown in the Fig.A.1:

$$\beta = \arccos\left(\frac{\vec{u}.\vec{v}}{\|\vec{u}\|.\|\vec{v}\|}\right) \quad \text{where} \quad \vec{u}\begin{pmatrix}1\\0\end{pmatrix} \quad \text{and} \quad \vec{v}\begin{pmatrix}1\\ \frac{\mathrm{d}P_y(t)}{\mathrm{d}t}\end{pmatrix} \tag{A.3}$$

Which gives :

$$\beta = \arccos\left(\frac{1}{\sqrt{1+\frac{\mathrm{d}P_y(t)}{\mathrm{d}t}^2}}\right) \tag{A.4}$$

And then we can compute Δ_y:

$$\begin{aligned}\Delta_y &= (y_d(x_i) - P_y(x_i))\cos(\beta) + P_y(x_i) - y_d(x_i) \\ &\text{with} \quad y_d(x_i) = (r + P_{ry}(x_i))\sin(\alpha + \varepsilon P_\theta(x_i)) + P_y(x_i)\end{aligned} \tag{A.5}$$

$$\Delta_y = (r + P_{ry}(x_i))\sin(\alpha + P_\theta(x_i))\left(\frac{1}{\sqrt{1+\frac{\mathrm{d}P_y(t)}{\mathrm{d}t}^2}}\right) - (r + P_{ry}(x_i))\sin(\alpha + P_\theta(x_i)) \tag{A.6}$$

$$\tan(\beta) = \frac{\Delta_y}{\Delta^y{}_x} \tag{A.7}$$

It is important to note that the simplification of cos(arcos) is possible because the argument is in]-1,1[The process to get the Δ_z is similar.

For coefficients used in the simulations, those secondary impacts were smaller than the integral precision of the helix portion. But this needs to be studied in case of bigger deformations (use of the sensor for civil engineering for example) or smaller uncertainties of the sensor.

List of acronysms

ALICE A large Ion Collider Experiment, one of the LHC detector.

ATLAS A Toroidal LHC Apparatus, one of the LHC multipurpose detector.

BBA Beam Based Alignment.

BCAM Boston CCD Angle Monitor, an optical metrology instrument developed by Open Source Instruments.

Belle II Particle physics experiment designed to study the properties of the B meson and other particles.

BEPCII Beijing electron-positron Collider II.

BIPM Bureau International des Poids et Mesures, International Bureau of Weights and Measures, an intergovernmental organisation defining measurement standards in chemistry, ionising radiation, physical metrology and coordinated universal time.

BPM Beam Position Monitor.

CCD charge-coupled device.

CEPC Circular Electron Positron Collider, a proposed particle collider in China.

CERN Organisation Européenne pour la Recherche Nucléaire, European Organisation for Nuclear Research.

CLIC Compact Linear Collider.

CMM Coordinate Measuring Machine.

CMOS Complementary Metal Oxide Semiconductor.

CMS Compact Muon Solenoid, one of the LHC multipurpose detector.

DAFNE Double Annular Φ Factory for Nice Experiments, an electron-positron collider at th INFN Frascati National Laboratory in Frascaty, Italy.

DESY Deutsches Elektronen-Synchrotron, German Electron Synchrotron.

DOMS Distance Offset Measurement Sensor, composed of a sensor, a cable and a aquisition electronic board, measuring the distance to a conducting plate.

E-FSI extrinsic FSI, named after the analogy with the Fabry-Perot interferometers and their intrinsic and extrinsic configurations.

FBG Fiber Bragg Grating, is a type of reflector constructed in an optical fiber that reflects particular wavelength of light while transmitting others.

FC-APC Fiber Connector Angled Physical Contact.

FCC Future Circular Collider.

FCC-ee Lepton stage of the FCC.

FCC-hh Hadron stage of the FCC.

FC-PC Fiber Connector Physical Contact.

FC-UPC Fiber Connector Ultra-Physical Contact.

HERA Hadron-Electron Ring Accelerator.

HL-LHC High-Luminosity LHC, upgrade of the LHC to improve the luminosity of the machine.

HLS Hydrostatic Leveling System, composed of a sensor, a cable and a aquisition electronic board, measuring the distance to an equipotential of the earth gravity field materialised by a water surface.

ILC International Linear Collider.

IMD-FSI In-lined Multiplexed and Distributed FSI.

IP Interaction point, were the particles of the beams are colliding.

KEK 高エネルギー加速器研究機構 , High Energy Accelerator Research Organisation, in Tsukuba, Japan.

KEKB Particule collider, located in Tsukuba, Japan.

KLOE K LOng Experiment.

L* Distance from the IP to the start of the magnetic field of the first magnet closest to the IP.

LED Light-Emitting Diode.

LGC++ Logiciel Général de Compensation, Global Compensation Software, software developped in C++ at CERN to perform least square adjustment computations.

LHC Large Hadron Collider.

LHCb LHC beauty, one of the LHC detector.

LumiCal A calorimeter inside the detector to precisely measure the luminosity.

MDI Machine Detector Interface, notion defined in the section1.3.

oHLS Optical Hydrostatic Levelling Sensor.

oWPS Optical Wire Positioning Sensor.

PACMAN Particle Accelerator Components' Metrology and Alignment to the Nanometer scale, an Innovative Doctoral Program Network composed of 10 PhD students working on solutions to improve the accuracy of alignment for the components to be installed in the next generation of particle colliders.

QD0 Last quadrupole before the IP in the CLIC and ILC projects.

RASCLIC Red Alignment System for CLIC, an alignment system developed at Nikhef, the Dutch National Institute for Subatomic Physics.

RASNIK Red Alignment System NIKhef, an alignment system developed at Nikhef, the Dutch National Institute for Subatomic Physics.

RF Radiofrequency.

RHIC Relativistic Heavy Ion Collider.

SCT SemiConductor Tracker.

SOFO Surveillance d'Ouvrages par Fibres Optiques, Structure Monitoring by Optical Fiber.

SSW Single Stretched Wire method, used to measure the position of quadrupoles inside the cryostats at SuperKEKB.

SuperKEKB Upgrade of the KEKB particule collider, located in Tsukuba, Japan.

QC1L1e QC1L2e QC1L3e QC1L1p QC1L2p QC1L3p
QC1R1e QC1R2e QC1R3e QC1R1p QC1R2p QC1R3p Names given to the final focusing quadrupoles of the FCC-ee MDI. "QC1" means it is part of the first cryostat, the closest to the IP. "L" or "R" indicates on which side of the detector it is, right or left. The second number is the number of the quadrupole, sorted by their distance to the IP. "e" or "p" corresponds to the particule beam circulating in the quadrupole, which can be electron or positron. Therefore, QC1R2p is the second final focusing quadrupole closest to the IP, installed in the QC1 cryostat, on the right side of the detector and handling the positron beam.

UV Ultraviolet.

WPM Wire Position Monitor.

WPS Wire Positioning System, composed of a sensor, a cable and a aquisition electronic board, measuring the offset between the sensor and a wire.